RESEARCH ADVANCES IN
NANOSCIENCES, MICRO AND NANOTECHNOLOGIES

VOLUM 5

EDITORS:

JOSÉ ABRAHAM BALDERAS LÓPEZ
MÓNICA ROSALÍA JAIME FONSECA
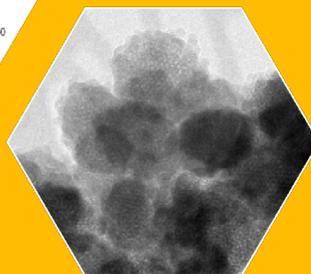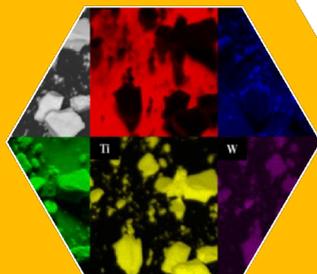
IPN

open access

OmniaScience

RESEARCH ADVANCES IN NANOSCIENCES, MICRO AND NANOTECHNOLOGIES

VOLUME 5

EDITORS

José Abraham Balderas López, Ph. D. •
Coordinator of the Nanoscience and Micro Nanotechnology Network
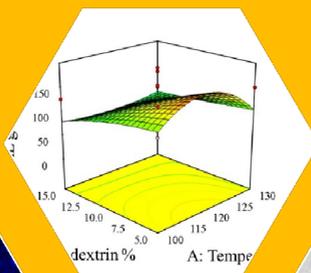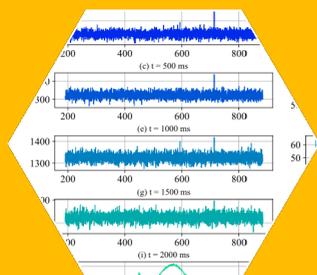Mónica Rosalía Jaime Fonseca, Ph. D. •

Research advances in nanosciences, micro and nanotechnologies. Volume V

Editors: José Abraham Balderas López and Mónica Rosalía Jaime Fonseca

EDITORIAL COMMITTEE

SEMICONDUCTORS AND MATERIALS AREA

Dr. Narcizo Muñoz Aguirre
Higher School of Mechanical and Electrical Engineering Azcapotzalco Unit (ESIME-AZC). Postgraduate Studies and Research Section. National Polytechnic Institute (IPN)

Dr. José Luis Jiménez
Interdisciplinary Professional Unit in Engineering and Advanced Technologies-National Polytechnic Institute (IPN)

HEATH AREA

Dra. Rocío Guadalupe Casañas Pimentel
Research Centre for Applied Sciences and Advanced Technology (CICATA - Legaria), National Polytechnic Institute (IPN)

Dr. Eduardo San Martín Martínez
Research Center for Applied Sciences and Advanced Technology (CICATA - Legaria), National Polytechnic Institute (IPN)

INDEX

PREFACE

This book, in its fifth iteration, includes valuable contributions from experts on topics related to nanotechnology, coordinated by Dr. José Abraham Balderas López, who is a researcher at the **Instituto Politécnico Nacional** (IPN) and who has coordinated the IPN Nanoscience and Micro-Nanotechnologies Research Network (RNMN) since January of 2024.

The field of nanotechnology is becoming increasingly important due to its impact in the areas of health, food, environment, energy and semiconductors. These areas are closely aligned with several of the missions presented by the Research and Postgraduate Secretariat, through the Coordination of Operation and Research and Postgraduate Networks of the IPN, at the **2024 Polytechnic Research and Postgraduate Networks Meeting**. These ten missions that will guide the research efforts at IPN in the coming years are:

1. Sustainable agriculture and food security.
2. Biodiversity, environment and water crisis.
3. Resilience and comprehensive risk management.
4. Transition towards renewable energies and energy sustainability.
5. Epidemiological surveillance and prevention of health risks.
6. Semiconductors and advanced electronics.
7. Strategic artificial intelligence and data science program.
8. Health for the future: prevention and control of chronic diseases.
9. Industry, value chains and infrastructure.
10. Aerospace research, telecommunications and connectivity.

Thus, this book compiles current research advances aligned to five of the missions presented above, standing out the advances made by researchers who participate in the Nanoscience and Micro-Nanotechnologies Research Network and contribute to the generation of scientific knowledge and cutting-edge technological development. The missions to which a closer alignment is shown by the chapters included in this book are: *Sustainable agriculture and food security*; *Biodiversity, environment and water crisis*; *Transition towards renewable energies and energy sustainability*; *Semiconductors and advanced electronics*; as well as *Health for the future: prevention and control of chronic diseases*. As can be seen, the collaboration of members of the IPN Research Networks arises as a key factor in solving problems of regional, national, or international interest.

LIST OF CHAPTERS BY RESEARCH AREA

Sustainable agriculture and food security

Among the main challenges that future generations will face is the lack of food and/or spaces to grow or store it, for this reason the book includes two chapters related to these topics: "Prototype hydroponic system with LED lighting control and parameter measurement for various horticulture crops" and "Microencapsulation of Nance (*Byrsonima crassifolia* L.) extraction by spray drying", for the production of functional foods.

The following two chapters are aligned with mission two, **biodiversity, environment and water crisis**.

"Mesoporous Silica Nanoparticles as Adsorbents of Methylene Blue Aqueous Solutions", this work discusses the risks posed by water contaminated with methylene blue, as well as the most used methods for the removal of this dye, highlighting the adsorption method and mesoporous silica nanoparticles as adsorbents.

"Dynamic System Development for Real-Time Light Spectra Acquisition for Optical Biosensor Applications in Python", this work presents the development of a dynamic real-time light spectrum acquisition software system utilizing Python, a high-level programming language, focusing on optical biosensor applications.

In the **transition towards renewable energies and energy sustainability**", the following contributions are presented:

"*Bio-jet fuel* production from the enhanced crops of *Botryococcus braunii* by MgO nanoparticles (MgO NPs)", in this work, bio-jet fuel was obtained from the lipids of the microalgae *Botryococcus braunii*, cultivated in pre-treated wastewater and adding MgO NPs to improve lipid and / or biomass production in the crop.

"TiO_2-WO_3 Heterojunctions for Photocatalytic Hydrogen Generation", in this research, it was synthesized TiO_2 nanosheets and a composite based on a TiO_2-WO_3 heterojunction using a hydrothermal method as a clean energy for hydrogen production.

In **semiconductors and advanced electronics** you can find the chapters titled:

"Effect of Density of States in electrical simulation of amorphous Indium-Gallium-Zinc-Oxide Thin Film Transistor", materials such as amorphous Indium-Gallium-Zinc-Oxide (a-IGZO) due to their optical transparency and low deposition temperatures are used in low-cost flexible electronics, which gives the possibility of a-IGZO TFTs in portable electronics for healthcare sensing.

"Numerical Modeling of Surface Acoustic Waves for Electronic Filter Design", in this work, a detailed methodology for the design and numerical simulation of a surface acoustic wave bandpass filter in a 128°YX $LiNbO_3$ piezoelectric material is presented.

Finally, in "**health for the future: prevention and control of chronic diseases**", the following research is presented:

"Silver and copper nanofluids, synthesis, characterization and their antimicrobial properties against pathogenic microorganisms", in this work, important applications related to the antimicrobial activity of nanoparticles are explored, which is an alternative to the use of antibiotics and may be a solution to the problem of microbial resistance to the latter.

"Synthesis of new chitosan-glutaraldehyde scaffolds for Tissue Engineering using Schiff reactions", development of suitable scaffolds for tissue engineering is still one of the most important fields in regenerative medicine.

I hope this book helps to disseminate the works of our scientists and to improve the knowledge of the subjects studied and developed in the area of nanoscience and micro-nanotechnology.

Dr. Itzamá López Yáñez
Coordinador de Operación y Redes de Investigación y Posgrado del IPN
Secretaría de Investigación y Posgrado del Instituto Politécnico Nacional

PROTOTYPE HYDROPONIC SYSTEM WITH LED LIGHTING CONTROL AND PARAMETER MEASUREMENT FOR VARIOUS HORTICULTURE CROPS

Brian Emmanuel Ascención-Martínez,
Diego Adrián Fabila-Bustos,
Luis Felipe de Jesús Hernández Quintanar,
Macaria Hernández-Chávez*

Laboratorio de Optomecatrónica y Energías, UPIIH, Instituto Politécnico Nacional, Distrito de Educación, Salud, Ciencia, Tecnología e Innovación, San Agustín Tlaxiaca, Hidalgo, 42162, México.

   * mhernandezch@ipn.mx

Abstract

Among the main challenges that future generations will face is the scarcity of food and the lack of space for its cultivation. Hydroponics is an agricultural technique that is based on the independence of plants from the soil, since it uses only water as a means of transporting the substances and nutrients that crops need for their proper development, increasing efficiency and reducing the time in which crops are ready for harvest. In addition, the implementation of alternative lighting systems that allow the growth of plants without depending on solar illumination, being the use of LEDs one of the most popular and with the best results. This work describes the design process of a prototype hydroponic system with LED lighting control and measurement of parameters (temperature, pH, conductivity and dissolved oxygen) for various horticulture crops.

1. Introduction

Agriculture is a fundamental part of the Mexican economy, accounting for 4 % of GDP in 2024 [1]. According to a projection study carried out by the National Population Council (CONAPO), it is estimated that Mexico will have a population of 138.1 million inhabitants by 2030 and 148.2 million by 2050 [2]. This population increase is directly related to the main challenge that agriculture will face in the coming years: ensuring food supply for the population. Demographic expansion coincides with the decrease in land available for agriculture, and it is therefore predicted that by 2050, only 0.16 ha of arable land will be available in the country to produce the food demanded by one person per year, compared to 0.27 ha per person in 1980 and 0.18 ha in 2015 [3].

In addition to the country's supply capacity, the environmental and biological problems present in the crops that affect their availability must be taken into consideration. According to the latest data collected by the National Institute of Statistics and Geography (INEGI), in 2017 there were 32,406,237 hectares in the country destined to agricultural production units, performing open-air agriculture. Of this total, 21 % (6,810,762 hectares) correspond to irrigated surface, while the remaining 79 % (25,595,475 hectares) correspond to rainfed surface. Of the 101,828 production units surveyed, only 17,388 used protected agriculture production strategies, the majority of which were of the greenhouse type (54.1 %). On the other hand, among the main problems presented during the development of activities in the production units, crop losses due to climatic causes (74.7 %), crop losses due to biological causes (44.2 %) and loss of soil fertility (28.4 %) stand out. It should be noted that among the main reasons for crop losses due to climatic causes are wind, excess humidity, hail, low temperatures and floods [4].

The environmental impact of agricultural development must also be taken into account. In terms of water availability and use, in Mexico in 2015, a total volume of water concessioned in the country of 266,569 million cubic meters was determined. Of this amount, it is estimated that 32.2% had a consumptive use. Of the consumptive use, more than 3 quarters was used for agricultural purposes, with a percentage of 76.3%, with costs per cubic meter of water ranging between $2.49 MXN and $78.67 MXN depending on the area in which it was obtained. Of the total amount of water used for agriculture, only 46 % is used efficiently [5]. In addition, agriculture represents the largest proportion of human land use and is a major source of emissions of gases that contribute

to the greenhouse effect, such as methane (CH_4), nitrous oxide (N_2O) and to a lesser extent, carbon dioxide (CO_2) [6].

As highlighted in the national agricultural planning 2017-2030 conducted by the Secretariat of Agriculture, Livestock, Rural Development, Fisheries and Food (SAGARPA), trends in food and agriculture should focus on technological development and innovation seeking new triggers in production systems [7]. The main strategies for increasing agricultural production should focus on improving yield per unit area and increasing the cultivated area [3].

This paper describes the design process of a prototype hydroponic system with LED lighting control and parameter measurement for vegetables. The prototype was developed with the intention of using it as a research and experimental tool, with the objective of comparing the results of growing crops of the same species under different lighting conditions. The development of hydroponic crops considers supplying the nutrients required by the plants through water, without the need of any substrate. In addition, the illumination received by the plants was controlled by means of light-emitting diodes (LEDs) with different wavelengths to compare their effect on plant growth. Finally, a graphic interface was implemented that, with the help of sensors located in the prototype, allows the user to visualize the history of some physical and chemical parameters (temperature, pH, conductivity and dissolved oxygen) in which the crop has been found. This prototype is intended to serve as an auxiliary in the promotion and development of new technologies for more efficient crop production in the country.

2. Methodology

Figure 1 shows a block diagram of the prototype. The system is composed of three main units, the physical design of the prototype, the circuit that is responsible for polarizing the LED light sources and sensors and monitoring the signals generated by the latter, and finally the control circuit of the luminous intensity of the LEDs.

2.1. *Case*

A case was built with four divisions, taking into account that the dimensions of each space will be determined by the maximum expected dimensions of the growth of each specimen of each plant, in this case the selected vegetables were lettuce and beans. Based on work done with lettuce under similar conditions, i.e., with LED

lighting and applying hydroponics as an agricultural technique, measurements were obtained after 35 days of testing on lettuce specimens with a maximum width of 12 cm and a height no greater than this measure [8]. On the bean side, the height can reach 28 cm in a growth period of 30 days [9]. Based on these two measures, it was decided to take as a basis the maximum width that lettuce plants could have and the maximum possible height of bean plants. This led to establish 30 cm x 12 cm x 24 cm as design parameters for the internal dimensions of the prototype. Considering that in each space of the prototype a lettuce specimen and a bean specimen will be placed, each plant will have a total volume for its development of 4320 cm^3 considering dimensions of 12 cm x 12 cm x 30 cm. It was decided to design a structure that allows each space to have the dimensions proposed and that isolates each space from the outside so that the light irradiated in each one is the desired one and that allows the correct oxygenation of the plants.
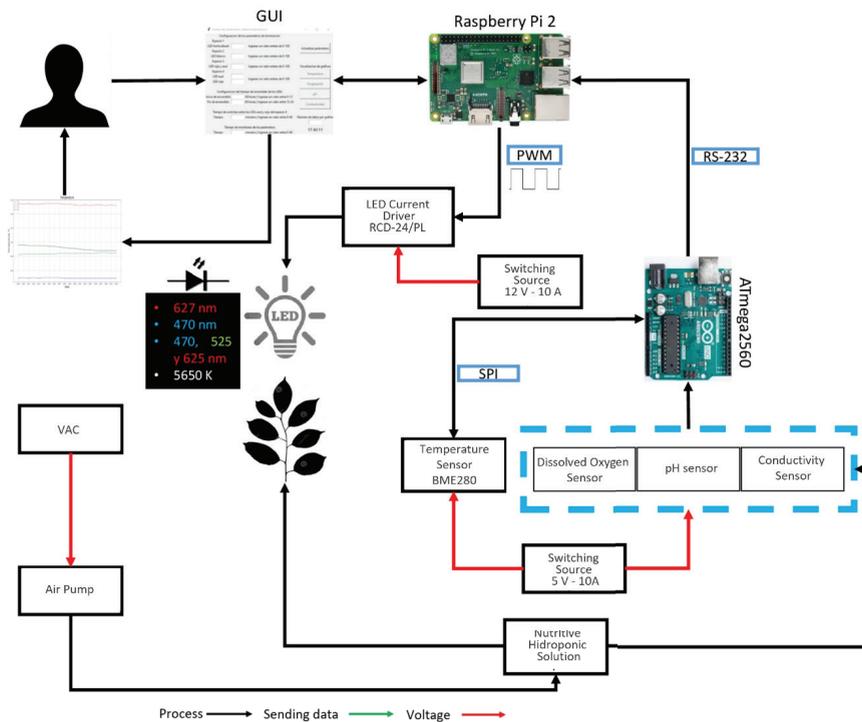
Figure 1. Block diagram of the developed system.

Figure 2 shows graphically how the prototype is physically constituted in a general way, in gray color the structure of each space is observed while in black color the water tank of the whole system is observed. The walls of each space

are made of acrylic with a thickness of 3 mm, where each wall will have eyebrows that allow the assembly of these under pressure.
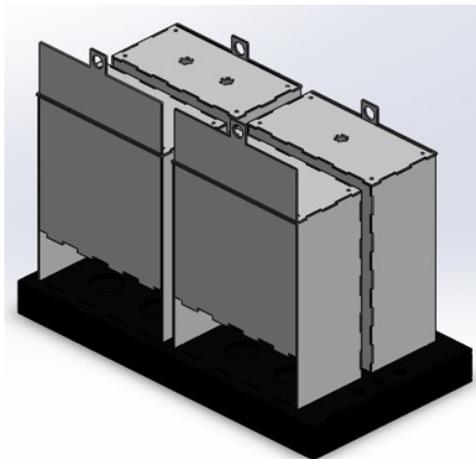
Figure 2. Representation of the physical design of the prototype.

The prototype must have the capacity to store at least one specimen of each crop to be analyzed in each of the 4 spaces destined for the comparison of the effects of the wavelengths of the LEDs, with one or two LEDs in each space as the case may be (see Table 1), these crops correspond to lettuce and beans.

Type of LED	Wavelength (nm)
Red	627
Blue	470
Multicolor (blue, green and red)	470, 525 y 625
White	400-700

Table No. 1 Types of LEDs used and their wavelengths.

2.2. *Graphical User Interface (GUI)*

As shown in Figure 1, the operation of the GUI consists of filling in all the input fields where the parameters for LED illumination intensity, LED on/off time, switching time between blue and red LEDs, update time for monitoring the parameters acquired from the sensors and the maximum number of data to be stored in the graphs are established. The GUI programming has default

PROTOTYPE HYDROPONIC SYSTEM WITH LED LIGHTING CONTROL AND PARAMETER MEASUREMENT FOR VARIOUS HORTICULTURE CROPS

parameters set so that if the user does not enter data, the system can function when the program is run. However, when entering data by filling in the input fields and executing the "Update parameters" button, the default values are updated to the values entered by the user, modifying the operation of the system. The buttons for displaying graphs remain disabled at startup until sensor data acquisition begins, when there is at least one data value, the graphs of the desired parameters are displayed.

Since the characteristics of the Raspberry Pi used as the main control element prevent it from reading analog signals and the oxygenation, pH and conductivity sensors handle signals of this type, it was decided to include an additional microcontroller as an intermediary for the sensor signals. The microcontroller chosen was the ATmega328P (Microchip Corp.), which is responsible for reading the sensor signals to send the corresponding data to the Raspberry Pi via serial communication. The choice of this microcontroller is due to the fact that it has the necessary interface for the acquisition of analog signals; in addition, using this platform reduces the cost and facilitates the assembly with respect to other options. For this reason, the programming of the Raspberry Pi includes the creation of a serial object, which is read to obtain the values of the sensors. For its part, a program was developed with the ability to interpret the signals from the sensors and send the corresponding values of these through serial communication.

2.3. *Sensors*

In order for the user to be able to observe the specific parameters for the water of each hydroponic crop (oxygenation, pH and electrical conductivity) and their correct measurement, it was decided to also take measurements of the oxygenation, pH and electrical conductivity in the water of the crops; for this, the sensors to be used were DFRobot® brand sensors, specifically the SEN0161 (pH), DFR0300 (electrical conductivity) and SEN0237-A (oxygenation) models. These sensors have a connector that converts the output signal of the measured parameter into an analog signal that will be interpreted by the controller to be used; which avoids a previous signal conditioning stage, also in its physical design the part of the sensor that needs to be in direct contact with the water has a length of up to 26 mm, with a diameter of up to 13 mm, which allows measurements in shallow water tanks [10].

In the case of sensors that are in direct contact with water: pH, conductivity and oxygenation sensors, based on their dimensions, a minimum depth of 13 mm and a diameter of 26 mm is necessary for them to have support and be able to perform measurements correctly. These characteristics were considered in the design by placing three holes with a diameter of 30 mm in the part corresponding to the water tank lid, and since the tank has a depth of 4 cm, it was only necessary to insert the sensors in these holes in order to carry out the measurement, as shown in Figure 3.

Figure 3. Mounting of pH, conductivity and oxygenation sensors in the prototype´s water tank.

Additionally, it was determined that in order to define the conditions in which each crop was according to the light conditions, it was necessary to measure the temperature in each space, so the BM280 sensor (Adafruit Industries) was used, which is a temperature sensor that uses the SPI communication protocol. On the other hand, to vmaintain better oxygenation of the water in the prototype tank, two water pumps in the fish tanks were used.

2.4. *Assembly of hydroponic baskets*

In the case of the hydroponic baskets, the space they would occupy was determined from the design stage of the acrylic pieces, locating two circles of 5 cm in diameter that were distributed uniformly in the spaces in each corresponding area for the development of crops, so it was only necessary to introduce the hydroponic baskets in the holes intended for this purpose as shown in Figure 4.

Figure 4. Assembly of the hydroponic baskets in the prototype.

2.5. *Crop germination*

The germination process of lettuce and bean crop seeds was carried out independently of the system, initiating germination in specialized phenolic foam for hydroponics, the procedure involved saturating the foam by immersing it in water until fully moistened, subsequently, bean and lettuce seeds were positioned within the foam, and the container was covered to maintain humidity. To expedite germination, twenty-four bean and 24 ball-type lettuce seeds were deployed, as depicted in Figure 4A. Once the specimens had germinated and developed their initial leaves, they were transferred to the hydroponic system. Figure 4B shows the germinated crop specimens.

A)

B)

Figure 4. (A) Placement of bean and lettuce seeds for germination in phenolic foam for hydroponics and (B) Germination of the cultures in the phenolic foam.

The preparation of the solution consists of a process where, in addition to adding nutritive salts from the Semillas de amor® brand to the water to be used, parameters such as pH and conductivity must be adjusted.

	Parameters	
	pH	Conductivity (mS/cm)
Pure water	7.1	0
Solution after adding nutritive salts	3.0	2.14
Solution after adjusting pH with 0.5 M solution of NaOH	5.5	2.27

Table 2. Parameters of the nutritive solution.

Epura® brand bottled water was selected, according to a study carried out with different brands of bottled water in Mexico [11], this is the brand that presents the lowest concentration of total dissolved solids (TDS) with 9 ppm and calcium with a value of less than 20 mg/L. The importance of maintaining a low value in this concentration lies in the fact that in order to optimize the efficiency of the nutrient solution, the pH and conductivity parameters must be controlled, and these values are modified when nutritive salts are added to the water. The appropriate parameters to optimize the efficiency of the nutrient solution are between 5.5 and 6.5 in the case of pH [12], and between 1 and 3 mS/cm for conductivity [13]. When measuring the bottled water, pH values of 7.1 and conductivity of 0 mS/cm were obtained; however, when the mineral salts were added, the pH value was reduced to 3.0 while conductivity increased to 2.14 mS/cm. In spite of complying with an adequate conductivity value, the pH value was very low; for this reason, 8 milliliters of a sodium hydroxide (NaOH) solution with a concentration of 0.5 mol/L were added to the nutrient solution to increase the pH, obtaining after this process a pH value of 5.5 and a conductivity of 2.27 mS/cm, complying with the adequate values in the solution parameters. Table 3 shows a concentration of these data.

With the elements assembled and working in the prototype, the GUI implemented in the Raspberry Pi and the nutrient solution with the appropriate parameters, the system was put into operation in order to validate its operation. For this, one lettuce and one bean species were introduced into the prototype for each space of the system, as shown in Figure 5, and the parameters were set in

Parámetro	Set Value
Luminous Flux of LEDs	75%
Turn-on Hour of LEDs	08:00
Turn-off Hour of LEDs	22:00
Switching time between Blue and Red LEDs in block 4	30 min
Acquisition time of sensors parameters	5 min
Points per graph	30

Table 3. Conditions established for system tests.

the GUI for its operation: all LEDs were set to an illumination power of 75 % of capacity, 14 hours of continuous illumination were set, turning on the LEDs at 08: 00 hours and turning them off at 22:00, a switching time between LEDs of space 4 was set, in addition to a sensor parameter acquisition time of 5 minutes and an amount of data per graph of 30, these values are concentrated in Table 3.

Figure 5. Implementation of the germinated crops in the prototype.

3. Results

At the end of the implementation stage and with the device in operation, the operation of the system was validated and the results were concentrated. 21 days after placing the germinated cultures in the system for their development, their growth was analyzed. Figure 6 shows photographs of the crops in the system; it should be noted that, due to problems with the low germination rate of beans,

only 3 specimens could be obtained; for this reason, only lettuce was placed in the space with intermittent blue and red LED lighting.
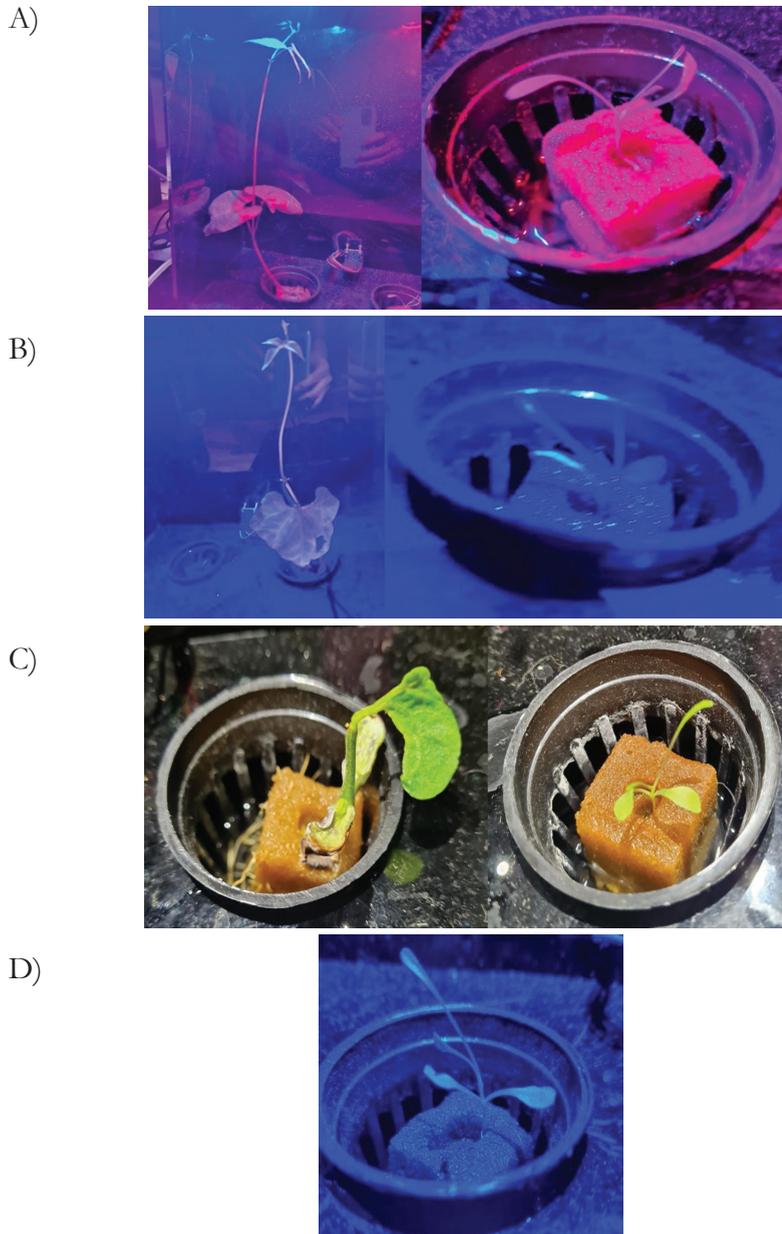
A)

B)

C)

D)

Figure 6. Crops under different sources of illumination: A) Constant with blue and red LEDs, B) Constant with LED Horticultural, C) Constant with white LEDs and D) Intermittent with blue and red LEDs.

It stands out the fact that the crops where the highest growth was obtained were with constant illumination of blue and red LEDs in the case of beans, and with intermittent illumination of blue and red LEDs in the case of lettuce. The lowest performance for both bean and lettuce was with white illumination. The data corresponding to the length of each crop and the number of leaves developed are shown in Table 4.

Type of LED	Crop	Length (cm)	Number of leaves
Blue and Red	Lettuce	30	8
	Beans	2	4
Horticultural	Lettuce	21	5
	Beans	2	5
White	Lettuce	4.5	3
	Beans	1.5	4
Blue and Red Modulated	Lettuce	3	4

Table 4. Conditions established for the system tests.

While, for beans, the minimum temperature during its growth phase is 10 °C [14], in the case of lettuce, the optimum temperature during this phase is considered to be 14 - 18 °C. This may explain the reason for the poor growth of lettuce so far, due to the fact that in the area where this practice is being carried out, during the winter period, the maximum temperature does not exceed the temperature range for optimal lettuce growth. It should be noted that although the prototype is capable of measuring the temperature, it does not have any actuator element that can modify it.

With the system running and the operating parameters configured through the GUI, it was verified that the sensors were working properly and that the interface was capable of storing the acquired data for later visualization. Performing a test for 20 minutes, where values of all parameters were stored every minute, the graphs shown in Figure 7 were obtained.

As can be seen in some graphs, the parameters remain constant over time, the variations are minimal, with a variation of 3.7 % for conductivity, 3.6 % for oxygenation, 1.2 % for pH and a percentage of less than 1 % in the temperature values; and these are only affected considerably after hours in the case of temperature and days in the case of conductivity and pH, in the case of oxygenation the values depend on the operation of the water pumps.

A)
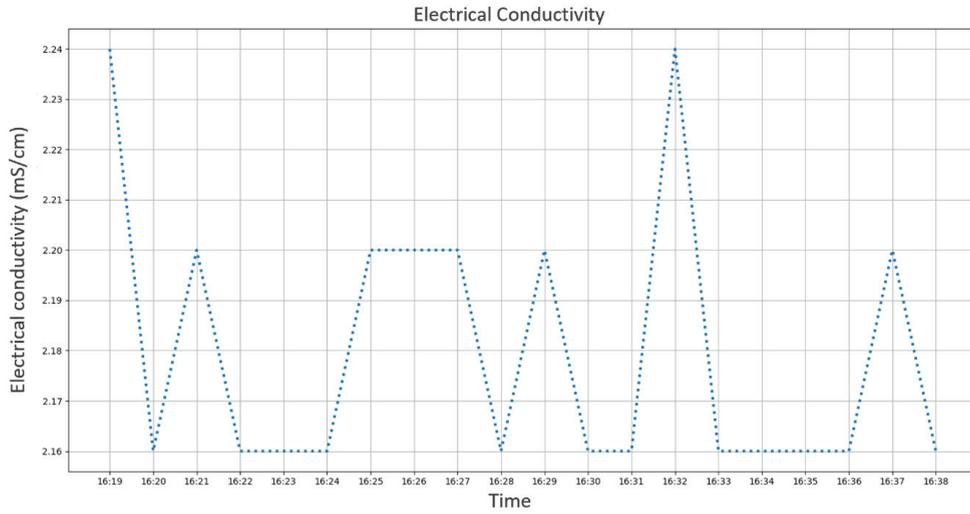
B)
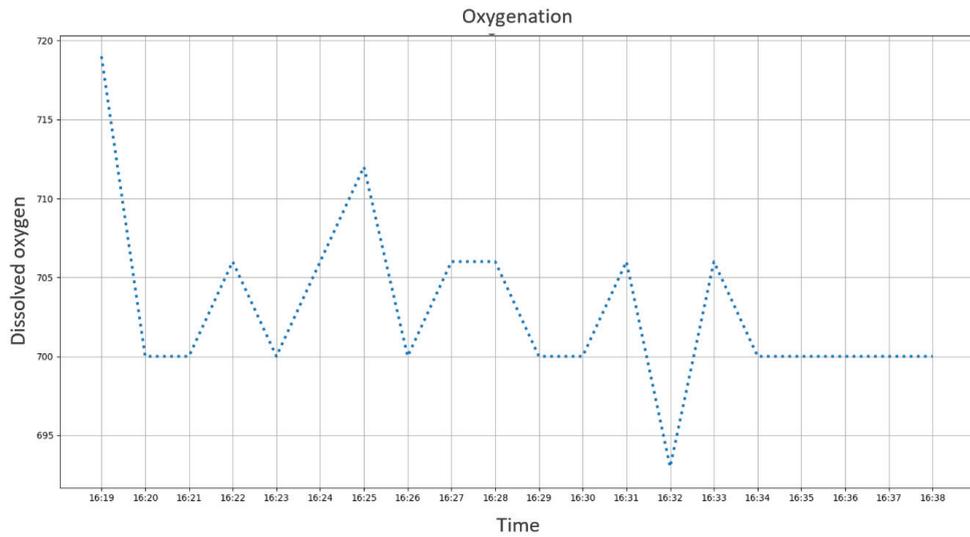
C)
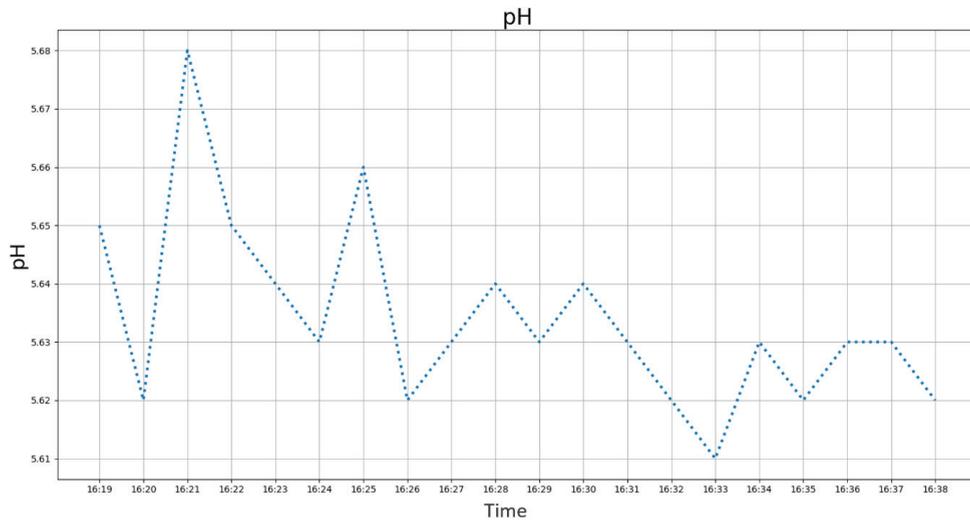
D)
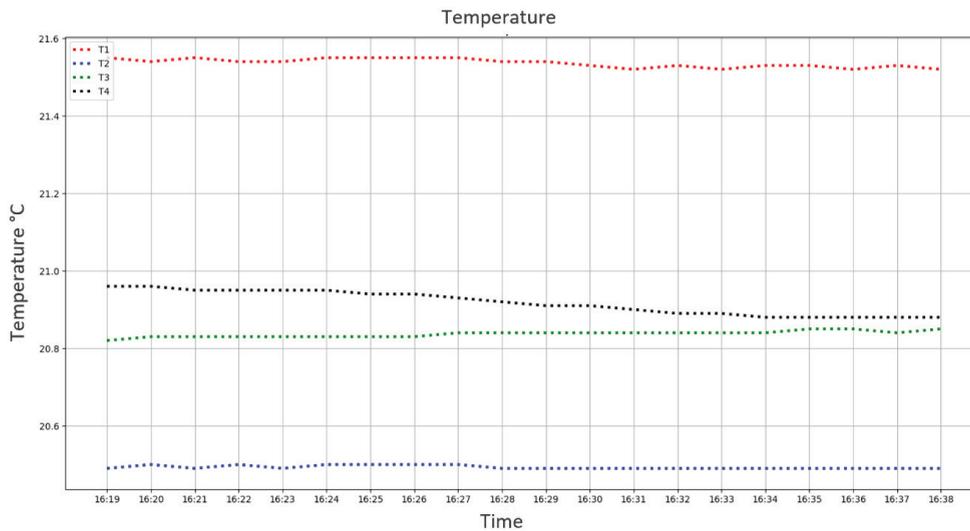
Figure 6. Behavior of: A) electrical conductivity, B) dissolved oxygenation in water,
C) water pH and D) temperature.

4. Conclusions

In this work a prototype of a functional hydroponic system was developed, which allows the development of crops while it is possible to monitor chemical parameters such as pH, and physical parameters such as electrical conductivity, which depends on the concentration of salts, and oxygen dissolved in the water. The system provides the user through a GUI the possibility to configure the conditions to operate automatically in the data acquisition times of the sensors, the amount of stored data of the parameters, the switching times between LEDs and the on and off of the LEDs, allowing to set the intensity of illumination required. In addition, the data obtained from the different measured parameters can be displayed graphically in the GUI.

References

1. World Bank. (2024, March 15). *World Bank*. Retrieved from Agriculture, value added (% of GDP)
    https://datos.bancomundial.org/indicador/NV.AGR.TOTL.ZS

2. National Population Council. (2018). *Projections of the population of Mexico and the states 2016–2050*. Mexico City: National Population Council.

3. Baldivia, A. S. (2017, February 17). *Population papers*. Retrieved from Food Availability in Mexico: An analysis of 35-year agricultural production and its projection for 2050
    https://www.redalyc.org/jatsRepo/112/11252977008/html/index.html#gt5

4. National Institute of Statistics and Geography. (2018, July 25). *INEGI*. Retrieved from the 2017 National Agricultural Survey.
    https://www.inegi.org.mx/contenidos/programas/ena/2017/doc/ena2017_pres.pdf

5. Fund for Environmental Communication and Education, A. C. (2016). *Water in Mexico: A handbook for correct decision-making*.

6. García, A., & Laurín, M. (2006). Contribution of organic farming to climate change mitigation compared to conventional farming. *Agrecology*.

7. Ministry of Agriculture, Livestock, Rural Development, Fisheries and Food. (2017, September 11). *Government of Mexico*. Retrieved from National Agricultural Planning 2017–2030.
    https://www.gob.mx/cms/uploads/attachment/file/255627/Planeaci_n_Agr_cola_Nacional_2017-2030-_parte_uno.pdf

8. Lin, K.-H., Huang, M.-Y., Huang, W.-D., Hsu, M.-H., Yang, Z.-W., & Yang, C.-M. (2013). The effects of red, blue, and white light-emitting diodes on the growth, development, and edible quality of hydroponically grown lettuce (Lactuca sativa L. var. capitata). *Scientia Horticulturae, 86*–91.
    https://doi.org/10.1016/j.scienta.2012.10.002

9. Bierhuizen, J. F., & Wagenvoort, W. A. (1974). Some aspects of seed germination in vegetables. 1. The determination and application of heat sums and minimum temperature for germination. *Scientia Horticulturae, 213*–219.
    https://doi.org/10.1016/0304-4238(74)90029-6

10. DFRobot. (2018, December 28). *DFRobot*. Retrieved from the Gravity Liquid Sensor Selection Guide.
    https://www.dfrobot.com/blog-1138.html

11. Filters and More. (2020, May 3). *YouTube*. Retrieved from What is the best brand of bottled water for your project?
    https://www.youtube.com/watch?v=YjAf4pW0N60

12. Hydro Environment. (2020, February 18). Retrieved from Hydro Environment Catalog.
    https://hydroenv.com.mx/catalogo/

13. Cardador, M. J. (2020, April 1). *Hydroponics to the cube*. Retrieved from Electrical Conductivity.
    https://hidroponiaalcubo.wordpress.com/conductividad-electrica/

14. Barrios-Gómez, E. J., & López-Castañeda, C. (2009). Base temperature and leaf extension rate in beans. *Agrociencia, 43*(1), 29–35.
    http://www.scielo.org.mx/scielo.php?script=sci_arttext&pid=S1405-31952009000100004&lng=es&tlng=es

MICROENCAPSULATION OF NANCE (*BYRSONIMA CRASSIFOLIA* L.) EXTRACT BY SPRAY DRYING

**A. Lozada-Zarate[1], P. López-Ordaz[1],
M. C. Fernández-Martínez[2], M. R. Jaime–Fonseca[2],
Miguel A. Aguilar-Méndez[2], J. Yáñez-Fernández[1*]**

[1]Unidad Profesional Interdisciplinaria de Biotecnología, Instituto Politécnico Nacional. Departamento de Bioingeniería. Av. Acueducto S/N Col. Barrio la Laguna, Ticomán, C.P. 07340, Ciudad de México, México.

[2]Centro de Investigación en Ciencia Aplicada y Tecnología Avanzada Unidad Legaria, Instituto Politécnico Nacional. Legaria 694 Col. Irrigación, 11500, Ciudad de México, México.

* jyanezfe@ipn.mx

Abstract

This study aimed to evaluate the effect of spray drying parameters on the antioxidant and physicochemical properties of a microencapsulated extract of *Byrsonima crassifolia* (Nance) fruit. An aqueous extract of nance pulp was analyzed for total phenolics, flavonoids, and antioxidant capacity before and after the spray-drying microencapsulation process. The microencapsulation was carried out using a spray dryer by varying the drying temperature (110-134 °C) and maltodextrin concentration (3-17%). The results showed that the nance extract contained 185.06 μg of gallic acid/mL and 18.38 μg of quercetin/mL in terms of total phenolics and flavonoids, respectively. The antioxidant capacity as a percentage inhibition of the extract was 30.11%, and that of the microencapsulates ranged from 9.25 to 45.64%. Conversely, microencapsulated total phenolics ranged from 173.11 to 4.75 μg/mL gallic acid. The yields for the microencapsulation process ranged from 80 to 90%, obtaining powders with moisture contents lower than 2.63%. The results indicate a strong interaction between drying temperature and maltodextrin concentration. High maltodextrin concentrations and high drying temperatures hurt the bioactive properties. The powders obtained in the different formulations show microparticles between 10 and 20 μm sizes, with smooth, collapsed, and rough surfaces.

Keywords: microencapsulation, nance, phenols, flavonoids, antioxidant capacity.

1. Introduction

Byrsonima crassifolia L., commonly known nance or changunga, is a fruit native to the tropical Americas and is distributed in different regions of Central and South America and in the southeastern part of Mexico. In Mexico, the main nance producing states are: Campeche, Chiapas, Guerrero, Jalisco, Michoacán, Morelos, Nayarit, Oaxaca, Sinaloa, Veracruz and Yucatán, with an annual production of 7,713.13 tons [1]. Nance is a rounded drupe that is produced in pendulous infructescences of 10 to 15 cm in length. When ripe, they are about 1.7 to 2 cm in diameter, slightly orange-yellow in color, with abundant sweet and sour flesh surrounding a large, hard stone [2]. The main bioactive compounds contained in the nance fruit are gallic acid and quercetin [3, 4]. It also contains trace amounts of catechin, epicatechin, rutin and kaempferol [5]. Several studies have demonstrated the antioxidant activity of nance leaves, fruits, and seeds. It is also reported to have anti-inflammatory, antiproliferative, and antihyperglycemic properties [6 - 8]. In addition, extracts of *Byrsonima crassifolia* L. have bactericidal, fungicidal, and topical anti-inflammatory activities [9]. This extract has been used medicinally since pre-Hispanic times, mainly for the treatment of gastrointestinal disorders and gynecological inflammation [10]. Nance is also highly valued as a dietary supplement due to its high vitamin and mineral content (thiamine, riboflavin, and niacin); it is also an excellent source of dietary fiber [11, 12].

Microencapsulation is a process that improves the properties of the spray-dried core, taking into account the matrices used and the operating conditions of the equipment. In addition, it facilitates the handling of the bioactive compounds, improves their solubility and stability, protects against the degradation of the cores, controls the release of the compounds and masks unpleasant tastes and odors. The type and characterization of the coating agent used for encapsulation determines the final properties of microencapsulated materials, such as efficiency and microcapsule size. Due to its low cost and its encapsulation efficiency of hydrophilic core materials such as anthocyanins and gallic acid, maltodextrin is the most used wall material in microencapsulation technology [13].

There has been an increase in interest in the use of raw materials for the development of products that are rich in bioactive compounds for use as health-promoting agents in the food, pharmaceutical and cosmetics industries. Thus, the nance fruit is considered as a feasible raw material for the application and development of products with functional properties, due to the growing

demand for foods with natural antioxidants and nutritional potential. Therefore, the objective of the present research was focused on the quantification and evaluation of bioactive compounds and antioxidant capacity of nance extract microencapsulates.

2. Materials and Methods

2.1. *Materials*

The nance fruits were procured from the local market in the city of Pátzcuaro, Michoacán. Prior to use, the fruits were subjected to a washing process and disinfected in a 0.1% solution of sodium hypochlorite. The size of the fruits was selected based on considerations of mechanical damage. Subsequent to this, the pulp was extracted and stored in a freezer at -20 °C until use.

2.2. *Preparation of the extracts*

For the extract preparation, 100 milliliters of distilled water was combined with 10 grams of nance pulp, which was then stirred for a period of 40 minutes at a temperature of 40 °C. After that, vacuum filtration was conducted. The extract was subsequently stored under refrigeration until required for use.

2.3. *Determination of Total Phenolic Contents (TFC)*

Total phenolic contents were determined by using the Folin–Ciocalteu method, according to the methodology reported by Robert et al., [13]. The nance extract (500 µL) was add to Folin–Ciocalteu reagent (1:10- diluted) and sodium carbonate (2 mL/7.5%). Then the mixture was kept for 60 minutes at room temperature. Following the incubation period, the absorbance was measured at 760 nm using a UV–Visible spectrophotometer (Perkin Elmer Lambda XLS, UK).

2.4. *Determination of Flavonoid Contents*

The flavonoid content of the aqueous extract was quantified using the method described by Chang et al. [14]. The results were expressed as µg/mL of quercetin. A standard curve was generated over the range of 0 to 50 µg/µL. A total of 500 µL of the aqueous extract was taken and subsequently combined with 1.5 mL of methanol, 100 µL of a 10% aluminum chloride solution, 100 µL of a 1M potassium acetate solution, and 2.8 mL of distilled water. Absorbance readings

were obtained at 415 nm using a UV–Visible spectrophotometer (Perkin Elmer Lambda XLS, UK).

2.5. *ABTS$^{\bullet+}$ radical cation scavenging activity*

The antioxidant capacity was determined according to the methodology developed by Kuskoski et al. [15], with some modifications. Then, 20 μL of the aqueous extract was taken and 2 mL of the ABTS$^+$ radical dilution was added, after which the absorbance (Abs) was taken. The results are expressed as percentage inhibition, which is calculated by the following equation:

$$inhibition(\%) = \frac{Initial\ absorbance\ of\ ABTS\text{-}Absorbance\ of\ the\ sample\ after\ 6\ min}{Initial\ absorbance\ of\ ABTS} \times 100$$

2.6. *Production of microcapsules*

Maltodextrin was dispersed in the aqueous extract of nance at different concentrations (Table **1**) by magnetic stirring for 30 minutes. The drying process was carried out in a Büchi mini spray-dryer B-290 (Flawil, Switzerland). The parameters were selected based on preliminary tests: a suction flow rate of 35 m^3/h and a solution volume flow of 2.61 mL/min. Central Composite Design (CCD) was used to evaluate the spray drying conditions (Design Expert 7.0v, USA). Furthermore, the hygroscopicity and moisture content of the microencapsulates obtained were evaluated.

Experiment	Maltodextrin concentration (%)	Inlet temperature °(C)	Key
1	10	120	MD10120
2	10	106	MD10106
3	10	120	MD10121
4	15	130	MD15130
5	5	110	MD05110
6	10	120	MD10122
7	10	120	MD10123
8	3	120	MD03120
9	15	110	MD15110
10	10	120	MD10124
11	5	130	MD05130
12	10	134	MD10134
13	17	120	MD17120

Table 1. Experimental design of microencapsulation.

2.7. *Characterization of the microcapsules*

2.7.1. *Moisture content*

The moisture content of the powder was determined gravimetrically according to AOAC method [16].

2.7.2. *Hygroscopicity*

The hygroscopicity was performed using the methodology described by Cai and Corke [17] with minor modifications. One gram of microcapsules was placed in a desiccator containing a saturated sodium chloride solution (85%) After seven days the samples were weighed and their hygroscopicity expressed as a percentage (%) of adsorbed moisture.

2.7.3. *Drying yield*

The drying yield for spray-drying was evaluated based on the percentage between the total mass of the product recovered upon its exit from the equipment and the mass of the extract fed into the system, according to Eq. (dry basis):

$$Y\% = \frac{Mass\ off\ microcapules\ (g)}{Total\ mass\ of\ extract\ fed\ into\ the\ system\ (g)} \times 100$$

2.8. **Total phenolic content (TFC) and surface phenolic content (SPC)**

Total phenolic content was determined by releasing the phenolic compounds from the microcapsules, according to the methodology described by Robert et al. [13], and Tolun et al., [18]. A total of 200 mg of microcapsules were weighed and added to 2 mL of a methanol-acetic acid-water mixture in a 50:8:42 ratio, respectively. Subsequently, the samples were centrifuged at 4,000 rpm for 15 minutes. Then, the sample was filtered and decanted, after which the Folin-Ciocalteu method was employed to determine the TFC.

To determine the surface phenolic content (SPC) of the microcapsules, 24 mg of microcapsules were washed with 3 mL of an ethanol: methanol mixture (1:1, v/v) for 5 minutes and then filtered through a microfilter (0.45 μm) [18].

2.9. *Total flavonoid content*

Total flavonoid content (TFC) in the microcapsules was determined using the methodology described by Robert et al.,[13] and Fuentes et al., [19]. A total of 200 mg of the microcapsules was taken and mixed with 2 mL of a methanol-ethanol solution (1:1, v/v). Subsequently, the solution was subjected to centrifugation at 4,000 rpm for a period of 15 minutes. Finally, a 500 µL sample was taken for the TFC using the aluminum chloride procedure. The TFC was calculated using a calibration curve with quercetin as the standard and expressed in milligrams of quercetin equivalent per gram of dry weight of the sample. Absorbance was then measured at 420 nm using a UV–Visible spectrophotometer (PerkinElmer Lambda XLS, UK).

2.10. *Antioxidant capacity in microcapsules*

The antioxidant capacity of the microcapsules was determined with brief modifications [13]. For that, 200 mg of the microcapsules were mixed with 2 mL of a methanol-ethanol solution (1:1) and vortexed for 1 min, then the solution was centrifuged at 4000 rpm for 15 min. Then, 20 µL of the aqueous extract was taken and mixed with 2 mL of the ABTS+ radical dilution following the methodology described in 2.5 The results are expressed in percentage inhibition, which is calculated by the following equation:

$$inhibition(\%) = \frac{Initial\ absorbance\ of\ ABTS\text{-}Absorbance\ of\ the\ sample\ after\ 6\ min}{Initial\ absorbance\ of\ ABTS} \times 100$$

2.11. *Encapsulation efficiency*

The encapsulation efficiency (%EE) is determined by the results of the % SPC according to Robert et al. (2010), which are expressed using the following equation:

$$\%EE = 100\% \text{ - } \%SPC$$

Where SPC is: % surface phenolic content.

2.12. *Total phenolic content*

Total phenolic content was determined by releasing the phenolic compounds from the microcapsules by destroying the coating material, according to a modified form of the methodology described by Tolun et al., [18]. The tests

were carried out in triplicate and the efficiency of encapsulation of the bioactive compounds was determined using the equation:

$$\% \ PCS = \frac{Phenolic \ compounds \ on \ the \ surface}{Initial \ phenolic \ compounds} \times 100$$

2.13. *Morphological analysis of microcapsule*

A scanning electron microscope was employed to evaluate the particle morphologies of microcapsules produced with different coating material concentrations and drying temperatures. The particle morphologies of the microcapsules produced with coating material concentrations and drying temperatures were evaluated by employing a scanning electron microscope (SEM). A small quantity of each powder was attached to a double-sided adhesive tape fixed to stubs, coated with gold, and examined with 5 kV in a JEOL JSM 7800F scanning electron microscope.

3. Results

3.1. *Total phenols and flavonoids in the aqueous extract*

The results for total phenols and flavonoids were 185.06 µg gallic acid/mL and 18.38 µg quercetin/mL, respectively (Table **2**). Values of 174.15 mg gallic acid/100 g fresh weight and 159.9 mg gallic acid/100 g total phenols, respectively [20, 21]. As reported by Barrett et al. [22], the content of phenols and flavonoids is highly influenced by fruit maturity. These compounds are found in higher proportion in an immature state than when the fruit is fully ripe. Miletić et al. [23] conducted a study on an endemic plum species finding a decrease in the quantity of total phenols during fruit ripening.

Titratable Acidity	0.034% 0.003	
Total phenolic content	185.06 0.53 µg gallic acid/mL	
Flavonoids	18.38 0.01µg quercetin/mL	
Antioxidant Capacity	Nance juice (untreated)	95.860.35 % Inhibition
	Aqueous extract	30.11 2.19 % Inhibition

Table 2. Characterization of the aqueous extract of nance

3.2. *Antioxidant Capacity*

The results of the antioxidant capacity of the aqueous extract shown in Table **2**, demonstrated a percentage inhibition of $ABTS^+$ radicals of 30.11%, whereas the fruit juice, which was not subjected to any processing, exhibited an antioxidant capacity inhibition of 95.86%. López-Vidaña et al. [24] indicated that the antioxidant activity is influenced by the temperature and the time of application, particularly during heating that may result in an oxidative process. In their study, Karaaslan et al. [25] reported that the use of high temperatures, ranging from 50-80°C, can result in a reduction of up to 65% in the phenolic compounds present in the extract. Similarly, Akowah et al. [26] found that the temperature at which the extraction is conducted has an impact on the stability of the phenolics and in the antioxidant capacity of the extract.

3.3. *Characterization of the microcapsules*

Response surfaces were produced to understand the behavior of physicochemical properties relevant to encapsulation concerning process temperature and concentration of encapsulating material encapsulating material. Figures 1a, 1b, and 1c show the effects of temperature and maltodextrin concentration on encapsulation yield, moisture, and hygroscopicity, respectively.

Table **3** shows the recovery performance results. The yield ranged from 82.84-94. 89%, with MD05110 and MD15110 showing the lowest and highest values, respectively. The results show (Figure 1a) that increases in maltodextrin concentration and temperature improve the recovery yield. Similar results have been reported by Millinia et al. [27], who observed an increase in the yield of anthocyanin encapsulates from roselle (*Hibiscus sabdariffa* L.). Thanh et al. [28] also observed this behavior by microencapsulating noni juice in maltodextrin-gum Arabic mixtures at temperatures from 140 to 180 °C. Karrar et al. [29] reported a microencapsulation yield between 85.25 and 92.80 % using the spray drying technique.

Furthermore, Bhusari and Kumar [30] mentioned that the increase in powder recovery yield is due to the reduction of stickiness and deposition of powder particles on the walls of the drying chamber. On the other hand, Quek et al. [31] found that maltodextrin could increase the total solids content and reduce the moisture content of the product, since it can alter the surface area of adhesion of low molecular weight sugars, such as glucose, sucrose, fructose and organic acids, facilitating drying and decreasing the stickiness of the product.

Nance microcapsules showed a moisture content ranging from 0.15 to 2.63 % (Table 3). These results agree with Rodrigues Pereira et al. [32] and Porras-Saavedra et al. [33] who reported values of 2.21 and 4.38 (% dry base, d. b.) in microencapsulated powders with maltodextrin and gum Arabic. According to Bhandari [34], the moisture content in powders should be less than 5%, and Baudelaire [35] mentions that microcapsules with moisture values between 2 and 8% can be stable for a period of 12 to 24 months. Moisture and hygroscopicity are relevant properties in spray-dried powders, which can directly affect the stability and storage properties of the powder [36].

Figure 1b shows that moisture decreases with increasing maltodextrin concentration and drying air temperature. This behavior was observed by Queck et al. [31], who reported that at a constant flow rate, the moisture content of the encapsulates decreases with increasing temperature. On the other hand, Kha et al. [37] found that increasing the quantity of solids in the feed solution decreases the initial total moisture to evaporate. Goula and Adamopoulos [38] mentioned that the increase in maltodextrin concentration could hinder the diffusion of water molecules, causing an increase in moisture content. Also, very low moisture contents can decrease the glass transition temperature, causing stickiness and hardening of the microcapsules [39].

Table 3 shows the formulations with the lowest hygroscopicity value (MD10106 and MD15110) and the highest hygroscopicity (MD05110 and MD03120). The results showed significant differences between treatments ($p = 0.05$), particularly with increasing encapsulant concentration. Figure 1c shows that low hygroscopicity occurs with low maltodextrin concentrations and drying temperatures. This behavior is also observed by Rodriguez-Hernandez et al. [40], Cai and Corke [17], and Laureanti et. al. [36]. They mentioned that hygroscopicity is affected by the concentration of the encapsulating agent and this can be inversely proportional to moisture content.

On the other hand, Tonon et al. [41] report that maltodextrin is a material with low hygroscopicity, which confirms its efficiency as an encapsulating agent. Other authors have also documented a reduction in hygroscopicity with increasing maltodextrin concentration [17, 40]. This is due to the fact that maltodextrin has the capacity to absorb water, thereby forming a moisture protection barrier on the surface of the hygroscopic particles. Furthermore, it increases the glass transition temperature, which stabilizes the carbohydrates and improves the stability of the microencapsulates [42, 43]. The highest hygroscopicity found in nance microencapsulates was 18.81g water/100g encapsulate (Figure 1c). This

can be attributed to the concentration of carbohydrates in the nance. The results also show that the temperature contributes positively to the hygroscopicity, since the higher the temperature, the higher the hygroscopicity of the microcapsules. Ferrari et al. [39] and Tonon et al. [41] reported that hygroscopicity is inversely proportional to moisture content. That is, encapsulates are more hygroscopic if their moisture content is low, which, tend to possess a better capacity to absorb water from the environment according to Akhavan. et al. [44].

Key	Inlet Temperature (°C)	Maltodextrin (%)	Yield (%)	Moisture (%)	Hygroscopicity (g of water/100 g of encapsulate)
MD10120	120	10	84.53 0.85	2.63 0.06	15.47 0.85
MD10106	106	10	90.29 2.99	1.47 0.07	13.49 0.13
MD10121	120	10	85.73 2.97	2.21 0.07	15.07 0.06
MD15130	130	15	90.76 1.56	1.07 0.14	15.04 1.34
MD05110	110	5	82.84 1.16	2.40 0.21	18.81 1.43
MD10122	120	10	89.82 1.19	2.15 0.53	15.23 1.09
MD10123	120	10	82.84 2.89	2.57 0.52	15.84 2.72
MD03120	120	3	86.39 2.74	0.90 0.05	18.21 0.18
MD15110	110	15	94.89 2.87	1.42 0.30	14.24 0.45
MD10124	120	10	85.82 2.04	1.79 0.09	14.79 0.72
MD05130	130	5	83.96 1.10	1.41 0.09	17.22 0.07
MD10134	134	10	89.78 1.38	0.15 0.09	15.30 0.16
MD17120	120	17	88.76 1.85	0.84 0.10	14.66 0.12

Table 3. Yields of the encapsulation process of the aqueous extract of nance.

3.4. *Total phenolic content*

Table 4 shows the total phenol content, and Figure 3d shows the behavior with respect to microencapsulation temperature. The highest phenol content was observed at 120 °C and above this temperature the concentration decreases. Additionally, phenolic compounds are heat-sensitive substances, and their biological properties may be affected by high [45, 46]. Mishra et al. [46] reported that above 175°C, microencapsulations with maltodextrin exhibit an increase in the quantity of phenols. This behavior may be attributed to the fact that as the temperature increases, polymerization or synthesis of phenolic compounds may occur. On the other hand, Kha et al. [37], and Ferrari et al. [39] mentioned that
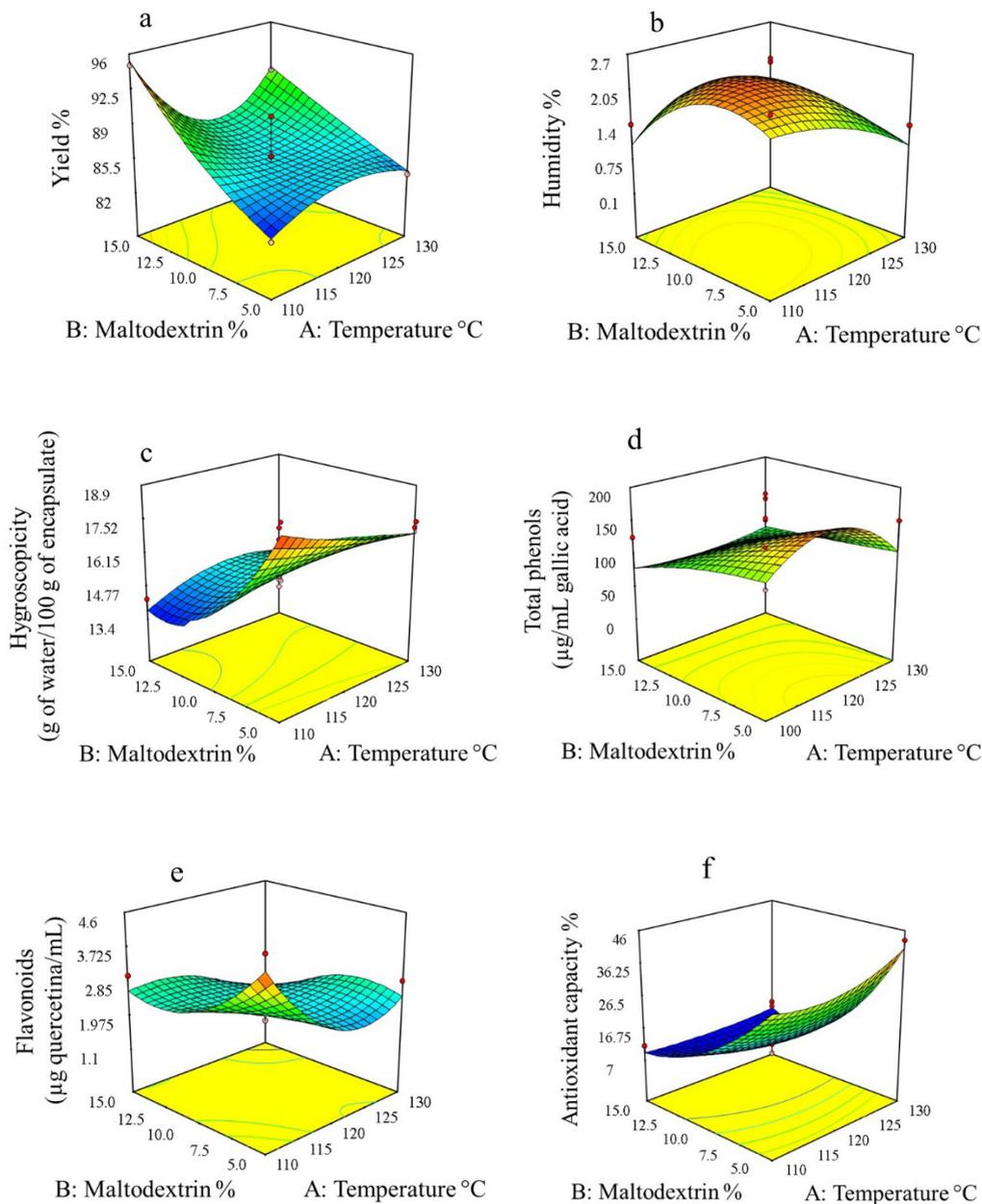
Figure 1. Responses surfaces of microcapsules a) yield; b) moisture; c) hygroscopicity; d) total phenols; e) Flavonoids and f) Antioxidant capacity (% inhibition).

the temperature negatively affects the content of phenolic compounds since there is a degradation and oxidation caused by high temperatures. Kha et al. [37] showed that the encapsulates with higher moisture content have more loss of components; however, when the encapsulates have a higher percentage of moisture they can form agglomerates which would give them greater protection by reducing the contact of the microencapsulates with the environment. In the case of the nance microencapsulates, the content of total phenols was higher in those obtained with high moisture content.

On the other hand, the behavior of the microencapsulation efficiency of phenolic compounds is shown in Figure 1a. It can be observed that the microencapsulation efficiency improves with high maltodextrin concentrations and low drying temperatures. Robert et al. [13], argue that the quantification of phenols may be affected since it is possible that a complete extraction of the compounds has not been performed due to the complexity of the matrix formed and the different polarity and solubility that phenolic compounds present. Queck et al. [31] also mentioned, that one of the disadvantages of using high concentrations of maltodextrin is that it can cause the phenolic components to be inaccurately quantified.

3.5. *The total flavonoid content*

As show in Figure 1f, the flavonoid concentration exhibits a positive correlation with decreasing temperature and maltodextrin concentration. A reduction in flavonoid concentration (MD15130) was observed when the drying temperature was elevated (130 °C), whereas the formulation MD05110 exhibited the highest flavonoid concentration. In this regard, Krishnaiah et al. [47], obtain a similar effect in *Morinda citrifolia* L. encapsulates, and Shahidi and Naczk [48], mention that phenolic compounds and flavonoids can form complexes with polysaccharides and the affinity of phenolics to polysaccharides depends on water solubility, molecular size, conformational mobility and shape of the polyphenol. Yousefi et al., [49] mention that maltodextrin ratio and core/coating ratio are the factors that most affect encapsulation efficiency.

3.6. *Antioxidant Capacity*

Table 4 shows that lower maltodextrin concentrations increase the antioxidant capacity of the microcapsules because the matrix formed by the maltodextrin releases the compounds more efficiently. The formulations that showed the

highest antioxidant capacity were MD03120, MD05130 and MD05110. It was also observed that the formulations MD10120, MD17120 and MD15110 show a decrease in antioxidant capacity when the maltodextrin concentration decreases. Likewise, those microencapsulates that obtained higher percentages of antioxidant capacity were MD05110, MD05130 and MD03120, which showed a high content of total phenols, total surface phenols and flavonoids. It has been observed that the determination of antioxidant capacity is negatively affected by the increase in maltodextrin concentration. Ahmed et al. [50], mentioned that antioxidant capacity is negatively affected by increasing maltodextrin concentration. Also, Mishra et al. [46] reported that the antioxidant capacity decreases when the temperature increases from 125 to 200 °C. Thus, exposure to high temperatures affects the structures of phenolic compounds causing their degradation and inducing the loss of their antioxidant capacity. Kha et al. [37] reported that the antioxidant capacity of microencapsulates decreases with increasing maltodextrin concentration at temperatures higher than 120 to 200 °C causing degradation of antioxidant compounds. High temperatures can lead to the synthesis or polymerization of phenolic compounds [46].

Key	Inlet Temperature (°C)	Total phenols (µg/mL gallic acid)	Flavonoids (µg Quercetin/mL)	Antioxidant capacity (% Inhibition)
MD10120	120	83.59 1.98	2.64 0.16	9.25 0.56
MD10106	106	48.35 1.25	2.60 0.37	18.12 0.22
MD10121	120	151.88 0.57	1.86 0.08	13.12 0.82
MD15130	130	131.22 0.33	1.53 0.32	12.42 0.36
MD05110	110	173.11 2.06	4.59 0.32	36.51 2.53
MD10122	120	153.98 1.54	2.41 0.08	13.42 0.33
MD10123	120	190.52 4.81	2.60 0.14	13.32 0.46
MD03120	120	138.79 1.13	1.86 0.21	45.64 9.70
MD15110	110	125.74 0.45	3.01 0.14	11.52 0.51
MD10124	120	45.91 3.92	2.18 0.24	12.02 1.79
MD05130	130	150.89 1.28	2.88 0.24	43.05 0.99
MD10134	134	22.87 0.87	2.32 0.14	11.97 0.79
MD17120	120	4.75 1.06	2.13 0.45	11.02 0.29

Table 4. Total phenols, Antioxidant capacity and flavonoids of the encapsulation process of the aqueous extract of nance

3.7. *Morphological analysis of microcapsule*

Figure 2 shows the micrographs of the microcapsules obtained by SEM for the different formulations and operating conditions of the spray drying process. The micrographs show the presence of irregular spherical particles with sizes ranging from 8 to 20 μm. The microcapsules with lower maltodextrin concentration presented particles smaller than 10μm. However, at low maltodextrin concentrations there was presence of agglomerates as seen in the microcapsules of MD03120. On the other hand, formulations MD10106, MD15110 and MD05110, obtained at low temperature presented smooth surfaces. The microcapsules of formulation MD10134 showed collapsed surfaces, which can be attributed to the temperature changes suffered by the particles inside the drying chamber. Rosenberg et al. [51] mention that high drying temperatures and fine spray leads to rapid water removal, causing collapsed microcapsules. On the other hand, formulations with higher maltodextrin concentrations (MD15110, MD15130 and MD17120) have larger particle sizes (10 - 20 μm). Rajabi et al. [52] observed this same behavior and attribute it to increased solids in the feed.
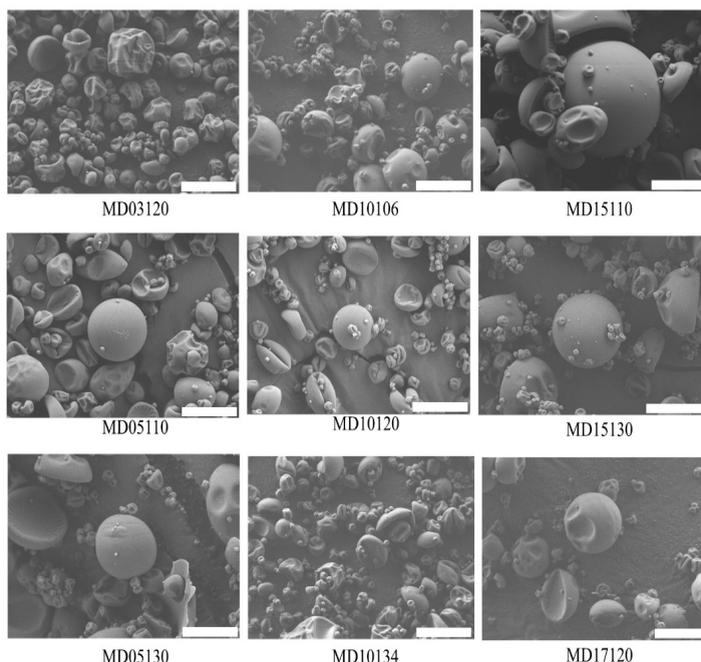

Figure 2. Micrographs of microcapsules of spray dried nance extract powder 2500 X magnification, 5 KV at 10 μm.

Alamilla-Beltrán et al. [53] reported that at low drying temperatures there is a better degree of particle shrinkage. Likewise, particle size tends to be smaller at low temperatures. On the other hand, Dolinsky [54], found that when particles are obtained by spray drying, they begin to dry at temperatures lower than those of the drying air, shrinking once the boiling point of the liquid phase is reached, thus, the particles inflate. This explains the behavior of the particles of the nance microcapsules, with collapsed particles MD05110. In addition, it is observed that the microcapsules MD10134 show deformation due to the high temperatures. Paramita et al. [55] reported that the smaller particles are compressed or roughened which may be due to shrinkage during the drying cycle. However, Tonon et al. [41] mention that at high temperatures particles with smooth surfaces are produced and at low temperatures particles with a rougher structure. This behavior is the opposite of that of the particles of the nance encapsulates.

4. Conclusions

In this study, the effect of spray drying conditions on microcapsules obtained from nance extract were investigated for the first time. It was found that different concentration maltodextrin and inlet temperature have significant effect on the yield, moisture, hygroscopicity and total phenolic content. With a temperature of 130 ° and a maltodextrin concentration of 5%, the highest antioxidant activity was achieved. Particle size is also directly affected by the quantity of solids contained in the feed solution and the drying temperature.

References

1. Servicio de Información Agroalimentaria y Pesquera (SIAP). (2024, mayo 20). *Estadística de producción agrícola*. SIAP.
    http://infosiap.siap.gob.mx/gobmx/datosAbiertos_a.php

2. Medina-Torres, R., Salazar-García, S., & Gómez-Aguilar, J. R. (2004). Fruit quality indices in eight Nance [Byrsonima crassifolia (L.) H.B.K.] selections. *HortScience, 39*(5), 1070–1073.
    https://doi.org/10.21273/HORTSCI.39.5.1070

3. Pires, F. C. S., Silva, A. P. S., Salazar, M. A. R., Da Costa, W. A., Da Costa, H. S. C., Lopes, A. S., & De Carvalho, J. R. N. (2019). Determination of process parameters and bioactive properties of the murici pulp (Byrsonima crassifolia) extracts obtained by supercritical extraction. *The Journal of Supercritical Fluids, 146*, 128–135.
    https://doi.org/10.1016/j.supflu.2019.01.014

4. Rodríguez, S. M., Moura, E. F., Ramos, G. K. S., & Oliveira, M. S. P. (2016). Genetic variability analysis of Byrsonima crassifolia germplasm collected in Pará state using ISSR markers. *Genetics and Molecular Research, 15*(4).
    https://doi.org/10.4238/gmr15048887

5. Mariutti, L. R. B., Rodrigues, E., & Mercadante, A. Z. (2013). Carotenoids from Byrsonima crassifolia: Identification, quantification, and in vitro scavenging capacity against peroxyl radicals. *Journal of Food Composition and Analysis, 31*, 155–160.
    https://doi.org/10.1016/j.jfca.2013.05.005

6. Carlos, N. D. A., Loss, R. A., e Silva, S. S., Guedes, F. S., & Carvalho, J. W. P. (2017). Avaliação físico-química e atividade antimicrobiana da casca, polpa e semente do murici (Byrsonima crassifolia). *Enciclopedia Biosfera, 14*, 232–243.
    http://doi.org/10.18677/EnciBio_2017A22

7. Herrera-Ruiz, M., Zamilpa, A., González-Cortazar, M., Reyes-Chilpa, R., León, E., García, M. P., & Huerta, R. M. (2011). Antidepressant effect and pharmacological evaluation of standardized extract of flavonoids from Byrsonima crassifolia. *Phytomedicine, 18*, 1255–1261.
    https://doi.org/10.101

8. Pérez-Gutierrez, R. M., Muñiz-Ramirez, A., Gómez-Gómez, Y., & Bautista-Ramírez, E. (2010). Antihyperglycemic, antihyperlipidemic, and antiglycation effects of Byrsonima crassifolia fruit and seed in normal and streptozotocin-induced diabetic rats. *Plant Foods for Human Nutrition, 65*, 350–357.
    https://link.springer.com/article/10.1007/s11130-010-0181-5

9. Maldini, M., Montoro, P., & Pizza, C. (2011). Phenolic compounds from *Byrsonima crassifolia* L. bark: Phytochemical investigation and quantitative analysis by LC-ESI MS/MS. *Journal of Pharmaceutical and Biomedical Analysis, 56*(1), 1–6.
    https://doi.org/10.1016/j.jpba.2011.03.032

10. Heinrich, M., Ankli, A., Frei, B., Weimann, C., & Sticher, O. (1998). Medicinal plants in Mexico: Healers' consensus and cultural importance. *Social Science & Medicine, 47*, 1859–1871. https://doi.org/10.1016/S0277-9536(98)00181-6

11. Gordon, A., Jungfer, E., Da Silva, B. A., Maia, J. G. S., & Marx, F. (2011). Phenolic constituents and antioxidant capacity of four underutilized fruits from the Amazon region. *Journal of Agricultural and Food Chemistry, 59*(14), 7688–7699. https://doi.org/10.1021/jf201039r

12. Rufino, M. S. M., Alves, R. E., De Brito, E. S., Pérez-Jiménez, J., Saura-Calixto, F., & Mancini-Filho, J. (2010). Bioactive compounds and antioxidant capacities of 18 non-traditional tropical fruits from Brazil. *Food Chemistry, 121*(4), 996–1002. https://doi.org/10.1016/J.FOODCHEM.2010.01.037

13. Robert, P., Gorena, T., Romero, N., Sepulveda, E., Chavez, J., & Saenz, C. (2010). Encapsulation of polyphenols and anthocyanins from pomegranate (*Punica granatum*) by spray drying. *International Journal of Food Science and Technology, 45*(6), 1386–1394. https://doi.org/10.1111/j.1365-2621.2010.02270.x

14. Chang, C. C., Yang, M. H., Wen, H. M., & Chern, J. C. (2002). Estimation of total flavonoid content in propolis by two complementary colorimetric methods. *Journal of Food and Drug Analysis, 10*(3), 178–182. https://doi.org/10.38212/2224-6614.2748

15. Kuskoski, E., Asuero, A., Troncoso, A., Mancini-Filho, J., & Fett, R. (2005). Aplicación de diversos métodos químicos para determinar actividad antioxidante en pulpa de frutos. *Ciencia y Tecnología de Alimentos Campinas, 25*(4), 726–732. https://doi.org/10.1590/S0101-20612005000400016

16. AOAC. (1996). *Official methods of analysis of AOAC International* (16th ed.). Gaithersburg, USA.

17. Cai, Y. Z., & Corke, H. (2000). Production and properties of spray-dried *Amaranthus* betacyanin pigments. *Journal of Food Science, 65*(6), 1248–1252. https://doi.org/10.1111/j.1365-2621.2000.tb10273.x

18. Tolun, A., Altintas, Z., & Artik, N. (2016). Microencapsulation of grape polyphenols using maltodextrin and gum arabic as two alternative coating materials: Development and characterization. *Journal of Biotechnology, 239*, 23–33. https://doi.org/10.1016/j.jbiotec.2016.10.001

19. Fuentes, Y., Giovagnoli-Vicuña, C., Faúndez, M., & Giordano, A. (2023). Microencapsulation of Chilean papaya waste extract and its impact on physicochemical and bioactive properties. *Antioxidants, 12*(10), 1900. https://doi.org/10.3390/antiox12101900

20. Murillo, E., Britton, G. B., & Durant, A. A. (2012). Antioxidant activity and polyphenol content in cultivated and wild edible fruits grown in Panama. *Journal of Pharmaceutical and Bioallied Sciences, 4*(4), 313-317.
https://doi.org/10.4103/0975-7406.103261

21. Beserra Almeida, M. M., Machado de Sousa, P. H., Campos Arriaga, Â. M., Matias do Prado, G., de Carvalho Magalhães, C. E., Arraes Mai, G., & Gomes de Lemos, T. L. (2011). Bioactive compounds and antioxidant activity of fresh exotic fruits from northeastern Brazil. *Food Research International, 44*(1), 2155–2159.
https://doi.org/10.1016/j.foodres.2011.03.051

22. Barrett, D. M., Somogyi, L., & Ramaswamy, H. S. (Eds.). (2004). *Processing fruits: Science and technology* (2nd ed.). CRC Press.
https://doi.org/10.1201/9781420040074

23. Miletić, N., Popović, B., Mitrović, O., & Kandić, M. (2012). Phenolic content and antioxidant capacity of fruits of plum cv. 'Stanley' (*Prunus domestica* L.) as influenced by maturity stage on-tree ripening. *Australian Journal of Crop Science, 6*(4), 681–687.
https://refri.institut-cacak.org/handle/123456789/254

24. López-Vidaña, E. C., Pilatowsky Figueroa, I., Cortés, F. B., Rojano, B. A., & Navarro Ocaña, A. (2017). Effect of temperature on antioxidant capacity during drying process of mortiño (*Vaccinium meridionale* Swartz). *International Journal of Food Properties, 20*(2), 294–305.
https://doi.org/10.1080/10942912.2016.1155601

25. Karaaslan, M., Yilmaz, F. M., Cesur, Ö., Vardin, H., Ilkinci, A., & Dalgiç, A. C. (2014). Drying kinetics and thermal degradation of phenolic compounds and anthocyanins in pomegranate arils dried under vacuum conditions. *International Journal of Food Science & Technology, 49*(1), 595–605.
https://doi.org/10.1111/ijfs.12342

26. Akhavan Mahdavi, S., Jafari, S. M., Assadpoor, E., & Deshnad, D. (2016). Microencapsulation optimization of natural anthocyanins with maltodextrin, gum arabic, and gelatin. *International Journal of Biological Macromolecules, 85*, 379-385.
https://doi.org/10.1016/j.ijbiomac.2016.01.011

27. Millinia, B. L., Mashithah, D., Nawatila, R., & Kartini, K. (2024). Microencapsulation of roselle (*Hibiscus sabdariffa* L.) anthocyanins: Effects of maltodextrin and trehalose matrix on selected physicochemical properties and antioxidant activities of spray-dried powder. *Future Foods, 9*, 100300.
https://doi.org/10.1016/j.fufo.2024.100300

28. Nguyen, C. T., Nguyen Di, K., Phan, H. C., Kha, T. C., & Nguyen, H. C. (2024). Microencapsulation of noni fruit extract using gum arabic and maltodextrin— Optimization, stability, and efficiency. *International Journal of Biological Macromolecules, 269*(Pt 2), 132217.
https://doi.org/10.1016/j.ijbiomac.2024.132217

29. Karrar, E., Mahdi, A. A., Sheth, S., Mohamed Ahmed, I. A., Manzoor, M. F., Wei, W., & Wang, X. (2021). Effect of maltodextrin combination with gum arabic and whey protein isolate on the microencapsulation of gurum seed oil using a spray-drying method. *International Journal of Biological Macromolecules, 171*, 208–216.
https://doi.org/10.1016/j.ijbiomac.2020.12.045

30. Bhusari, S. N., Muzaffar, K., & Kumar, P. (2014). Effect of carrier agents on physical and microstructural properties of spray dried tamarind pulp powder. *Powder Technology, 266*(1), 354–364.
https://doi.org/10.1016/j.powtec.2014.06.038

31. Quek, S. Y., Chok, N. K., & Swedlund, P. (2007). The physicochemical properties of spray-dried watermelon powders. *Chemical Engineering and Processing: Process Intensification, 46*(5), 386-392.
https://doi.org/10.1016/j.cep.2006.06.020

32. Pereira, H. V. R., Saraiva, K. P., Carvalho, L. M. J., Andrade, L. R., Pedrosa, C., & Pierucci, A. P. T. R. (2009). Legumes seeds protein isolates in the production of ascorbic acid microparticles. *Food Research International, 42*(1), 115–121.
https://doi.org/10.1016/j.foodres.2008.10.008

33. Porras-Saavedra, J., Palacios-González, E., Yáñez-Fernández, J., Mazzobre, M. F., Buera, M. P., & Alamilla-Beltrán, L. (2015). Caking process and microstructural changes of wall materials used in spray-drying process. In *Water Stress in Biological, Chemical, Pharmaceutical and Food Systems* (pp. 629–636). Springer.
https://doi.org/10.1007/978-1-4939-2578-0_60

34. Bhandari, B. R., Patel, K. C., & Chen, X. D. (2008). Spray drying of food materials—process and product characteristics. In *Drying Technologies in Food Processing* (pp. 113–157). Springer.

35. Baudelaire, E. D. (2013). Grinding for food powder production. In *Handbook of Food Powders* (pp. 132–149). Woodhead Publishing.
https://doi.org/10.1533/9780857098672.1.132

36. Laureanti, E. J. G., Paiva, T. S., de Matos Jorge, L. M., & Jorge, R. M. M. (2023). Microencapsulation of bioactive compound extracts using maltodextrin and gum arabic by spray and freeze-drying techniques. *International Journal of Biological Macromolecules, 253*(Pt 4), 126969.
https://doi.org/10.1016/j.ijbiomac.2023.126969

37. Kha, T. C., Nguyen, M. H., & Roach, P. D. (2010). Effects of spray drying conditions on the physicochemical and antioxidant properties of the Gac (*Momordica cochinchinensis*) fruit aril powder. *Journal of Food Processing Engineering, 98*(1), 385–392.
https://doi.org/10.1016/j.jfoodeng.2010.01.016

38. Goula, A. M., & Adamopoulos, K. G. (2010). A new technique for spray drying orange juice concentrate. *Innovative Food Science and Emerging Technologies, 11*(1), 342–351.
https://doi.org/10.1016/j.ifset.2009.12.001

39. Ferrari, C. C., Germer, S. P. M., & de Aguirre, J. M. (2012). Effects of spray-drying conditions on the physicochemical properties of blackberry powder. *Drying Technology, 30*(2), 154-163.
https://doi.org/10.1080/07373937.2011.628429

40. Rodríguez-Hernández, G. R., Zulueta, A., Ramos, M., & Lobo, M. G. (2013). Chemical composition, bioactive compounds, and antioxidant activity of the native fruits of *Peru. Food Research International, 54*(2), 1248–1257.
https://doi.org/10.1016/j.foodres.2013.08.025

41. Tonon, R. V., Brabet, C., & Hubinger, M. D. (2008). Influence of process conditions on the physicochemical properties of açai (*Euterpe oleracae* Mart.) powder produced by spray drying. *Journal of Food Engineering, 88*(3), 411–418.
https://doi.org/10.1016/j.jfoodeng.2008.02.029

42. Valenzuela, C., & Aguilera, J. M. (2015). Effects of maltodextrin on hygroscopicity and crispness of apple leathers. *Journal of Food Engineering, 144*(1), 1–9.
https://doi.org/10.1016/j.jfoodeng.2014.07.010

43. Górska, A., Szulc, K., Ostrowska-Ligęza, E., Wirkowska, M., & Bryś, J. (2013). The influence of trehalose-maltodextrin and lactose-maltodextrin matrices on thermal and sorption properties of spray-dried β-lactoglobulin-vitamin D3 complexes. *Journal of Thermal Analysis and Calorimetry, 112*(1), 429–436.
https://doi.org/10.1007/s10973-013-2980-z

44. Akhavan Mahdavi, S., Jafari, S. M., Assadpoor, E., & Deshnad, D. (2016). Microencapsulation optimization of natural anthocyanins with maltodextrin, gum Arabic, and gelatin. *International Journal of Biological Macromolecules, 85*, 379–385.
https://doi.org/10.1016/j.ijbiomac.2016.01.011

45. Andrade, R. A. M., da Silva, D. C., de Souza, M. M. B., de Oliveira, R. L., Maciel, M. I. S., Porto, A. L. F., Melo, E. A., Arruda, L. L. A. L., & Porto, T. S. P. (2023). Microencapsulation of phenolic compounds from cashew apple (*Anacardium occidentale* L.) agro-food waste: Physicochemical characterization, antioxidant activity, biodisponibility and stability. *Food Chemistry Advances, 3*, 100364.
https://doi.org/10.1016/j.focha.2023.100364

46. Mishra, P., Mishra, S., & Mahanta, C. L. (2014). Effect of maltodextrin concentration and inlet temperature during spray drying on physicochemical and antioxidant properties of amla (*Emblica officinalis*) juice powder. *Food and Bioproducts Processing, 92*(3), 252–258.
https://doi.org/10.1016/j.fbp.2013.08.003

47. Krishnaiah, D., Bono, A., Sarbatly, R., Nithyanandam, R., & Anisuzzaman, S. M. (2015). Optimisation of spray drying operating conditions of *Morinda citrifolia* L. fruit extract using response surface methodology. *Journal of King Saud University – Engineering Sciences, 27*(1), 26–36.
https://doi.org/10.1016/j.jksues.2012.10.004

48. Shahidi, F., & Naczk, M. (2003). *Phenolics in food and nutraceuticals*. CRC Press.
https://doi.org/10.1201/9780203508732

49. Yousefi, M., Shadnoush, M., Sohrabvandi, S., Khorshidian, N., & Mortazavian, A. M. (2021). Encapsulation systems for delivery of flavonoids: A review. *Biointerface Research in Applied Chemistry, 11*(6), 13934–13951.
https://doi.org/10.33263/BRIAC116.1393413951

50. Ahmed, M., Aketer, M. S., Lee, J. C., & Eun, J. B. (2010). Encapsulation by spray drying of bioactive components, physicochemical and morphological properties from purple sweet potato. *LWT - Food Science and Technology, 43*(1), 1307-1312.

51. Rosenberg, M., Kopelman, I. J., & Talmon, Y. (1985). A scanning electron microscopy study of microencapsulation. *Journal of Food Science, 50*(1), 139–144.
https://doi.org/10.1111/j.1365-2621.1985.tb13295.x

52. Rajabi, H., Ghorbani, M., Jafari, S. M., Sadeghi, A., & Rajabzadeh, G. (2015). Retention of saffron bioactive components by spray drying encapsulation using maltodextrin, gum Arabic, and gelatin as wall materials. *Food Hydrocolloids, 51*(1), 327–337.
https://doi.org/10.1016/j.foodhyd.2015.05.033

53. Alamilla-Beltrán, L., Chanona-Pérez, J. J., Jiménez-Aparicio, A. R., & Gutiérrez-López, G. F. (2005). Description of morphological changes of particles along spray drying. *Journal of Food Engineering, 67*(1), 179–184.
https://doi.org/10.1016/j.jfoodeng.2004.05.063

54. Dolinsky, A. A. (2001). High-temperature spray drying. *Drying Technology: An International Journal, 19*(5), 785–806.
https://doi.org/10.1081/DRT-100103770

55. Paramita, V., Iida, K., Yoshii, H., & Furuta, T. (2010). Effect of additives on the morphology of spray-dried powder. *Drying Technology: An International Journal, 28*(3), 323–329.
https://doi.org/10.1080/07373931003627098

CHAPTER 3 ENVIRONMENTAL AREA

MESOPOROUS SILICA NANOPARTICLES AS ADSORBENTS OF METHYLENE BLUE AQUEOUS SOLUTIONS

C. Proa-Coronado, J. A. Balderas-López*

Instituto Politécnico Nacional-UPIBI, Basic Science Department, Av. Acueducto S/N, col. Barrio la Laguna, Ticomán, C. P. 07340, México City, México.

* abrahambalderas@hotmail.com

Abstract

Methylene blue (MB) is one of the most popular cationic dyes that is environmentally persistent. It has several uses in industry such as synthetic dye for dyeing fabrics in clothing, textile industries and for dyeing paper and leathers. However, the periodical use of dyes generates waste, wastewater is one of the most worrying problems, not only because it can cause detrimental health issues for humans but because it can be a source of damage to the environment. Thus, it is highly necessary to eliminate MB dye from wastewater. Various methods are reported to remove MB and other textile dyes of water. The adsorption method is one of the most used methods to remove MB of contaminated water. Nanomaterials such as mesoporous silica nanoparticles have been used as adsorbents for dyes showing excellent results. This work discusses the risks posed by water contaminated with MB, as well as the most used methods for the removal of this dye, highlighting the adsorption method and mesoporous silica nanoparticles as adsorbents. In addition, presents a study of these nanostructure's efficiency as methylene blue adsorbents.

Keywords: Methylene blue dye; Mesoporous Silica nanoparticles; Optical properties.

1. Introduction

Access to drinking water is crucial for the community and fundamental for economic and social development. However, urban growth and industrialization have negatively affected this resource. According to a report from the Organization for Economic Cooperation and Development (OECD, 2017), the textile industry stands out as one of the largest consumers of water [1].

The use of dyes is prevalent in several industries, including textiles, pharmaceuticals, food and cosmetics, among others. However, the textile industry is mainly responsible for dye pollution, since it is estimated that between 10% and 15% of the dyes used in its processes end up contaminating the environment [2].

According to the Scopus database, MB is widely used in various applications. From 2014 to 2023, the number of articles on MB dye degradation has increased steadily, as shown in Figure 1.
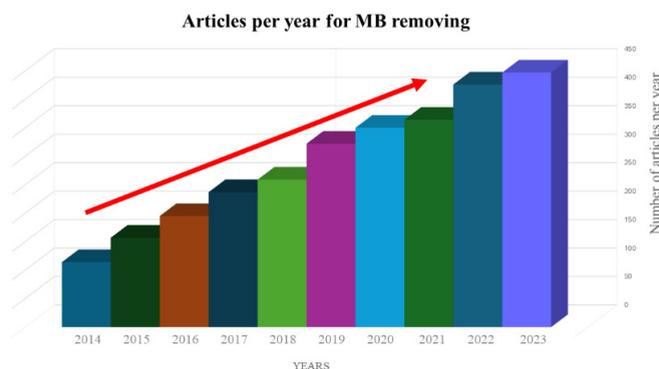

Figure 1. Graphic of articles per year for methylene blue removing.

Methylene blue (MB) is one of the most used materials in the dye industry, being commonly used to dye silk, wool, cotton and paper [3]. The presence of MB in water, even at low concentrations, can reduce sunlight transmission, decrease oxygen solubility, affect the photosynthetic activity of aquatic organisms, and reduce the diversity and aesthetics of biological communities [4].

It is crucial to implement strategies to remove methylene blue from contaminated water as soon as possible. Until now, some of the most widely

used methods include biological methods (using microorganisms), chemical methods (using advanced oxidation processes), and physicochemical methods (such as adsorption). With the advancement of nanotechnology in various scientific areas, some nanomaterials have been proposed as dye adsorbents, obtaining positive results in their elimination. Mesoporous silica nanoparticles are applicable in areas such as adsorption, catalysis, and electrochemistry, due to their large specific surface area, porous structure, and numerous functional groups on their surface [5].

This article discusses the damage that can be caused by water contaminated with methylene blue to the environment and to humans, as well as the use of silica mesoporous nanoparticles as adsorbents.

1.1. *Methylene Blue Dye*

Dyes are molecules that have great resistance to biodegradation due to their organic and inorganic compounds [6]. These dyes have various applications in industry and are generally classified as anionic, cationic and nonionic. Methylene blue (MB) was first synthesized by Heinrich Caro in 1800 [7 - 10]. MB is a cationic dye, with the molecular formula $C_{16}H_{18}N_3ClS$, and has maximum absorption in the visible region. It is highly soluble in water, forming a stable solution at room temperature [11, 12]. MB acts as a redox indicator, not as a pH indicator [13]. The chemical structure of the MB molecule is shown in Figure 2.
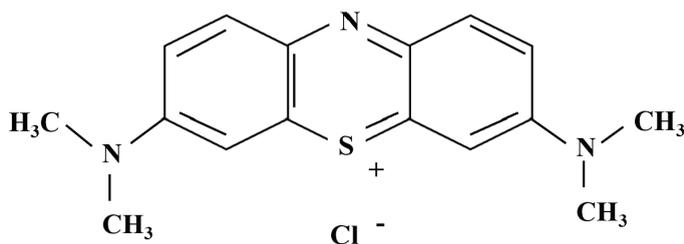
Figure 2. The chemical structure of methylene blue molecule.

The absorption spectra of methylene blue (MB) show a more intense absorption peak around 664 nm, associated with its monomer, and a signal around 612 nm, attributed to its dimer. Furthermore, in the ultraviolet region, two additional bands are observed around 290 and 245 nm, corresponding to benzene rings [14]. Due to its high molar absorption coefficient, approximately

8×10^4 L mol^{-1} cm^{-1} at 664 nm [15], this region of highest absorption is optimal for determining the presence of this dye in water.

1.2. *Toxicity of Methylene Blue Dye*

Wastewater generated by industries, which is often dumped near lakes or rivers, not only damages the ecosystem but also affects human health. Methylene blue (MB), in certain concentrations, can be considered toxic and cause irreversible damage to health [16]. MB can cause dermatological, central nervous system, gastrointestinal and cardiovascular diseases (see Figure 3)
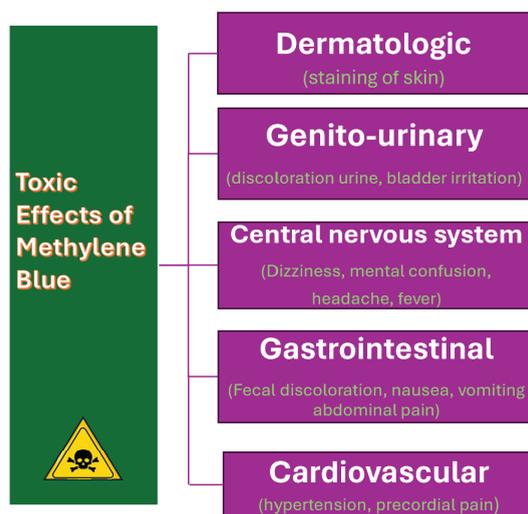

Figure 3. Toxic effects of methylene blue of exposure of methylene blue in humans [17].

Contact of methylene blue (MB) with the skin can cause spots and itching. Additionally, it can cause discoloration of urine, bladder irritation, dizziness, mental confusion, headaches, and fever. In the gastrointestinal system, MB can cause abdominal pain, nausea, vomiting, and discoloration of stool. Cardiovascular problems, such as hypertension and chest pain, have also been reported due to exposure to methylene blue [17].

The damage that this dye can cause not only to the environment, but also the negative effects it has on health, requires methodologies that eliminate or remove the highest possible concentration of methylene blue contained in wastewater.

1.3. *Removal Methods of Methylene Blue*

The removal of dyes from water is a major problem due to the difficulty of treating this type of wastewater with conventional methods. There are various techniques for dye removal, including photocatalytic degradation, adsorption, membrane filtration, biological degradation, microwave catalysis, and oxidation [18].
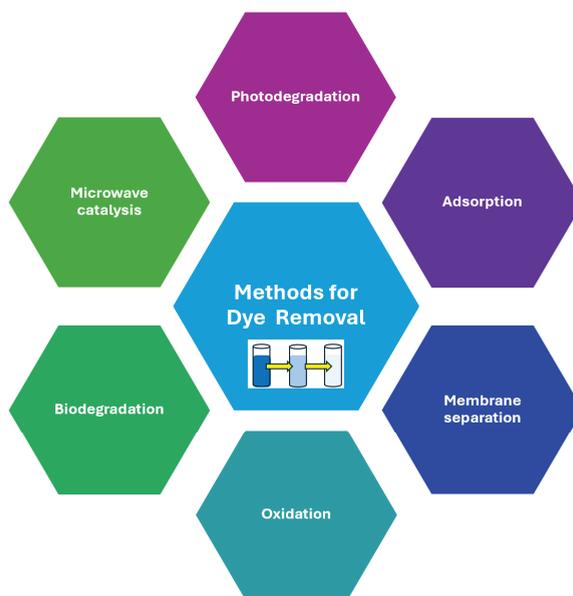

Figure 4. Methods for dye removal.

The removal of dyes through photocatalysis is considered a viable technology at an industrial level. This photocatalytic degradation process is based on the production of highly reactive radicals, such as photographically generated hydroxyl and superoxide anions, which attack the dye molecules and completely mineralize them into less harmful species, such as CO_2 and H_2O [19]. However, the main challenge of photocatalytic degradation of pollutants in wastewater is the long time required and the difficulty in recovering the photocatalysts. Microwave catalytic degradation involves ion conduction. When a catalyst is exposed to microwave radiation, a uniform superheating action is generated [20]. Achieving uniform heating throughout the reaction mixture can be difficult. Biological treatment has several advantages, such as its simplicity, low cost, and being an environmentally friendly process. Additionally, there are many microorganisms available that are easy to maintain and require little preparation [21]. However, this method requires

careful optimization and monitoring. Membrane separation technology offers both the removal and recovery of synthetic dyes from wastewater, representing a promising avenue in engineering [22]. However, in membrane filtration techniques, the decrease in flow rate due to membrane clogging is a problem, along with the complexity and high cost in manufacturing the membranes.

1.4. *The Absorption Method*

The adsorption method for the removal of dyes, such as methylene blue, uses solid sorbents. Recently, this process has become one of the most effective and attractive for the treatment of wastewater containing dyes. In this process, liquid contaminants adhere to the surface of a solid, and it is considered one of the most advanced technologies for water treatment due to its low cost, sustainability and ease of use [23]. A notable feature of this technology is that it does not generate secondary pollutants and does not require complicated setup or operating costs. Compared to technologies such as chemical oxidation, membrane technologies and biological treatment processes that involve the generation of toxic sludge, extensive setup operations are not cost-effective [24].

The adsorption mechanism can be physical or chemical, depending mainly on the aromatic and/or functional groups present in the organic contaminants. Physical adsorption involves weak interactions, such as van der Waals forces, between the adsorbate and the adsorbent. On the other hand, chemical adsorption occurs when chemical bonds form between the adsorbate and specific functional groups on the surface of the adsorbent [25].

Nanomaterials have become one of the most applicable materials for adsorption, thanks to their versatility and nanoscale properties, which makes them extremely useful. Silica nanoparticles have attracted significant attention as nanoadsorbents due to their regular structural characteristics, larger surface area, tunable pore diameters, good thermal and chemical stability, and ease of surface modification [26]. Mesoporous silica nanoparticles (MSNs) are porous materials that have been widely chosen as adsorbents due to their unique surface and pore properties as well as their high surface area [27]. The adsorption of dyes on MSNs is carried out both by chemical interactions and by their porous properties. In general, the functional group on the surface of MSNs is the hydroxyl group, which can interact with the active sites of dye molecules [28].

1.5. *Mesoporous Silica Nanoparticles as Adsorbent Dyes*

Mesoporous silica nanoparticles have become one of the nanomaterials with the greatest variety of applications due to their morphological characteristics, such as their variable size, large surface area (more than 700 m²), adjustable pore size, surfaces that are easy to functionalize and biocompatibility [29]. MSNs have significant applications in various research fields, including catalysis, adsorption, separation, detection and release of drugs [30]. Mesoporous materials are generally prepared using self-assembled surfactant molecules as templates around which silica precursors condense [31]. The template is then removed by heat treatment, resulting in a porous material. By varying conditions such as temperature, pH, surfactant concentration, pore size and morphology, these characteristics can be controlled

There are several synthesis methods for MSNs, such as the sol-gel method, the microwave-assisted technique and chemical etching. However, the sol-gel method is widely used due to its ease and the uniform and controllable growth of nanoparticles. The Stöber method involves the hydrolysis and condensation of tetraethyl orthosilicate (TEOS) in the presence of water and a basic catalyst (ammonium hydroxide) at room temperature.

1.6. *Parameters Affecting Methylene Blue Adsorption by MSN*

1.6.1. *Effect of particle size*

Particle size in adsorption can be an important factor. In 2019, *S. Irudhaya Raj* **[21]** observed the adsorption efficiency of MSNs with sizes of 100, 200, and 500 nm. Analysis was performed for methyl orange (MO), bromocresol green (BCG), methylene blue (MB), and rhodamine B (RB). UV-Vis spectroscopy was used to verify the adsorption of the dyes. In all adsorption experiments, the decrease in absorbance maxima for MO, BCG, RB, and MB was analyzed at 464, 617, 561, and 661 nm, respectively. The analysis confirmed that only the anionic dyes were adsorbed by the 100 nm nanoparticles, while the cationic dyes were adsorbed by the 500 nm nanoparticles, and both types of dyes were adsorbed by the 250 nm nanoparticles. The study reported that the 100 nm MSNs had an absorption of 295.05 mg L⁻¹ for MO and BCG, and 297.54 mg L⁻¹ for MB; for the 250 nm MSNs, the adsorption of MO, BCG, RB and MB was 271 mg L⁻¹, 272 mg L⁻¹, 274 mg L⁻¹ and 277 mg L⁻¹, respectively; and

finally, the 500 nm MSNs had adsorption values of 286 mg L^{-1} for RB and 290 mg L^{-1} for MB.

The authors explain that the observed behavior can be attributed to the fact that in the 250 nm MSNs there was a partial removal of the surfactant layer, allowing the adsorption of both anionic and cationic dyes. On the other hand, for 100 nm MSNs, calcination was not sufficient to eliminate the surfactant layer, which maintained a positive surface charge. On the other hand, in the 500 nm MSNs, the surfactant layer was completely removed, leaving negatively charged silica particles.

1.6.2. *Effect of experimental conditions on the removal efficiency of dyes*

R. Chueachot [26], analyzed different parameters such as pH, adsorbent dose and contact time, which can optimize adsorption. The optimal pH for the removal of dyes from aqueous solutions highlights the role of pH in the surface charge of the adsorbent. The pH range was expanded from 1 to 3; At a pH of 3, a low adsorption rate was observed, which the author probably attributes to the positive charge of the surface, which decreases the amount of adsorbed dye. As the pH increases, the surface appears to become negative, and the adsorption rate increases.

The effect of adsorbent dosage on the removal of methylene blue (MB) was analyzed to determine the optimal amount of adsorbent required for effective adsorption of the dye in aqueous solutions. The dose variation was from 0.01 to 0.20 g for a concentration of 3 mg L^{-1}. It was observed that the adsorbed dose decreased with increasing adsorbent dose, which could be attributed to the overlap or aggregation of the adsorption sites, resulting in a decrease in the total surface area of the adsorbent available for the MB.

In relation to the contact time (the time during which the silica nanoparticles are in contact with the methylene blue solution), this can affect the adsorption kinetics independently of other experimental parameters. Starting from the same initial concentration (3 mg L^{-1}), the contact time varied from zero to 120 minutes. It was found that the amount of adsorbed methylene blue increased with the increase in contact time. The adsorption of MB by the MSNs stabilized after 30 minutes of contact; After this period, no notable increase in the process was observed. Therefore, the authors indicate that 30 minutes is the optimal contact time.

1.6.3.   Effect of added materials on the removal efficiency of dyes

The development of functionalized mesoporous silica adsorbents with appropriate functional groups for dyes has been an area of recent interest. Ying Li [32] synthesized chitosan magnetic mesoporous silica nanoparticles with a diameter of 105 nm, which showed a saturated methylene blue adsorption capacity of 43.03 mg g^{-1}. This highlights the importance of their recycling and reuse, since this type of nanoparticle demonstrated high adsorption efficiency even after being used for up to 4 cycles.

Similarly, Yul Hong [33] synthesized small iron oxide nanoparticles embedded in mesoporous silica nanoparticles as a regenerative adsorbent for methylene blue. In this study, a comparison was made between SiO_2 and Fe-Oxide/SiO_2, reporting a greater adsorption capacity for the latter even after 4 cycles. The regeneration process of Fe-Oxide/SiO_2 indicated that iron oxide nanoparticles can catalyze the thermal degradation of adsorbed MB molecules, regenerating the adsorption sites, which can be applied to other cationic organic dyes.

1.7. **Photothermal Techniques for MSNs Characterization**

Photopyroelectric (PP) techniques have been used to characterize the thermo-optical properties of SiO_2 colloids [34]. The highly dispersive of these nanostructures need modulated light sources that can provide reliable results.

These techniques are characterized by using this intensity- modulated radiation for optical characterization of liquids at a fixed modulation frequency *f*. The material absorb the radiation and generates temperature fluctuations, also named thermal diffusions waves, and for detecting these waves is used a pyroelectric sensor [35, 36].

The experimental setup to measure the optical absorption coefficient is shown in Figure 5. In this, the liquid sample absorbs the modulated radiation that travels through an optical window until it reaches the sample and crosses it. According to the model of Beer-Lambert this is the optical absorption coefficient β. taking the appropriate limiting conditions and employing a mathematical model for heat diffusion [34], the pyroelectric signal for amplitude, expressed as a function of the sample thickness (L) is given by:

$$VL = Ce^{-\beta L}$$

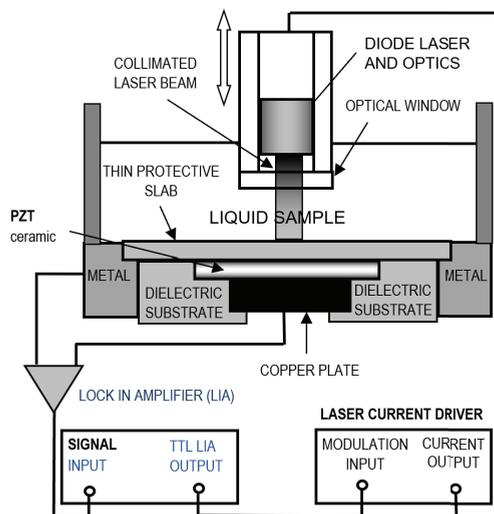On the other hand, the pyroelectric phase, , remains constant.

Figure 5. Cross section of the photopyroelectric setup for optical
absorption coefficient measurements of liquids.

The slope of linear fit be the optical absorption coefficient for pyroelectrical amplitude as a function of the sample thickness (L) [37]. The constant phase is taken here as an experimental criterion to select a suitable range of sample thickness for reliable analysis.

2. Materials and Methods

The experiment consists of two phases, the synthesis of the MSNs and the testing of the effectiveness of these nanostructures as methylene blue adsorbents in aqueous solutions of different concentrations employing the Photopyroelectric techniques, to determine the optical absorption coefficient of each concentration.

2.1. *MSNs Synthesis*

The Stöber method reported by Ortiz-Islas [38] was used with some variations for the synthesis of MSNs. The reagents used were purchased from Sigma Aldrich. First 0.28 g of NaOH and 0.45 g of cetyltrimethylammonium ammonium bromide (CTAB) diluted in 479 mL of Milli-Q water were mixed, and then was heated at 70 °C. Subsequently 49 mL of Tetraethyl orthosilicate (TEOS at 98%) was added to the mixture. A dull white solution formed after mixing for 2 hours. Finally, the sample was calcinated at 550 °C to remove the CTAB.

2.2. *MSNs adsorption efficiency*

To probe the MSNs adsorption capacity different solutions of methylene blue at various concentrations (0.025, 0.05 and 0.1 mM) were elaborated. Then 5 ml of solution was taken apart and 0.01g of MSN were added, for later stirring for 35 min to enhance pigment's adsorption to the nanoparticles [26]. The samples were centrifuged at 10,000 rpm for 12 min until achieved the MSN precipitation. The MSNs precipitated was redispersed in 5 ml of milli Q water, to bring the volume closer to the initial volume after the dye's remotion. Finally optical absorption coefficients for the original suspension, the MSN resuspended and the supernatant were measured to determine the adsorption efficiency.

3. Results and discussion

Figure 6 shows the silica mesoporous nanoparticles synthetized in this work. The average size reported by Transmission Electron Microscopy (TEM, JEM1010, Japan) was 95 ± 12 nm.
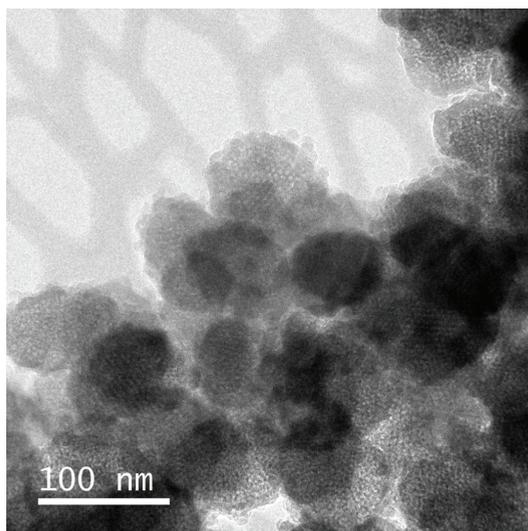

Figure 6. Micrography TEM of MSNs synthetized.

In Figure 7 is shown the optical absorption coefficient for different concentration of dye solutions at a wavelength of 660 nm. An excellent linear correlation is evident in the case between the absorption coefficient values and the increase of concentration samples. The results indicate that for these samples
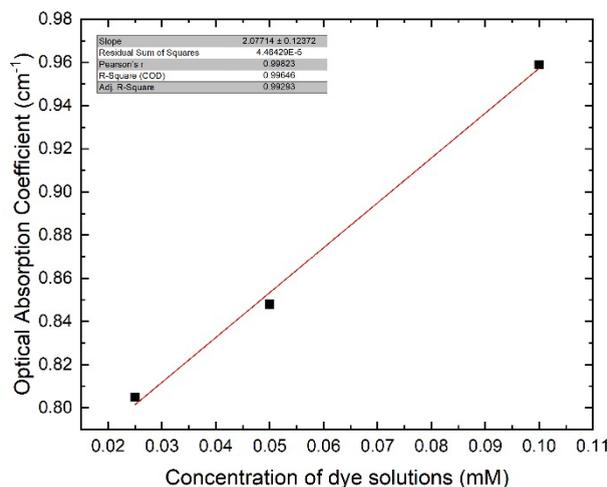
Figure 7. Micrography TEM of MSNs synthetized.

the Beer-Lambert law is fulfilled, which suggests that the optical characterization of this type of nanostructure to measure the adsorption efficiency by the absorption coefficient is reliable. The slope of the linear fit for the optical absorption coefficients with concentration corresponds to the absorptivity of the MSNs "loaded" with the MB dye, which resulted in a value of ε (660 nm) = 2.1 cm^{-1}/mM.

4. Conclusions

This article reports the toxicity of methylene blue, as well as the various strategies to remove this organic dye from contaminated waters. The adsorption method is easy to use due to its simplicity, low cost and sustainability. Nanomaterials are ideal as adsorbents, especially mesoporous silica nanoparticles (MSN), since, as observed by using photothermal techniques for optical characterization, it is possible to determine the adsorption efficiency of methylene blue of these nanoparticles.

Acknowledgments

References

1. Bilińska, L., & Gmurek, M. (2021). Novel trends in AOPs for textile wastewater treatment: Enhanced dye by-products removal by catalytic and synergistic actions. *Water Resources and Industry, 26*, 100160.
    https://doi.org/10.1016/j.wri.2021.100160

2. Takele, T., Angassa, K., Abewaa, M., Mengistu Kebede, A., & Tessema, I. (2023). Adsorption of methylene blue from textile industrial wastewater using activated carbon developed from H3PO4 activated khat stem waste. *Scientific Reports, 13*(1), 5724.
    https://doi.org/10.1038/s41598-023-32628-1

3. Rathi, B. S., & Kumar, P. S. (2021). Application of adsorption process for effective removal of emerging contaminants from water and wastewater. *Environmental Pollution, 280*, 116995.
    https://doi.org/10.1016/j.envpol.2021.116995

4. Lawagon, C. P., & Amon, R. E. C. (2019). Magnetic rice husk ash "cleanser" as efficient methylene blue adsorbent. *Environmental Engineering Research, 25*(4), 685–692.
    https://doi.org/10.4491/eer.2019.226

5. Ali, M. M., Ahmed, M. J., & Hameed, B. H. (2018). NaY zeolite from wheat (Triticum aestivum L.) straw ash used for the adsorption of tetracycline. *Journal of Cleaner Production, 172*, 602-608.
    https://doi.org/10.1016/j.jclepro.2017.10.126

6. Derakhshan, Z., Baghapour, M. A., Ranjbar, M., & Faramarzian, M. (2013). Adsorption of methylene blue dye from aqueous solutions by modified pumice stone: Kinetics and equilibrium studies. *Health Scope, 2*(3), 136–144.
    https://doi.org/10.17795/jhealthscope-13098

7. Allouche, F. N., & Yassaa, N. (2017). Potential adsorption of methylene blue from aqueous solution using green macroalgae *Posidonia oceanica*. In *Proceedings of the IOP Conference Series: Materials Science and Engineering* (Vol. 323, p. 012006). IOP Publishing.
    https://doi.org/10.1088/1757-899X/323/1/012006

8. Han, T. H., Khan, M. M., Kalathil, S., Lee, J., & Cho, M. H. (2013). Simultaneous enhancement of methylene blue degradation and power generation in a microbial fuel cell by gold nanoparticles. *Industrial & Engineering Chemistry Research, 52*(19), 8174–8181.
    https://doi.org/10.1021/ie400548r

9. Slama, H. B., Bouket, A. C., Pourhassan, Z., Alenezi, F. N., Silini, A., Cherif-Silini, H., Oszako, T., Luptakova, L., Golinska, P., & Belbahri, L. (2021). Diversity of synthetic dyes from textile industries, discharge impacts and treatment methods. *Applied Sciences, 11*(14), 6255.
    https://doi.org/10.3390/app11146255

10. Pomicpic, J., Dancel, G. C., Cabalar, P. J., & Madrid, J. (2020). Methylene blue removal by poly (acrylic acid)-grafted pineapple leaf fiber/polyester nonwoven fabric adsorbent and its comparison with removal by gamma or electron beam irradiation. *Radiation Physics and Chemistry, 172*, 108737.
https://doi.org/10.1016/j.radphyschem.2020.108737

11. Makeswari, M., & Saraswathi, P. (2020). Photocatalytic degradation of methylene blue and methyl orange from aqueous solution using solar light onto chitosan bi-metal oxide composite. *SN Applied Sciences, 2*, 336.
https://doi.org/10.1007/s42452-020-2361-0

12. Cheng, J., Zhan, C., Wu, J., Cui, Z., Si, J., Wang, Q., Peng, X., & Turng, L. S. (2020). Highly efficient removal of methylene blue dye from an aqueous solution using cellulose acetate nanofibrous membranes modified by polydopamine. *ACS Omega, 5*(9), 5389–5400.
https://doi.org/10.1021/acsomega.9b04059

13. Kahlert, H., Meyer, G., & Albrecht, A. (2016). Color maps of acid–base titrations with colour indicators: How to choose the appropriate indicator and how to estimate the systematic titration errors. *ChemTexts, 2*(1), 7.
https://doi.org/10.1186/s40544-016-0021-2

14. Mondal, S., De Anda Reyes, M. E., & Pal, U. (2017). Plasmon-induced enhanced photocatalytic activity of gold-loaded hydroxyapatite nanoparticles for methylene blue degradation under visible light. *RSC Advances, 7*, 8633–8645.
https://doi.org/10.1039/c6ra27291a

15. Khan, I., Saeed, K., Zekker, I., Zhang, B., Hendi, A. H., Ahmad, A., Ahmad, S., Zada, N., Ahmad, H., Shah, L. A., et al. (2022). Review on methylene blue: Its properties, uses, toxicity and photodegradation. *Water, 14*(2), 242.
https://doi.org/10.3390/w14020242

16. Cheng, J., Zhan, C., Wu, J., Cui, Z., Si, J., Wang, Q., Peng, X., & Turng, L. S. (2020). Highly efficient removal of methylene blue dye from an aqueous solution using cellulose acetate nanofibrous membranes modified by polydopamine. *ACS Omega, 5*, 5389–5400.
https://doi.org/10.1021/acsomega.9b04059

17. Oladoye, P. O., Ajiboye, T. O., Omotola, E. O., & Oyewola, O. J. (2022). Methylene blue dye: Toxicity and potential elimination technology from wastewater. *Results in Engineering, 16*, 100678.
https://doi.org/10.1016/j.rineng.2022.100678

18. Bafana, A., Devi, S. S., & Chakrabarti, T. (2011). Environmental reviews on dyes: Removal technologies. *Environmental Reviews, 19*(4), 350–371.
https://doi.org/10.1139/a11-004

19. Khan, I., Saeed, K., Ali, N., Khan, I., Zhang, B., & Sadiq, M. (2020). Heterogeneous photodegradation of industrial dyes: An insight into different mechanisms and rate affecting parameters. *Journal of Environmental Chemical Engineering, 8*(5), 104364.
https://doi.org/10.1016/j.jece.2020.104364

20. Asati, H., Mondal, R., & Tripathi, K. M. (2024). Ultra-fast microwave catalytic degradation of multiple dyes by waste derived carbon nano onions. *Materials Today Sustainability, 26*, 100724.
https://doi.org/10.1016/j.mtsust.2023.100724

21. Varjani, S., Rakholiya, P., Yong Ng, H., You, S., & Teixeira, J. A. (2020). Microbial Degradation of Dyes: An overview,.*Bioresource* Technology, 314, 123728.
https://doi.org/10.1016/j.biortech.2020.123728

22. Moradihamedani, P. (2022). Recent advances in dye removal from wastewater by membrane technology: a review. *Polym. Bull., 79*, 2603–2631.
https://doi.org/10.1007/s00289-021-03603-2

23. Abewaa, M., Mengistu, A., Takele, T., Fito, J., & Nkambule, T. (2023). Adsorptive removal of malachite green dye from aqueous solution using *Rumex abyssinicus* derived activated carbon. *Scientific* Reports, 13, 14701.
https://doi.org/10.1038/s41598-023-41957-x

24. Arunima, N., Brij, B., & Shreya, K. (2024). Fundamentals of absorption. Sustainable Remediation Technologies for Emerging Pollutants in Aqueous Environment, 29-62.

25. Ambaye, T. G., Vaccari, M., van Hullebusch, E.D., Amrane, A., & Rtimi, S. (2021). Mechanisms and adsorption capacities of biochar for the removal of organic and inorganic pollutants from industrial wastewater. *International Journal of Environmental Science and Technology, 18*, 3273–3294.
https://doi.org/10.1007/s13762-020-03060-w

26. Gibson, L.T. (2017). Mesosilica materials and organic pollutant adsorption: part B removal from aqueous solution. *Chemical Society Reviews*, 15.

27. Escuin, P. C., Bennett, A. G., Vicente, J., Foix, A. A., Andrés, A. (2017). *Food Chem, 217*, 360–363.
https://doi.org/10.1016/j.foodchem.2016.08.027

28. Chueachot, R., Wongkhueng, S., Khankam, K., Lakrathok, A., Kaewnon, T., Naowanon, W. T. et al. (2018). Adsorption efficiency of methylene blue from aqueous solution with amine-functionalized mesoporous silica nanospheres by co-condensation biphasic synthesis: adsorption condition and equilibrium studies. *Materials Today: Proceedings*, *5*,14079–14085.
https://doi.org/10.1016/j.matpr.2018.02.066

29. Ortiz-Islas, E., Sosa-Arróniz, A., Manríquez-Ramírez, M. E., Rodríguez-Pérez, C. E., Tzompantzi, F., & Padilla, J. M. (2021). Mesoporous silica nanoparticles functionalized with folic acid for targeted release Cis-Pt to glioblastoma cells. *Adv. Mater. Science, 60*, 25–37. https://doi.org/10.1515/rams-2021-0009

30. Manzano, M., & Vallet-Regí, M. (2018). Mesoporous silica nanoparticles in nanomedicine applications. *Journal of Materials Science: Materials in Medicine, 29*(5), 1-14. https://doi.org/10.1007/s10856-018-6069-x

31. Wu, S.H., Mou, C.Y., & Lin, H. P. (2013). Synthesis of mesoporous silica nanoparticles. *Chemical Society Reviews, 42*(9), 3862–3875. https://doi.org/10.1039/c3cs35405a

32. Li, Y., Zhou, Y., Nie, W., Song, L., & Chen, P. (2015). Highly efficient methylene blue dyes removal from aqueous systems by chitosan coated magnetic mesoporous silica nanoparticles. *J. of Porous Mater., 22*, 1383–1392. https://doi.org/10.1007/s10934-015-0017-7

33. Hong, Y., Cha, B. J., Kim, Y. D., & Seo, Y. O. (2019). Mesoporous SiO2 Particles Combined with Fe Oxide Nanoparticles as a Regenerative Methylene Blue Adsorbent. *ACS Omega, 4*, 9745–9755. https://doi.org/10.1021/acsomega.9b00726

34. Proa-Coronado, C., Balderas-López, J. A., Sánchez-Fuentes, Y., Linares-Duarte, L. A., & Hernández-Sánchez, E. (2024). Photopyroelectric Techniques for Thermal Diffusivity and Optical Absorption Coefficient Measurements of SiO2 Colloids. *Thermochim. Acta, 739*. https://doi.org/10.1016/j.tca.2024.179806

35. Balderas-López, J. A. (2012). Generalized 1D photopyroelectric technique for optical and thermal characterization of liquids. *Meas. Sci. Technol., 23*(6). https://doi.org/10.1088/0957-0233/23/6/065501

36. Balderas-López, J. A., & Mandelis, A. (2020). *Photopyroelectric Spectroscopy of Pure Fluids and Liquid Mixtures: Foundations and State-of-the-Art Applications*. Springer. https://doi.org/10.1007/s10765-020-02662-3

37. Balderas-López, J. A., Jaime-Fonseca, M. R., Gálvez-Coyt, G., Muñoz-Diosdado, A., & Díaz-Reyes, J. (2015). Generalized Photopyroelectric Setup for Thermal-Diffusivity Measurements of Liquids. *Int. J. Thermophys., 36*(5–6), 857–861. https://doi.org/10.1007/s10765-014-1693-2

38. Ortiz-Islas, E., Sosa-Arróniz, A., Manríquez-Ramírez, M. E., Rodríguez-Pérez, C. E., Tzompantzi, F., & Padilla, J. M. (2021). Mesoporous silica nanoparticles functionalized with folic acid for targeted release Cis-Pt to glioblastoma cells. *Rev. Adv. Mater. Sci., 60*(1), 25–37. https://doi.org/10.1515/rams-2021-0009

DYNAMIC SYSTEM DEVELOPMENT FOR REAL-TIME LIGHT SPECTRA ACQUISITION FOR OPTICAL BIOSENSOR APPLICATIONS IN PYTHON

Christian Isaac Hurtado-Esquivel[1],
Erika Maricruz Gallardo Pinal[1], Luis Alfonso Villa-Vargas[2],
Miguel Ángel Alemán-Arce[2], Verónica Iraís Solís-Tinoco[2,3*],
Marco Antonio Ramírez-Salinas[2]

[1] Unidad Profesional Interdisciplinaria en Ingeniería y Tecnologías Avanzadas UPIITA-IPN. Ingeniería Biónica. Ciudad de México, C.P. 07340.

[2] Centro de Investigación en Computación del Instituto Politécnico Nacional, Laboratorio de Microtecnología y Sistemas Embebidos. Ciudad de México, 07738, México.

[3] Instituto de Ciencias Aplicadas y Tecnología, Universidad Nacional Autónoma de México, Ciudad de México, 04510, México.

* irais.solis@cic.ipn.mx

Abstract

This work presents the development of a dynamic real-time light spectrum acquisition software system utilizing Python, a high-level programming language, focusing on optical biosensor applications. This software provides a versatile tool for acquiring, processing, and visualizing white light spectra obtained by connecting to an Ocean Optics spectrometer.

Dynamic term denotes the system's ability to adjust acquisition parameters in real-time, both in software and hardware, in response to user inputs. This adaptability is achieved via thread-based concurrent programming, guaranteeing precision sampling time (T_s) of up to 99.98 %. By configuring a 500 ms period and an integration time equivalent to 10 ms, offset levels are minimized and noise in captured spectra is reduced: SNR reaches up to 38.54 dB, RMSE is minimized to 27.83, and a maximum R-Squared of 0.9998 is attained. To improve signal quality, a zero-phase second-order Butterworth filter is applied, effectively suppressing noise above the normalized 0.04 rad/sample cut-off. Each captured spectrum is presented by a graphical user interface, with optimized axis boundaries, facilitating real-time analysis. Thus, this work provides an accessible methodology for scientists and technicians to develop a real-time data acquisition program, free from limitations and technological dependencies associated with commercial devices.

Keywords: optical biosensors, python programming, data acquisition, threads, spectrometer

1. Introduction

The implementation of sensors enables to comprehend, monitor, and regulate the environment. Sensors convert physical phenomena into other physical quantities, mainly electrical signals for qualification and quantification purposes. Research advances have driven an interdisciplinary path to emerging biosensors [1, 2]. The Union of Pure and Applied Chemistry (IUPAC) defines a biosensor as a device that uses specific biochemical reactions to detect compounds usually by electrical, thermal, or optical signals [3]. Biosensors are analytical devices designed to interpret biological events mediated by two key components: biological or biomimetic compounds and transducers. The initial stage of a biosensor involves incorporating an element sensitive to an analyte, while the transducer is responsible for detecting the interaction between the analyte and the biorecognition component. When the biological recognition reaction occurs, a series of physicochemical changes takes place, which are detected by the transducer. The transducer transforms this stimulus into a quantifiable output signal [4]. Some transducers recognize the reactions through optical properties changes, facilitating direct, real-time, and label-free detection of biological and chemical substances. Electrical components that contain these transducers are classified as optical biosensors, constituting the central theme of discussion in this work [5].

In the realm of optical biosensors, light is the energy source used to interact with samples. When light falls on an analyte, a portion of it may be absorbed by the sample's constituents. Absorbance is a measure that quantifies the ability of a medium to absorb incident light, while transmittance refers to the medium capacity to transmit energy. Furthermore, some of the incident light may be reflected off the surface of the sample, a phenomenon known as reflectance. Reflectance measures the proportion of incident light that is redirected from the sample's surface. Optical sensors discern and quantify these changes in absorbance, transmission, and reflectance to analyze samples for the presence of certain components, such as biomolecules or specific chemical compounds [4]. The high specificity of these sensors, their sensitivity, compactness and cost-effectiveness enable applications spanning healthcare, environmental monitoring and biotechnology [5].

A spectrum represents the amplitudes of a system's wave components, and light can be seen as this. The measurement of interactions between light and

matter, reactions and measurements of radiation intensity and wavelength, is called spectrometry. Spectrometers are scientific-technical field instruments that are used for the analysis of different forms of matter in the form of a signal [6]. Spectral data analysis is crucial for many fields, where accurate measurements are fundamental. The demand for real-time signal analysis requires faster execution of analytical operations to process all signal components within the designated frequency spectrum. Therefore, it is imperative that signal display occurs quickly and that all computational procedures persist uninterrupted, adapting to variations in the input signal [7].

Ocean Optics spectrometers provide various data acquisition methods, which have their own spectroscopic application. It is a software that has a graphical interface that provides fast and stable data acquisition and processing [8]. However, the license comes with a hefty price tag, making it unaffordable. Moreover, it includes additional advanced features that enable users to engage with the spectrometer data, incurring an additional expense. Then, this program has limitations and technological dependencies associated with commercial devices.

Another software that is capable of interfacing with these spectrometers is MATLAB. This is a platform that provides the Instrument Control Toolbox, which allows the connection with Ocean Optics spectrometers. A wide range of tasks can be carried out in MATLAB, such as acquiring a spectrum, adjusting integration time, applying dark current and non-linear spectral corrections, and viewing all connected devices [9]. Despite being a powerful tool, it is important to be aware of its drawbacks. One significant disadvantage is the high cost associated with it. Moreover, licenses need to be renewed annually, which can be quite expensive for businesses and organizations relying on MATLAB regularly.

Therefore, to overcome these challenges, it is essential to understand how to develop software that allows efficient and seamless access to spectrometer data. This would unlock new possibilities for researching and analyzing spectroscopic data, eliminating the need to purchase costly licenses or additional software packages.

On the other hand, Python is an open-source high-level programming language which has become indispensable in science and technology. Cross-platform portability, wide variety of packages and component integration are the main characteristics that allow the user to do multiple tasks successfully. Its

versatility makes it popular in software development, due to the simplicity in syntax and robustness in functionality [10].

Another feature of Python is the fact that it is an interpreted language. This means that the Python interpreter alternately reads and performs the calculations for each of the lines of code. It then repeats this process if there are no errors. This allows to test language functionality while programming [11, 12]. Part of Python's technological development focuses on communication protocol implementation for several purposes, taking advantage of libraries such as PySerial and PyUsb. These protocols generate data exchange and communication between devices, which guarantees efficient operation and joint operability between platforms. Thus, Python represents aids for developers, who can create reliable and scalable solutions for their communication needs across different domains.

In the field of spectrophotometry, Python emerges as a functional tool for spectral analysis purposes, specifically, to interact with hardware devices like spectrometers: Python-SeaBreeze. That is why it is important to understand the underlying protocols in this context. Python-SeaBreeze plays a critical role, bridging the gap between Python's analytical capabilities and the complexities of spectrometer communication. SeaBreeze library facilitates communication with Ocean Optics spectrometers, offering two distinct backends: cseabreeze, which wraps the SeaBreeze library, and pyseabreeze, which uses PyUsb for communication [13]. Attributable to Python's flexibility and scalability, it is possible to develop software for the acquisition, processing, and visualization of spectrometer data. Developers can focus more on problem-solving and less on the complexities of programming languages, resulting in faster development cycles and more efficient software delivery. Due to the versatility of the language and its wide applications in science and engineering, libraries and built-in functions were used to process signals, plot, and control sub-processes [14].

To execute Python programs or *scripts*, a code editor, or an integrated development environment, called an IDE, is required [15]. Likewise, it is possible to use a *shell* to write and run Python code. A *shell* is a command interpreter, which means a program that translates commands entered by the user into instructions for accessing operating system services [16]. It is possible to access the Python Shell once the language has been installed. In this work, Windows PowerShell served as the primary tool for executing a variety of installation processes due to the operating system [17].

In addition, although Python can establish parallel processing, its application is limited depending on the computer architecture [18]. When a processor has only one core, it is not possible to perform multiple tasks simultaneously. On the other hand, for multi-core processors, it is possible to create several processes running in separate memory spaces and avoiding deadlocks; a concept known as parallel programming [19, 20]. A process represents a running program which requires resources allocated during its execution. Each process operates within its own memory space and execution context. The operating system manages the processes, enabling them to run simultaneously [14, 21]. This limitation poses problems in efficiently utilizing multiple processors or cores, particularly in scenarios where computational tasks need to be executed concurrently.

For this reason, to enhance compatibility with single-core processors, a multi-threaded task execution flow, referred to as threads, was introduced. One or more threads can be executed within a single process and Python provides a few modules to create and manipulate these threads. However, due to the Global Interpreter Lock (GIL) in CPython (the standard implementation of Python), only one thread can execute Python code at a time. This means that even if threads are used, only one thread can be running at any given time [22, 23].

However, developing spectral acquisition software using Python presents notable challenges. First, the spectrometer's quality directly affects the precision and reliability of the obtained data. Additionally, successful integration requires handling each device's specific communication protocols, which can be complex due to the variety of interfaces and standards used by manufacturers. Another consideration is the libraries and requirements necessary to interact with the spectrometer hardware. This involves installing and setting up additional dependencies, which can complicate the development process.

In this work, we present a step-by-step methodology for developing a Python program to facilitate the real-time acquisition and control of spectra from sources such as halogen light sources, standard flashlights, and LED light sources. The spectrometer utilized is the Ocean Optics Flame-T model, which is widely employed for acquiring and measuring electromagnetic spectra from optical sensors.

First, the acquisition system is explained. It starts by presenting the general model of the designed software and continues with the creation of the environment that allows access to the SeaBreeze library functions. This is a process that only needs to be performed once. Subsequently, the multithreaded processing is discussed

to make the system modifiable in its acquisition parameters and asynchronously. Likewise, it is detailed how the recognition is performed with the device, the reading of the spectra, and the adjustment to the signals to increase their quality by attenuating the noise present. To conclude the section, the strategy for displaying the spectra on the screen and storing them in the computer is mentioned. Finally, the spectra obtained are presented and analyzed. In this work, a LED light source was used, and 10 spectra captured every 5 seconds were analyzed.

This Python program could be used for real-time detection of electromagnetic spectra generated by optical biosensors. The acquisition of spectrometer data can be applied in measuring optical properties such as transmittance, reflectance, or absorbance. Furthermore, acquiring data from the spectrometer in real-time enables the calculation of sensorgrams generated during biofunctionalization experiments of biosensors, which may last for minutes or even hours. This Python program can be used for detecting changes in optical properties with the help of specific optical biosensors, depending on the type of study.

2. Methodology

This section elaborates on the design of the acquisition system. A representation of the connections used is depicted in Figure 1. Initially, an LED light source was positioned in proximity to the spectrometer detector (Figure 1A). Additionally, a Flame T spectrometer was employed (Figure 1B), connected to the computer via the USB communication protocol (Figure 1C). The dynamic real-time spectrum acquisition system was developed using the Python programming language. In this acquisition process, the utilization of a *shell* was imperative to establish communication with the software. It enabled user data input and provided information display regarding the various ongoing processes, as illustrated in Figure 1D. Ultimately, throughout the acquisition process, a printout of each spectrum was generated (Figure 1E).

For the development of this system, we utilized Python version 3.9.6 along with numerical data manipulation and visualization libraries such as *NumPy* and *Matplotlib*. Additionally, we incorporate the spectrum acquisition package *SeaBreeze*, as well as modules for time monitoring (*time*), thread management (*threading*), and interaction with the operating system to control program inputs and outputs (*sys*). The general block diagram of the proposed system is shown in Figure 2 and it is described in the following sections.

2.1. *SeaBreeze Execution Environment Set Up*

The SeaBreeze library facilitates communication between the spectrometer and the computer. Before using SeaBreeze functions, it is necessary to complete an installation process for dependencies and libraries. This configuration is a one-time process, establishing an environment capable of transmitting data, reading hardware parameters, and facilitating the development of new functions. Figure 3 illustrates the proposed sequence, with each sub-process detailed below.
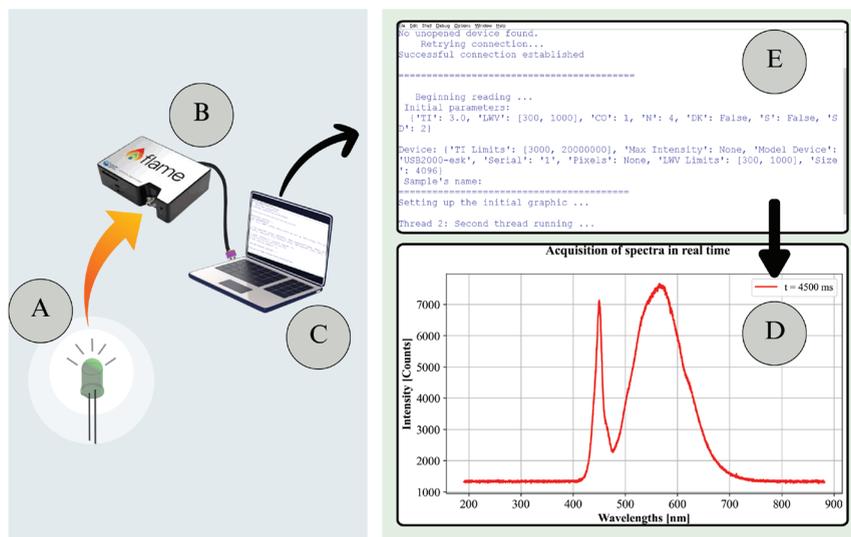

Figure 1. Components of the proposed spectrum acquisition system: (A) representation of the LED light source, (B) example of Ocean Optics spectrometer, (C) computer compatible with the requirements of the proposed system detailed in section 2.2, (D) example of the history produced when running the system through a terminal, (E) example of wavelength distribution associated with the light source used; spectrum saved at instant 4.5 s after starting the run.
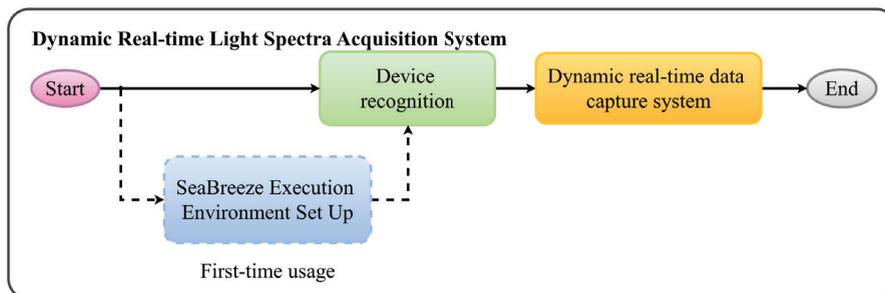

Figure 2. Block diagram illustrating the implementation and configuration of a dynamic real-time spectrum acquisition system.
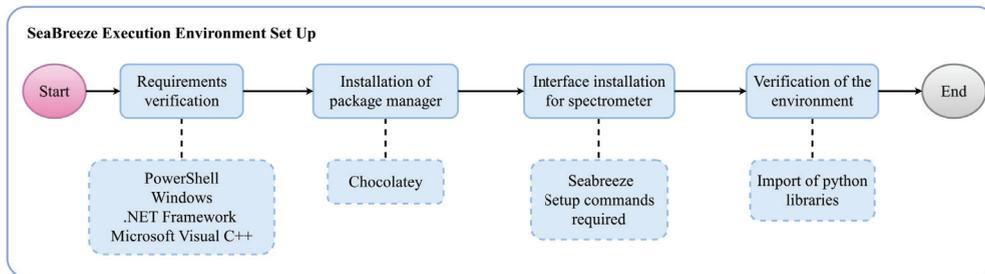
Figure 3. Flowchart outlining the proper configuration of the environment required
for utilizing the SeaBreeze library.

2.2. *Requirements Verification*

The initial requirements for establishing communication with the measurement
hardware are summarized in Table 1.

Software	Version	More information
Windows	+8	-
Windows PowerShell	+3	PowerShell Installation
.NET Framework	+4.8	.NET Framework Download
Microsoft Visual C++	+4.8	Microsoft Visual Studio Download

Table 1. Software versions. Information revised in 2024.

To begin the installation process on Windows, a minimum of Windows 8
or Windows Server 2012 version is required. Operating systems are generated
through PowerShell, enabling subsequent installations. The version of PowerShell
must be reviewed, which, according to current technologies, should be equal to
or greater than 3.

```
Windows PowerShell

PS C:\Windows\system32> $PSVersionTable.PSVersion

Major  Minor  Build  Revision
-----  -----  -----  --------
5      1      19041  4170
```

In this example, based on the Major and Minor attributes, the Windows
PowerShell version is 5.1. Configuring the execution policy is necessary. This
adjustment allows the execution of scripts, which are essentially programming

code designed to automate certain processes, but only those scripts signed by a trusted publisher [24, 25].

The first step is to run PowerShell as an administrator and grant permissions to access as a superuser. Next, the security level is verified by executing the following line:

```
Windows PowerShell
PS C:\Windows\system32> Get-ExecutionPolicy
```

If the result in the terminal is Restricted, the level must be changed to *Allsigned*. The command to set up the execution policy is as follows:

```
Windows PowerShell
PS C:\Windows\system32> Set-ExecutionPolicy AllSigned
```

On non-Windows computers running PowerShell 6.0, the default execution policy is Unrestricted and cannot be changed [26]. The following prerequisite is .NET Framework version 4.8 or higher. This framework facilitates the creation and running of various applications, including desktop apps, web services, and more [27, 28]. Finally, Microsoft Visual C++ compilation tools are necessary with a version greater than or equal to 4.8. These tools are essential for compiling and debugging C++ code, which is particularly valuable for low-level device communication and hardware control. The SeaBreeze library primarily operates via C/C++, even though the interface is in Python, making these tools crucial for its functionality [29, 30].

2.3. *Package Manager Installation*

Once the requirements have been fulfilled, the *Chocolatey* package manager was chosen to facilitate the installation process of the SeaBreeze library, following [13, 31] recommendation. The following batch of commands is executed in Windows PowerShell.

```
Windows PowerShell
PS C:\Windows\system32> Set-ExecutionPolicy Bypass -Scope Process -Force;

    PS C:\Windows\system32> [System.Net.ServicePointManager]::SecurityProtocol =
  [System.Net.ServicePointManager]::SecurityProtocol -bor 3072;

    PS    C:\Windows\system32>    iex    ((New-Object    System.Net.WebClient).
  DownloadString('https://chocolatey.org/install.ps1'));
```

Note: using semicolon *(;)* at the end of each command is a method used to distinguish the beginning and end of long instructions. To verify the correct package manager installation, the next command is used:

```
Windows PowerShell
PS C:\Windows\system32> choco
Chocolatey v2.2.2
```

This example displays *Chocolatey* version 2.2.2 installed.

2.4. *Spectrometer Interface Installation*

After installing *Chocolatey*, basic operation requirements are obtained by executing the following code in the terminal.

```
Windows PowerShell
PS C:\Windows\system32> choco install visualcpp-build-tools
PS C:\Windows\system32> choco install windows-sdk-10.1
PS C:\Windows\system32> choco install windowsdriverkit10
```

These three packages are essential for compiling and executing SeaBreeze code, facilitating hardware manipulation using Python commands executed in C++. They collectively streamline the compilation and execution processes. Table 2 provides further details on these commands.

Commands	Actions
choco install visualcpp-build-tools	Installs Microsoft Visual C++ compilation tools.
choco install windows-sdk-10.1	Installs Windows 10.1 Software Development Kit (SDK) for building applications.
choco install windowsdriverkit10	Installs Windows 10 Driver Development Kit (WDK), which includes building and deploying driver tools (programs that support hardware-operating system interaction), [13].

Table 2. Requirements installation using Chocolatey.

The subsequent task is SeaBreeze library installation using the commands below:

```
   Windows PowerShell
   PS  C:\Windows\system32>  git  clone  https://github.com/ap--/
 python-seabreeze.git python-seabreeze;
PS C:\Windows\system32> cd python-seabreeze;
And then,
PS C:\Windows\system32> python -m pip install .;
Or
   PS C:\Windows\system32> python -m pip install --no-binary :all:
 seabreeze;
```

Each line of code is described below, including the actions it performs.

♦ **Copy a directory:** The command *git clone https://github.com/ap--/python-seabreeze.git python-seabreeze*, makes a copy of the GitHub repository (according to the specified path) into a new directory on the computer named "python-seabreeze".

♦ **Change directory:** The *cd python-seabreeze* command indicates that you are moving to another path, in this case, to the "python-seabreeze" directory, which is the one you just cloned. The *cd* (change directory) statement is who performs the directory change action [32].

♦ **Installation:** The instruction [*python -m pip install .*] installs the SeaBreeze library in the current directory, which is specified with the dot (.).

♦ **Second way of installation:** If the binary versions are not available, it is possible to install using *python -m pip install --no-binary :all: seabreeze*. This installation is done from source code instead of using precompiled versions, also called binary.

Finally, it was necessary to install the drivers responsible for establishing correct communication with the hardware. This was achieved by executing the following command.

```
Windows PowerShell
PS C:\Windows\system32> seabreeze_os_setup
```

After pressing the *Enter key*, a confirmation menu appeared on the screen. To proceed with the installation, the affirmative option was selected, initiating the installation process. Once the previous operation has been completed, it

is possible to establish the correct connection between the spectrometer and the computer [13]. To verify all previous installations, it is suggested to use the commands described in section 2.5.

2.5. *Verification of the environment*

As the last step in setting up the environment, it was necessary to follow the following commands, which check that the installation processes were executed without errors.

2.6. *Open Windows PowerShell and activate the Python environment*

To activate the Python virtual environment, the command *"py"* was entered into the shell, followed by pressing the Enter key:

```
Windows PowerShell

PS C:\Users\USERNAME> py

Python 3.9.6 (tags/v3.9.6:db3ff76, Jun 28 2021, 15:26:21)
[MSC v.1929 64 bit (AMD64)] on win32
Type "help", "copyright", "credits" or "license" for more
information.
>>>
```

This results in displaying the current version of Python being used. Now, *Windows PowerShell* can be used as the language interpreter, recognizing all the language's commands. It is important to note that the ">>>" symbols now appear, indicating a change in shell behavior. With this change, the Python interpreter has been initiated, enabling the writing and execution of Python code in real-time, establishing a text input and output environment. This is referred to as the Terminal [33].

2.7. *Import SeaBreeze libraries*

These instructions are necessary to establish the connection to the spectrometer.

```
Python

>>> import seabreeze
>>> seabreeze.use('cseabreeze')
>>> import seatease.cseatease as emu_Spectrometer
```

After successful import, it is recommended to connect the device to the computer and execute the following command block.

2.8. *Connection verification*

With these sentences, it was possible to verify the connection to the spectrometer. The result on the screen depends on the model of the device you are working with.

```Python
>>> spec = Spectrometer.from_first_available()
>>> print(spec)
<Spectrometer USB4000:USB4H10178>
```

In case the physical device is not available, it is still possible to perform the verification by means of a spectrometer simulation. The instructions for this were:

```Python
>>> emu_spec = emu_Spectrometer.SeaTeaseAPI().list_devices()[0]
>>> print(emu_spec)
<SeaTeaseDevice: 1>
>>> type(emu_spec)
<class 'seatease.cseatease.SeaTeaseDevice'>
```

The *print()* instruction is used to display the list of available compatible devices on the screen. In the case of the simulation, it only returned *<SeaTeaseDevice: 1>*. Finally, the *type()* instruction displays the type of variable being introduced. In this case, it corresponds to an object of class *'seatease.cseatease.SeaTeaseDevice'*, which is correct and indicates that the virtual device recognition process is correct. The spectrometer model utilized in this work was the *Ocean Optics Flame-T model.* Table 3 displays some parameters of this device.

Specification	FLAME-T
Integration Time	3.8 *ms* to 10 *seconds*
Dynamic Range of system[1]	3.4×10^6
Scan rate (max)[2]	260 Hz

Table 3. Optical and spectroscopic specifications.

---

1. Dynamic range of the system is the range of the detectable light level and can be thought of as the maximum detectable light level at the minimum integration time divided by the minimum detectable light level at the maximum integration time.

2. Scan rate is dependent on the operating computer and not the spectrometer. These figures assume a non-real-time operating system [51].

Before concluding the section, the code statements used in the processes described above are presented in Table 4, along with their representation in pseudocode form, which is used throughout this work. The process of installing the required libraries, packages, and software was performed only once on the computer. Once the device recognition test was successful, we proceeded to design the acquisition system, which is detailed in sections 2.9 and 2.10.

Code	Pseudocode	Action
`Spectrometer. from_first_available()`	spec ← Spectrometer_ connection( )	Connection to the first available spectrometer.
`emu_Spectrometer. SeaTeaseAPI().list_ devices()[0]`	emu_Spec ← emu_ Spectrometer_connection( )	Spectrometer simulation.
`spec._wavelengths`	range_wv ← spec_ wavelengths	Reads the accepted wavelength range.
`spec.integration_time_ micros_limits`	range_ti ← spec_ integration_time_micros_ limits	Reads the accepted integration time interval (*us*).

Table 4. Pseudocode representation of the functions to connect to the spectrometer.

2.9. *Device Recognition*

According to Figure 2, the proposed acquisition system begins with the recognition of the spectrometer. To initiate the readings, it was necessary to create a PY file and import the corresponding libraries into the environment. The following libraries were imported: the *SeaBreeze* library, facilitating the connection with the spectrometer; *NumPy*, for manipulating measurements as matrix data; *Matplotlib* for graph visualization; and *time* for controlling the flow of time in data sampling. Additionally, *threading* and *signal* were utilized to create and manage actions in two processing threads: one dedicated to data capture (Main Thread) and the second to review and update parameters modifying the hardware acquisition behavior according to user requirements. Finally, *sys* was used to successfully complete the script execution.

Subsequently, a connection request loop was executed. This involves attempting to connect to the spectrometer, and if any issues arise, the system continues

attempting to connect. If a certain number of attempts are exceeded, it indicates an unsuccessful connection and prompts the user to either continue in simulation mode or terminate the program. This functionality can be beneficial, particularly when the device is not owned, and the user wishes to learn how to manipulate spectrogram data available with the SeaBreeze library. Another scenario is when the computer requires additional time to recognize the external device.

Upon a successful connection, the system creates an object of the *Spectrometer* class, which is defined by the model and serial number of the hardware. In this work, the model obtained was *<Spectrometer USB4000:USB4H10178>*. This information is available in the attributes of the spec variable, specified in the pseudocode of Table 4 and Table 5. With this entity, it became feasible to access the captured data and configure spectrometer parameters for the reading, such as: integration time T_I, number of samples to be averaged N, and the desired wavelength limits $wv_{L_{min}}$ and $wv_{L_{max}}$ according to the desired analysis.

Details regarding these parameters and their modifications are presented in section 2.13. The logic used is shown in Table 5 by means of pseudocode.

Following successful linkage with the spectrometer, a synchronous data acquisition system was implemented. This system enables the acquisition of spectral data according to a sampling time T_S, determined by two factors: the user's choice and the integration time T_I required during experimental tests. The process is applicable for both available modes, namely using the Hardware or Virtual mode. This system is explained in detail in section 2.10.

2.10. *Dynamic Real-Time Data Capture System*

This subsection elaborates on the strategies devised to initiate the real-time reading process. This system possesses the characteristic of accommodating the user's external requests and adjusting the reading data accordingly. This is achieved while the system acquires signals from the spectrometer, avoiding any undesired pauses. Consequently, the system is termed dynamic. Figure 4 illustrates the block diagram of this system.

To ensure that the system can manage external user requests, two processing threads have been implemented. These threads enable achieving a concurrency effect, allowing two different processes to run seemingly simultaneously. The components comprising this system are described below.

1. Device Recognition

Algorithm 1: Device Recognition

Data: $attempts$

Result: $features, spec$

1 $count \leftarrow 1$;

2 **while** $count \leq attempts$ **do**

3   **try**

4        $hard_{Spec} \leftarrow Spectrometer\_connection()$;

5        $status \leftarrow hard_{Spec}$;

6        $break$;

7   **catch**

8        $count \leftarrow count + 1$;

9        $status \leftarrow None$;

10 **end**

11 **if** $status = None$ **then**

12     $r_{user} \leftarrow Input()$;

13   **if** $r_{user} = {'E'}$ **then**

14        $Exit()$;

15   **else**

16        $emu_{Spec} \leftarrow emu\_Spectrometer\_connection()$;

17        $spec \leftarrow emu_{Spec}$;

18        $s_{type} \leftarrow {'Virtual'}$;

19   **end**

20 **else**

21     $spec \leftarrow status$;

22     $s_{type} \leftarrow {'Hardware'}$;

23 **end**

24 **if** $s_{type} = {'Hardware'}$ **then**

25     $range_{wv} \leftarrow spec\_wavelengths$;

26     $range_{ti} \leftarrow spec\_integration\_time\_micros\_limits$;

27 **else**

28     $range_{wv} \leftarrow [300, 1000]$;

29     $range_{ti} \leftarrow [3000, 10000000]$;

30 **end**

31 $features \leftarrow [range_{wv}, range_{ti}, s_{type}]$

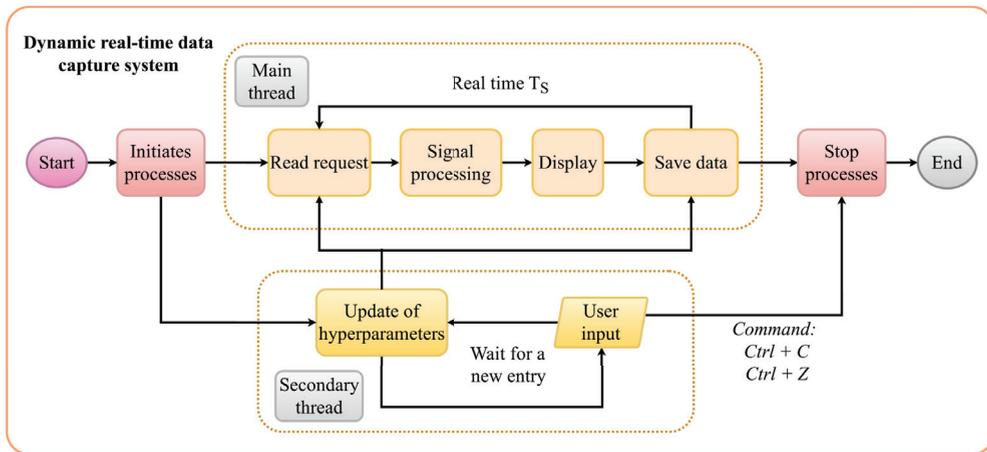Table 5. Pseudocode of the Device Recognition process.

Figure 4. Flowchart diagram of the spectrometer acquisition system.

2.11. *Initiates Processes*

In this block, both threads or sub-processes are initialized: the Main thread and the secondary thread. In the first thread, all the logic related to real-time acquisition was established, and a reading request period of (T_S) was set. Within this interval, the functions related to signal acquisition and processing are executed. It is important to note that this time represents the speed of spectrum reading and should not be confused with the integration time (T_I), which is a parameter of the spectrometer.

To enhance the quality of recorded data, it is necessary to adjust the configuration of the device's hyperparameters. A methodology was implemented to execute these changes, possibly in an aperiodic manner, as indicated by the user. This process is carried out in the second thread and does not affect the acquisition process of the main thread.

The hyperparameters mentioned above are:

♦   Integration time T_I.
♦   Limits of the wavelengths of interest wv_L.
♦   Number of spectra to average N_S to attenuate the present noise.
♦   Instruction to consider the Background Spectrum (B_S) to eliminate it. This signal level is captured by the device when the sample to be analyzed is absent [34].

Finally, the possibility of terminating the program at any time by using the *Ctrl + C* or *Ctrl + Z* instructions was established. The logic used is illustrated in Table 6 through pseudocode.

2. Dynamic Real-Time Data Capture System

2.1. Initialization process

Algorithm 2: Initialization Processes
Data: N,T_{S_0},T_{I_0},N_{S_0}
Result: $hyperparameters$
1 $attempts \leftarrow N$;
2 $T_S \leftarrow T_{S_0}$;
3 $T_I \leftarrow T_{I_0}$;
4 $N_S \leftarrow N_{S_0}$;
5 $B_S \leftarrow True$;
6 $features \leftarrow device\_recognition(attempts)$;
7 $hyperparameters \leftarrow [features, T_S, T_I, N_S B_S]$;
8 $Activate : key\_board_{interrupt}$;
9 $Start : Second\_thread$;

Table 6. Pseudocode of the initialization process.

Next, sections 2.12 and 2.17 detail the methodology employed in the main processing thread as well as in the secondary thread.

2.12. *Main Thread*

This block corresponds to the process of acquisition, digital treatment, and display of the captured signal. Four main actions were established sequentially: (i) data reading, (ii) application of filtering and adjustment techniques, (iii) screen display, and (iv) the option of storing the readings in the computer. Each task is described in detail below.

2.13. *Read Request*

Every T_S seconds, a new read request is made with the hyperparameters allowed by the device. These were initialized in the Initiates processes block in section 2.11. In this work, the accepted hyperparameters corresponding to the device model are presented in Table 7.

Hyperparameters	Value
T_I	3.8 *ms* to 10 *seconds*
wv_L	[191.0969 – 881.4172] *nm*
N_S	Natural number
B_S	True or False
T_S	[500 - 5000] *ms*

Table 7. Options for hyperparameter values employed in the proposed methodology.

The data reading was conducted using the SeaBreeze library, resulting in the acquisition of the spectrum. It was feasible to identify the vector storing the wavelengths present and the count vector. These data are contingent on the nature of the light source, as well as the integration time T_I configured. Table 8 presents the main statements used and their corresponding pseudocode.

Code	Pseudocode	Action
`spec.integration_time_micros(TI)`	set_integration_ time(TI)	Sets the TI for spectrum reading.
`spec.wavelengths()`	$x \leftarrow$ read_wv()	Read vector wavelengths.
`spec.intensities()`	$y \leftarrow$ read_int()	Reads vector of intensities.
`spec.f.spectrometer.` `set_integration_time_micros(Ts)`	vset_integration_ time(TI)	Sets the TI for simulation.
`spec.f.spectrometer.get_wavelengths()`	$x \leftarrow$ read_wv_ virtual()	Read vector of virtual wavelengths.
`spec.f.spectrometer.get_intensities()`	$y \leftarrow$ read_int_ virtual()	Read vector of virtual intensities.

Table 8. Main instructions and their representation in pseudocode.

Finally, with the equivalences provided in Table 8, the logic employed in the Read Request block is presented; refer to Table 9.

2.14. *Signal Processing*

This block was responsible for reducing the signal offset and attenuating the noise present in the data. Since this work primarily focused on capturing absorbance spectra, the signal to be processed indicates the behavior of the light captured solely by the spectrometer. This spectrum can be primarily represented as a composition of three signals: the real physical signal $(y_p(t))$, the noise mainly stemming from the effect of ambient illumination $(y_l(t))$, and the noise caused by electromagnetic effects added during the digital conversion processes, $y_e[n]$. Therefore, the actual physical signal tends to be contaminated.

The above can be described by equation (1).

$$y(t) = y_p(t) + y_l(t), \quad t \geq 0,$$

$$\therefore y[n] = y_p[n] + y_l[n] + y_e[n], \quad n \geq 0.$$

$$(1)$$

Where $y[n]$ corresponds to the contaminated digital signal, which can be plotted on the computer. The digital signals $y_l[n]$ and $y_e[n]$ represent the ambient and electronic noise, respectively. The objective of this processing block was to decrease the effects of noise and ambient light (the latter causing an offset). Therefore, it is possible to reduce the signal offset by subtracting the minimum value present in the reading.

This is expressed in equation (2).

$$y_{adj} = y - min\{y\} \qquad (2)$$

where y_{adj} represents a correction of the signal for the offset effect caused by a base noise signal (*Background Spectrum*). This adjustment aligns the values to estimate the maximum readout count and determine its corresponding wavelength. However, this process does not eliminate the noise present. Therefore, it was proposed to use a low-pass discrete Fourier domain filter with a 2nd order Butterworth response. The Butterworth response was chosen because this type of filter maintains a linear phase in the passband [35]. Additionally, due to the nature of the analyzed signal, it is necessary to preserve the correspondence between the wavelengths and their counts. Therefore, the zero-phase Butterworth filter was utilized. This type of filter has the advantage of avoiding a lag with respect to the original signal. Additionally, the filtering process is performed twice: once in the forward direction and the second in the reverse direction in the signal, enhancing

the noise attenuation effect [36]. This approach ensures that critical points in absorbance spectra detection are not interfered with. Finally, the cut-off point at which the filter began to attenuate the noise was chosen experimentally, set at 0.1.

2.2.   Read Request

Algorithm 3: Read Request

Data: $hyperparameters$

Result: x_select, y_select

1 **if** $Valid\_hyperparameters = True$ **then**

2 | $Update : T_S$;

3 | $Update : T_I$;

4 | $Update : range_{wv}$;

5 | $Update : N_S$;

6 | $Update : B_S$;

7 **else**

8 | $T_S^{new} \leftarrow T_S^{old}$;

9 | $T_I^{new} \leftarrow T_I^{old}$;

10 | $range_{wv}^{new} \leftarrow range_{wv}^{old}$;

11 | $N_S^{new} \leftarrow N_S^{old}$;

12 | $B_S^{new} \leftarrow B_S^{old}$;

13 **end**

14 **if** $s_{type} = 'Hardware'$ **then**

15 | $set\_integration\_time(T_I)$;

16 | $x = read_{wv}()$;

17 | $y = read_{wv}()$;

18 **else**

19 | $vset\_integration\_time(T_I)$;

20 | $x = read\_wv\_virtual()$;

21 | $y = read\_int\_virtual()$;

22 **end**

23 $Update : hyperparameters$;

24 $x\_select \leftarrow x[range_{wv}^{new}]$;

25 $y\_select \leftarrow y[range_{wv}^{new}]$;

Table 9. Pseudocode of the Read Request block.

In this work, the FFT algorithm was implemented using the *fft.fft* function of the NumPy library for the choice of the cut-off point [37]. For the design and application of the filter, *signal.butter* and *signal.sosfiltfilt* from SciPy were utilized [38]. This filtered signal was displayed on the screen and stored in the computer in a CSV format file. Table 10 below presents the pseudocode that explains the previously detailed process.

2.3. Signal processing

Algorithm 4: Signal Processing

    Data: x, y_select, l_c

    Result: $\hat{y}$

1 **if** $First\_reading = True$ **then**

2      $Order \leftarrow 2$;

3      $\Delta_x \leftarrow (max\{x\} - min\{x\})/(length(x) - 1)$;

4      $f_s \leftarrow 1/\Delta_x$;

5      $\Phi_n \leftarrow l_c/(f_s/2)$;

6 **else**

7      $pass$;

8 **end**

9 $y\_adj \leftarrow y\_select - min\{y\_select\}$;

10 $sos_{coefficients} \leftarrow butter_{coeff}(order, \Phi_n, type = 'filtfilt')$;

11 $\hat{y} = filter(sos_{coefficients}, y\_adj)$;

Table 10. Pseudocode of the Signal Processing block.

2.15. *Display*

After signal processing, an interactive graph was created that updates with each reading. This means that the display automatically adjusts the limits of the coordinate axes according to the light input to the spectrometer to achieve correct visualization. This function updates according to the time T_s and accommodates changes made by the user, particularly those from the secondary thread. In this graph, the most important hyperparameters are the limits of the wavelengths to be displayed, according to the desired experimental process.

Section 3.2 showcases the graphs obtained with the proposed methodology. Likewise, the structure of the code used is presented in Table 11.

2.4. Display

Table 11. Pseudocode of the Display block.

Algorithm 5: Display

    Data: $x\_select, \hat{y}$

    Result: $None$

1 **if** $First\_reading = True$ **then**

2      $Initialize : graph$;

3      $Set : Title$;

4      $Set : X\_Label$;

5      $Set : Y\_Label$;

6 **else**

7      $pass$;

8 **end**

9 $X\_data \leftarrow x\_select$;

10 $Y\_data \leftarrow \hat{y}$;

11 $Set : X\_lim(range_{wv}^{new})$;

12 $Set : Y\_lim([0.98 \cdot min\{\hat{y}\}, 1.02 \cdot max\{\hat{y}\}])$;

13 $Graph\_Draw(X\_data, Y\_data)$;

14 $Graph\_uptade()$;

2.16. *Save Data*

Finally, the recorded and processed samples are stored in a CSV format file. After each save action, the acquisition loop restarts to initiate a new read request. As previously mentioned, the hyperparameter update and verification process were implemented in the secondary thread to avoid halting the acquisition loop and to concentrate the functions on signal processing. Section 2.17 provides details about this secondary thread.

2.17. *Secondary Thread*

This system was designed with the possibility of making changes in the hyperparameters at any time, allowing the updating of the spectrum capture process, as well as in the visualization of the graph. Due to the use of the *input( )* function, the program constantly waits for a change. Once a correct input is detected, the system updates the old hyperparameters used in the *Read Request* and *Display* blocks. Subsequently, the system returns to waiting for a new input. Each hyperparameter update is performed at the end of each reading and signal processing, avoiding errors during the acquisition process. If two previous consecutive inputs were the same, a workflow was designed to avoid unnecessary updates. This process continues until the user finishes the program from the terminal, having not only the secondary thread, but also the main thread.

2.5. Secondary thread

Algorithm 6: Secondary Thread

Data: $hyperparameters^{old}$
Result: $hyperparameters^{new}$
1 $def\ \ hyper\_uptade\_Function(hyperparameters^{old}, hyperparameters^{new})\{$
2 **if** $hyperparameters^{old} \neq hyperparameters^{new}$ **then**
3 | $Update : hyperparameters;$
4 **else**
5 | $pass;$
6 **end**
7 $\}$
8 **while** $True$ **do**
9   **try**
10     $str\_hyper \leftarrow input();$
11     $data\_hyper \leftarrow str2float\_hyper\_Function(str\_hyper);$
12     $hyperparameters^{new} \leftarrow data\_hyper;$
13     $hyper\_uptade\_Function(hyperparameters^{old}, hyperparameters^{new})$
14   **catch**
15     $print('Invalid\ \ entry');$
16     $continue;$
17 **end**

Table 12. Pseudocode of the secondary thread.

2.18. *Stop Processes*

As the last block of the dynamic real-time data capture system, for this application, the use of the terminal was proposed as a method of program completion. Both threads were kept running until the *Ctrl + C/Z* command was entered in the Python Terminal while the script was running.

A process terminates when it completes the execution of its final statement and requests the operating system to terminate it via the *exit( ) system call*. At this point, the process can return a status value, typically an integer, to its parent process awaiting it (via the *wait( ) system call*). All process resources, including physical and virtual memory, open files, and I/O buffers, are deallocated, and reclaimed by the operating system [21].

In section 3, we present what was obtained during the execution of the proposed methodology for a cell phone light source, since being a low-quality signal, it allowed the design of a robust methodology. The quality metrics utilized to assess the feasibility of the signal processing stage are presented in section 2.19 below.

2.19. *Validation*

It is necessary to verify that the signal adjustment and filtering process does not diminish the quality of the captured information. Therefore, it is proposed to use three metrics to evaluate the processing block: the signal-to-noise ratio (SNR), the root mean square error (RMSE), the coefficient of determination (R-squared) and two indicators based on the amplitude of the signals (DA) and the Shannon entropy (DE) [39-41]. According to [42, 43], higher SNR values generate more efficient results, and the lower the RMSE, the more desirable the result. Likewise, it is desired that R-square be as close to 1 as possible; see equation (3).

$$SNR(dB) = 10 \cdot log \left(\frac{\sum_{i=0}^{N-1} (y_a[i])^2}{\sum_{i=0}^{N-1} (y_a[i] - \hat{y}[i])^2} \right), \qquad (3)$$

$$RMSE = \sqrt{\frac{1}{N} \sum_{i=0}^{N-1} (y_a[i] - \hat{y}[i])^2} \,,$$

$$R_{square} = 1 - \frac{\sum_{i=0}^{N-1} \left(y_a[i] - \hat{y}[i]\right)^2}{\sum_{i=0}^{N-1} \left(y_a[i] - \overline{y}_a\right)^2} \ .$$

Where $y_a[i]$ is the i-th value of the adjusted spectrum; the adjusted signal was taken to prevent the offset level from modifying the result of the metrics. The signal $\hat{y}[i]$ is the i-th data of the filtered signal. Finally, N is the length of the signals, in this work for the version of the spectrometer used, it was 3520 data. Since the low-pass filter tends to attenuate the signal at points higher than the cut-off point, in this work set at 0.1. A metric was proposed that indicates the variation of the amplitudes of the original and the filtered signal. This is especially useful in scenarios where the value associated with local maxima must be faithfully identified. The mathematical relationship is expressed in equation (4).

$$DA = \frac{|\Delta y - \Delta \hat{y}|}{\Delta y} \cdot 100\%. \qquad (4)$$

Where $\Delta y = y_{max} - y_{min}$, knowing that is the sample captured by the spectrometer. Similarly, $\Delta \hat{y} = \hat{y}_{max} - \hat{y}_{min}$ represents the maximum amplitude of the filtered signal. This metric helped to quantify the attenuation effect due to filter action.

Finally, a coefficient indicating the difference between the information preserved in the filtered signal by Shannon entropy was used. Equation (5) shows the relationship.

$$DE = \frac{|Hy - H\hat{y}|}{Hy} \cdot 100\%. \qquad (5)$$

Where is the entropy calculated for the original signal y, $H_{\hat{y}}$ is the entropy for the filtered signal $\hat{y}$. The *scipy.stats.entropy* function from the SciPy library was used for this metric [38]. Section 3 presents the results obtained during the execution of the proposed methodology.

3. Results and discussion

The programming and execution of this methodology was performed using the Visual Studio Code editor version 1.88 and using Python 3.9.6. The computer used was a DELL laptop with 8 Gb of RAM and AMD Ryzen 5 2500U processor with Windows 10. The following are the spectra captured from a cell phone LED light, as well as those obtained when processing the virtual data provided by the SeaBreeze library.

3.1. *Hardware*

Ten shots were taken every 500 *ms* (T_s), from an LED light source with an integration time T_I set at 10 *ms*. The number of samples to be considered for averaging N_S was 5. Figure 5 shows all the captured spectra.

3.2. *Acquisition and processing*

The total acquisition time was 4.5 seconds. In Figure 5, in each sample, there was a variation in the distance between the detector and the light source. For this reason, a variation in the amplitude of the captured signals is observed.
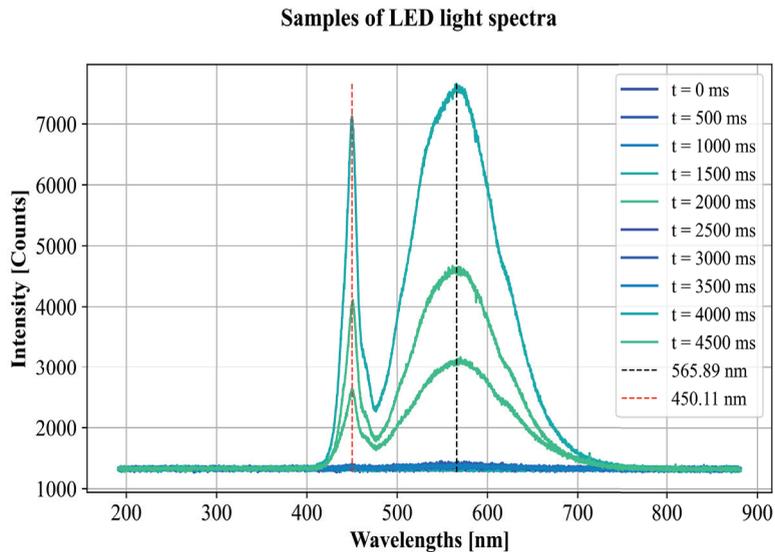
Samples of LED light spectra

Figure 5. LED light spectra of 10 readings taken every 500ms. The wavelengths associated with the two peaks are approximately 450 nm and 565 nm, corresponding to the blue and green color range, respectively.

It is observed that wavelengths corresponding to violet and ultraviolet are not present. Likewise, infrared light is not captured as a component of this light source. The samples that capture the most information are at times $t = [2000, 4000, 4500]$ *ms*. Thus, the rest of the signals are mainly noise; this was caused by the movement of the light source and to corroborate the real-time change of the spectrum. The following is a series of comparisons between some samples of these signals and their respective processing.

Figure 6 shows the different acquired signals and what was obtained after processing, i.e., offset adjustment and a low-pass filter. In the samples, the signals that did not capture the LED light spectrum, Figure 6a, 6c, 6e and 6g possess an average level of approximately 1330 [Counts], while the amplitudes of the samples at t = [2000, 4000, 4500] ms are 3174.76, 7656.53 and 4670.18 [Counts], respectively. This implies that there is a difference in amplitude of up to 5 times between the noise signals and the maximum recorded intensity. Being mainly noise signals, the adjustment and filtering performed do not reveal new relevant information; this can be seen in Figures 6a, 6b, 6d, 6f and 6h.

In the case of Figures 6k, 6m and 6o, which correspond to the moments when the light source had the greatest distance from the detector, the filter accentuated the waveform and allowed us to observe that both peaks are around the same wavelengths of Figure 5. Therefore, using the proposed processing it was possible to identify more accurately the presence of blue tones (Figure 6n and 6p), a situation that is more complex to identify in the unprocessed signals due to the noise present and its amplitude levels. Finally, the offset adjustment and the second-order flat response zero offset filter attenuated the noise while preserving the amplitude and coincidence characteristics with the original wavelengths. The above can be seen in the pairs of Figure 6i, 6j, 6q, 6r and 6s, 6t.

To analyze the filter efficiency, 5 metrics were implemented: the SNR signal to noise ratio, the RMSE value, the R-square coefficient, the DA Amplitude difference and the DE Shannon entropy difference. Section 3.3 presents the value of these metrics for each of the samples.

3.3. *Analysis of adjustment and processing*

To validate that the filter preserves as much useful information as possible, the 5 metrics proposed in section 2.19 were calculated for each filtered signal. Table 13 shows the values according to the time at which they were acquired.

The SNR, RMSE and R-Square values of the signals captured at times t = [2000, 4000, 4500] ms turned out to be the highest of all samples. For DA metrics low values represent little discrepancy in amplitudes, while for DE, high values indicate that the filtered signal information is more representative compared to the original spectrum. Therefore, the application of the filter at the 0.1 cut-off point was effective in preserving the waveform of the signals categorized as Light type and maintaining a difference in the original amplitude of up to 4.9 %. Likewise, these signals had an
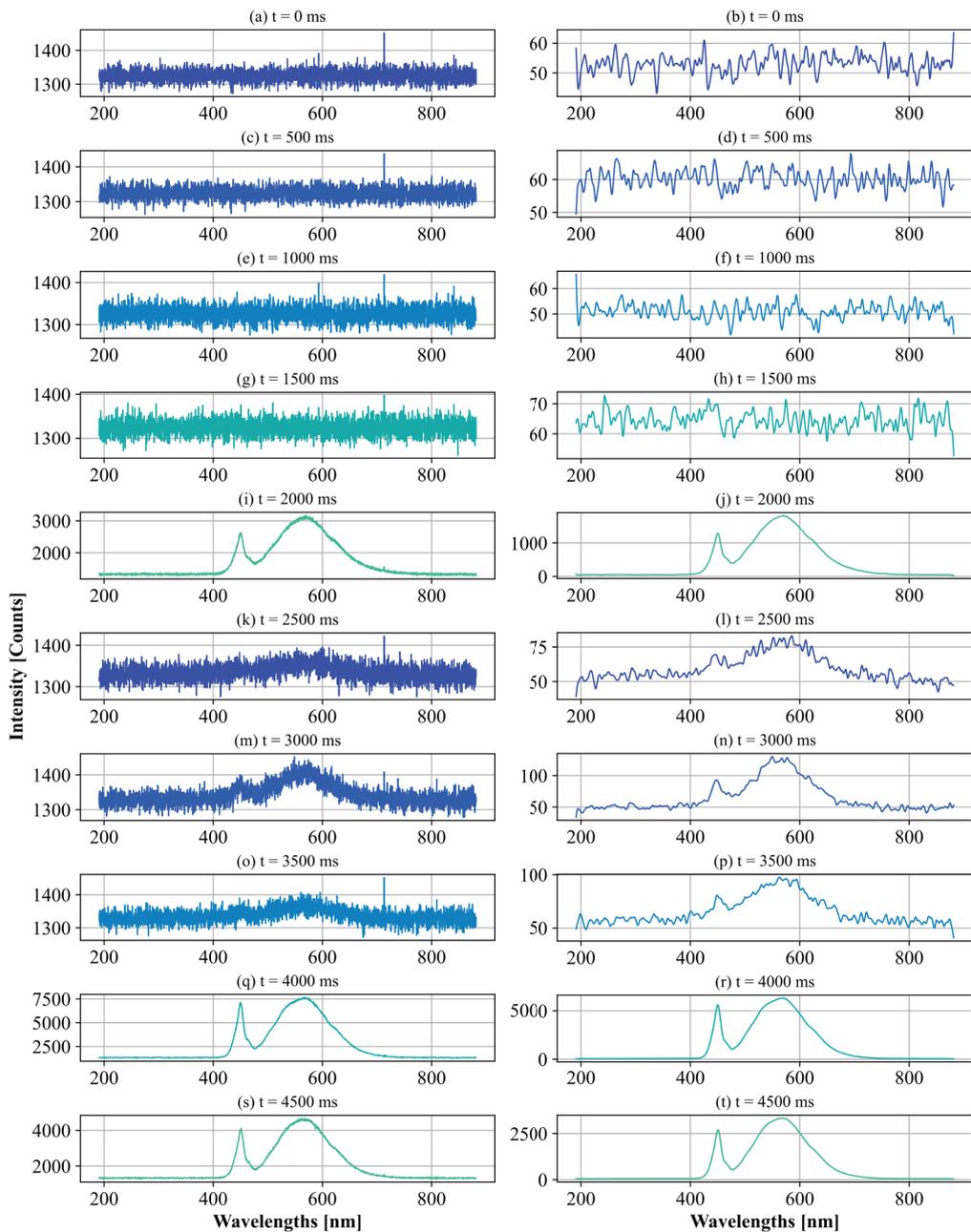
Figure 6. The first column displays the unadjusted spectra. In the second column are the fitted signals filtered by the 2nd order zero offset filter.

SNR of up to 38.54 %, a maximum RMSE value of 27.83 % and a maximum determination coefficient of 0.9998, resulting in a correct performance of the proposed processing block.

For the signals $t = [2500, 3000, 3500]$ *ms* which were captured with a greater distance between the light source and the detector, the result of applying the offset adjustment and filtering, were signals with a coefficient of determination of up to 0.68. That is, the filtered signal managed to maintain 68 % of the information of interest present in the original signal. Likewise, in the spectrum $t = 3000$ *ms* the change in entropy was up to 0.71; this magnitude is low because the filter eliminated the noise components, but due to the low SNR ratio (12.99 *dB*), the resulting signal still maintains information that is not of interest.

Finally, it is possible to observe that, in all the signals without the presence of the light source of interest, the difference in amplitudes is greater than 83.37 %. This is because of attenuating the noise components that are higher than the cut-off point in the Fourier domain. It can also be seen that these signals have the lowest SNR of the group of samples.

Time [*ms*]	SNR	RMSE	R - Squared	DA (%)	DE (%)	Type
0	10.9253	15.7542	0.0547	88.6760	0.0190	Noise
500	11.9471	15.7301	0.0458	89.4279	0.0114	Noise
1000	10.6042	15.7757	0.0467	83.3754	0.0184	Noise
1500	12.4802	15.8233	0.0509	85.3460	0.0113	Noise
2000	**31.6326**	**18.209**	**0.9989**	**4.9052**	**8.1775**	**Light**
2500	11.8748	15.8183	0.2609	70.1125	0.1395	Noise
3000	12.9992	15.8471	0.6887	44.7016	0.7118	Noise
3500	12.7887	15.7033	0.3956	69.0415	0.2112	Noise
4000	**38.5495**	**27.8310**	**0.9998**	**1.8674**	**9.0734**	**Light**
4500	**35.4580**	**20.8991**	**0.9996**	**3.1997**	**9.4096**	**Light**

Table 13. Validation metrics applied to the LED light test spectra ($T_1 = 10$ *ms*).

To visualize the effect of the processing block on all the resulting signals, the comparative bar chart in Figure 7 was made. Each bar was normalized according to the maximum values of each metric in Table 13.

3.4. *Dynamic real-time data capture system analysis*

During the acquisition tests, the double thread functionality was used to attend requests for changes in the system hyperparameters. Likewise, tests were performed with different sampling times T_S to demonstrate the accuracy of the system. 1000 readings were taken for each desired T_S sampling time, and the actual time spent during the $\overline{T_S}$ program run was averaged. The results are shown in Table 14.

All measurements were performed using a constant value of $T_I = 10$ *ms*, an average of $N_S = 5$ and a selection of the full range of wavelengths available in the spectrometer: $wv_L = [191.09, 881.41]$ nanometers.

T_I *(ms)*	$\overline{T_S}$ *(ms)*	Error (%)
5000	5001.0	0.0193
1000	1004.1	0.4134
500	511.0	2.1975
200	230.2	15.0936
100	129.1	29.0974
50	120.9	141.7637

Table 14. System accuracy with respect to sampling time.

According to the recorded data, the system has an accuracy of up to 99.98 % when the sampling time is equal to 5 seconds. As T_S decreased, the actual average reading time stabilized at approximately 120 *ms*. This time is the time used to execute the Processing block, the Display block and the Save action, in addition to the time it takes for the system to fully transmit the spectrum to the computer. According to the tests performed, the greatest number of resources is occupied by the interactive graphic, which is updated every time there is a new reading, averaging 105.02 *ms*.

Thus, it is possible to establish that the designed software allows manipulating parameters during the acquisition stage and without stopping it, allowing the system to be implemented in experiments involving different sampling times. Because the system is dynamic and real-time, it can be used in a wide variety of

Evaluation of spectra processing
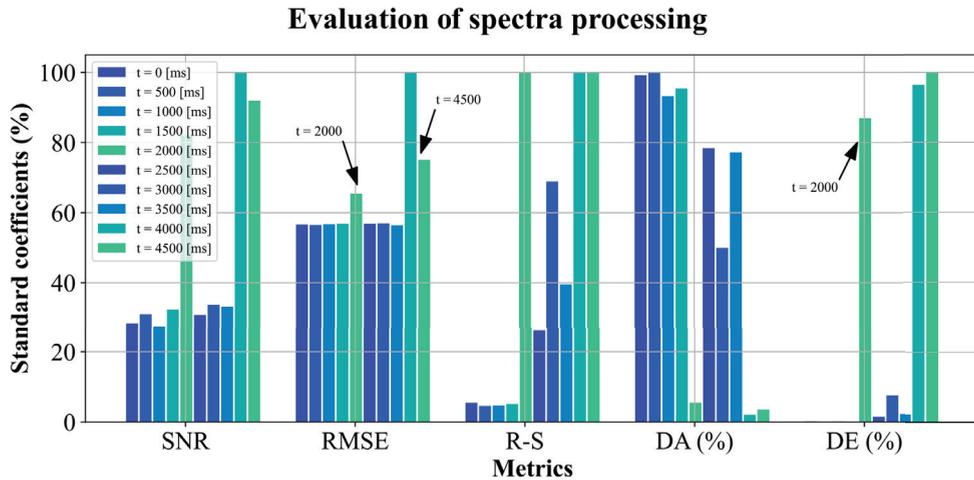
Figure 7. Comparative plot by metric of the 10 LED light test samples. The bars with seaweed green shades are mostly distinguishable from the set of readings. Signals with noise do not show a large variation in bar height (colors with sea-blue shades). Finally, signals at times t = [2500, 3000, 3500] *ms* have bars with values that can be considered intermediate because they still have information about the distribution of LED light intensities.

applications in the field of optical biosensors. Since many biological processes take minutes to hours, it is possible to analyze changes using spectrophotometric techniques [44-47]. For example, in [48] it is indicated that they used 3 hours to analyze changes in the refractive indices of cells sitting on a plasmo-mechanical sensor integrated with microfluidics; during this process, readings were taken every 30 minutes. Likewise, in [49], they state that most detection studies of SARS-COV2 and other viruses take between 10 minutes to 3 hours.

Therefore, the designed system is capable of being potentially useful during the detection process of metabolites or pathogens present in biological tissue, food, and beverages and even in studies of environmental pollutants, since it allows establishing sampling times of the spectra with high precision for values greater than 500 *ms*; considering the use of T_I in 10 *ms*.

The system responded to requests to update the hyperparameters at any instant and was able to display the changes related to the graph (wv_L and T_I), in addition to saving the data in a CSV file in different sheets, according to the T_I and T_S. It is necessary to mention that, so far, the adjustment of these times was totally manual. This implies that the T_I required by the experiment had to be considered to establish an optimal T_S sampling time. It is proposed to use

prediction techniques based on neural networks that find the relationship between both times as a function $T_S = f(T_I)$. This in order that the sampling time does not interfere with the reading process of the experiment and affect its performance. In addition, for new versions of the system, it is possible to contribute to the decrease of the latency time of the processing block by making a third thread dedicated to writing the data in the CSV file and extending the possibility of using sampling times lower than 500 *ms* (considering the integration time, as previously mentioned).

Finally, the system was able to perform the readings in real-time and allowed to save the spectra of interest every nT_S seconds, with $n \in N$. This has practical effects when observing the behavior of the phenomenon and not saving the information until a multiple of T_S time. This helps to reduce the complexity of the subsequent analysis processes required.

This system has the potential to be introduced, for the most part, inside a microcontroller. Opening the possibility of generating a portable system dedicated to the acquisition and cleaning of spectra. Moreover, in the era of Industry 4.0, it is possible to integrate IoT technology, cloud computing and analytics, AI, and machine learning techniques to the proposed system to analyze and process the information and finally contribute to detection in less time and with higher accuracy, depending on the field of application [50].

4. Conclusions

The presented software achieves a sampling time accuracy exceeding 99 %, and its multithreaded processing capability allows for the dynamic management of hyperparameters in response to user requests, resulting in reduced overall latency times. The captured spectra could be displayed on-screen in real-time, with properties of the coordinate axis boundaries automatically adjusted based on the amplitudes of the recorded signal or the selection of wavelengths of interest.

The use of second-order filters with flat response and zero-phase are effective for attenuating noise present in spectral signals, even when the R-Square value is approximately 60 %. Additionally, the system maintained a difference in maximum amplitudes of less than 5 %; however, filter efficiency tends to increase when the SNR of the original signal itself is higher from the beginning.

As an additional feature, it was found that it is possible to store the light spectrum data at a rate different from that stipulated by T_s. Thereby, it is possible to store spectra at each update interval of the T_s plot. In practice, this feature is intended to support the visualization of the dynamics of the studied system while controlling the size of the generated file.

Thus, a Python-based system developed for real-time acquisition and processing of light spectra offers a versatile and efficient solution for a wide variety of applications, with notable potential in sensors. By enabling the real-time detection and analysis of electromagnetic spectra, particularly in optical biosensors, the system contributes significantly to measuring optical properties such as transmittance, reflectance, or absorbance. This capability extends to calculating sensograms during biofunctionalization experiments, enhancing research possibilities.

Finally, the system's adaptability allows for seamless integration into different hardware setups, reducing technological dependencies on other software solutions. This aspect is particularly advantageous as it eliminates the need for costly licenses or additional software packages associated with commercial options like Ocean Optics spectrometers or MATLAB. Leveraging Python's open-source nature and libraries like Python-SeaBreeze, developers can create tailored solutions without constraints imposed by proprietary software, thereby fostering innovation and exploration in spectroscopy research and analysis.

Acknowledgement

References

1. Togawa, T., Tamura, T., & Öberg, P. Å. (2011). *Biomedical sensors and instruments* (2nd ed.). Taylor & Francis Group.
    https://doi.org/10.1201/b10775

2. Khandpur, R. S. (2003). *Handbook of biomedical instrumentation* (2nd ed.). McGraw-Hill.

3. International Union of Pure and Applied Chemistry (IUPAC). (2014). Biosensor. In *IUPAC eBooks.*

4. Gómez, D. R. (2012, February 23). *Biosensores ópticos de alta sensibilidad basados en técnicas de modulación plasmónica.* [Online]. Available:
    http://hdl.handle.net/10347/5134

5. Damborský, J. K., & Š., J. (2016). Optical biosensors. *Essays in Biochemistry*, 60, 91–100.
    https://doi.org/10.1042/EBC20150010

6. Marín Silva, D. A. (2022). *Funcionalización de matrices a base de polímeros biodegradables mediante incorporación de nanopartículas.* Universidad Nacional de La Plata.

7. Tektronix. (2023). *Analysis, Fundamentals of Real-Time Spectrum.* [Online]. Available:
    https://www.tek.com/en/documents/primer/fundamentals-real-time-spectrum-analysis

8. Optics, O. (n.d.). *USB Programmer: Installation and Operation Instructions.* Florida.

9. Simulink, M. &. (n.d.). *Ocean Optics Spectrometer support from Instrument Control toolbox.* [Online]. Available: https://la.mathworks.com/hardware-support/ocean-optics-spectrometers.html

10. Lutz, M. (2010). *Programming Python: Powerful object-oriented programming* (4th ed.). O'Reilly Media, Inc.

11. Python Documentation. (2024, April 6). *Python frequently asked questions.* [Online]. Available:
    https://docs.python.org/es/3/faq/general.html

12. Datta, S. (2022, July 14). *FreeCodeCamp.org.* [Online]. Available:
    https://www.freecodecamp.org/news/run-python-script-how-to-execute-python-shell-commands-in-terminal/

13. Poehlmann, A. (2019). *Python-Seabreeze documentation.* [Online]. Available:
    https://python-seabreeze.readthedocs.io/en/latest/

14. Nagar, S. (2017). *Introduction to Python for engineers and scientists: Open source solutions for numerical computation.* Apress.
    https://doi.org/10.1007/978-1-4842-3204-0_2

15. Halvorsen, H. P. (2020). *Python for science and engineering.*

16. Burn, I. (2022, November 8). *CCM.* [Online]. Available:
    https://es.ccm.net/ordenadores/linux/3810-que-es-un-shell-y-para-que-se-utiliza/

17. Wheeler, S., & Buck, A. (2023, June 28). *Microsoft Learn*. [Online]. Available: https://learn.microsoft.com/en-us/powershell/scripting/overview?view=powershell-7.4

18. Brownlee, J. (2023, November 22). *Python Multiprocessing: The complete guide*. Super Fast Python. [Online]. Available: https://superfastpython.com/multiprocessing-in-python/

19. Patrizio, A. (2022, September 23). *Single-core vs. multi-core CPUs*. [Online]. Available: https://www.networkworld.com/article/971425/single-core-vs-multi-core-cpus.html

20. Ramanathan, R. M. (2015). *Intel multi-core processors.*

21. Silberschatz, A., Galvin, P. B., & Gagne, G. (2018). *Operating system concepts* (10th ed.). WILEY.

22. Bala, P. C. (2022, December 8). *Python Threading: An Introduction*. [Online]. Available: https://geekflare.com/python-threading/

23. Python Software Foundation. (2024, April 6). *Threading - thread-based parallelism*. [Online]. Available: https://docs.python.org/3/library/threading.html

24. Coursera Staff. (2023, November 29). *What are scripting languages? (And why should I learn one?)* Coursera. [Online]. Available: https://www.coursera.org/articles/scripting-language

25. Wheeler, S. (2024, April 3). *About execution Policies - PowerShell*. Microsoft Learn. [Online]. Available: https://learn.microsoft.com/en-us/powershell/module/microsoft.powershell.core/about/about_execution_policies?view=powershell-7.4

26. Wheeler, S. (n.d.). *Set-ExecutionPolicy (Microsoft.PowerShell.Security) - PowerShell*. Microsoft Learn. [Online]. Available: https://learn.microsoft.com/en-us/powershell/module/microsoft.powershell.security/set-executionpolicy?view=powershell-7.4. [Accessed April 1, 2024]

27. Microsoft. (n.d.). *Download .NET Framework | Free official downloads*. [Online]. Available: https://dotnet.microsoft.com/en-us/download/dotnet-framework

28. Microsoft. (n.d.). *Download .NET Framework 4.8 | Free official downloads*. [Online]. Available: https://dotnet.microsoft.com/en-us/download/dotnet-framework/net48

29. Saleh, M. (2024, February 24). *Latest supported Visual C++ Redistributable downloads*. Microsoft Learn. [Online]. Available: https://learn.microsoft.com/en-us/cpp/windows/latest-supported-vc-redist?view=msvc-170

30. CodeOp. (2023, March 24). *7 key backend programming languages explained*. [Online]. Available: https://codeop.tech/7-key-backend-programming-languages-explained/

31. Chocolatey Software. (n.d.). *Chocolatey - the package manager for Windows*. [Online]. Available: https://chocolatey.org/

32. Gerend, J. (2023, February 3). *CD*. Microsoft. [Online]. Available: https://learn.microsoft.com/en-us/windows-server/administration/windows-commands/cd

33. GeeksforGeeks. (2021, June 29). *Difference between Terminal, Console, Shell, and Command Line*. [Online]. Available: https://www.geeksforgeeks.org/difference-between-terminal-console-shell-and-command-line/

34. Ocean Insight. (n.d.). *Glossary on Spectroscopy and Technical terms | Ocean Insight*. [Online]. Available: https://www.oceaninsight.com/knowledge-hub/glossary/

35. Proaki, J. G., & Manolakis, D. G. (2007). *Digital signal processing: Principles, algorithms and applications*. Pearson Education.

36. The MathWorks, Inc. (n.d.). *Zero-phase digital filtering - MATLAB filtfilt- MathWorks*. [Online]. Available: https://la.mathworks.com/help/signal/ref/filtfilt.html?lang=en

37. NumPy Team. (2023, September 16). *NumPy*. [Online]. Available: https://numpy.org/

38. The SciPy Community. (2024, April 3). *SciPy documentation*. [Online]. Available: https://docs.scipy.org/doc/scipy/index.html

39. Semmlow, J. (2005). *Circuits, systems, and signals for bioengineers: A MATLAB-based introduction*. Academic Press.

40. Hagan, M. T., Demuth, H. B., Beale, M. H., & Jesús, O. D. (2014). *Neural network design*. Martin Hagan.

41. Date, S. (2022, March 21). *The complete guide to R-squared, adjusted R-squared and pseudo-R-squared*. Medium. [Online]. Available: https://towardsdatascience.com/the-complete-guide-to-r-squared-adjusted-r-squared-and-pseudo-r-squared-4136650fc06c

42. Zheng, Q.-W., Lingping, K., Jeng-Shyang, P., & Wei-Min, W. (2024). A novel discrete artificial bee colony algorithm combined with adaptive filtering to extract fetal electrocardiogram signals. *Expert Systems with Applications*, 247, 123173. https://doi.org/10.1016/j.eswa.2024.123173

43. Li, C., Deng, H., Yin, S., Wang, C., & Zhu, Y. (2023). sEMG signal filtering study using synchrosqueezing wavelet transform with differential evolution optimized threshold. *Results in Engineering*, 18, 101150.
https://doi.org/10.1016/j.rineng.2023.101150

44. Sehrish, B., Aqsa, T., Ijaz, K., Maham, L., Silvana, A., Hongxia, Z., & Akhtar, H. (2024). A review of nanophotonic structures in optofluidic biosensors for food safety and analysis. *Trends in Food Science & Technology*, 147, 104428.
https://doi.org/10.1016/j.tifs.2024.104428

45. Alemayehu, G. K., Abebe, B. G., Alemu, K. H., Tamirat, A. D., Mulubirhan, D., & Habtamu, D. M. (2023). Optoplasmonic biosensor for lung cancer telediagnosis: Design and simulation analysis. *Sensors International*, 4, 100232.
https://doi.org/10.1016/j.sintl.2023.100232

46. Domínguez García, V., & Ramírez Durán, N. (2017). *Temas selectos de biomedicina en Ciencias de la Salud*. Ediciones Eón/Universidad Autónoma del Estado de México.

47. Katey, B., Voiculescu, I., Penkova, A. N., & Untaroiu, A. (2023). A review of biosensors and their applications. *ASME Open Journal of Engineering*, 2, 020201.
https://doi.org/10.1115/1.4063500

48. Solís Tinoco, V. I., Lechuga, L. M., Sepúlveda, B., & Jiménez Jiménez, D. (2016). Development of integrated plasmomechanical sensors in microfluidic devices for live cell analysis. [Art]. Universitat Autònoma de Barcelona.

49. Bakr, A. T., Qussay, A.-J., Surjeet, C., Yousif, A. M., Sarvesh, R., Vishal, C., & Arsad, N. (2024). State-of-the-art telemodule-enabled intelligent optical nano-biosensors for proficient SARS-CoV-2 monitoring. *Microchemical Journal*, 197, 109774.
https://doi.org/10.1016/j.microc.2023.109774

50. IBM. (2024, April 8). *What is Industry 4.0 and how does it work?* [Online]. Available:
https://www.ibm.com/topics/industry-4-0

51. Ocean Insight. (2015). *FLAME Scientific-Grade Spectrometer: Installation and Operation Manual*.

BIO-JET FUEL PRODUCTION FROM THE ENHANCED CROPS OF *BOTRYOCOCCUS BRAUNII* BY MgO NANOPARTICLES (MgO NPs)

Blanca Estela Chávez-Sandoval[1], Susana Amador-Jiménez[2], José Abraham Balderas-López[3*]

[1]Escuela Nacional de Ciencias Biológicas, Depto. De Zoología, Instituto Politécnico Nacional. Manuel Carpio, Plutarco Elías Calles, Miguel Hidalgo, 11350 Ciudad de México, México.

[2]Universidad Autónoma Metropolitana, Unidad Azcapotzalco, Depto. de Energía. Av. San Pablo Xalpa No. 180, Col. San Martín Xochinahuac, CP. 02200, Ciudad de México, México.

[3]Unidad Profesional Interdisciplinaria de Biotecnología, Depto. De Ciencias Básicas, Instituto Politécnico Nacional. Av. Acueducto, La Laguna Ticomán, Gustavo A. Madero, 07340 Ciudad de México, México.

*abrahambalderas@hotmail.com

Abstract

One of the most pressing challenges facing humanity at this time, and that will surely define our future in a few years, is that of energy. The finite nature of fossil fuels and concerns regarding environmental impact, especially on greenhouse gas (GHG) emissions, have established the need to search for new energy sources.

Biofuels from biomass will cover a large part of the energy demand required for transport. The economic and environmental impacts of the production of biofuels have recently been studied, highlighting the importance of knowledge biodiesel and bio-jet fuel (bio-kerosene) production because they are technologies capable of replacing the consumption of fuels derived from petroleum, mainly those destined for the transport sector. Bio-jet fuel can be used in aircraft engines without modification.

In this work, bio-jet fuel was obtained from the lipids of the microalgae *Botryococcus braunii*, cultivated in pre-treated wastewater and adding MgO NPs to improve lipid and / or biomass production in the crop. Carrying out this type of research the challenges, and opportunities what this technology represents for its implementation in developing countries is of great environmental relevance, since the combustion of energy is responsible for just over 61% of CO_2 emissions and 46% of GHG, according to whit global stock take.

Keywords: Microalgae, crop improvement, domestic wastewater, metallic nanoparticles, non-fossil fuels.

1.   Introduction

After a decade of record passenger traffic growth and unprecedented profitability, the global airline industry is facing an unprecedented, sharp, and sustained drop in demand from the coronavirus pandemic. Since the global lockdown began, the number of daily flights has fallen by between 90 and 95% in some regions and almost all passenger traffic has been suspended worldwide [1].

Under these circumstances, the optimal development of the transportation industry in general, and particularity aeronautics, in addition, should reduce its greenhouse gas emissions (GHG) and its high dependence on fossil fuels; It should be noted that in 2009, the aviation industry put in place an ambitious and robust carbon emissions, the goal aims to achieve carbon neutral growth starting in 2020 and achieve the goal of reducing net carbon emissions by 50% by 2050 [2].

One of the most promising strategies is to develop and industrialize alternative aviation fuels produced from renewable resources, like biomass [2, 3].

Biomass is the organic material that has been most used as fuel throughout the entire history of humanity. It is produced by plants by fixing light, water, and carbon dioxide through the photosynthesis process: Solar energy is stored in chemical bonds, and can be released through processes such as combustion, digestion, decomposition or through its hydrolysis and fermentation to liquid or gaseous fuels. Using biomass as an energy source is one of the most promising ways to reduce energy dependence on non-renewable fossil resources, while reducing the carbon footprint [4,5].

Biofuels are those produced from biomass, and which are considered as a renewable energy source; can be presented in solid (vegetable waste, biodegradable fraction of urban or industrial waste), liquid (bio-alcohols, biodiesel, bio-jet fuel) and / or gaseous (biogas, hydrogen) forms [4].

Biofuels can be classified according to the biomass used for their production in first, second and third generation. In the first-generation food crops were used that endangered food security, in the second-generation non-food crops were used, but they still occupied farmland and in the third-generation microorganisms such as algae, bacteria or yeasts produced at big scale. (Figure 1).

Currently on a commercial level, mass cultivation of microalgae is of greater importance to produce high purity chemical compounds, such as: biofuels, biofertilizers, ion exchangers and carotenes; likewise, for the treatment of
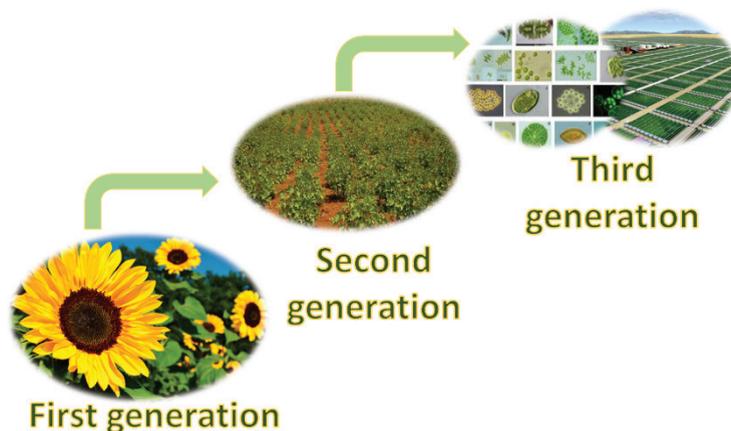
Figure 1. Evolution of the biomass used in the production of biofuels.

wastewater, obtaining therapeutic compounds and as food for human and animal consumption [6].

Despite the existence of technologies to capture solar, hydro and wind energy, the use of liquid and gaseous biofuels from biomass will cover a large part of the energy demand required for transport (Balat 2011). Also, the production of these biofuels offers environmental advantages such as the reduction of emissions (GHG) by up to 70-90% [7].

As far as nanoparticles, strictly speaking, nanoparticles are those particles between 1 to 100 nm, where the physical properties of solid materials change dramatically, they have very different physical and chemical properties from the same materials on a conventional scale. Its properties depend on its shape, size, surface characteristics and internal structure. Another fundamental aspect of nanoparticle synthesis is its stabilization, so that its size and shape can be maintained over time [8 - 11].

Concerning microalgae and biofuels [12], carried out a study on the behavior of *Chlorella pyrenoidosa* and on how to accelerate its metabolism by adding CaO and MgO| to stimulate lipid production, because for plant growth and development, MgO is essential [13]. Nanomaterials are added since the microalgae are cultivated to stress it and have a higher percentage of lipid production than just using sugars from CO_2.

Therefore, in this work, bio-jet fuel was obtained from the lipids of the microalgae *Botryococcus braunii*, cultivated in pre-treated wastewater and adding MgO nanoparticles to improve lipid and / or biomass production in the crop.

2. Methodology

2.1. *Materials and reactives*

All the reagents used were analytical grade; also, all analyzes were carried out in triplicate.

2.2. *Botryococcus braunii*

The choice of species is the first step in the development of a production process. Among the main desirable characteristics for large-scale crops are rapid growth, elevated content of high added value products, development in extreme environments, large cells in colonies or filaments, great tolerance to environmental conditions, tolerance to high levels of CO_2 (15 % or more), to contaminants and to the physical effect of agitation or turbulence [14].

In this work the algae species *Botryococcus braunii* was used, due to its high lipid content (Table 1). These types of algae are useful to produce biofuels, chemicals, or chemical precursors. For commercial production of these compounds, adapted algal strains and optimized growing conditions are mandatory [15].

Species	Lipid content (% dry biomass weight)
Botryococcus braunii	25-75
Chlorella sp.	28-32
Crypthecodinium cohnii	20
Cylindrotheca sp.	16-37
Dunaliella primolecta	23
Isochrysis sp.	25-33
Monallanthus salina	20

Table 1. Lipid content of some species of microalgae.
Modified from [15].

This species is notable for its ability to produce large amounts of hydrocarbons, especially oils in the form of triterpenes, hydrocarbons known as *botryococcenes,*

which come to represent around 30-40% of its dry weight, that can be used as renewable feedstocks for producing combustion engine fuels [16].

The strain to this work was purchased from the University of Texas in the USA with the code UTEX B 2441 (Figure 2).
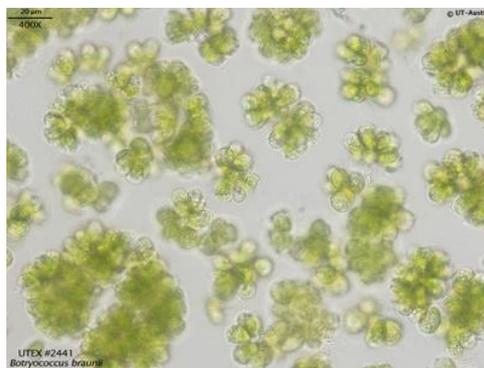
Figure 2. *Botryococcus braunii* UTEX 2441.
(Image obtained from the UTEX culture collection).

The cultivation conditions throughout five months, were:

♦ Light intensity 33 µE / m2s1
♦ Stirring 125 rpm
♦ Photoperiods 16/8
♦ pH 6.7 - 7.2
♦ Temperature 25 ± 1 ° C

The optical density (OD) was monitored weekly using the Perkin Elmer Lambda 35 UV-Vis spectrophotometer, at a maximum wavelength of 683.6 nm, to determine the growth kinetics of this microalgae. In this study we determined that optical density, since other authors like kawamura *et al* 2021, reported an optical density of 660 nm for *B. braunii* [17].

Botryococcus braunii UTEX 2441 was cultivated in domestic wastewater, obtained from the pilot plant for wastewater treatment of the UAM-Azcapotzalco and this water was characterized using physicochemical methods and sterilized in a vertical laboratory autoclave of soil model ATV 850; considering that comes from human feces and urine, from personal and kitchen care and house cleaning, they usually contain a large amount of organic matter and microorganisms, as well as traces of soaps, detergents, bleach and fats, among others [5].

2.3. *MgO Nanoparticles (MgO NPs)*

MgO NPs synthesis was performed by the method described by Chavez-Sandoval et al 2021 b [11], with some modifications briefly: A stock solution of 250 mM magnesium oxide was prepared in deionized water; 6.5 mL of this solution was taken to reach a volume of 650 mL with a concentration of 2.5 mM. A reflux system was installed using an Erlenmeyer flask on a heating grill and constant stirring until boiling was reached. 16.25 mL of 1% sodium citrate (Na3C6H5O7·2H2O), was added as a reducing and stabilizing agent. It was kept boiling and stirring for 15 minutes. Afterward, it was transferred to a grill with only stirring to cool for at least 15 minutes. Finally, it was stored at 4°C until use.

The MgO NPs were characterized by UV-Vis Spectrometry techniques, using a Perkin Elmer UV 35 spectrophotometer, by scanning from 200 to 235 nm.

MgO NPs were added to the 1000 mL photobioreactors in concentrations of 5 %V, 10 %V and 20 %V. A photobioreactor was used as a blank, no MgO NPs were added (Table 2).

Photobioreactor	Concentration of MgO NPs %V
1	0 (Blank)
2	5
3	10
4	20

Table 2. Addition of OMg NPs in the photobioreactors

2.4. *Microalgae harvest*

Centrifugation, sedimentation, filtration, and flocculation, either individually or in combination, are the most practical harvesting procedures, whose application depends on the properties of the cultivated microalgae species (morphologies, presence of gaseous vacuoles, etc.), since some have characteristics that facilitate its collection [18]. Oils are extracted from the harvested biomass, using organic solvents, mainly hexane.

Biomass was obtained by centrifugation in this work, an Eppendorf brand Centrifuge 5810R centrifuge was used, at 4000 rpm for 4 minutes and at a temperature of 4 °C. The technique used to obtain the biomass can also be first by filtration and then by centrifugation, depending on the volume of the sample.

2.5. *Microalgae drying*

The biomass obtained was placed in Petri dishes previously sterilized and weighed for drying. Drying was carried out using a Binder brand redLine culture oven at 29 °C for 12 hours.

2.6. *Transesterification*

The transesterification reaction is the most usual form of biodiesel production. This reaction consists of the reaction of a lipid with an alcohol, preferably of low molecular weight, to produce an ester and a by-product, glycerol. The global process is developed through three reversible and consecutive reactions in which the intermediate products formed are diglycerides and monoglycerides (Figure 3).
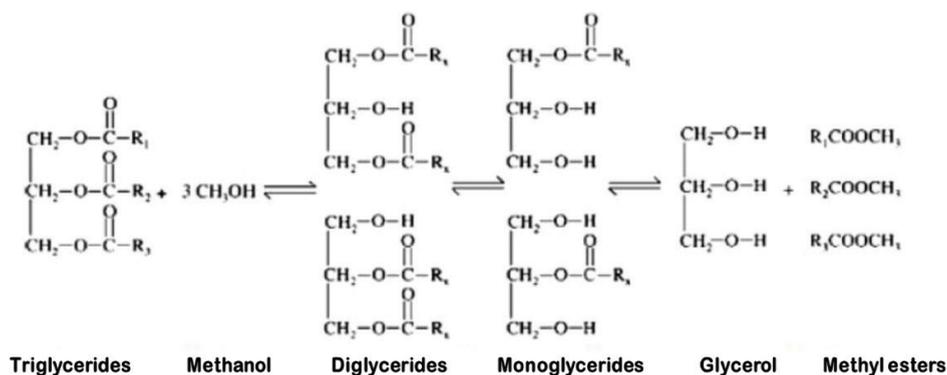
Figure 3. General transesterification reaction. Modified from [19].

Stoichiometrically 3 moles of alcohol are required for each mole of triglyceride, but in practice an excess of alcohol should be used to increase the formation of esters and facilitate the separation of glycerin. Higher reaction temperatures speed up the reaction and shorten the reaction time [20,22].

The use of ethanol is preferable in the transesterification reaction, because it can be generated from agricultural products, it is renewable and environmentally friendly, however, methanol is the alcohol most used for its physical, chemical and low-cost advantages [20].

The dry biomass was removed from the Petri dish using a spatula and placed in thin cloth bags, to carry out the extraction of lipids using the Soxhlet equipment and hexane as a solvent, in accordance with the requirements of the Mexican

standard [21] as an analysis method for the determination of recoverable fats and oils in natural, waste and treated wastewater. It should be noted that the treated water is analyzed at the UAM-Azcapotzalco wastewater treatment plant and in our case the donated water was only sterilized in an autoclave to later use it as a culture medium.

In this work, the method of chemical transesterification with methanol was used employing sodium hydroxide as catalyst [22]. Sodium hydroxide was placed in a grill and a magnetic stirrer was placed, then methanol was added.

Once the oil and sodium methoxide have the same temperature (60 °C), at which the reaction was carried out, the methoxide was added to the oil obtained from *Botryococcus braunii* and allowed to react for 10 minutes.

2.7. *Determination of amount of catalyst (sodium hydroxide)*

A basic catalyst (NaOH Sigma-Aldrich) was chosen as they have been reported to be more effective than acid catalysts and enzymes; the recommended amount of catalyst is between 0.1 and 1% w / w of oils and fats [22]. Thus, the amount of NaOH was determined as follows:

Amount of NaOH = Weight of oil (g) * (0.1-1% w / w of oil and fats).

2.8. *Determination of amount of methanol*

As mentioned before stoichiometrically 3 moles of alcohol are required for each mole of triglyceride, however using an excess of alcohol allows to increase the formation of esters and facilitate the separation of glycerin, so in this stage the ratio of methanol 6: 1 was used [22,23].

Once the biodiesel was obtained, it was placed in a settling funnel for 24 h to separate from the glycerin that was obtained as a by-product of the reaction [22,23].

The biodiesel obtained was characterized by means of Infrared PerkinElmer FT-IR Spectrometer Frontier equipment, which allowed to verify that it contains the functional groups of biodiesels. The characteristic signs of biodiesel are two groups of bands of own absorption of the methyl esters that make it up, in the region of the fingerprints the band appears between (1200-1300) cm-1 originated by the asymmetric axial deformation C-O and in the region of the functional

groups between 1750 cm-1 and 1730 cm-1 is the intense peak corresponding to the group carbonyl (C = O) typical of esters; which is related to the vibration of relatively constant and interference-free stretching, this signal being the greater difference with the spectrum of diesel; for both spectra the absorption band between 2950 and 3000 cm-1, corresponding to the stretching of the CH3, CH2 and CH bonds of aliphatic carbons [5,22].

Gas chromatographic analysis of biodiesel was performed on a PerkinElmer Clarus 580 gas chromatograph, by a temperature ramp of 10°C/min, from 160°C to 230°C for 8 min, with an injector temperature of 225°C, 1mL / min Helium flow and an Elite-Wax column of 30 m long and a maximum temperature of 240°C [5].

2.9. *The Bio-Jet fuel obtention*

The biodiesel obtained from renewable sources can be used in aviation engines either as the only component or in mixtures with conventional kerosene; the main aim is to obtain biofuels from products that do not compete with the fertile land necessary for food production; however, to achieve truly sustainable production, methodologies must be urgently implemented of third generation biofuels such as microalgae.

In this work, the biodiesel obtained from the algae was distilled using a vacuum pump and micro-distillation equipment. The boiling range was 60-70°C. Once the distillation was carried out, a light fraction and another heavy fraction were obtained. The light fraction is bio-jet fuel.

The Biodiesel yield was obtained according to Cao *et al.,* 2013 [12].

The bio-jet fuel sample was characterized using the Perkin Elmer Frontier brand FT-IR Frontier Spectrometer as follows, 20 μL of sample was used, and a scan was made in the wavelength range of 400 cm-1 to 4000 cm-1.

3. Results and discussion

3.1. *Physicochemical parameters in photobioreactors*

The temperature oscillated from 20-25 ° C; The pH presented stable dynamics at the beginning of the process, rising from 8 to 10 in the first ninety days of growth, however after 60 days of growth the pH varied in each one in ranges

from 7 to 11, possibly due to the solubility, ionization state and bioavailability of nutrients in the medium, during the growth time of *B. braunii* [15].

3.2.   Botryococcus braunii *biomass*

The growth of the biomass in the photobioreactor of 5%V MgO NPs reached a maximum concentration of 60 mg/ml, during the first 80 days of growth, as well as the growth kinetics of the control treatment and the treatment with 20 % MgO NPs presented similar kinetics during the first eighty days, growing dramatically towards the last forty-five final days, reaching a concentration of 130 mg/ml for the control treatment, at 125 days and for the treatment of 20% MgO NPs concentrations were obtained up to 80 mg/ml, for the treatment of 10% *B. braunii* a similar growth was obtained in the last stage reaching concentrations of 67 mg/ml at 119 days, the photobioreactor with 10% MgO NPs was the one with the lowest concentration of biomass and the photobioreactor without MgO NPs was the one with the highest (Figure 4).
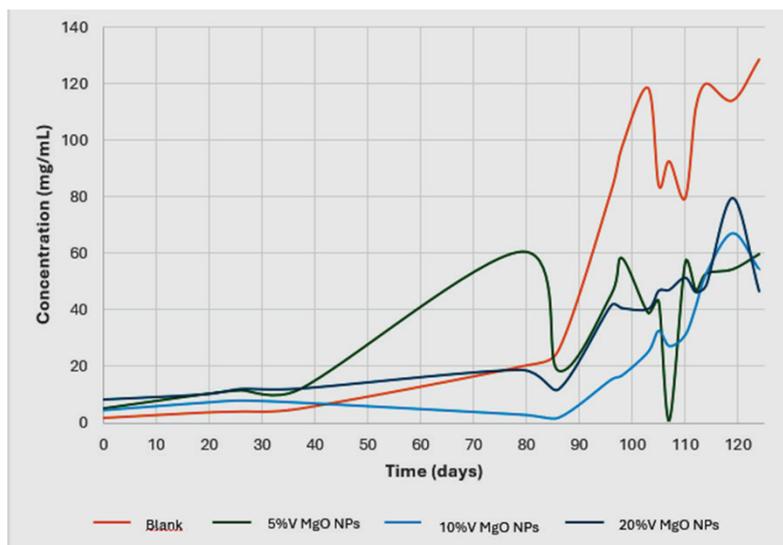
Figure 4. Growth kinetics in the different treatments with NPs of MgO.

The highest concentration of lipids was obtained in the 10% treatment with MgONPs, reaching a total of 3.1 g, and for the photobioreactors without NPs a maximum concentration of 2.77 g lipids was present (Fig. 5).
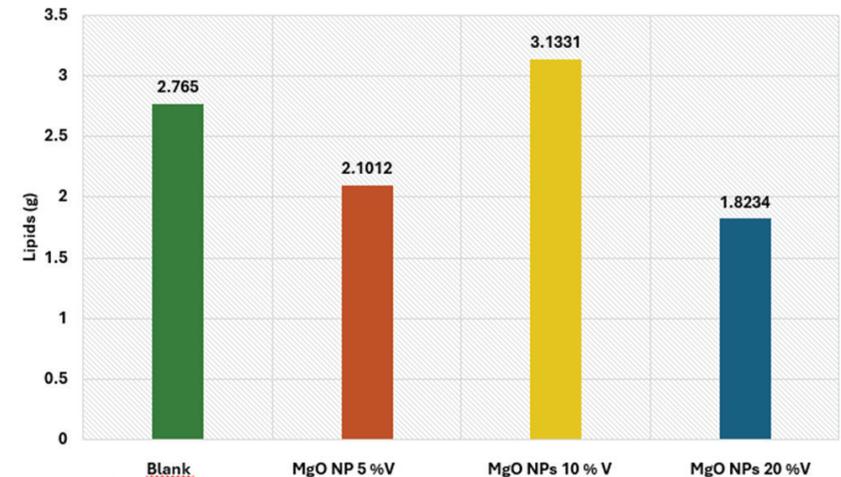
Figure 5. Lipids obtained from the culture of *B. braunii* at
different concentrations of MgO nanoparticles.

3.3. *Analysis of variance of growth kinetics*

The analysis of variance showed significant differences between the growth
concentration of *B. braunii* of the control treatment with respect to the other
treatments with MgO NPs (p = 0.000002), with respect to the concentrations
between 5 %V MgO NPs, and 20 %V MgO NPs presented significant differences,
observing the 5 %V with higher concentrations with respect to those of 10 %V
and 20 %V (Figure 6).
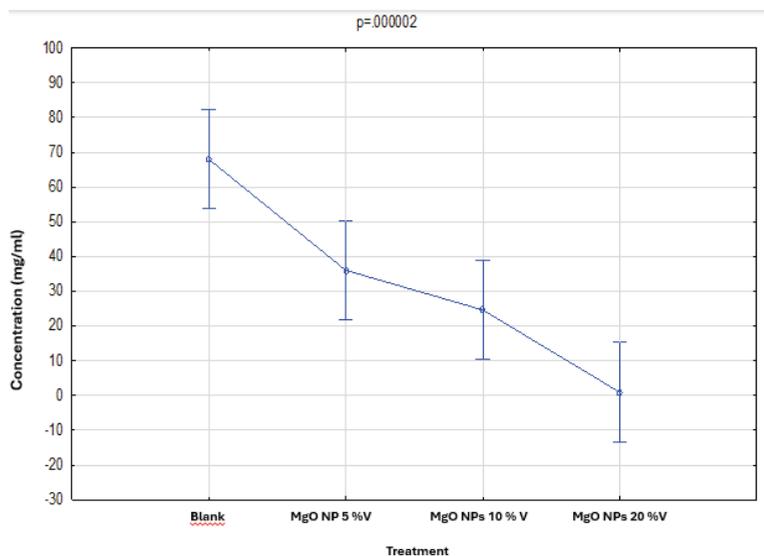
Figure 6. Analysis
of variance
of the growth
kinetics between
the different
concentrations of
NP´s MgO.

These results indicate that, even though more biomass is obtained, more lipids that can be used in transesterification are not necessarily obtained. On the other hand, the percentage of MgO NPs is of great relevance, since as we have seen there is a concentration where more biomass is obtained (blank and 5 %V), but there is a concentration where more lipids are obtained (10 %V), and this is evident since the differences between treatments are statistically significant [5,22].

Furthermore, MgO NPs are influencing both the growth and lipid production of *B. braunii* even perhaps in an easier obtaining of lipids for transesterification by the granzyme-perforin-dependent mechanism, in accordance what is reported by Al-Omar *et al.*, 2021[24] for 9-13 nm flake-type graphene oxide nanoparticles.

3.4. *MgO Nanoparticles (MgO NPs) characterization*

The synthesized MgO nanoparticles were characterized by UV-Vis spectroscopy, the maximum wavelength was 209.49 nm (Figure 7).
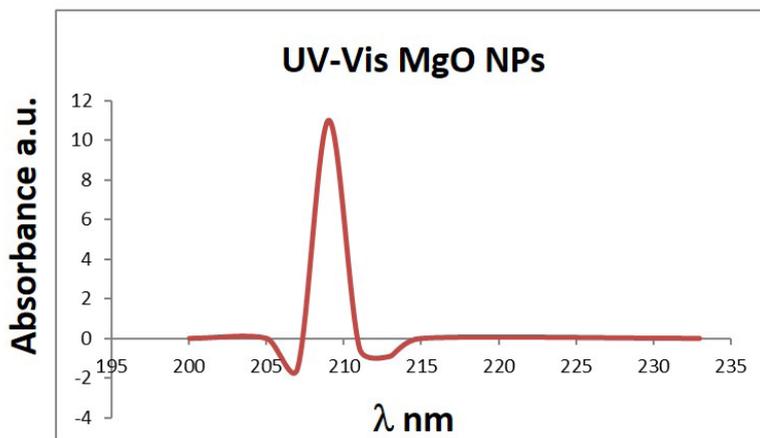
Figure 7. Uv-Vis spectroscopy of MgO Nanoparticles.

This result indicates that sodium citrate acts as a reducing and stabilizing agent [9].

The characterization by TEM shows that we obtained "flake-like" particles of approximately 10 nm in diameter (Figure 8 A-C).

Al-Omar *et al.*, 2021[24] report graphene oxide flake nanoparticles of 9-13 nm, that increased the activation of phagocytic cells by augmenting the cell mortality through the granzyme-perforin-dependent mechanism. This is a promising strategy for controlling cancer cells. Perforins are proteins that integrate into the cell membrane and induce the formation of pores that cause osmotic lysis of the
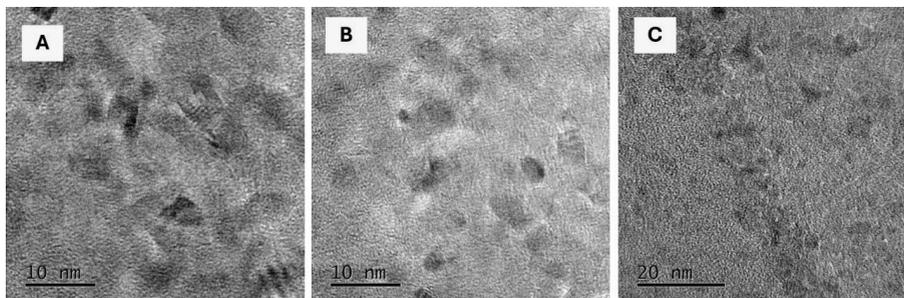
Figure 8. Shows the "flake-like" shape of approximately 10 nm magnesium oxide nanoparticles A-B. In panel C a view with the 20 nm measurement.

target cell. Meanwhile, granzymes enter the cell through endocytosis and induce apoptosis. In our case, these mechanisms could facilitate the exit of lipids from the algae for the subsequent transesterification process.

3.5. *Biodiesel*

The biodiesel obtained by transesterification was characterized using infrared spectrometry equipment (Figure 9). The characteristic signals of biodiesel are two groups of absorption bands of the methyl esters that make it up. In the fingerprint region, the band appears between (1200-1300) cm-1, caused by the asymmetric C-O axial deformation, and in the region of the functional groups between 1750 cm-1 and 1730 cm-1 there is the intense peak corresponding to the carbonyl group (C=O) typical of esters; which is related to the relatively constant and interference-free stretching vibration, this signal being the biggest difference with the diesel spectrum; For both spectra, the absorption band between (2950
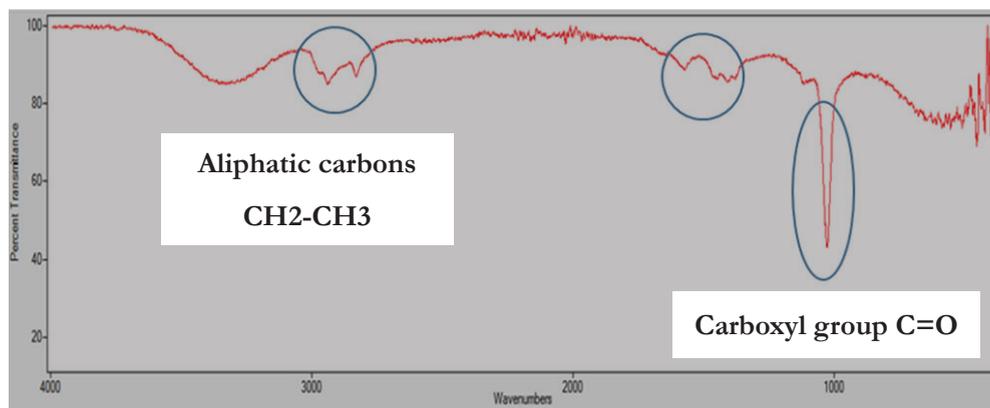
Figure 9. IR spectrum of the biodiesel obtained.

and 3000) cm-1 is common, corresponding to the stretching of the CH3, CH2 and CH bonds of aliphatic carbons, like Chávez-Sandoval *et al.,* 2021 a [5].

As we know, biodiesel absorbs in the region of 2,750 cm-1 -3,000 cm-1 corresponding to the vibration modes of -CH2 and -CH3. As the triglycerides present in the oil are converted to methyl esters when the reagent is methanol, the -CH3 groups increase in biodiesel composed mainly of fatty acid alkyl esters and therefore the intensity of the peak by ~ 2924 cm-1 also increases [5,25].

3.5.1. *Biodiesel yield*

The biodiesel yield from microalgae biomass was calculated with the following formula:

$$\text{Biodiesel yield (\%)} = \frac{\textit{Biodiesel mass g}}{\textit{algae mass (g)* oil content (\%)}} \ *100$$

In this work we obtained a biodiesel yield were 86%. Has been reported that these values over 100% are obtained when processing the well-dried biomass, since when the humidity increases the yield drops considerably, and because perhaps other molecules such as phospholipids, or accumulation of lipids on the cell surface, are also transformed into biodiesel [5, 12, 26].

3.6. *Bio-jet fuel*

Figure 10 shows the result of the characterization of bio-jet fuel obtained, using IR. With respect to the IR of biodiesel, a change is noted in the intensity of the 1200 cm-1 band and in the bands from 2950 to 3000 cm-1, which indicates the consumption of the hydroxyl group and the formation of hydrocarbons, at 1730 cm -1 only two bands are observed and there was an increase in the intensity of the 1750 cm-1 band, indicating the conversion of biodiesel into bio-jet fuel.

Bio-jet fuel obtained from the microalgae *B. braunii* is a good option to mitigate the problems surrounding fossil fuels and with this help contribute to the production of new fuels derived from third generation biomass [27]. Likewise, this work shows a path to innovate techniques that allow greater efficiency in the biokerosene production process, furthermore, if a direct transesterification were carried out, costs would also be reduced in the production of these biofuels, as reported by Chavez-Sandoval *et al.*, 2021a and Wang *et al.,* 2022 [5,28]. Insomuch as the American Society for Testing and Materials (ASTM) has certified several biofuel production technologies including kerosene, since hydroprocessed esters and fatty acids can now be commercialized [5, 26, 28].
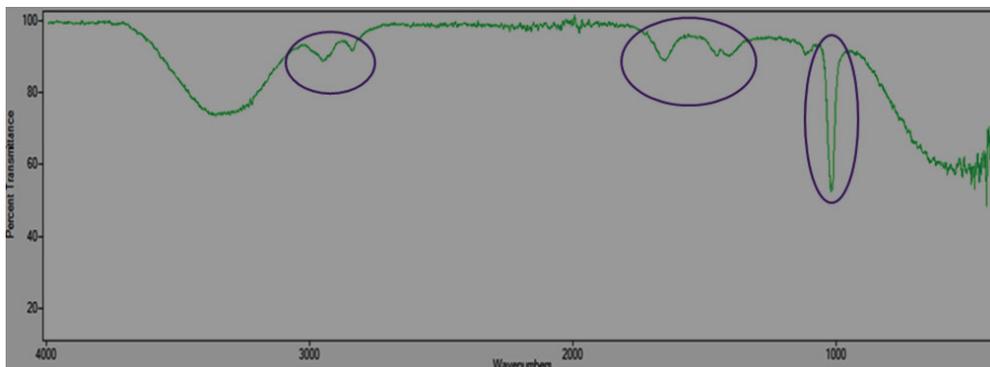
Figure 10. IR spectrum of bio-jet fuel obtained.

4. Conclusions

Botryococcus braunii UTEX 2441 was cultivated in domestic wastewater, thus reducing costs.

MgO NPs were obtained with a maximum wavelength of 209.5 nm. sodium citrate acts as a reducing and stabilizing agent.

TEM characterization showed that the obtained magnesium oxide nanoparticles (MgO NPs) are approximately 10 nm in size and flake shaped.

The effect of the MgO NPs depends on the concentration, since in the photobioreactor without MgO NPs (Blank) greater biomass growth was observed, but in the photobioreactor with 10% MgO NPs a greater amount of lipids was obtained.

We obtained a biodiesel yield were 86%. Since when the humidity increases the yield drops considerably. However perhaps other molecules such as phospholipids, or accumulation of lipids on the cell surface, are also could transformed into biodiesel. Furthermore, if a direct transesterification were carried out, costs would also be reduced in the production of these biofuels.

Bio-jet fuel obtained from the microalgae *B. braunii* is a good option to mitigate the problems surrounding fossil fuels and with this help contribute to the production of new fuels derived from third generation biomass.

This work shows a path to innovate techniques that allow greater efficiency in the biokerosene production process; Considering the economic characteristics

of developing countries and even the maturity of technology; bio-kerosene production is a promising short-term alternative.

All authors have read and agree to the manuscript and there is no conflict of interest between them, any additional information or data may be requested from the corresponding author (JABL).

Acknowledgements

References

1.   Ramon-Vilarasau, D. (2020). Impacto de la COVID: la epidemia que cortó las alas a la aviación comercial. *Hosteltur*. Retrieved May 19, 2024, from: https://www.hosteltur.com/137711_impacto-de-la-covid-la-epidemia-que-corto-las-alas-a-la-aviacion-comercial.html

2.   IATA. (2020). Working towards ambitious targets. Retrieved May 19, 2024, from: https://www.iata.org/en/programs/environment/climate-change/

3.   Wei, H., Wenzhi, L., Xinyu, C., Qing, Y., Jiashuo, L., & Chena, H. (2019). Renewable bio-jet fuel production for aviation: A review. *Fuel, 254*, 115599. https://doi.org/10.1016/j.fuel.2019.06.007

4.   Plante, L., Sheehan, N. P., Bier, P., Murray, K., Quell, K., Ouellette, C., et al. (2019). Bioenergy from biofuel residues and waste. *Water Environment Research, 91*(10), 1199–1204. https://doi.org/10.1002/wer.1214

5.   Chavez-Sandoval, B. E., & Hernández-Salgado, M. F. (2021). Obtaining biodiesel by direct transesterification of *Botryococcus braunii* and *Coccomyxa subellipsoidea*. *Journal of the Mexican Chemical Society, 65*(3), 318–330. https://doi.org/10.29356/jmcs.v65i3.1430

6.   Fiorella, K. J., Okronipa, H., Baker, K., & Heilpern, S. (2021). Contemporary aquaculture: Implications for human nutrition. *Current Opinion in Biotechnology, 70*, 83–90. https://doi.org/10.1016/j.copbio.2020.11.014

7.   Moretti, C., Vera, I., Junginger, M., López-Contreras, A., & Shen, L. (2022). Attributional and consequential LCAs of a novel bio-jet fuel from Dutch potato by-products. *Science of the Total Environment, 813*, 152505. https://doi.org/10.1016/j.scitotenv.2021.152505

8.   Chávez-Sandoval, B. E., Balderas-López, J. A., Padilla-Bernal, G., Moreno-Rivera, M. L., Franco-Hernández, M. O., & Martínez-Jiménez, A. (2015). Photopyroelectric techniques for thermo-optical characterization of gold nanoparticles. *Journal of Physics: Conference Series, 582*, 012027. https://doi.org/10.1088/1742-6596/582/1/012027

9.   Chavez-Sandoval, B. E., Ibáñez-Hernández, M. A. A., García-Franco, F., Galindo-Pérez, E. J., Abrica González, P., & Martínez-Jiménez, A. (2016). Biological synthesis and characterization of gold nanoparticles (AuNPs), using plant extracts. *Journal of Nanomaterials & Molecular Nanotechnology, 5*(4). https://doi.org/10.4172/2324-8777.1000192

10. Chavez-Sandoval, B. E., Balderas-López, J. A., García-Franco, F., Galindo-Pérez, E. J., Martínez-Jiménez, A., & Ibáñez-Hernández, M. A. A. (2020). The pH role in synthesis, distribution, and potential applications of gold nanoparticles (AuNPs). *International Journal of Biomedical Nanoscience and Nanotechnology, 4*(1/2), 120–138. https://doi.org/10.1504/IJBNN.2020.10029083

11. Chavez-Sandoval, B. E., Flores-Mendoza, N., Chavez-Recio, A., Balderas-López, J. A., & García-Franco, F. (2021). Biosynthesis of gold nanoparticles (AuNPs) and reducing agents in the process. *Mundo Nano: UNAM, 14*(27), 1e–12e. https://doi.org/10.22201/ceiich.24485691e.2021.27.69658

12. Cao, H., Zhang, Z., Wu, X., & Miao, X. (2013). Direct biodiesel production from wet microalgae biomass of *Chlorella pyrenoidosa* through in situ transesterification. *Journal of Biomedicine and Biotechnology.* https://doi.org/10.1155/2013/930686

13. Abbas, Z., Hassan, M. A., Huang, W., Yu, H., Xu, M., Chang, X., et al. (2024). Influence of magnesium oxide (MgO) nanoparticles on maize (*Zea mays* L.). *Agronomy, 14*(617). https://doi.org/10.3390/agronomy14030617

14. Griffiths, M. J., & Harrison, S. (2009). Lipid productivity as a key characteristic for choosing algal species for biodiesel production. *Journal of Applied Phycology, 21*(5), 493–507. https://doi.org/10.1007/s10811-008-9392-7

15. Yeesang, C., & Cheirsilp, B. (2011). Effect of nitrogen, salt, and iron content in the growth medium and light intensity on lipid production by microalgae isolated from freshwater sources in Thailand. *Bioresource Technology, 102*, 3034–3040. https://doi.org/10.1016/j.biortech.2010.10.013

16. Tatli, M., Jin, H., Camp, C. H., Li, J., Cicerone, M., Shih ,W. et al. (2017). Raman spectra and DFT calculations for botryococcene and methylsqualene hydrocarbons from the B race of the green microalga *Botryococcus braunii. Journal of Molecular Structure, 1147,* 427–437. https://doi.org/10.1016/j.molstruc.2017.06.126

17. Kawamura, K., Nishikawa, S., Hirano, K., Ardianor, A., Nugroho, R. A., & Okada, S. (2021). Large-scale screening of natural genetic resource in the hydrocarbon-producing microalga *Botrycoccus braunii* identified novel fast-growing strains. *Sci Rep., 11*(1), 7368. https://doi.org/10.1038/s41598-021-86760-8

18. Dismukes, G. C., Carrieri, D., Bennette, N., Ananyev, G. M., & Posewitz, M. C. (2008). Aquatic phototrophs: efficient alternatives to land-based crops for biofuels. *Biotechnol*, 235–240. https://doi.org/10.1016/j.copbio.2008.05.007

19. Fernández, G.. (2024). Química Orgánica. Retrieved from: www.quimicaorganica.net on 2024-05-19.

20. Balat, M., & Balat, H. (2010). Progress in biodiesel processing. *Applied Energy, 87*(6), 1815–1835.
https://doi.org/10.1016/j.apenergy.2010.01.012

21. PROY-NMX-AA-005-SCFI-2021. (2024). Análisis de agua-medición de grasas y aceites recuperables en aguas naturales, residuales y residuales tratadas-método de prueba (cancelará a la NMX-AA-005-SCFI-2013). Retrieved from: https://biblioteca.semarnat.gob.mx/janium/Documentos/Ciga/agenda/DOFsr/PROY-NMX-AA-005-SCFI-2021.pdf on 2024-05-19.

22. Fukuda, H., Kondo, A., & Noda, H. (2001). Biodiesel fuel production by transesterification of oils. *Bioscience*, 405–416.
https://doi.org/10.1016/S1389-1723(01)80288-7

23. Lafont, J. J., Páez, M. S., & Torres, Y. C. (2011). Análisis Químico de Mezclas Biodiesel de Aceite de Cocina Usado y Diesel por Espectroscopia Infrarroja. *Información* Tecnológica, 22(4), 35–42.
https://doi.org/10.4067/S0718-07642011000400005

24. Al-Omar M. S., Jabir, M., Karsh, E., Kadhim, R., Sulaiman, G. M., Taqi, Z. J. et al. (2021). Gold Nanoparticles and Graphene Oxide Flakes Enhance Cancer Cells' Phagocytosis through Granzyme-Perforin-Dependent Biomechanism. *Nanomaterials (Basel), 11*(6), 1382.
https://doi.org/10.3390/nano11061382

25. Pryshchepa, O., Pomastowski, P., & Buszewski, B. (2020). Silver nanoparticles: Synthesis, investigation techniques, and properties. *Adv Colloid Interface Sci.*, 284, 102246.
https://doi.org/10.1016/j.cis.2020.102246

26. Silverstein, R., Bassler, G., & Morrill, T. (1991). *Spectrometric identification of organic compounds.* (5th Ed.). New York: John Wiley. pp. 430. ISBN 0471 63404 2.

27. Suzuki, R., Ito, N., Uno, Y., Nishii, I., Kagiwada, S., Okada, S. et al. (2013). Transformation of Lipid Bodies Related to Hydrocarbon Accumulation in a Green Alga, *Botryococcus braunii* (Race B). *PLOS* 8(12).
https://doi.org/10.1371/journal.pone.0081626

28. Wang, S., Yang, H., Yan, R., Fu, Z., Zhao, J., & Tao, Z. (2022). Development of bio-jet fuel production technology: a review. *Sheng Wu Gong Cheng Xue Bao, 38*(7), 2477–2488. Chinese.

TiO$_2$-WO$_3$ HETEROJUNCTIONS FOR PHOTOCATALYTIC HYDROGEN GENERATION

X. González-Bautista[1], M. L. Hernández-Pichardo[2*], J. V. Méndez -Méndez[3*]

[1]Instituto Politécnico Nacional, Escuela Nacional de Ciencias Biológicas (ENCB), UPALM, C.P. 07738, CDMX, México.

[2]Instituto Politécnico Nacional, Laboratorio de nanomateriales sustentables, Escuela de Ingeniería Química e Industrias Extractivas (ESIQIE), UPALM, C.P. 07738, CDMX. México.

[3]Instituto Politécnico Nacional – Centro de Nanociencias y Micro y Nanotecnologías Luis Enrique Erro s/n, C. P, 07738, CDMX. México.

* mhernandezp@ipn.mx, jmendezm@ipn.mx

Abstract

Clean energy and water pollution are significant challenges that demand innovative solutions. Photocatalysis, as an emerging technology, holds the potential to address these issues. In our research, we have synthesized TiO_2 nanosheets and a composite based on a TiO_2-WO_3 heterojunction using a hydrothermal method. Different characterization techniques were used, and the formation of the anatase phase directly interacting with WO_x clusters was observed. In samples prepared with WO_3, the presence of the W=O vibrational mode was observed, and TEM studies confirmed the formation of the heterojunction between TiO_2 and WO_3. The higher H_2 production is attributed to the formation of this heterojunction, which inhibits the recombination of electrons and holes. The bandgap of the TiO_2-WO_3 catalysts was slightly smaller than that of pristine TiO_2. The heterojunction formation inhibits the e^-/h^+ recombination rate, thus favoring the separation of photoproduced carriers. The TW5 catalyst demonstrated the highest production rate, reaching 663.54 $\mu mol \cdot g^{-1}$ within 4 hours. These findings underscore the potential of TiO_2-WO_3 heterojunctions in the field of photocatalytic hydrogen production, inspiring further research and development in this area.

Keywords: TiO_2-WO_3 heterojunction, photocatalysis, hydrogen production

1. Introduction

The US Academy of Sciences report [1] indicates that global energy consumption is projected to increase by two and three times in 2050 and 2100 compared to 2001 (13.5 TW). This forecast reflects a challenging scenario that calls for urgent action to avoid a major energy crisis with the least possible environmental impact. Against this background, it has become imperative to explore and develop alternative energy sources that are clean, renewable, economically viable, and sustainable as an alternative to traditional fossil fuels to meet the growing energy demands of human society. In this context, hydrogen stands out as a regenerative and environmentally friendly energy carrier, attracting significant attention from the scientific community in recent decades. However, the current hydrogen production process, which mainly derives from fossil fuels through natural gas steam reforming processes, raises significant concerns regarding sustainability and the negative environmental impact. These challenges underscore the importance of our research in proposing a solution to these issues. Therefore, future hydrogen generation is anticipated to be based on harnessing renewable energy sources [2].

Solar energy is a promising option for effectively addressing global energy challenges in this context. Photocatalytic hydrogen production through solar and semiconductor-driven water splitting has emerged as a key strategy to address both solar energy storage and green hydrogen production [3 - 5]. However, this approach presents significant challenges, particularly in identifying highly efficient and stable visible-light active photocatalysts capable of providing excited charge carriers for H$_2$ or O$_2$ evolution reactions under visible light irradiation.

In this regard, tungsten trioxide (WO$_3$) has emerged as a promising co-catalyst due to its light absorption properties at wavelengths up to 480 nm, its relatively narrow bandgap (approximately 2.8 eV), and its stability and safety under acidic and oxidative conditions [5, 6]. Furthermore, tungsten oxide (WO$_3$) exhibits a high gap mobility of 10 cm^2 V^{-1} s^{-1} and a gap migration distance of 150 nm. This facilitates charge separation in the TiO$_2$-WO$_3$ heterojunction. The combination of these materials forms a perfect interface, thanks to the similarity in ionic radius (Ti^{4+}: 0.0605 nm; W^{6+}: 0.0600 nm) and metal-to-metal distance (Ti-Ti: 3.78 Å; W-W: 3.84 Å) [7].

This study is focused on optimizing the interaction between titanium oxide and tungsten oxide by forming nanosheets and/or nanobelts to increase the

charge transport efficiency. The optimization is based on the morphology, which allows a linear passage of the charge carriers along two-dimensional planes. This improves the photocatalytic activity by extending the absorption range of TiO_2 through heterojunction with WO_3.

2. Experimental Methodology

2.1. *Synthesis of Titanium Dioxide (TiO₂) by the hydrothermal method*

The synthesis of TiO_2 was carried out using a process described in [8]. Briefly, 12.5 mL of $C_{16}H_{36}O_4Ti$ (titanium (IV) butoxide) and 1.5 mL of hydrofluoric acid (70 wt.%) were added, and the mixture was stirred for 2 h until a gel was obtained. The gel was transferred to a Teflon autoclave and kept at 180 °C for 36 h. After cooling, the product was washed with ethanol and distilled water several times. Subsequently, the product was dispersed in a 0.01 M NaOH solution and stirred for 8h. The precipitate was recovered by centrifugation at high speed, washed with distilled water and ethanol several times, and dried at 80 °C for 6 h.

2.2. *Synthesis of TiO₂-WO₃ catalysts (TW) by the hydrothermal method*

The synthesis of TiO_2-WO_3 was performed using a hydrothermal method. The following materials were used: 12.5 mL of $C_{16}H_{36}O_4Ti$, AMT (ammonium metatungstate) at 5, 10, and 15 wt.% with respect to WO_3, and 1 mL of hydrofluoric acid (70 wt.%). These were added and kept under stirring for 2 h. The gel was transferred to a Teflon autoclave and kept at 180 °C for 36 h. After cooling, the product was cooled. Once cooled, the product was washed with ethanol and distilled water several times. Subsequently, the product was dispersed in a 0.01 M NaOH solution and stirred for 8 h. The precipitate was recovered by centrifugation. The precipitate was recovered by centrifugation, washed with distilled water and ethanol several times, and dried at 80 °C for 6 h.

2.3. *Photocatalytic activity tests*

The photocatalytic behavior of the samples for the generation of H_2 was carried out using a water/methanol solution under UV irradiation. In a typical experiment, 0.1 g of photocatalyst is dispersed in 150 mL of water/methanol solution (1:1 volume). A Pen Ray Hg UV lamp (254 nm, 4.4 mW/cm²) is used to irradiate the

solution. The products were identified using a Perkin-Elmer model Clarus 480 chromatograph. H$_2$ evolution was monitored by online gas chromatography.

The photocatalytic degradation of methyl orange (MO) was carried out in a photoreactor (Photo Q 200 brand Prendo), using a concentration of 20 mg/L of MO and 100 mg of catalyst. Before illumination, the suspension was magnetically stirred in the dark for 30 min to establish adsorption-desorption equilibrium at room temperature. Subsequently, the sample is subjected to UV-Vis light irradiation (UV-C ~400 nm). Sampling was carried out at regular time intervals.

3. Results and discussion

3.1. *Structural and textural properties of photocatalysts*

Figure 1 shows the diffractogram of the catalysts. The T0 sample exhibited peaks at 2θ = 25.33, 36.99, 37.83, 38.63, 48.07, 53.93, 55.09, 62.13, 62.73, 68.79, 70.31, 75.07 and 76.09 degrees (JCPDS No. 21-1272) [9, 10], and it is possible to observe traces of the rutile phase (2θ = 27.45º). Additionally, the sample has been found to exhibit high crystallinity, with a crystal size of 32 nm obtained from Scherrer's equation (1).

$$D = \frac{K \cdot \lambda}{\beta \cos\theta} \quad (1)$$

For TW5, TW10 and TW15 catalysts, it was observed that the anatase phase of titania predominates, as indicated by peaks around 2θ = ~25.30, 38.01, 48.01, 53.93, 54.97, 62.71, 68.83, 70.19, 75.11 y 75.93 degrees (JCPDS No. 89-4921) [11]. The absence of WO$_3$ signals indicates that tungsten nanostructures may exist in sizes smaller than 3 nm. Furthermore, the TW catalysts exhibit comparable crystallinity, although it is less pronounced than that of T0. Concurrently, it was observed that the crystallite size of the samples with tungsten oxide decreased as the tungsten oxide content increased. The crystallite sizes were 13, 10, and 8 nm for samples TW5, TW10, and TW15, respectively.

It is important to note that the catalysts were not subjected to additional heat treatment. This is because such a process involves a higher energy consumption during preparation. It is important to note that hydrothermal synthesis allows for direct control of reaction conditions. Consequently, there is no need to use calcination or other similar treatment methods to obtain crystallized products, as this synthesis method provides crystalline and uniform products [12].
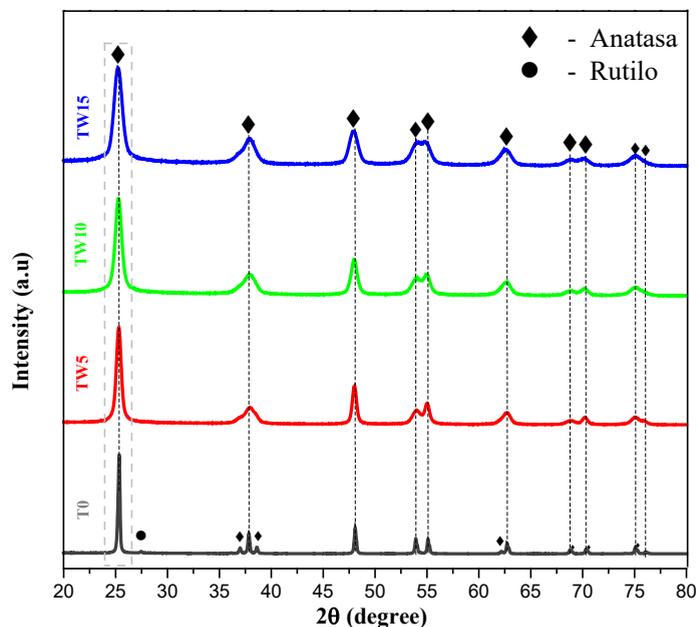
Figure 1. Diffractogram of the TiO_2 and TiO_2-WO_3 samples.

Figure 2 shows the Raman spectra of the T0 samples in comparison to the TW catalysts. In the case of the T0 sample, we can observe the characteristic vibrational modes of titania, which are 142, 196, 396, 517, and 639 cm^{-1}. The 142, 517, and 639 cm^{-1} modes correspond to the O-Ti-O bond vibrations, the 196 cm^{-1} mode to O-Ti, and the 396 cm^{-1} mode to Ti-O [13, 14]. For samples TW5, TW10, and TW15, we observed the characteristic vibrational modes of titania.

In the case of sample TW5, we did not observe the presence of WO_x nanostructures, but we did observe a characteristic signal at 966 cm^{-1} only for samples TW10 and TW15. The signal corresponds to the stretching mode of the terminal W=O double bonds present in WO_x clusters (Figure 2b) [15]. The 966 cm^{-1} signal of the TW10 and TW15 catalysts becomes broader and weaker as the WO_3 content increases. This could indicate an increase in defects in the titania crystal lattice [16], favoring the capture of photogenerated electrons and inhibiting the recombination of e^-/h^+ [15]. At the same time, we observed a shift towards higher frequencies of the main TiO_2 signal at 142 cm^{-1}, especially in the TW catalysts. This shift could indicate the formation of a heterojunction between TiO_2 and WO_3, which would result in certain changes in the titania structure due to the incorporation and increase in %wt. of WO_3 [11].
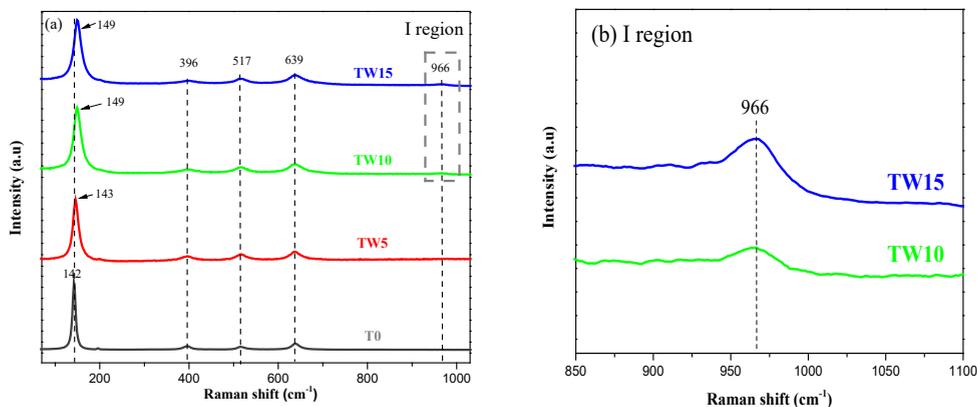
Figure 2. a) Raman spectra of catalysts T0 and TW; b) Magnified view of region I.

The morphologies of the T0 and TW catalyst samples were observed by SEM. Figure 3 shows the morphology of T0; we can observe a morphology of agglomerates with irregular structures; its EDS revealed the presence of Ti, O, and impurity of Si, which is attributable to the synthesis method of the distributor.
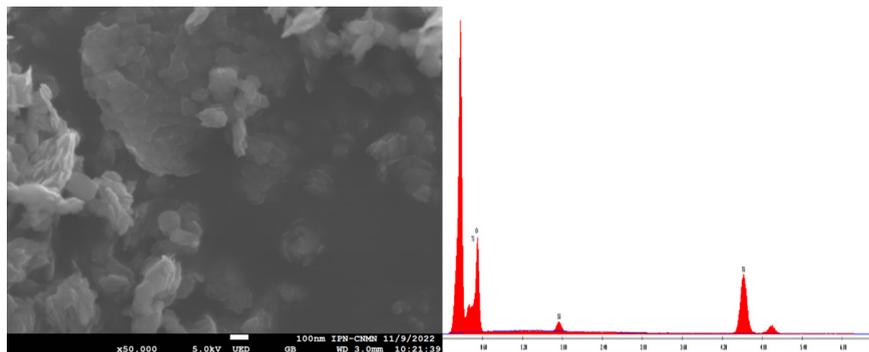
Figure 3. SEM images of sample T0 and EDS results.

In Figure 4, we can observe the morphology of the TW catalysts; in the case of TW5 (Figure 4A), aggregates and agglomerates are observed, but no defined morphology was observed for this catalyst. In Figure 4B, we can observe the morphology of the TW10 catalyst; again, we observe agglomerates without any type of morphology in the same way it is observed for the TW15 catalyst (Figure 4C). We can suggest that this type of irregularly shaped aggregate is due to the failure to develop crystals [17], and this can be observed with XRD (Figure 1), as the crystalline phases of WO$_3$ were not observed, suggesting that WOx may be grown from small TiO$_2$ structures. The EDS results for the TW catalysts identified and confirmed the presence of O, F, Ti, and W. The uniform

distribution of the O, Ti, and W elements of each TW catalyst detected by EDS can also be seen below.
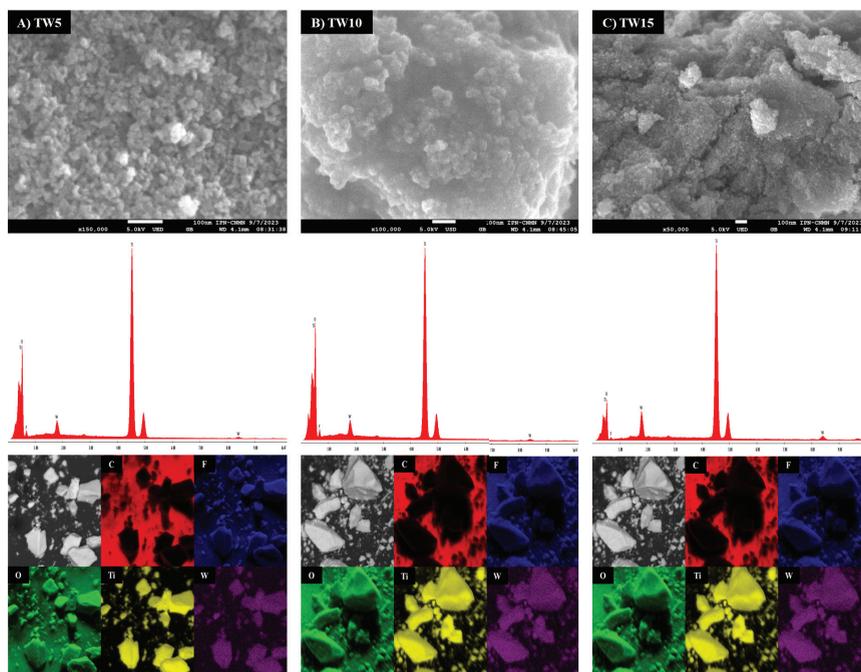
Figure 4. SEM images of A) TW5, B) TW10, and C) TW15, and EDS and mapping results (bottom).

Figure 5 shows the TEM images of the TiO_2-WO_3 samples, it shows the effect of the tungsten oxide on the particle size (Figures 5a-5c). It is observed that the particle size is decreasing as the tungsten oxide is increasing. Also, Fig 5d. shows the HAADF images of the TW5 sample showing the typical formation of the TiO_2-WO_3 heterojunction. The WO_3 phase is present as small WOx clusters, as is observed in the HAADF images as brighter spots corresponding to tungsten atoms deposited on the TiO_2 crystals ensuring intimate contact between the two phases.
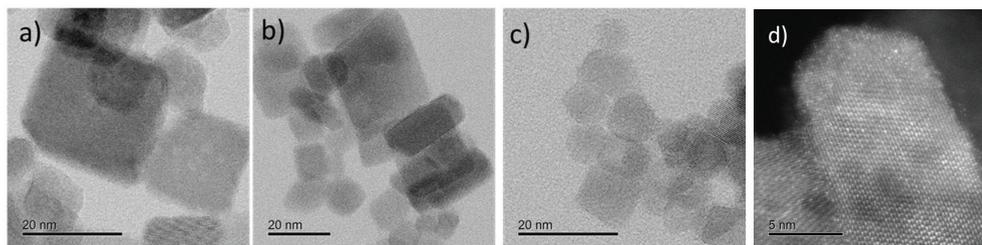
Figure 5. HRTEM images of the TW5. TW10 and TW15 samples (5a, 5b, and 5c, respectively) and HAADF images of the TW5 sample.

3.2. Band gap

The Tauc model was used to determine the optical band gap energy of the catalysts (T0, TW0, TW5, TW10 and TW15). The equation is as follows [17]:

$$(\alpha h v)^{\frac{1}{n}} = A\,(h v - E_g) \quad (2)$$

where α is the absorbance coefficient; hv is the photon energy; A is a Tauc material property coefficient and an energy-independent constant; and E_g is the energy gap. The optical band gaps of the semiconductors T0, TW0, and TW were determined by extrapolating the straight section of the plot of (αh) and the straight section of the plot of $(\alpha hv)^{1/2}$ versus photon energy (Table 1).

Catalysts	λ (nm)	E_g reported (eV)	E_g obtained (eV)
T0	405	3.15 [14]	3.27
TW5	414	3.25 [18]	3.11
TW10	418	2.9 [19]	3.11
TW15	411	3.18 [18]	3.16

Table 1. Band gap energy values for the catalysts.

Figure 6 shows the optical band energy of the catalysts. The T0 sample has a band gap of 3.27 eV, consistent with the findings reported in the literature [14]. In the case of the TW5 and TW10 catalysts, they have a similar optical band gap (3.11 eV), while the case of the TW15 catalyst has an optical band gap of 3.16 eV.

The literature [20 - 22]photoluminescence, UV-Vis, and DRS spectroscopies; and by tensile tension tests. Results showed the successful formation and impregnation of NPs on the cotton fabric, with negligible leaching of NPs after several washing cycles. The photocatalytic activity of supported NPs was assessed by the degradation of methyl blue dye (MB indicates that the prohibited band gap of a crystalline semiconductor is related to the crystallite and particle size. When these are smaller, the energy band gap increases. This is consistent with the results of previous XRD studies, which reported an energy band gap of ~3.1 eV for TW catalysts. H. Lin and colleagues [21]3.8–5.7 nm propose that this is due to the spatial confinement of charge carriers, which results in the e$^-$ and h$^+$ in the semiconductor being confined in a potential well.

On the other hand, the reduction in the energy band gap suggests a potential interaction between tungsten oxide and titania. The objective is to minimize the recombination of e$^-$ and h$^+$ in the TW photocatalysts (TiO$_2$-WO$_3$). This could be

achieved by allowing electrons in the conduction band (CB) of titania to diffuse into the CB of tungsten. This process could be observed in the TW catalysts, potentially leading to enhanced photocatalytic activity.
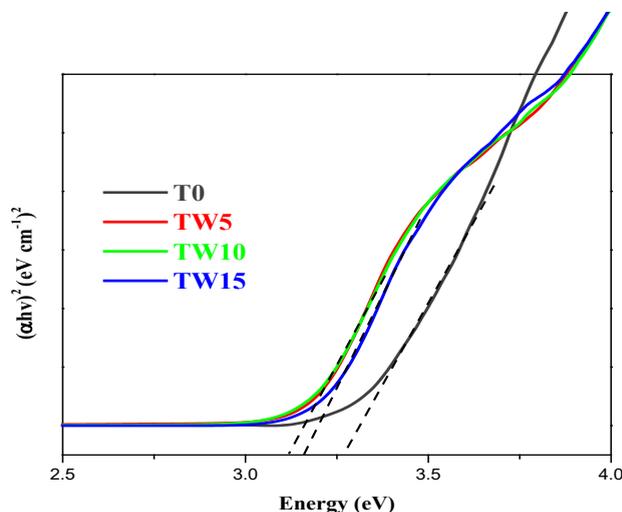

Figure 6. Optical band energies of the TiO$_2$ (T0) and TiO$_2$-WO$_3$ catalysts (TW).

3.3. *Photocatalytic evaluation of catalysts*

The catalysts were evaluated in two photocatalytic processes: the photocatalytic production of hydrogen and the decomposition of methyl orange (MO) (Figure 7a). The reaction kinetics of the photodegradation of organic pollutants is described by the Langmuir-Hinshelwood model [23]electrochemistry, analytical chemistry, radiochemistry, material chemistry, surface science, electronics, and hopefully catalysis. Since heterogeneous photocatalysis belongs to catalysis, all the bases of this discipline must be respected: (i. The rate constant (*kapp*) is the kinetics parameter that allows the determination of the photocatalytic activity independently of the adsorption process and the concentration of the remaining solute in the solution. In the case of these photocatalysts applied in the decomposition of MO, first-order kinetics was approximated and is described by equation (3):

$$\ln ln \frac{C}{C_0} = - kt \qquad (3)$$

The results of the analysis of the apparent reaction constant (*kapp*) of the catalysts T0 and TW, irradiated in UV and UV-Vis, are shown in Table 2. The R^2 values indicate that these catalysts present a first-order model, which means

that the degradation rate depends mainly on the amount of dye molecules in the solution [19]. The photocatalytic activity is compared by the value of the apparent rate constant, which is shown in Figure 7a. As expected, the highest *kapp* value was obtained for the TW15 catalyst, with a value of 0.0266 min^{-1}, showing a higher photocatalytic performance than the other photocatalysts in this reaction.

The TW15 photocatalyst offers a relatively large E$_g$, small crystal size, and large surface area (Table 1), which sets it apart from other photocatalysts; on the other hand, it also exhibits a higher photocatalytic activity, which corroborates the homogeneous dispersion of the titanium oxide and tungsten oxide particles. These results demonstrate the formation of a TiO$_2$-WO$_3$ heterojunction, which benefits the photocatalytic activity of titania for the degradation of dyes. According to the photoexcitation mechanism [24]I systematically discuss the properties of hetero junction photocatalysts in all cases. The formation of space charge regions, built-in electric field and potential barriers at the interface regions of thermally equilibrated heterojunctions are analyzed in details. When the heterojunctions are used for photocatalysis, the transfer behavior and mechanism of photo-excited non-equi librium carriers between the constituent semiconductors are discussed. It is demonstrated that the heterojunction properties, carrier transfer behavior and photocatalytic mechanism depend highly on the semiconductivity (Ntype or P-type, the e$^-$ from the CB of titania is diffusing to the CB of WO$_3$. The WO$_3$ acts as an acceptor of e$^-$ from the CB of titania, while the photogenerated h$^+$ from WO$_3$ migrates to the VB of titania, separating the electron-hole pair.
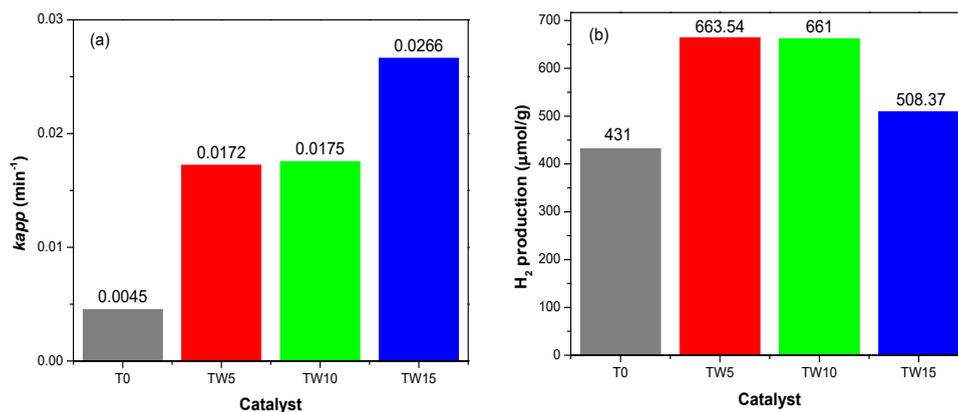
Figure 7. a) Apparent rate constant of catalysts in MO degradation; b) Catalytic evaluation of H$_2$ evolution of T0 and TW.

Also, Figure 7b compares the T0 sample with the TW catalysts for H_2 evolution using methanol (CH_3OH) as a sacrificial agent under UV-Vis irradiation for 4 h of reaction. The use of methanol as a sacrificial agent in the hydrogen production reaction serves two main purposes: 1) It has been reported that H_2 production increases considerably using methanol as a sacrificial agent, and 2) by performing this methanol degradation, the decomposition occurs, and the methanol is mineralized into less toxic substances [25].

This investigation demonstrates a higher H_2 generation in tungsten-containing catalysts. This research used a mixture of water and methanol with a 1:1 ratio; the methanol acted as a hydrogen ion scavenger. Figure 7b shows that the lower activity of T0 for H_2 generation was due to lower absorption of visible light. It is also important to note that it has a higher recombination rate of e^-/h^+. Adding WO_3 as a co-catalyst led to an improvement in the activity of TiO_2. In the presence of 5 %wt. of WO_3, an H_2 production of 663.54 µmol/g was achieved within 4 h, followed by the TW10 catalyst with an H_2 production of 661 µmol/g. This improvement can be attributed to the catalyst's ability to produce hydrogen rapidly. This improvement can be attributed to the fast charge separation observed in the case of the TW5 catalyst. In this case, using a sacrificial agent reduces the amount of WO_3 required in the sample, resulting in enhanced photocatalytic hydrogen production activity.

Particle size is a crucial factor in hydrogen production. It has been observed that smaller nanoparticles can exhibit higher photocatalytic activity compared with larger particles. In some cases, the small size of nanoparticles can give rise to a quantum effect. This results in the widening of the band gap [26], which, in turn, is related to a higher number of active sites on the smaller nanoparticles, allowing a higher exposure of these active sites to the reactant. Additionally, there is a higher interaction with the adsorbed molecules [27].

Finally, it can be observed that as the %wt. of WO_3 increases, the production of H_2 decreases; this can be observed in the TW15 catalyst, which catalyst has higher photocatalytic activity. However, the same does not happen to produce H_2; this could be attributed to the fact that there is a higher WO_3 charge, and it could possibly be acting as a shield effect and creating charge recombination centers, which subsequently decreases the evolution of H_2. In other words, the decrease of the H_2 could be due to three factors: 1) electronic band structure [28], 2) charge recycling [29], or 3) adsorption of species on the surface of the material [29]. The 15% wt incorporation of WO_3 into the heterojunction may alter these

band structures, affecting the availability of electronic states needed to facilitate the H$_2$ production reaction. It could also be because the tungsten could obstruct the transfer of e$^-$ or h$^+$ across the interface between the two semiconductors.

According to the results, we can propose a reaction mechanism related to the activation of TiO$_2$-WO$_3$ heterojunction under UV-Vis light irradiation for MO degradation and hydrogen evolution. To know the VB and CB of the heterojunction between titania and tungsten, we used the Mott-Shottky diagram (Figure 8) and calculated from empirical formulae [24]I systematically discuss the properties of hetero junction photocatalysts in all cases. The formation of space charge regions, built-in electric field and potential barriers at the interface regions of thermally equilibrated heterojunctions are analyzed in details. When the heterojunctions are used for photocatalysis, the transfer behavior and mechanism of photo-excited non-equi librium carriers between the constituent semiconductors are discussed. It is demonstrated that the heterojunction properties, carrier transfer behavior and photocatalytic mechanism depend highly on the semiconductivity (Ntype or P-type using the equations:

$$E_{VB} = \chi - E_e + 0.5\ E_g \qquad (4)$$

$$E_{CB} = E_{VB} - E_g \qquad (5)$$

where χ is the electronegativity of the material, E_{VB} is the VB potential, E_{CB} is the CB potential, E_g is the bandgap energy of the semiconductor, E_e is the energy of the free electrons (4.5 V). From this it can be seen that the E_{VB} of TiO$_2$ is 2.68 eV, and its E_{CB} is -0.24 eV; while, for the case of WO$_3$, its E_{VB} is 3.64 eV and its E_{CB} is 0.54 eV.

Catalyst	$kapp$ (min^{-1})	R^2	H$_2$ production (μmol/g)
T0	0.0045	0.9764	431
TW5	0.0172	0.9712	663.54
TW10	0.0175	0.9669	661
TW15	0.0266	0.9301	508.37

Table 2. Apparent rate constant values for OM degradation and H$_2$ evolution.
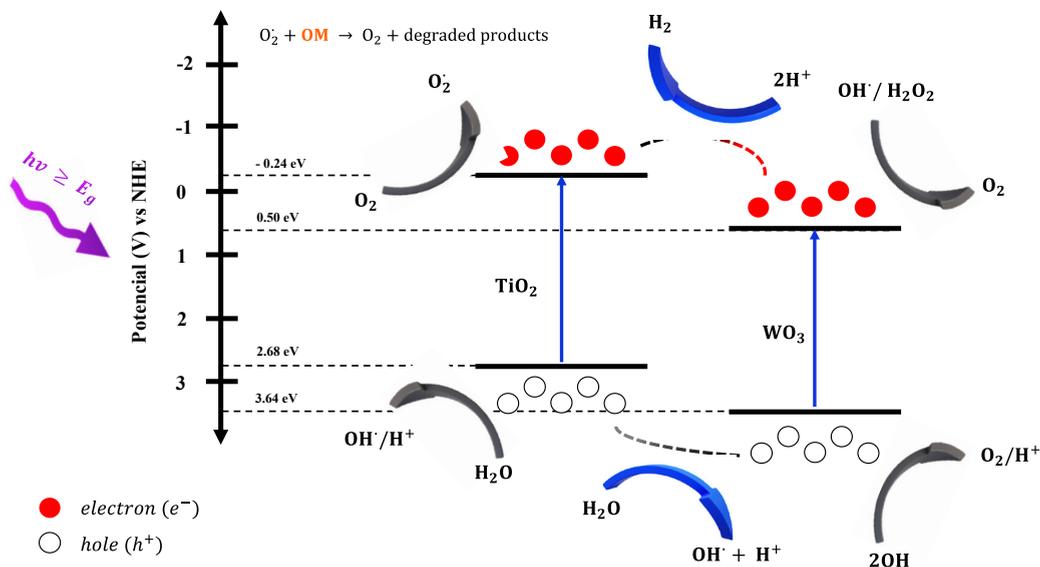
Figure 8. Mechanism of TiO_2-WO_3 heterojunction under UV-Vis.

4. Conclusions

Catalysts with a TiO_2-WO_3 heterojunction were synthesized by a hydrothermal method, modifying the tungsten oxide content (WO_3 % wt). The structural, morphological, and optical properties and chemical composition of the samples were investigated using different methods such as XRD, Raman, SEM, and UV-Vis.

XRD analysis showed that the anatase phase of TiO_2 predominates in samples T0, TW5, TW10, and TW15. The presence of WO_3 was not observed in XRD, so these species are smaller than 3 nm or highly dispersed on the titania surface. Raman showed the characteristic vibrational modes of TiO_2 at 142, 196, 396, 517, and 639 cm^{-1}; however, a shift towards higher frequencies was observed in the main band 142 cm^{-1} for the case of the TW catalysts, suggesting that this shift indicates that there could be a heterojunction between TiO_2 and WO_3, there could be some changes in the titania structure due to the incorporation and increase of WO_3. Also, for the TW10 and TW15 catalysts, we observed the signal at 966 cm^{-1}, which corresponded to the WO_x clusters and the W=O vibrational mode.

Using SEM, it was observed that the morphologies of the catalysts are irregular agglomerates, which could be attributed to the acid hydrolysis in the sol-gel phase of the synthesis and to the pH that we would obtain, since, according to the

literature, pHs lower than 5 are characteristic of agglomerated morphologies in these materials. The HRTEM analyses indicated that the particle size decreases as the tungsten oxide increases; also, by HAADF, it was observed that WO$_3$ is present in the form of small clusters of WOx deposited on the TiO$_2$ crystals, showing the formation of the heterojunction.

Using UV-Vis, it was observed that T0 absorbs in the UV region and, in the case of the TW catalysts, begins to absorb towards the visible region. In turn, the optical band energy of the catalysts was determined. The band gap energy value for the commercial sample (T0) was obtained according to the literature at about 3.27 eV. In the case of the TW5 and TW10 catalysts, the values slightly diminished at 3.11 eV and TW15 with 3.16 eV, showing that the particle size is important; the smaller the particle size, the higher the optical band energy. For the photocatalytic H$_2$ evolution, the TW5 catalyst presented a higher H$_2$ evolution because the band gap energy is narrow and the heterojunction between TiO$_2$ and WO$_3$ separates the e$^-$/h$^+$ pairs, however, for the TW10 and TW15 catalysts, although they presented a higher photocatalytic activity, they did not present a higher H$_2$ evolution, this could be because there is a higher WO$_3$ charge and possibly it would be working as a shielding effect and create charge recombination centers which subsequently reduce the H$_2$ evolution.

Acknowledgments

References

1. Lewis, N. S., & Nocera, D. G. (2006). Powering the planet: Chemical challenges in solar energy utilization. *Proceedings of the National Academy of Sciences, 103*(43), 15729–15735.
    https://doi.org/10.1073/pnas.0603395103

2. Holladay, J. D., Hu, J., King, D. L., & Wang, Y. (2009). An overview of hydrogen production technologies. *Catalysis Today, 139*(4), 244–260.
    https://doi.org/10.1016/j.cattod.2008.08.039

3. Hisatomi, T., & Domen, K. (2019). Reaction systems for solar hydrogen production via water splitting with particulate semiconductor photocatalysts. *Nature Catalysis, 2*(5), 387–399.
    https://doi.org/10.1038/s41929-019-0242-6

4. Kudo, A., & Miseki, Y. (2009). Heterogeneous photocatalyst materials for water splitting. *Chemical Society Reviews, 38*(1), 253–278.
    https://doi.org/10.1039/B800489G

5. Pinaud, B. A., Benck, J. D., Seitz, L. C., Forman, A. J., Chen, Z., Deutsch, T. G., et al. (2013). Technical and economic feasibility of centralized facilities for solar hydrogen production via photocatalysis and photoelectrochemistry. *Energy & Environmental Science, 6*(7), 1983–2002.
    https://doi.org/10.1039/c3ee40831k

6. Toledo Camacho, S. Y., Rey, A., Hernández-Alonso, M. D., Llorca, J., Medina, F., & Contreras, S. (2018). Pd/TiO2-WO3 photocatalysts for hydrogen generation from water-methanol mixtures. *Applied Surface Science, 455*, 570–580.
    https://doi.org/10.1016/j.apsusc.2018.05.122

7. Kim, Y. H., Park, H., Kim, S., Jeong, H., Lee, C., Shin, S., et al. (2020). Directional change of interfacial electric field by carbon insertion in heterojunction system TiO2/WO3. *ACS Applied Materials & Interfaces, 12*(13), 15239–15245.
    https://doi.org/10.1021/acsami.0c00669

8. Wan, J., Chen, X., Zeng, C., Zhong, X., Xu, Z., Jiang, D., et al. (2018). Defect effects on TiO2 nanosheets: Stabilizing single atomic site Au and promoting catalytic properties. *Advanced Materials, 30*(11), 1705369.
    https://doi.org/10.1002/adma.201705369

9. Zhu, J., Liu, Z., Yang, F., Long, D., Jian, Y., & Pu, S. (2022). The preparation of {001} TiO2/TiOF2 via a one-step hydrothermal method and its degradation mechanism of ammonia nitrogen. *Materials, 15*(18), 6465.
    https://doi.org/10.3390/ma15186465

10. Liu, X., Du, G., & Li, M. (2019). True photoreactivity origin of Ti3+-doped anatase TiO2 crystals with respectively dominated exposed {001}, {101}, and {100} facets. *ACS Omega, 4*(12), 14902–14912.
    https://doi.org/10.1021/acsomega.9b01648

11. Basumatary, B., Basumatary, R., Ramchiary, A., & Konwar, D. (2022). Evaluation of Ag@TiO2/WO3 heterojunction photocatalyst for enhanced photocatalytic activity towards methylene blue degradation. *Chemosphere, 286*, 131848.
https://doi.org/10.1016/j.chemosphere.2021.131848

12. Yuan, Y., Tian, J., Zhao, H., Zhang, Q., Zhang, X., Li, Q., & Zhao, L. (2021). A review of metal oxide-based Z-scheme heterojunction photocatalysts: Actualities and developments. *Materials Today Energy, 21*, 100829.
https://doi.org/10.1016/j.mtener.2021.100829

13. Tian, F., Zhang, Y., Zhang, J., & Pan, C. (2012). Raman spectroscopy: A new approach to measure the percentage of anatase TiO2 exposed (001) facets. *The Journal of Physical Chemistry C, 116*(13), 7515–7519.
https://doi.org/10.1021/jp301256h

14. Doševic-Mitrovic, Z., Jankovic, S., Živković, J., Cvjetićanin, N., & Grguric-Sipka, S. (2016). WO3/TiO2 composite coatings: Structural, optical and photocatalytic properties. *Materials Research Bulletin, 83*, 217–224.
https://doi.org/10.1016/j.materresbull.2016.06.011

15. Gutiérrez-Alejandre, A., Ramírez, J., & Busca, G. (1998). A vibrational and spectroscopic study of WO3/TiO2-Al2O3 catalyst precursors. *Langmuir, 14*(3), 630–639.
https://doi.org/10.1021/la970993n

16. Leghari, S. A. K., Sajjad, S., Chen, F., & Zhang, J. (2011). WO3/TiO2 composite with morphology change via hydrothermal template-free route as an efficient visible light photocatalyst. *Chemical Engineering Journal, 166*(3), 906–915.
https://doi.org/10.1016/j.cej.2010.11.065

17. Dolgonos, A., Mason, T. O., & Poeppelmeier, K. R. (2016). Direct optical band gap measurement in polycrystalline semiconductors: A critical look at the Tauc method. *Journal of Solid State Chemistry, 240*, 43–48.
https://doi.org/10.1016/j.jssc.2016.05.010

18. Habtamu, A., & Ujihara, M. (2023). The mechanism of water pollutant photodegradation by mixed and core–shell WO3/TiO2 nanocomposites. *RSC Advances, 13*(19), 12926–12940.
https://doi.org/10.1039/D3RA01582C

19. Pinedo-Escobar, J. A., Fan, J., Moctezuma, E., Gomez-Solís, C., Carrillo Martinez, C. J., & Gracia-Espino, E. (2021). Nanoparticulate double-heterojunction photocatalysts comprising TiO2(Anatase)/WO3/TiO2(Rutile) with enhanced photocatalytic activity toward the degradation of methyl orange under near-ultraviolet and visible light. *ACS Omega, 6*(18), 11840–11848.
https://doi.org/10.1021/acsomega.0c06054

20. Chacon-Argaez, U., Pacheco-Sánchez, J. H., & May-Pat, A. (2023). Photocatalytic activity and biocide properties of Ag–TiO2 composites on cotton fabrics. *Materials, 16*(13), 4513.
    https://doi.org/10.3390/ma16134513

21. Lin, H., Huang, C., Li, W., Ni, C., Shah, S., & Tseng, Y. (2006). Size dependency of nanocrystalline TiO2 on its optical property and photocatalytic reactivity exemplified by 2-chlorophenol. *Applied Catalysis B: Environmental, 68*(1–2), 1–11.
    https://doi.org/10.1016/j.apcatb.2006.07.018

22. Kumar, S., Verma, N. K., & Singla, M. L. (n.d.). Size dependent reflective properties of TiO2 nanoparticles and reflectors made thereof.

23. Herrmann, J.-M. (2010). Photocatalysis fundamentals revisited to avoid several misconceptions. *Applied Catalysis B: Environmental, 99*(3–4), 461–468.
    https://doi.org/10.1016/j.apcatb.2010.05.012

24. Yang, H. (2021). A short review on heterojunction photocatalysts: Carrier transfer behavior and photocatalytic mechanisms. *Materials Research Bulletin, 142*, 111406.
    https://doi.org/10.1016/j.materresbull.2021.111406

25. Pulido Melián, E., et al. (2013). Efficient and affordable hydrogen production by water photo-splitting using TiO2-based photocatalysts. *International Journal of Hydrogen Energy, 38*(5), 2144–2155.
    https://doi.org/10.1016/j.ijhydene.2012.12.005

26. Kudo, A., & Miseki, Y. (2009). Heterogeneous photocatalyst materials for water splitting. *Chemical Society Reviews, 38*(1), 253–278.
    https://doi.org/10.1039/B800489G

27. Suresh, R., Gnanasekaran, L., Rajendran, S., & Soto-Moscoso, M. (2023). Doped nanomaterials: Application in hydrogen production via photocatalytic water splitting. *Fuel, 348*, 128528.
    https://doi.org/10.1016/j.fuel.2023.128528

28. Hao, Y., et al. (2021). Energy band engineering and interface transfer strategies to optimize photocatalytic hydrogen evolution performance. *Applied Surface Science, 546*, 149137.
    https://doi.org/10.1016/j.apsusc.2021.149137

29. Xu, J., et al. (2024). Recent advances in heterogeneous catalysis of solar-driven carbon dioxide conversion. *Journal of Environmental Sciences, 140*, 165–182.
    https://doi.org/10.1016/j.jes.2023.06.028

EFFECT OF DENSITY OF STATES IN ELECTRICAL SIMULATION OF AMORPHOUS INDIUM-GALLIUM-ZINC-OXIDE THIN FILM TRANSISTOR

Arturo Torres-Sánchez, Isai Hernández-Luna, Francisco Hernández-Cuevas, Cuauhtémoc León-Puertos, Norberto Hernández-Como

Centro de Nanociencias y Micro y Nanotecnologías, Instituto Politécnico Nacional, México City, México.

Abstract

Amorphous oxide semiconductors (AOS) used as channel in Thin Film Transistors (TFTs) have extended their applications not only as switching devices in display technologies, but also as main elements in logic circuits such as inverters, logic gates, etc. In addition, materials such as amorphous Indium-Gallium-Zinc-Oxide (a-IGZO) due to their optical transparency and low deposition temperatures are used in low-cost flexible electronics, which gives the possibility of a-IGZO TFTs in portable electronics for healthcare sensing. The electrical performance of amorphous and microcrystalline transistors made of organic, inorganic and metal oxides materials is determined by the density of states (DOS) in the bandgap of the semiconductor material. In materials such as a-IGZO the DOS is composed of two exponentials describing the tails of acceptor/donor states and two Gaussians representing the deep acceptor/donor states. In this work, simulations were carried out on the density of the deep donor states (N_{GD}) related to the oxygen vacancies (OV) in a-IGZO, the results show that the off current (I_{OFF}) in the transfer curve rises as the density of states of N_{GD} increases due to greater electron density release from OV.

Keywords: amorphous oxide, a-IGZO, thin film transistors, oxygen vacancies, Silvaco.

1. Introduction

Thin Film Transistors (TFTs) made up of mature technology like amorphous silicon (a-Si) have been utilized as switching elements in display panel technologies. However, TFT composed of relative novel semiconductor materials like amorphous oxide semiconductors (AOS) have extended their applications as main elements in logic circuits such as inverters, logic gates, etc. Because amorphous Indium-Gallium-Zinc-Oxide (a-IGZO) is an AOS, it has a wide bandgap (>3eV) [1] and low process temperature [2-4], therefore is widely used in low-cost flexible electronics, which offer significantly improved performance compared to conventional semiconductors. a-IGZO, characterized by its amorphous structure, and high electron mobility (from 10 to 100 $cm^2/V \cdot s$) [5], has emerged as a preferred material for the following applications: integrated logic digital circuit design, touch sensor for flexible and portable devices, gas detection sensing and glucose sensor [5-8]. Other advantages of IGZO are the variety of deposition methods with which it can be obtained, which include: Sputtering, Spin-coated, Atomic layer deposition (ALD) and pulsed layer [4, 9 - 12].

The high field-effect electron mobility in a-IGZO is a consequence of the electronic transport path, which is realized through the overlapping of spherically ns (n>4) orbitals. These orbitals, belonging to the metal cation conduction bands [13, 14], are insensitive to the degree of disorder in films; thus, the mobility is almost unaffected by the amorphous phase in the films [15]. One aspect to consider is that a-IGZO has a high intrinsic carrier density ($>10^{17}\,cm^{-3}$) [16] due to a great density of free electrons originating from oxygen vacancies. Therefore, it is important to adjust deposition parameters or realize subsequence annealing treatments to achieve an a-IGZO material in which the intrinsic electron concentration can be reduced to a lower level ($<10^{15}\,cm^{-3}$), to obtain a low off current and, consequently, a high On/Off current ratio (I_{ON}/I_{OFF}). Efforts to overcome the above include suppressing the generation of oxygen vacancies [10]. Nonetheless, despite the promising attributes of a-IGZO TFT technology, challenges remain regarding performance and reliability due to sub-gap defects induced by oxygen-vacancy defects.

The electrical performance of amorphous and microcrystalline transistors made of organic, inorganic, and metal oxide materials is determined by the density of states (DOS) in the bandgap of the semiconductor material. In materials such as a-IGZO, the DOS is composed of two exponentials describing the tails of

acceptor/donor states and two Gaussians representing the deep acceptor/donor states [17]. Therefore, it is necessary to carry out simulations of the effects of the density of states within the a-IGZO bandgap and how this affects the transfer and output characteristics. In particular, the effect of the properties of the Al source-drain and DOS, through oxygen vacancies, on the electrical characteristics of a-IGZO TFTs will be simulated. The simulation of the a-IGZO TFT was conducted using the physical properties of semiconductor materials provided by the Silvaco® simulator. The physical structure of the device is achieved through ATHENA®, which simulates fabrication sequences and defines a «mesh» of the device, while the electrical characteristics are obtained by analyzing its DC response using ATLAS®.

2.   Experimental part

The a-IGZO TFT was fabricated on a Corning glass substrate (Eagle XG) with a staggered bottom gate contact structure with source and drain top contacts. First, Aluminum (Al) with a thickness of 50 nm was deposited as the gate electrode by e-beam evaporation and patterned by direct lithography, followed by wet etching of Al using a phosphoric solution. Next, as gate dielectric layer, 22 nm of Al_2O_3 was obtained at 150 °C by ALD using precursors such as trimethylaluminum and water. Subsequently, a 15 nm layer of a-IGZO was obtained at room temperature using a Sputtering system operating at 70 W with argon plasma, followed by annealing at 150 °C in air for 1 hour. Then, the gate and dielectric layers were patterned through lithography and solutions of Diluted HCl and a BOE (6:1), respectively. Finally, the drain and source contacts were deposited using 100 nm of Al via sputtering at 150 W in an Ar plasma environment, after those were defined through a lift-off process. The width and channel length of the a-IGZO TFT were 160 μm and 40 μm, respectively. The figure 1 a) and1 b) shows the top-view and cross section, respectively, of a-IGZO TFT bottom gate structure fabricated in this work.
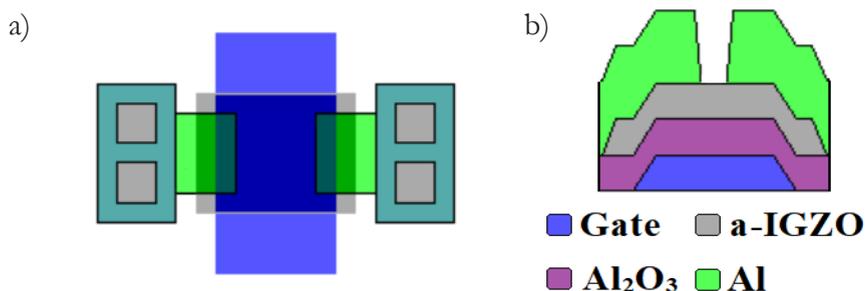
Figure 1. a) Top view and b) croos-section view of staggered bottom gate a-IGZO TFT fabricated.

2.1. *Electrical simulation of staggered bottom gate a-IGZO TFTs*

We initialize the simulation creating the mesh of staggered bottom gate a-IGZO TFT, it was defined along x-axis from 0 to 70 µm, while y-axis it was from o to 1.136 µm, the width and channel length were 160 µm and 40 µm, respectively. Nitride was chosen as mechanical support for a-IGZO TFT. Then, different materials were deposited with the same thickness that these were obtained experimentally, with thickness of 22 nm, 15 nm for Al_2O_3 and a-IGZO, respectively, 50 nm of Al for gate electrode, and 100 nm of Al for source and drain electrodes. Figure 2 shows the a-IGZO TFT cross section generated by ATHENA.

In a-IGZO material the DOS can be described by means of two exponentials representing the density of "tail" states localized near of the valence and conduction band originated from oxygen p-band and metal ions s-band [17], respectively, moreover of two Gaussian distribution indicating the density of deep states. An approximation of the DOS as a function of energy is given by the following expression [18]:

$$g(E) = N_{TA}exp\left(\frac{E-E_C}{W_{TA}}\right) + N_{GA}exp\left(-\left(\frac{E_{GA}-E}{W_{GA}}\right)^2\right) + N_{TD}exp\left(\frac{E_V-E}{W_{TD}}\right) +$$

$$N_{GD}exp\cdot\left(-\left(\frac{E-E_{GD}}{W_{GD}}\right)^2\right)$$
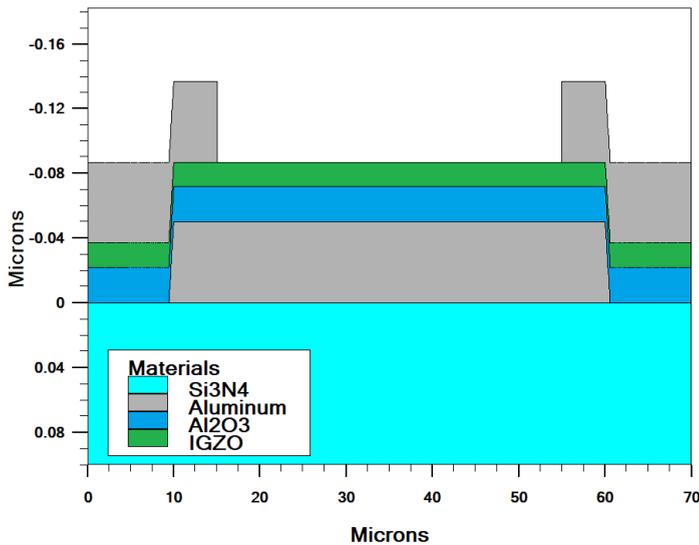
Figure 2. a-IGZO TFT cross section generated by ATHENA.

where N_{TA} and N_{TD} are the density of acceptor/donor tail states from the conduction and valence band, respectively, and W_{TA} and W_{TD} are the slopes of the exponentials representing decay energies of those states. Meanwhile, N_{GA} and N_{GD} are the density of acceptor/donor deep states, respectively, W_{GA} and W_{GD} are the slopes of the Gaussians curves and E_{GA} and E_{GD} are the position of the peaks of energy of those Gaussian distribution in the bandgap. Figure 3 shows the schematic DOS distribution used for a-IGZO TFT simulated at this work. In a-Si TFTs the deep states are originated of dangling bonds [18] and can be represented by two exponential or two Gaussian distributions, when the last are used in the simulations, E_{ga} is placed little above in the middle of E_g, while E_{gd} is placed just below in the middle of E_g. However, for a-IGZO TFTs, deep donor states (N_{GD}) have to be represented by a Gaussian distribution near to the conduction band [17 - 19]. In a-IGZO, deep donor states are originated from oxygen vacancies (OV) which is linked to films with high electron density [18]. The OV model can be written in the following notation [17]: $V_O^X \rightarrow V_O^{+2}$; V_O^X means vacancies of oxygen and those are charged neutral when those are filled and positively charged when are empty. The above expression describes an OV acting like electron donors by removing oxygen bonding [19] when an OV is fully ionized (V_O^{+2}) two electrons (*2e*) are released. Otherwise, deep acceptor states (N_{GA}) are produced by excess of oxygen which is related with low electron density in the films. The oxygen, weakly bonded, capture electron through: $O^0 + e^- \rightarrow O^{-1}$ or $O^{-1} + e^- \rightarrow O^{2-}$ [18]. The acceptor states are neutral when those are unoccupied and negatively charged when are filled by electrons.
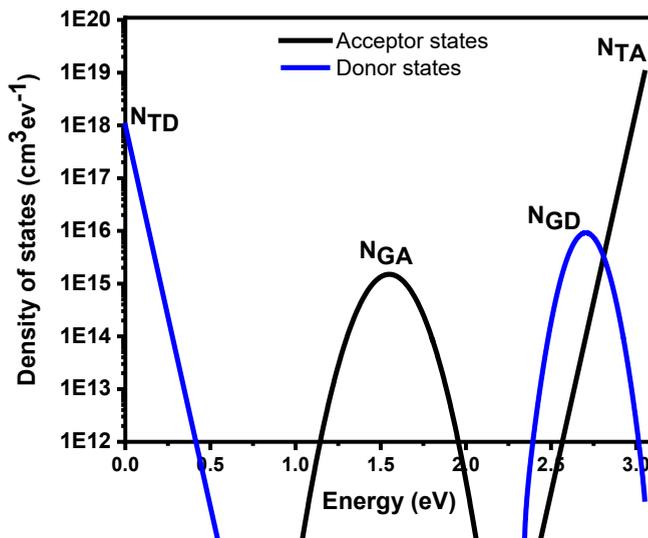
Figure 3. Schematic DOS distribution for a-IGZO.

Kai-Hsiang et al. [18] and Kyun Kim et al. [19] placed N_{GA} just 1.0 eV and 0.5 above valence band, respectively, while Ching Fun et al. [17] not considered deep-gap states in their work. In our simulation deep acceptor-type states and deep donor-type states were collocated at 1.5 eV and 2.8 eV, respectively. Table 1 shows all simulation parameters used in ATLAS® for IGZO TFT. The initial DOS parameters values were set taking into account those reported for a-IGZO in references [17 - 19]. For the simulation, a-IGZO properties like band gap, electron affinity and permittivity were set according to the default values provided by ATLAS® [20], while a field electron mobility of 8.9 cm2/V·s extracted experimental of our a-IGZO TFT fabricated was considered. Moreover, firstly a work-function of 4.2 eV for gate, source and drain contacts was set in the simulation. The DOS parameters values that fitted the simulated and experimental transfer (ID vs VGS) and output (ID vs VDS) curves of a-IGZO TFT were: N_{TA} = 2 x 1019 cm-3 eV-1, N_{GD} = 1 x 1018 cm-3 eV, N_{GA} = 1.5 x 1018 cm-3 eV-1, N_{GA} = 1.5 x 1018 cm-3 eV-1, N_{GD} = 1.5 x 1018 cm-3 eV-1, W_{TA} = 0.02 eV, W_{TD} = 0.02 eV. Figure 4 a) presents the simulated and experimental transfer curve of a-IGZO TFT. The experimental curve was measured using the Keithley 4200 semiconductor analyzer (DC resolution of 10^{-18} A and 0.2 μV), sweeping the gate voltage from -1 to 5 V and then reversing it, both with steps of 0.1 V. As can be seen the simulated graph reproduces well the experimental transfer curve in saturation region (V_{DS}= 5V). However, in Figure 4 b), we can observe that simulated output curve doesn´t matches the experimental output curve in low drain voltages (V_{DS}< 0.5V) and for V_{GS}= 5V. The last may be due to
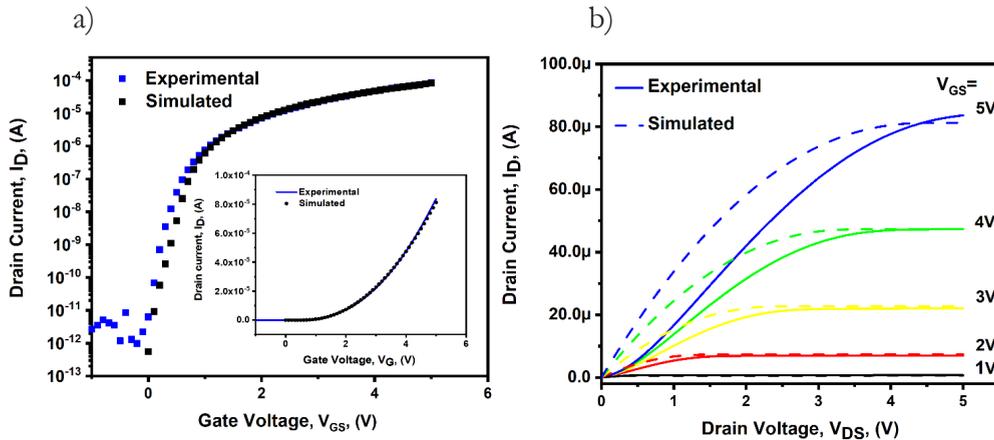
Figure 4. a) Simulated and experimental transfer curves and b) output curve of a-IGZO TFT.

initially the simulation has been realized with a work-function of Al contacts near to electron affinity value of a-IGZO, and according to the expression [21]: $q\theta_B = q(\Phi_m - \chi_s)$; where is the Schottky barrier height, Φ_m is the work-function of metal (Al=4.2 eV), is the electron affinity of semiconductor (IGZO= 4.16 eV) and q is the electron charge; $q\theta_B = 0.04\ eV$, therefore in the simulated output graph we have ohmic contacts. However, due to interface states between Al and a-IGZO, the experimental work-function of Al is higher than 4.2 eV, then $q\theta_B$ too will be greater, thus presenting Schottky contacts and a non-linear relation between I_D and V_{DS} as can we see in Figure 4 b).

2.2. *Effect of work-function S/D Al-contacts*

To fit the simulated and experimental output curves, we need to increase work-function of Source/Drain (S/D) Al-contacts until a non-ohmic contact is present in the simulated graph. First, we assign a work-function of S/D Al-contacts of 4.7 eV keeping the DOS parameters unchanged relative to previous simulation. Figure 5 a) shows the simulated output graph with a wok-function S/D Al-contact of 4.7 eV. As can we notice, a Schottky contact is achieved in the output curves and then fitting better both graphs in lows values of V_{DS}. However, by increasing the work-function has decreased the maximum drain current to 64 μA in comparison to 81 μA got in previous simulation with a work-function of 4.2 eV. The above is due to the fact that simulation has been realized unaffected the DOS, therefore is necessary to carry out simulation varying DOS and observe how this affect the transfer and output graphs. If we observe the initial DOS parameters (Table 1) we can see that conduction band tail slope (W_{TA}) value (0.1 eV) is well above of 0.011 eV and 0.012 eV reported in [18] and [17] respectively. Then simulations were performed varying W_{TA} parameter until the simulation graphs had a better fit. Figure 5b) shows both output curves where can be seen that I_D has increased near of value of I_D achieved experimentally. To understand the physical origin of this increase we have plotted contour graph of electron concentration (**n**), in saturation region, when W_{TA} is 0.1 eV Figure 6a) and 0.020 eV, Figure 6c). We can notice in Figure 6c) that maximum **n** (3.6×10^{19} cm^{-3}) is slightly larger than the maximum **n** (3.1×10^{19} cm^{-3}) when W_{TA} is 0.1 eV (Figure 5a), however in the former the minimum **n** (1.5×10^{17} cm^{-3}) is almost an order of magnitude larger that when W_{TA} is 0.1 eV (3.4×10^{16} cm^{-3}). The above is due with a higher W_{TA} there are a larger tail acceptor-states therefore part of free electrons are trapped in these states and reducing I_D. Additionally, in Figures 6b) and d) we have plotted electron concentration and

Parameter	Values	Description
N_{TA}	1.0×10^{19} cm^{-3}eV^{-1}	Acceptor tail states density
N_{TD}	1.0×10^{18} cm^{-3}eV^{-1}	Donor tail states density
W_{TA}	0.1 eV	Slope energy of acceptor tail states
W_{TD}	0.02 eV	Slope energy of donor tail states
N_{GA}	1.5×10^{18} cm^{-3}eV^{-1}	Acceptor deep states density
N_{GD}	1.0×10^{17} cm^{-3}eV^{-1}	Donor deep states density
W_{GA}	0.14 eV	Slope energy of acceptor deep states
W_{GD}	0.07 eV	Slope energy of donor deep states
E_{GA}	1.5 eV	Peak energy of acceptor deep states
E_{GD}	2.8 eV	Peak energy of donor deep states
n_i (a-IGZO)	7×10^{11} cm^{-2}	Intrinsic carrier concentration in TFT channel
E_g (a-IGZO)	3.1 eV	Band gap
Permittivity (a-IGZO)	9	Dielectric constant
Nc	5×10^{18} cm^{-3}eV^{-1}	Density of states for conduction band
Nv	5×10^{21} cm^{-3}eV^{-1}	Density of states for Valence band
	8.9 cm^2/ V·s	Electron mobility
SRH	Activated	Shockley-Read-Hall recombination
UST	Activated	Universal Schottky Tunneling Model
TRAP. TUNNEL	Activated	Trapp-assisted Tunneling
TRAP. COULOMBIC	Activated	Poole-Frenkel barrier lowering for coulombic wells will used for traps
TAUN0	1×10^{-6}	SRH lifetimes for electrons
TAUP0	1×10^{-6}	SRH lifetimes for holes
D.TUNNEL	1×10^{-6}	Maximum tunneling distance used for the UST model
ME.TUNNEL	0.2	Electron effective mass used for the UST model

Table 1. Initial parameters used in ATLAS® for a-IGZO TFT simulation.
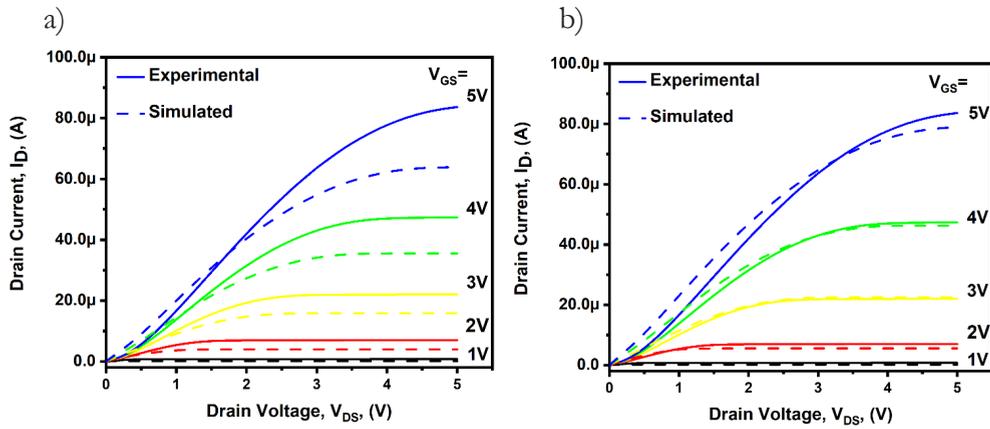
Figure 5. Output graphs with a workfunction of Source/Drain contacts of 4.7 eV and a) W_{TA}=0.1 eV and b) W_{TA}=0.020 eV.
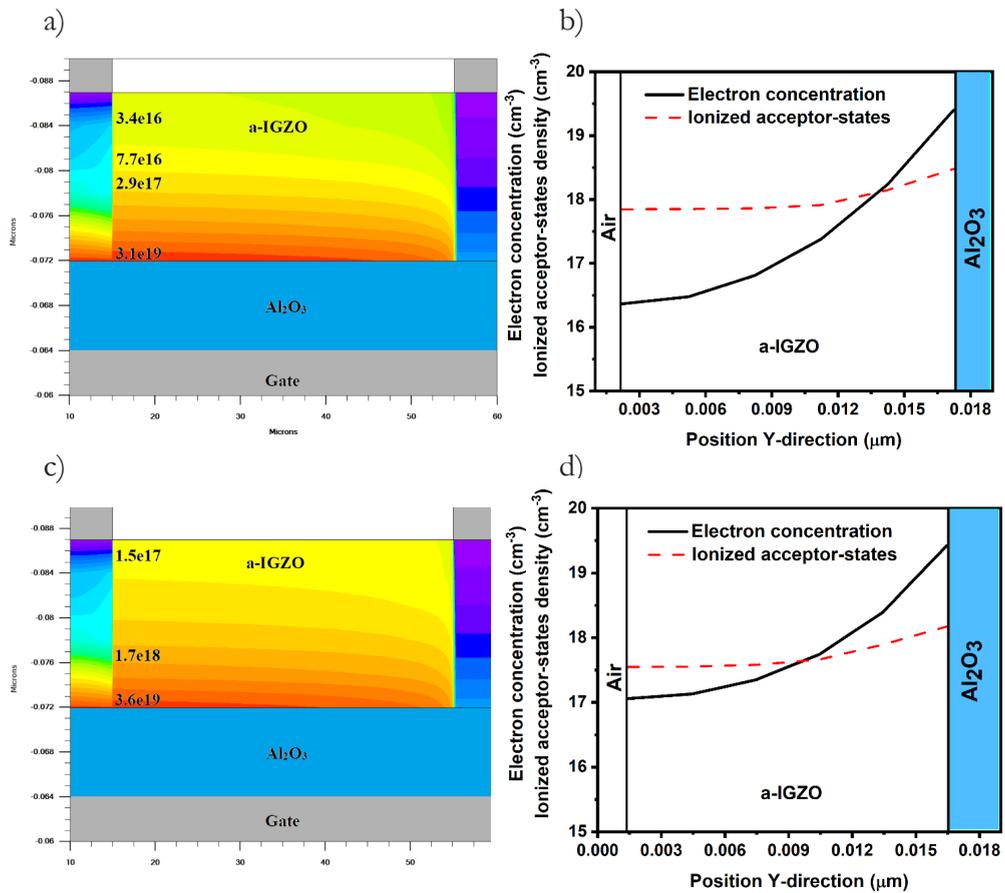

Figure 6. Contour graph of electron concentration for a) W_{TA}=0.1 eV and c) W_{TA}=20 meV; electron concentration and ionized acceptor-states density for b) W_{TA}=0.1 eV and b) W_{TA}=20 meV.

the ionized acceptor-states. We can observe in Figure 6b) that there are more ionized acceptor-states with respect of ionized acceptor-states in figure 6 d), as a consequence of a higher W_{TA} in former. The acceptor-states are ionized when are occupied with electrons, thus if more traps have been ionized, then the total electron concentration in a-IGZO channel is lower.

2.3. *Effect of Vacancies of Oxygen*

Figure 7a) shows the characteristic transfer curves in saturation region ($V_{DS}= 5V$) for different deep donor-states densities (N_{GD}) varying from $1x10^{16}$ cm^{-3} to $1x10^{18}$ cm^{-3} and fixing the Gaussian peak energy position in 2.8 eV in the bandgap, all other DOS parameter has been keeping constants during the simulations. As can be seen, an incresing of N_{GD} from $1x10^{16}$ cm^{-3} to $1x10^{18}$ cm^{-3} decreases the I_{ON}/I_{OFF} ratio ($5.2x10^7$) practically two orders of magnitude ($7.7x10^5$) by means increasing I_{OFF} current by the same amount and keeping the maximum I_{ON} current unaffected. Moreover, a subthreshold slope values of 65 meV and 185 meV for N_{GD} of $1x10^{16}$ and ax10^{18}, respectively, were extraided of simulations. In order to clarify the reduction of I_{ON}/I_{OFF} with increased of N_{GD}, we have plotted in figure 7 b) both the ionized donor states density (N^+_{GD}) and electron concentration in off condition of a-IGZO TFT (i.e. $V_{GS}= V_{DS}= 0V$). We can notice that N^+_{GD} for $N_{GD}= 1x10^{18}$ is higher than N^+_{GD} for $N_{GD}= 1x10^{16}$ practically for two orders of magnitude, thus the electron concentration has risen 10^{12} to 10^{14} cm^{-3}. As was
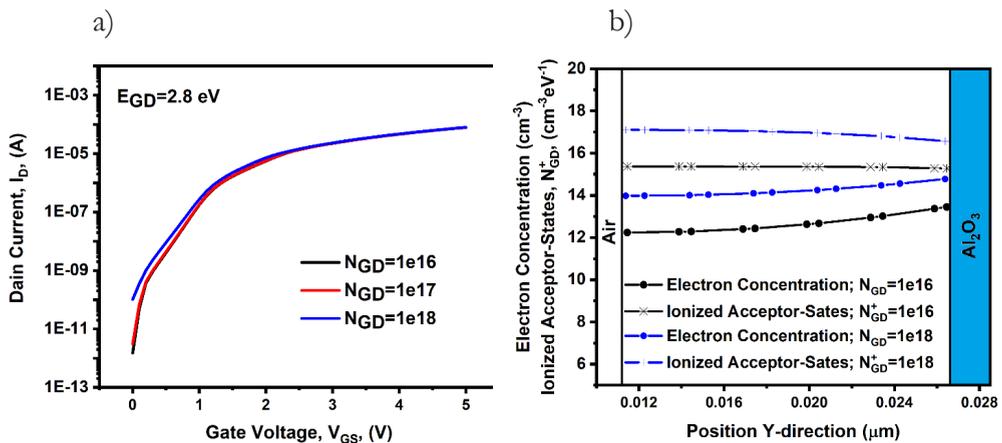
Figure 7. a) Transfer curve in saturation region for $N_{GD}=1x10^6$ to $1x10^{18}$ cm^{-3} keeping $E_{GD}=2.8$ eV near of conduction band; b) electron concentration and ionized acceptor states to $N_{GD}= 1x10^{16}$ and $1x10^{18}$ cm^{-3}eV^{-1}.

mentioned early, N_{GD} is related with oxygen vacancies which when ionized are empty and acting as electron donors, therefore lowering the I_{ON}/I_{OFF} ratio for a higher N_{GD}. The mechanism of increment of electron concentration, in off condition, related with vacancies of oxygen is called "auto-doping".

3. Conclusions

In this work, we have performed simulations of a-IGZO TFT based on the physical properties of different materials that comprise the TFT, such as the work function of the source and drain (S/D) contacts and the density of states through oxygen vacancies (OV) in a-IGZO. The results of our simulations show that when the work function of Al is considered, there is a reduction of drain current (less than an order of magnitude) and non-linear relation of ID vs VGS due Schottky contacts present in the S/D contacts. On the other hand, the oxygen vacancies are modeled by the density of deep-donors states (NGD) near the conduction band, the simulation shows that an excess of OV generates a large density of free electrons when the TFT is off, thus decreasing the I_{ON}/I_{OFF} ratio up two orders of magnitude when the TFT is in the saturation region. Finally, the simulation results show that the device does not present a good interface between the metal and the a-IGZO, which decreased the drain current.

References

1. Mativenga, M. (2021, December). Highly stable thin-film transistors for flexible and transparent displays. *2021 International Conference on Electrical, Computer, and Energy Technologies (ICECET)*, 1–6.
    https://doi.org/10.1109/ICECET52533.2021.9698710

2. Zhang, S., et al. (2024, January). Reduction of internal stress in InGaZnO (IGZO) thin-film transistors by ultra-thin metal oxide layer. *Materials Science in Semiconductor Processing*, 173, 108093.
    https://doi.org/10.1016/j.mssp.2023.108093

3. Lin, C., Fang, Y., Chang, W., Chiou, M., & Chen, C. (2014). Effect of gate barrier and channel buffer layer on electric properties and transparence of the a-IGZO thin-film transistor. *Microelectronics Reliability*, 54(5), 905–910.
    https://doi.org/10.1016/j.microrel.2014.01.015

4. Toledo, P., Hernandez, I. S., & Hernandez-Cuevas, F. (2023, July). Electrical instabilities of a-IGZO TFTs under different conditions of bias and illumination stress. *Microelectronics Reliability*, 148, 115186.
    https://doi.org/10.1016/j.microrel.2023.115186

5. Eadi, S. B., et al. (2022). Indium-gallium-zinc oxide (IGZO) thin-film gas sensors prepared via post-deposition high-pressure annealing for NO2 detection. *Sensors and Actuators B: Chemical*, 353(2), 131082.
    https://doi.org/10.1016/j.snb.2021.131082

6. Kim, J., et al. (2020, July). Effect of IGZO thin films fabricated by pulsed-DC and RF sputtering on TFT characteristics. *Materials Science in Semiconductor Processing*, 120, 105264.
    https://doi.org/10.1016/j.mssp.2020.105264

7. Du, X., & Herman, G. S. (2018). Transparent In-Ga-Zn-O field-effect glucose sensors fabricated directly on highly curved substrates. *Sensors and Actuators B: Chemical*, 268, 123–128.
    https://doi.org/10.1016/j.snb.2018.04.087

8. Kim, J. S., et al. (2017). Dynamic logic circuits using a-IGZO TFTs. *IEEE Transactions on Electron Devices*, 64(10), 4123–4130.
    https://doi.org/10.1109/TED.2017.2738665

9. Sahoo, A. K., & Wu, G. M. (2016). Effects of argon flow rate on electrical properties of amorphous indium gallium zinc oxide thin-film transistors. *Thin Solid Films*, 605, 129–135.
    https://doi.org/10.1016/j.tsf.2015.12.016

10. Xu, W., et al. (2018). Low-temperature solution-processed IGZO thin-film transistors. *Applied Surface Science*, 455, 554–560.
    https://doi.org/10.1016/j.apsusc.2018.06.005

11. Cho, M. H., et al. (2018). High-performance amorphous indium gallium zinc oxide thin-film transistors fabricated by atomic layer deposition. *IEEE Electron Device Letters*, 39(5), 688–691.
https://doi.org/10.1109/LED.2018.2812870

12. Chen, J., Wang, L., & Su, X. (2012). InGaZnO thin films grown by pulsed laser deposition. *Vacuum*, 86(9), 1313–1317.
https://doi.org/10.1016/j.vacuum.2011.12.001

13. Zhou, F., et al. (2012). Top-gate amorphous IGZO thin-film transistors with a SiO buffer layer inserted between active channel layer and gate insulator. *Current Applied Physics*, 12, 228–232.
https://doi.org/10.1016/j.cap.2011.06.006

14. Hernandez-Luna, I. S., Toledo, P., Hernandez-Cuevas, F., & Hernandez-Como, N. (2023). Reliability of flexible amorphous In-Ga-Zn-O (a-IGZO) thin-film transistors. *Research Advances in Nanosciences, Micro and Nanotechnologies*, IV, 249–262.

15. Kamiya, T., & Hosono, H. (2010, January). Material characteristics and applications of transparent amorphous oxide semiconductors. *NPG Asia Materials*, 2, 15–22.
https://doi.org/10.1038/asiamat.2010.5

16. Nomura, K., Takagi, A., Kamiya, T., Ohta, H., Hirano, M., & Hosono, H. (2006). Amorphous oxide semiconductors for high-performance flexible thin-film transistors. *Japanese Journal of Applied Physics, Part 1: Regular Papers, Short Notes and Review Papers*, 45(5B), 4303–4308.
https://doi.org/10.1143/JJAP.45.4303

17. Fung, T., Chuang, C., Chen, C., Abe, K., & Cottle, R. (2009, November). Two-dimensional numerical simulation of radio-frequency sputter amorphous In-Ga-Zn-O thin-film transistors. *Journal of Applied Physics*, 15.
https://doi.org/10.1063/1.3234400

18. Yu, E., Kim, T. O., & Kanicki, J. (2014). Density of states of amorphous In-Ga-Zn-O from electrical and optical characterization. *Journal of Applied Physics*, 116.
https://doi.org/10.1063/1.4898567

19. Kim, D. K., Park, J., Zhang, X., Park, J., & Bae, J. H. (2020). Numerical study of sub-gap density of states dependent electrical characteristics in amorphous In-Ga-Zn-O thin-film transistors. *Electronics*, 9(10), 1652.
https://doi.org/10.3390/electronics9101652

20. Silvaco International Inc. (2016). *Atlas User's Manual: Device Simulation Software*.

21. Kano, K. (1998). *Semiconductor Devices*. Prentice Hall.

NUMERICAL ANALYSIS OF PLASMONIC NANOHOLE DIAMETERS IN THIN GOLD FILMS

**Verónica Iraís Solís-Tinoco[1,3]*, Ana Elisa Pérez Tovar[2],
Hatzyri Ismerai Hernandez Mercado[2],
Berenice Montiel Pitalua[2], Karen Lyzeth Alonzo García[2],
Luis Alfonso Villa-Vargas[1], Marco Antonio Ramírez-Salinas[1],
Miguel Ángel Alemán-Arce[1]**

[1]Centro de Investigación en Computación del Instituto Politécnico Nacional, Laboratorio de Microtecnología y Sistemas Embebidos. Ciudad de México, 07738, México.

[2]Unidad Profesional Interdisciplinaria en Ingeniería y Tecnologías Avanzadas UPIITA-IPN. Ingeniería Biónica. Ciudad de México, C.P. 07340, México.

[3]Instituto de Ciencias Aplicadas y Tecnología, Universidad Nacional Autónoma de México, Ciudad de México, 04510, México.

*irais.solis@cic.ipn.mx

Abstract

We present a numerical analysis of the optical properties of a gold nanohole with diameters ranging from 90 nm to 130 nm to examine the behavior of the LSPR phenomenon. We utilized COMSOL Multiphysics software to calculate the changes in optical transmittance, absorbance, and reflectance over a wavelength range from 400 nm to 900 nm. The calculated transmittance curves for diameters of 90 nm, 100 nm, 110 nm, 120 nm and 130 nm show that the LSPR initial position shifts from 675 nm to 690 nm. A similar behaviour was observed in the absorbance and reflectance spectra. The maximum absorbance ranges from 686 nm to 710 nm while the reflectance maximum shifts from 659 nm to 673 nm. The results suggest that these diameters are suitable for generating the LSPR phenomenon; however, the 100 nm diameter showed the highest electromagnetic field value of 9.28×10^8 V/m. Additionally, an optical transducer based on gold nanoholes with a diameter of 100 nm is feasible to fabricate using low-cost techniques like colloidal lithography. Therefore, this work provides a tool for students and researchers to design optical transductors based on nanostructures, leveraging the potential offered by numeric simulations.

Keywords: numerical simulation, gold nanohole, plasmonics, diameters.

1. Introduction

The fascination with the optical properties of metal nanostructures arises from their distinctive phenomenon called localized surface plasmon resonance (LSPR). This phenomenon is caused by collective oscillations of electron gas on the surface of metal nanostructures, particularly noble metals like gold and silver. These oscillations take place within a surrounding dielectric medium. LSPR is characterized by distinct spectral peaks in optical absorption, transmittance, and reflectance, as well as strong enhancements in the electromagnetic field, which occur at specific wavelengths [1, 2]. The position of these peaks is highly sensitive to changes in the refractive index of the surrounding dielectric medium. Therefore, any molecules adsorbed at the nanoparticle surface induce a modification of the local refractive index consequently causing a shift of the LSPR position [3], which forms the basis for detecting analytes using LSPR sensors [4 - 6].

Researchers have proposed that LSPR sensing techniques utilizing nanoparticle or nanostructures substrates could retain the advantages of traditional SPR methods while significantly expanding their scientific and technological applicability. This is because LSPR sensing fundamentally relies on straightforward optical extinction measurements, exhibits minimal temperature sensitivity, and can be implemented using widely available, standard laboratory equipment. Thereby, nanoparticle based LSPR sensing could open challenging application avenues across diverse fields [7, 8]. For example, LSPR sensors have been applied to detect bladder cancer [9]; determining chemicals in urine such as creatinine, albumin and glucose, three of the most abundant components in urine [10]; and detecting cardiovascular disease [11]; among many others.

LSPR sensor sensitivity can be influenced by nanostructure size, shape, aspect ratio, spacing, and material dielectric constant. In this way, optimizing the nanostructure geometry is critical to maximize sensitivity and the limit of detection (LOD) and take full advantage of the material's properties. For instance, while spherical gold nanostructures have advantages in terms of chemistry and fabrication, other shapes such as stars, pyramids, tips, and rods may be more sensitive to changes in the refractive index [12 - 21]. Among the nanostructures, metallic nanoholes are very attractive due to their extraordinary optical transmission that produces LSPR. Hence, nanoholes have been

employed in diverse application areas such as sensing. Those have been used for the direct optical probing of proteins, viruses, bacteria, and even cancer cells [22 - 25].

Consequently, the research and fabrication of noble metal nanostructures as optical transducers have gained importance for the development of LSPR sensor technology, therefore, we can discover a multitude of techniques for their creation [26 -29]. However, selecting each transducer parameter based on nanoholes is challenging, and an error could result in significant time and material losses.

Numerical simulations have emerged as a potent tool for researching and designing plasmonic transducers allowing the study of optical parameters in a virtual environment, reducing the need to manufacture them. Also, they facilitate testing a multitude of design parameters for optical transducers, including geometry, dimensions, materials, light excitation sources, and dielectric mediums. This enables the evaluation of their impact on the transducer's optical properties, facilitating informed decision-making for future manufacturing projects.

The ability to use the software and all its functionalities may require time for users to learn because of the extended list of attributes involved in numerical simulations and its properties. Also, obtaining useful information to guide the step-by-step design of an optical transducer in such detailed way is a challenging task. In this work, we describe the design of a plasmonic transducer based on gold nanoholes. A single gold nanohole is simulated using COMSOL Multiphysics 6.1, exploring different diameters ranging from 90 nm to 130 nm within a 300 nm by 300 nm area on a glass substrate.

The nanohole is excited by a white light source reaching wavelengths from 400 nm to 900 nm, with air as the dielectric medium. We start by performing a numerical analysis to evaluate the impact of nanohole diameter on significant optical properties such as transmittance, reflectance and absorbance, and determine the wavelength of the LSPR, as well as the distribution of the electromagnetic field. The objective of this numerical analysis is to illustrate how variations in nanohole size affect optical properties, including the position of the LSPR and the distribution of the electric field, understanding these factors is determining for designing effective plasmonic transducers and developing advanced optical sensors.

2. Methodology

This section outlines the methodology employed to design and execute a simulation aimed at analyzing the behavior and response of a plasmonic nanohole with different diameters. The structural configuration consists of a glass substrate supporting a 20 nm gold film with a singular nanohole, and air serving as the dielectric medium. The system is stimulated by an electromagnetic field with a wavelength ranging from 400 nm to 900 nm. This simulation's main objective is to investigate the impact of nanohole diameter on its optical properties. To achieve this, the diameters at values of 90 nm, 100 nm, 110 nm, 120 nm, and 130 nm were varied.

To generate this simulation, COMSOL Multiphysics software 6.1, which enables the customization of simulation parameters, including physics modules, system geometry, boundaries, materials, and other physical parameters, was used. Additionally, with this software, graphical representations of three optical properties, absorbance, transmittance, and reflectance over the wavelength range were obtained. Furthermore, COMSOL enables to visualize the electric field behavior around the gold nanohole. These graphs and animation provide valuable information about the nanohole's optical behavior. This section details each phase of the methodology to generate this 3D simulation, including simulation set-up, parameter variation, and analysis techniques. This is shown in Figure 1.
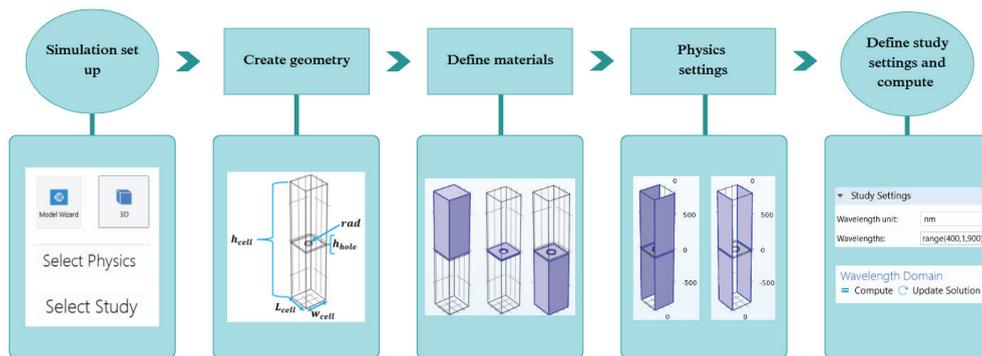
Figure 1. Phases of the methodology to generate the 3D simulation for the analysis of the behavior and response of a nanohole with different diameters, including simulation set-up, parameter variation and analysis techniques.

2.1. *COMSOL Simulation Settings*

First, the simulation in COMSOL Multiphysics was set up, as summarized in Table 1. The first step was to create a new model with Model Wizard, and then the modeling space was established as three-dimensional (3D). Next, the electromagnetic waves, Frequency domain (ewfd) interface was selected in the Physics window, allowing the simulation of the electromagnetic source across a range of frequencies and its interaction with the plasmonic nanohole structure. Finally, on the Study selection page, the wavelength domain was chosen to compute the structure's optical properties versus wavelength and the propagation of electromagnetic waves through it.

Settings	Details
Space dimension	3D
Physics	Electromagnetic waves, Frequency domain (ewfd)
Study	Wavelength domain

Table 1. COMSOL simulation settings for the gold nanohole.

2.2. *Nanohole geometry*

Figure 2a illustrates the cell design and the parameters required to design the gold nanohole in COMSOL Multiphysics. To start building the nanohole geometry, the width, length and height of each structure (glass, gold and air) were defined: **wcell** for the cell width, **Lcell** for the cell length, **hcell** for the cell height, **hhole** for the height of the gold nanofilm, and **rad** for the nanohole radius, as shown in Figure 2b.
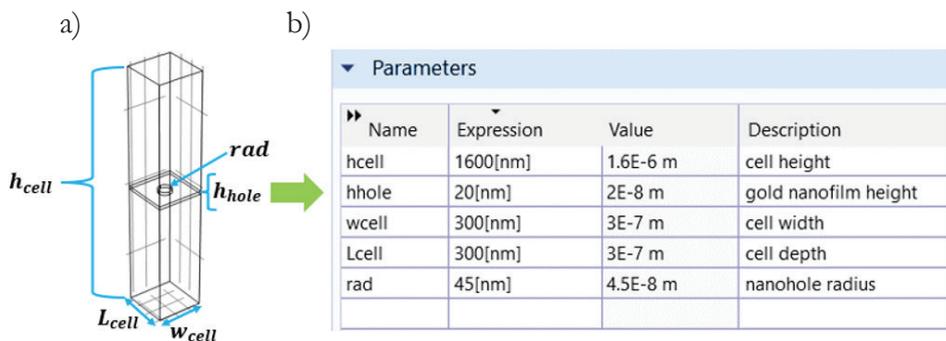
Figure 2. Parameters to design the gold nanohole. (a) Represents the nanohole geometry and the parameters of each section. (b) Parameters used to design nanohole geometry.

COMSOL Multiphysics offers predetermined primitive structures. To create the cell, the block option from the top menu twice was selected, resulting in two blocks: one for the whole structure, designated as block1, as shown in Figure 3a, and the second one for the thin 20 nm gold film, designated as block 2, illustrated in Figure 3b. Then, we select the cylinder option to create the nanohole inside the gold film, as shown in Figure 3c. The following Table 2 summarizes the parameters (width, length, height, base) to configure each structure. While all the measures remain constant, the diameter value ranges from 90 to 130 nm.

Size and shape	Block 1	Block 2	**Cilinder**	
Width	Wcell	wcell	Radius	rad
Depth	Lcell	Lcell	Height	hhole
Height	Hcell	hhole	Position	Z -10
Base	Center	Center		

Table 2. Parameters to create each section of nanohole geometry.
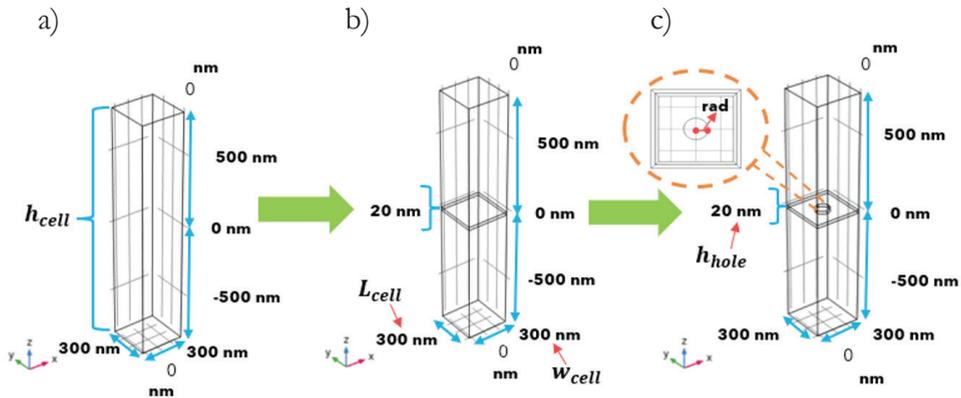
Figure 3. Steps and parameters for each section. (a). First step to start building the geometry and the parameters for the first block corresponding to the entire cell. (b) Second step, where the second block, the gold film, and its parameters are added. (c) Third step, where the cylinder and its measures are added to create the nanohole's geometry, notice that in this step the diameter varies from 90 to 130 nm.

2.3. *Gold nanohole materials*

The COMSOL Multiphysics material selection allowed to define the electromagnetic properties of the materials present in the model. By selecting and setting these properties for the dielectric medium, it was possible to model optical properties, such as transmittance, reflectance, and absorbance of

electromagnetic waves in different types of materials. To observe the behavior of the electric field as it passed through the gold cell and propagates through a dielectric medium, materials for each domain in the geometry had to be selected. First, air was chosen for the top domain of the geometry and the cylinder domain (Figure 4a). Air has a refractive index of n =1 and is already established by the software.

The second material selected for the simulation was gold, a noble metal that exhibits unique electronic and plasmonic properties including LSPR. Gold is biocompatible, making it suitable for biological applications. Gold was assigned to the second domain representing the thin gold film between the dielectric medium (air) and the glass substrate (see Figure 4b). The material Johnson and Christy 1972: n.k 0.188-1.937 μm was chosen because its refractive index is predefined by COMSOL. The plasmonic resonance of gold nanoparticles is influenced by their size, shape, and surrounding environment, therefore control over these characteristics determines the optical properties of gold nanoholes. Changes in the refractive index of the surrounding medium can significantly impact the optical properties of gold nanoholes. Finally, the bottom layer in the geometry (as shown in Figure 4c) represents the glass substrate, which can be composed of either Corning® Eagle XG® Glass or Corning® Gorilla® Glass Victus®. These materials are pre-defined in COMSOL with a refractive index of n = 1.5. Table 3 shows the materials with their refractive indices.
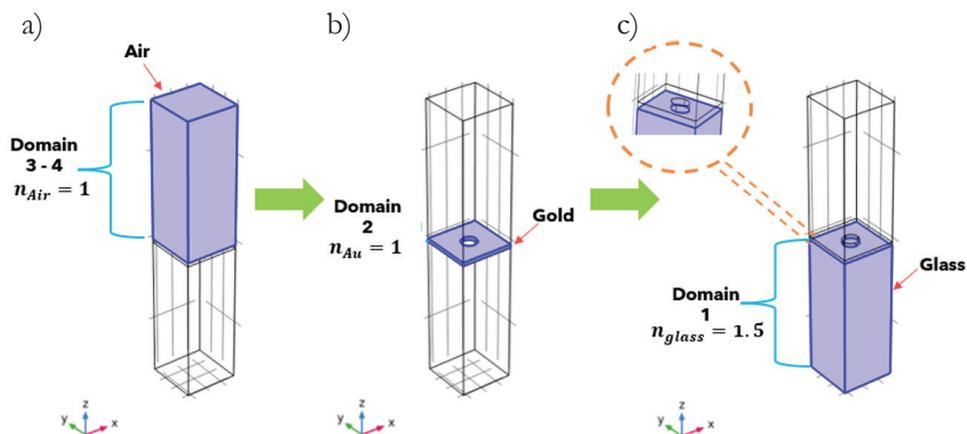
Figure 4. Structure's geometry sections. (a) The upper section (highlighted in blue) constitutes domains 3 and 4; this section represents air in the model with refractive index of *n = 1*.
(b) Domain 2 represents the gold nanofilm in the model with a refractive index defined by COMSOL. (c) The bottom section of the geometry, designated as Domain 1, is made of glass with refractive index of *n* = 1.5.

Material	Type	Extra settings
Air	Built in → Air	Refractive Index: Real part: 1 Imaginary part: 0
Gold	Au (Gold) (Johnson and Christy 1972: n,k 0.188-1.937 µm).	Refractive Index: Real part: n Imaginary part: k Predefined in COMSOL
Glass	Corning ® Eagle XG ® Glass. Or Corning® Gorilla® Glass Victus®.	Refractive Index: Real part: 1.5 Imaginary part: 0

Table 3. Material specifications of gold nanohole dielectric media.

2.4. *Physics configuration*

For this work, the Electromagnetic Waves, Frequency Domain (*ewfd*) physics interface was used in COMSOL Multiphysics to model and simulate the behavior of an electromagnetic field across a range of wavelengths interacting with the gold nanohole. This section includes defining boundary conditions, setting up the source properties and establishing the mesh definition.

2.4.1. *Ports*

To start the physics configuration, Ports were set up to define the regions where the electromagnetic field enters and exits the model domain, as well as indicate the direction and amplitude of the electromagnetic field. In this model, the bottom face of the block labeled as Boundary 3 in COMSOL, was designated as the entry point (Figure 5a), thereby wave excitation was activated here, as specified in Table 4. The top face, labeled boundary 10 in COMSOL, was designated as the exit point for the transmitted light (Figure 5b) and the wave excitation option is turned off. The objective of this set up was to compute the amount of light absorbed, reflected, and transmitted through the nanohole at certain wavelengths.

Port	Type	Wave excitation	Input Quantity	Electric mode field amplitude	Refractive index, real part
Port 1	Periodic	On	Electric field	x → 1 y → 0 z → 0	1.5
Port 2	Periodic	Off	Electric field	x → 1 y → 0 z → 0	1

Table 4. Port properties set up.
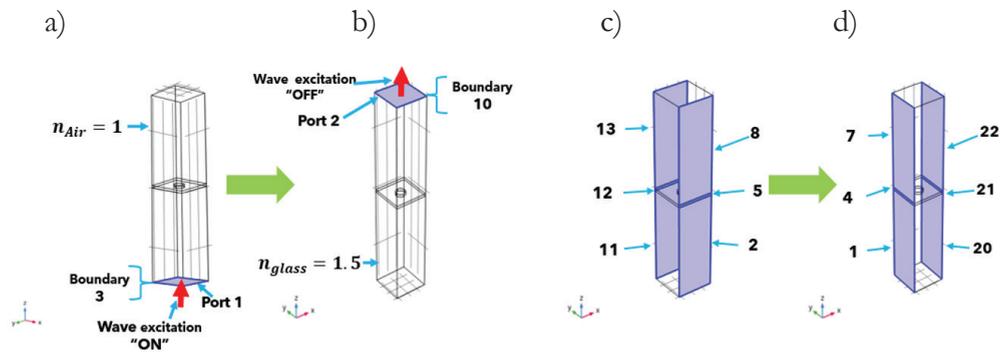
Figure 5. Physics configuration for the model. (a) Configuration of Port 1 (Boundary 3, bottom face), which serves as the Light source entry point. (b) Configuration for Port 3 (top face, boundary 10). (c) Boundary selection for periodic conditions 1. (d) Boundary selection for periodic conditions 2.

2.4.2. *Periodic Conditions*

Periodic conditions were applied to confine the flow of the electromagnetic field within the model geometry and prevent energy leakage. In this simulation, which features a 4-sided block geometry, periodic boundary conditions are applied to two pairs of parallel sides, the selection process is illustrated in Figure 5c-d, which highlights the necessary parallel selection for the simulation. To avoid leakage during the simulation, all regions from each side must be selected.

2.5. *Mesh*

The mesh divides the computational domain into smaller elements, allowing for the discretization of equations governing the model, for this study COMSOL Multiphysics uses FEM equations to solve for the electromagnetic fields within the gold nanohole and its surrounding medium.

In this simulation, the mesh is automatically generated by COMSOL Multiphysics, breaking down the domain into manageable units and maintain computational efficiency. The mesh coverage is shown in Figure 6a.

a)   b)
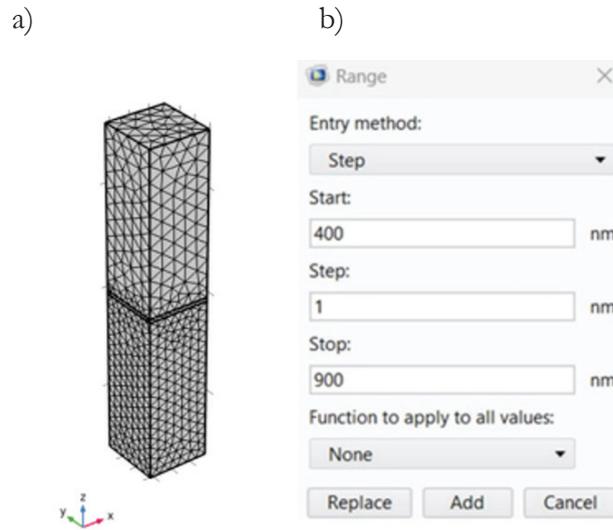
Figure 6. Mesh and wavelength. (a) Mesh selected determines the number of points examined, and the time the software will take to perform the calculations, thereby with a fine mesh, the computing time will take longer. (b) Wavelength range of interest for studying the optical properties of the gold nanohole. Note: The Step can be increased to minimize the time of computing, but the information will not be the same and the statistical values may be slightly different from each other.

2.6. *Study configuration*

The Study section in COMSOL is where the studies to be performed on the model were defined and configured, allowing to determine what type of analysis were carried out. In this simulation, the study section allowed the analysis of plasmonic gold nanohole behavior as a function of frequency to obtain optical properties (transmittance, reflectance, absorption), electromagnetic fields, and COMSOL solves the point-to-point mesh equations.

After setting up the physical characteristics of the system and establishing the geometry, the next step was to analyze the behavior of the electric field through the gold nanohole. This study was done by varying the wavelength of the electric field across a range from 400 nm to 900 nm in increments of 1 nm (Figure 6b). This wavelength range has been specifically selected because it corresponds to the excitation of the plasmon. The main objective of this study is to generate a

light transmittance spectrum across the entire cell, which provides information about the wavelengths that most excite the plasmon in the simulation.

2.7. *Data extraction and export*

The Results section in COMSOL provided an important tool for analyzing and understanding of the simulations performed by visualizing the data, generating graphs, and extracting important information about the behavior of the simulated system, including the electric field and optical properties. Once the simulation was completed, the behavior of each cell, as the plasmonic nanohole diameter was varied, can be easily analyzed by examining the optical properties and electric field. To visualize the electric field in COMSOL (Figure 7a), the "Volume" option in the Electric Field section was selected and the expression "ewfd.Ex" was entered, since it propagates in the x-direction through the cell. The Plot button on the Electric Field (ewfd) toolbar was selected to generate the appropriate visualization. Figure 7c shows graphs of transmission, reflection, and absorption properties. These properties are displayed in Reflectance, Transmittance, and Absorbance (ewfd) 1. To obtain each property, the above plot was duplicated, and the property of interest was selected in the Y-Axis Data Configuration window. The options for exporting the data obtained are shown in Figure 7b.

a)

b)

c)
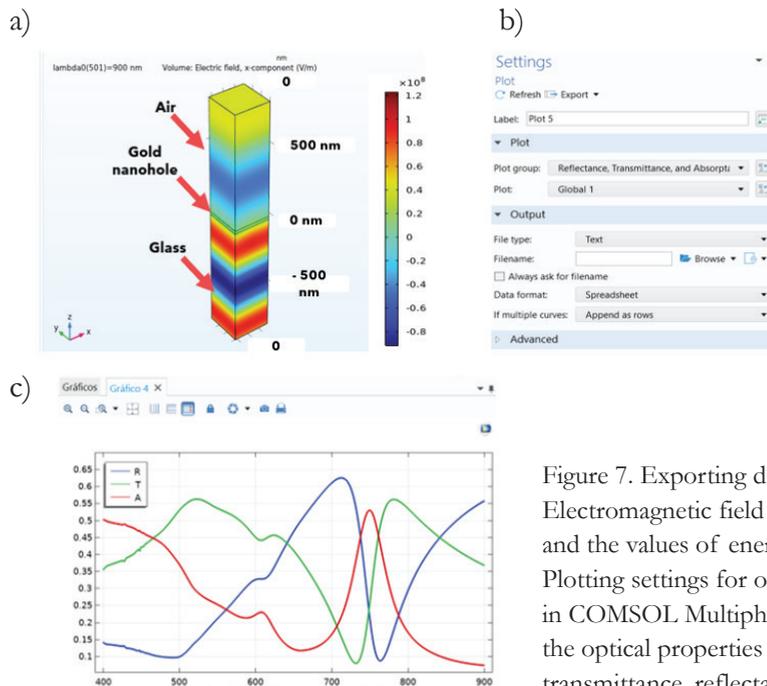
Figure 7. Exporting data. (a) Electromagnetic field of the gold nanohole and the values of energy at the scale. (b) Plotting settings for obtaining graph results in COMSOL Multiphysics. (c) Graphs of the optical properties of interest, such as transmittance, reflectance, and absorbance.

3. Results and Discussion

This section entails a numerical analysis comprising five simulations of a gold nanohole, each with varying diameters: 90 nm, 100 nm, 110 nm, 120 nm, and 130 nm. Within each simulation, the optical properties alongside the electric field in the x-direction for the nanohole to analyze the behavior of the cell when increasing the diameter of the nanohole were examined.

3.1. *Optical properties: 90 nm diameter nanohole*

The initial diameter under examination is 90 nm for the nanohole. Figure 8 illustrates three optical properties representing the behavior of light through the cell, using the parameters established in the preceding section. These properties are correlated, and the simulation's accuracy can be confirmed by scrutinizing a specific wavelength on the graph. Summing all properties at their intersecting points along a vertical line in a point of interest should yield 1.0. In Figure 8, the arbitrary unit (a.u.) for each property is evident. For example, the transmittance value at 675 nm that wavelength measures 0.13985 a. u., reflectance stands at 0.4197 a. u., and absorbance records at 0.44045 a. u. When these properties are combined, they sum to 1.0 a. u., affirming that all incident light interacts with the cell and that there is no light leakage in the cell's configuration. The 675 nm wavelength value was selected because it represents the lowest point in transmittance, where the LSPR is manifested. However, any wavelength can be chosen, since the sum of all properties is equal 1 a. u.
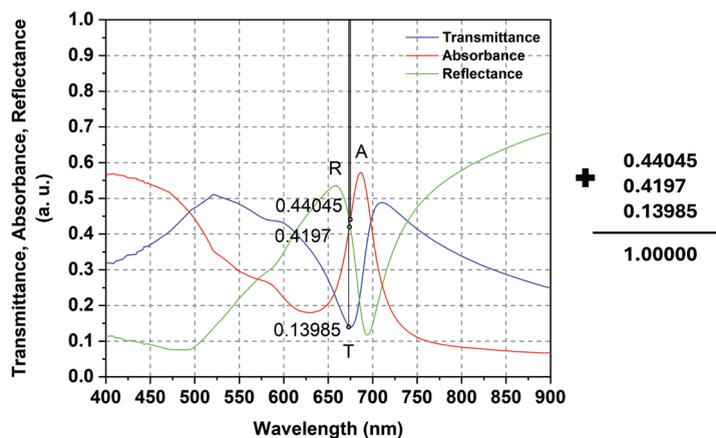
Figure 8. Correlation between the optical properties at one specific wavelength and its sum which equals 1 a.u. to prove the settings simulation by having all the energy interaction in the geometry.

Each property provides information about different behavior in geometry, each of them is useful for different applications. The transmittance (Figure 9a) gives information of the amount of light that arrives to the detector (output) for every wavelength in a range of 400 nm to 900 nm, this interaction is represented by the blue curve, the point of interest in this curve is the lowest point in the graph seeing that it is the value where the light is interacting all over the cell and a plasmon dipole is created by having oscillations with gold electrons and interactions with each other. This phenomenon can only be created with very stable noble metals like gold, due to its plasmonic properties. It is important to note that every design alters the LSPR wavelength. Changes in characteristics such as size, composition, and geometry in the simulation could provoke different LSPR responses. In this case, the plasmon dipole is created at the wavelength of 675 nm and generates an electric field in x direction with a value of 8.033×10^8 V/m (see Table 6 for the maximum values of energy at each point of interest) [30, 31]. This can be observed in Figure 9b-c. The Figure 9b is the top view of the nanohole and the dipole can be seen on the gold film, while in the side view, Figure 9c, it is seen the interaction of the light all over de geometry and it is observed how the dipole is created only in the surface of the nanohole by having gold electron oscillations. With the sidebar color, it is evident that interactions primarily occur within the noble metal, resulting in the highest electric field value (red color) concentrated around the nanohole.
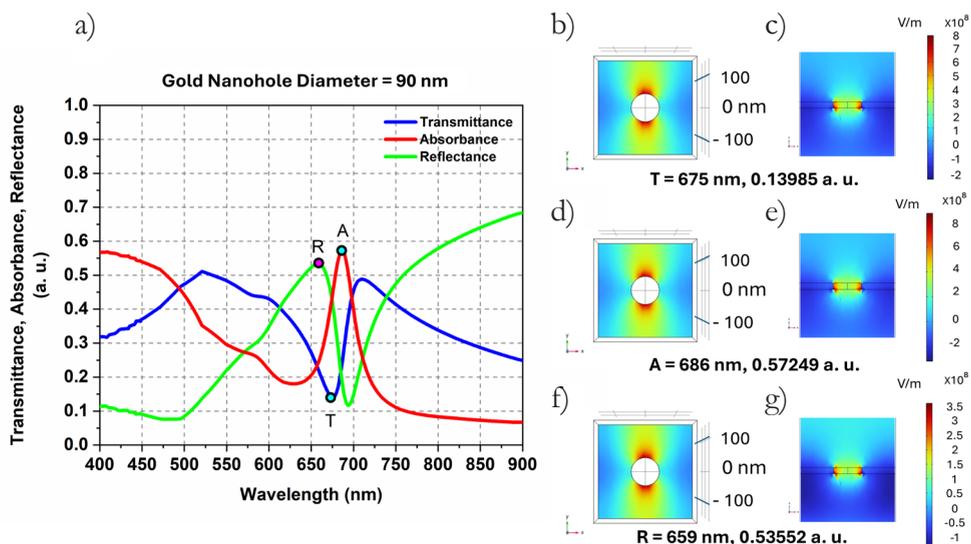
Figure 9. (a) Transmittance, absorbance, and reflectance curves for the 90 nm diameter gold nanohole and its wavelengths at which the plasmon originates for each property. (b), (d), (f) Top view of the gold film at those points of interest for transmittance, absorbance, and reflectance, and (e), (f), (g) side view of plasmon interaction with air (top), gold (center), and glass (bottom) at those same points.

The absorbance (Figure 9d-e) gives information of the amount of light that is absorbed by the gold. In this case, the red curve exhibits the light interaction over the cell for every wavelength with a range of 400 nm to 900 nm where the point of interest is the highest point where the energy is interacting with the nanohole in a wavelength of 686 nm and creating an Ex of $8.65x10^8$ V/m.

For the reflectance (Figure 9f-g), this property gives information of the amount of light that returns to the light source when it is interacting over the cell, this interaction is represented by the green curve and the point of interest is the highest point of the curve because it is the greatest amount of light that returns to the light source at the wavelength of 659 nm. At this wavelength the plasmon interaction has an Ex of $3.63x10^8$ V/m, in this value the plasmon dipole is generated. Thus, it was shown that LSPR is present at the point of interest of each property.

3.2. *Optical properties: 100 nm diameter nanohole*

For the 100 nm nanohole and the subsequent ones (110 nm, 120 nm, and 130 nm) the image distribution is the same as indicated for the 90 nm nanohole. Figure 10a shows a graph with three different curves with the following colors: blue for transmittance (T), red for absorbance (A) and green for reflectance (R). In every curve there is a highlighted point for T, A, R, respectively, that indicates where the plasmon dipole is created. Then, Figure 10b, Figure 10d, and Figure 10f show the top view of the nanohole at that specific wavelength and Figure 10c, Figure 10e, and Figure 10g the side view of the entire geometry and how the light interacts with the different cell materials (air at the top, gold at the center and glass at the bottom).

In this case, for the T point, the minimum value of the curve indicates that the plasmon originates at a wavelength of 684 nm and has a maximum energy value of $9.28x10^8$ V/m. The A point, the maximum value of the curve, originates at a wavelength of 697 nm and has a maximum energy value of $6.48x10^8$ V/m, and finally the R point, the maximum of the curve, originates at a wavelength of 663 nm and has a maximum energy value of $4.03x10^8$ V/m. Notice that the wavelength at which the plasmon originates, has shifted to the right compared to the 90 nm diameter nanohole: 9 nm for T, 11 nm for A, and 4 nm for R. Since the accuracy of the simulation was established, the verification process with the vertical line in the three optical properties for this diameter or subsequent one was done. This step was previously demonstrated and confirmed in Figure 8, affirming the validity of the results obtained.
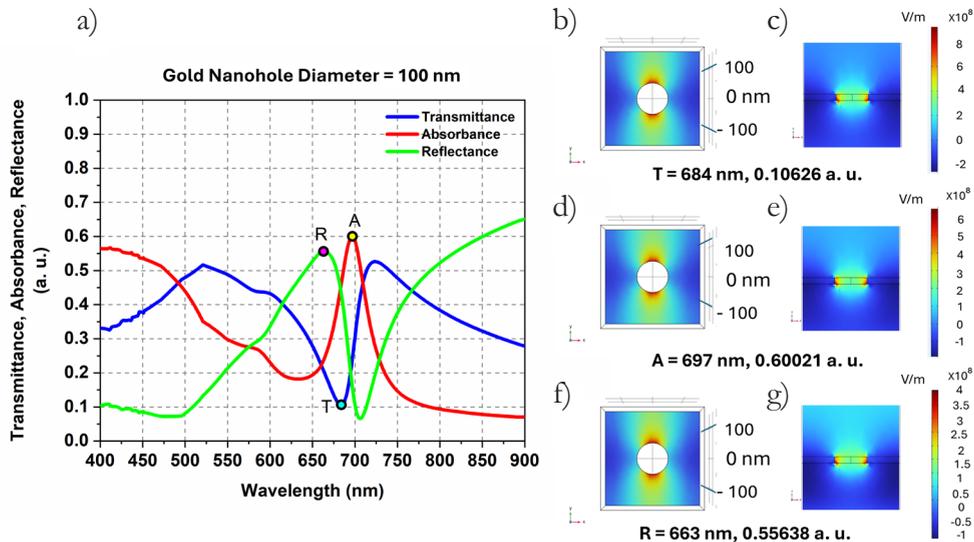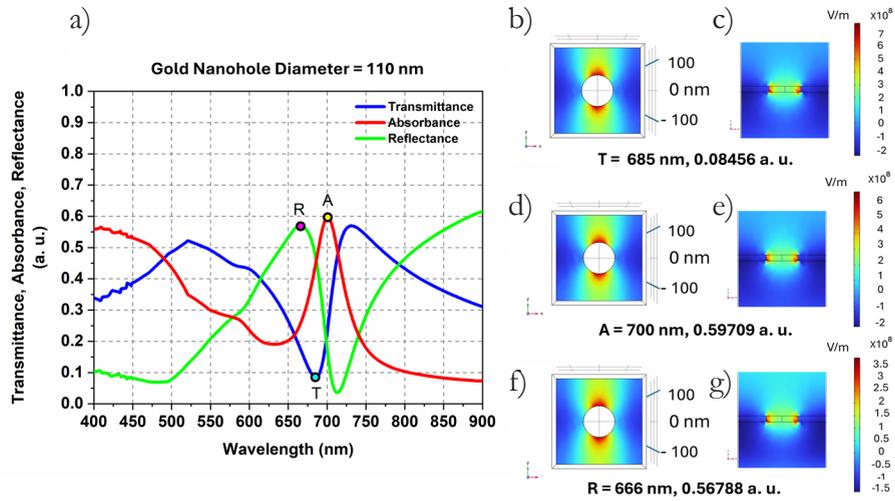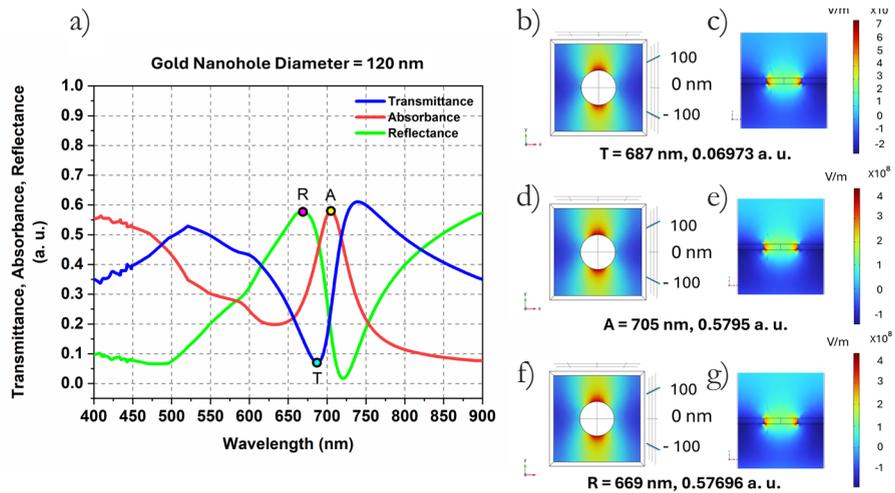
Figure 10. (a) Transmittance, absorbance, and reflectance curves for the 100 nm diameter gold nanohole and its wavelengths at which the plasmon originates for each property. (b), (d), (f) Top view of the gold film at those points of interest for transmittance, absorbance, and reflectance, and (e), (f), (g) side view of plasmon interaction with air (top), gold (center), and glass (bottom) at those same points.

3.3. *Optical properties: 110 nm diameter nanohole*

With the 110 nm diameter nanohole (Figure 11) for the T point the plasmon originates at a wavelength of 685 nm, has a maximum energy value of 7.8×10^8 V/m. For the A point originates at a wavelength of 700 nm and has a maximum energy value of 6.65×10^8 V/m, and for the R point originates at a wavelength of 666 nm and has a maximum energy value of 3.81×10^8 V/m. Focus on the displacement of the wavelength where the plasmon originates, which has been shifted to the right compared to the 100 nm diameter nanohole: 1 nm for T, 3 nm for A, and 3 nm for R. However, this time the shifts have not been as significant as with the previous one.

In this scenario, we note a decrease in the values of the electric field for transmittance (T), which contrasts with the observed increase from a diameter of 90 nm to 100 nm. This observation prompts a more detailed analysis of the electric field values for subsequent diameters to pinpoint where the highest electric field energy is concentrated. Such insight can guide in identifying the most optimal diameters for transducer nanofabrication.

Figure 11. (a) Transmittance, absorbance, and reflectance curves for the 110 nm diameter gold nanohole and its wavelengths at which the plasmon originates for each property. (b), (d), (f) Top view of the gold film at those points of interest for transmittance, absorbance, and reflectance, and (e), (f), (g) side view of plasmon interaction with air (top), gold (center), and glass (bottom) at those same points.

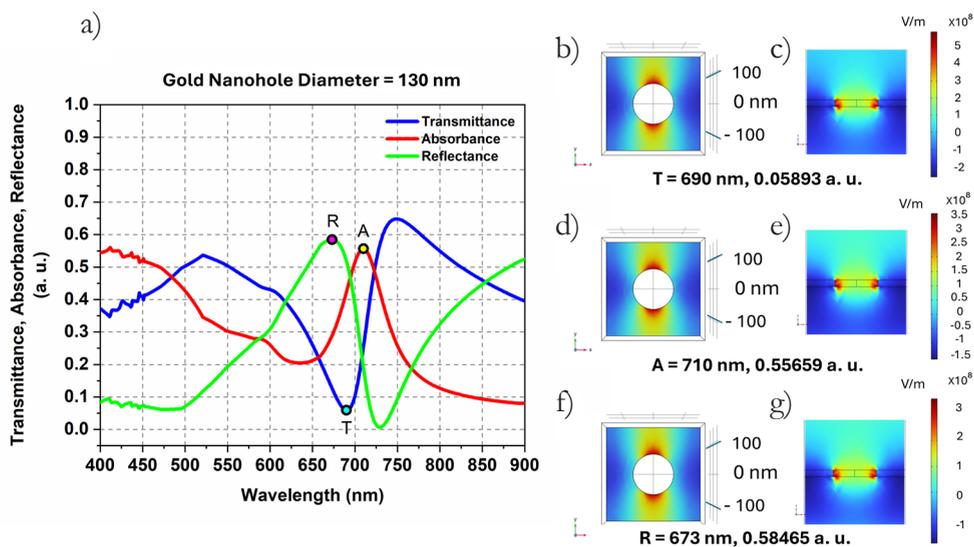## 3.4. *Optical properties: 120 nm diameter nanohole*

Figure 12. (a) Transmittance, absorbance, and reflectance curves for the 120 nm diameter gold nanohole and its wavelengths at which the plasmon originates for each property. (b), (d), (f) Top view of the gold film at those points of interest for transmittance, absorbance, and reflectance, and (e), (f), (g) side view of plasmon interaction with air (top), gold (center), and glass (bottom) at those same points.

Subsequently, we increment the diameter by 10 units to 120 nm (Figure 12) and observe the peak energy values: for the T point, originating at a wavelength of 687 nm, the electric field strength reaches 7.42×10^8 V/m; for the A point, originating at a wavelength of 705 nm, it measures 4.28×10^8 V/m, and for the R point, originating at a wavelength of 669 nm, it registers at 4.36×10^8 V/m. Notably, the wavelength of plasmon excitation shifts further rightward: by 2 units for T, 5 units for A, and 2 units for R. Remarkably, energy levels decrease at every point except for point R, where an increase is observed.

3.5. *Optical properties: 130 nm diameter nanohole*

Finally, for the 130 nm diameter hole (Figure 13), we get the maximum energy values: for the T point at a wavelength of 690, with 5.88×10^8 V/m; for the A point originated at a wavelength of 710 nm, with 3.52×10^8 V/m, and for the R point originated at a wavelength of 673 nm, with 3.6×10^8 V/m. The wavelength at which the plasmon originated keeps on moving to the right: 3 units for T, 5 units for A, and 4 units for R. The energy has decreased at every point without exceptions.

Figure 13. (a) Transmittance, absorbance, and reflectance curves for the 130 nm diameter gold nanohole and its wavelengths at which the plasmon originates for each property. (b), (d), (f) Top view of the gold film at those points of interest for transmittance, absorbance, and reflectance, and (e), (f), (g) side view of plasmon interaction with air (top), gold (center), and glass (bottom) at those same points.

The optical properties analysis reveals a notable wavelength displacement as the nanohole diameter increases. This displacement is observed in the transmittance (Figure 14a-b), absorbance (Figure 14c-d), and reflectance spectra (Figure 14e-f). Notably, altering the cell geometry by enlarging the diameter while reducing the gold area induces a rightward shift in the curves.
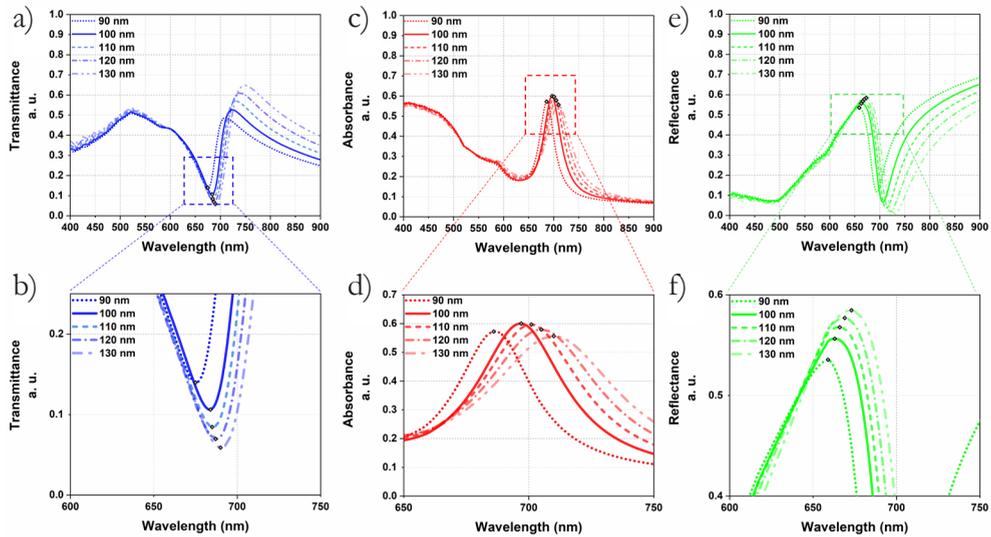

Figure 14. (a) Transmittance, (b) Absorbance and (c) Reflectance graphs for different gold nanohole diameters: 90 nm, 100 nm, 110 nm, 120 nm, and 130 nm.

For instance, with a 90 nm diameter, the transmittance curve initiates at a wavelength of 675 nm and terminates at 690 nm for the 130 nm diameter, resulting in a 15 nm rightward displacement. Similarly, the absorbance curve commences at 686 nm for the 90 nm diameter and extends to 710 nm for the 130 nm diameter, producing a 24 nm shift to the right. Reflectance, beginning at 659 nm and concluding at 673 nm, generates a 14 nm displacement. These findings highlight the influence of geometry alterations on optical properties, primarily attributed to increased diameter and reduced gold area. Notably, despite these changes, each proposed diameter retains the ability to induce Localized Surface Plasmon Resonance (LSPR), as evidenced by the consistent shape of the optical property curves across different geometries, with only the displacement varying (Figure 14). Detailed values of these curves are presented in Table 5.

Nanohole Diameter	LSPR Wavelength (nm) / Minimum in Transmittance (a. u.)	LSPR Wavelength (nm) / Maximum in Absorbance (a. u.)	LSPR Wavelength (nm) / Maximum in Reflectance (a. u.)	Gold Area (%)
90	675, 0.13985	686, 0.57249	659, 0.53552	92.93
100	684, 0.10626	697, 0.60021	663, 0.55638	91.27
110	685, 0.08456	700, 0.59709	666, 0.56788	89.44
120	687, 0.06973	705, 0.5795	669, 0.57696	87.43
130	690, 0.05893	710, 0.55659	673, 0.58465	85.25

Table 5. Comparison between the different diameters and its arbitrary units (a.u.) maximum, for absorbance and reflectance, and minimum values, for transmittance, at which the plasmon dipole (LSPR) originates, and the percentage of gold area obtained with every diameter, that match the literature. [30, 32].

Furthermore, the analysis of the electric field at the focal point of interest, particularly in relation to transmittance, offers significant insights into the light's behavior within the geometry. It elucidates how oscillations in gold electrons generate a dipole effect. Note that the intensity of the electric field (see Table 6) is notably higher in the first two diameters, namely 90 nm and 100 nm, with the highest value recorded at 100 nm, reaching 9.98×10^8 V/m.

Based on these numerical findings, it is recommended that for the nanofabrication of optical transducers relying on nanoholes, a diameter of 100 nm should be chosen. This diameter presents several advantages, including the availability of various vendors guaranteeing its specific size, thus simplifying the nanofabrication process. Conversely, opting for other diameters would necessitate meticulous nanofabrication techniques to ensure precise diameter consistency across all holes.

Therefore, the recommendation stands to fabricate optical transducers with a 100 nm diameter to achieve optimal performance within the geometry and streamline the nanofabrication process.

Nanohole Diameter	Optical property	Electric field maximum value (V/m)	LSPR Wavelength (nm)
90 nm	Transmittance	8.03×10^8	675
	Absorbance	8.65×10^8	686
	Reflectance	3.63×10^8	659
100 nm	Transmittance	9.28×10^8	684
	Absorbance	6.48×10^8	697
	Reflectance	4.03×10^8	663
110 nm	Transmittance	7.80×10^8	685
	Absorbance	6.65×10^8	700
	Reflectance	3.81×10^8	666
120 nm	Transmittance	7.42×10^8	687
	Absorbance	4.28×10^8	705
	Reflectance	4.36×10^8	669
130 nm	Transmittance	5.88×10^8	690
	Absorbance	3.52×10^8	710
	Reflectance	3.60×10^8	673

Table 6. Electric field maximum energy values for each diameter nanohole at its different properties at the wavelength where the plasmon originated, that match the literature. [20, 21].

4. Conclusions

In this work, a numerical analysis of the diameter of a nanoplasmonic transducer based on gold nanoholes is presented. Thereby, a study of the gold percentage to induce plasmonic resonances is analyzed.

Simulations explored nanohole diameters ranging from 90 nm to 130 nm, revealing significant effects on optical properties. As the diameter increased, the wavelength of Localized Surface Plasmon Resonance (LSPR) for transmittance (T, 675 nm), absorbance (A, 686 nm), and reflectance (R, 659 nm) shifted 15 nm, 24 nm and 14 nm towards longer wavelengths, respectively. Despite a reduction in the percentage of gold area (900 nm²) from 92.93 % to 85.25 %, the curves for transmittance, absorbance, and reflectance continued to exhibit

the LSPR phenomenon. The optical curves showed slight changes in the width and depth. The transmittance (T) changed from 0.139 a. u to 0.058 a. u, the absorbance (A) from 0.572 a. u. to 0.556 a. u. and reflectance (R) from 0.535 a. u. to 0.584 a. u. Additionally, the electric field distributions of the plasmon dipole indicated that a gold nanohole with a diameter of 100 nm had the highest intensity of 9.28×10^8 V/m, suggesting this configuration for optical transducer fabrication. Despite variations in nanohole diameter, all configurations maintain the ability to induce LSPR within the visible spectrum. This recommendation is supported by practical benefits like easier access from various suppliers and simpler fabrication processes. Therefore, this study emphasizes the importance of diameter selection to optimize the performance of optical transducers, which could enhance sensitivity, selectivity, and detection limits. By considering these insights, researchers and new students can improve the functionality and effectiveness of plasmonic transducers, particularly in bioanalytical applications.

Acknowledgement

References

1. Lu, X., Rycenga, M., Skrabalak, S. E., Wiley, B., & Xia, Y. (2009). Chemical Synthesis of Novel Plasmonic Nanoparticles. *Annual Review of Physical Chemistry, 60*(1), 167–192. https://doi.org/10.1146/annurev.physchem.040808.090434

2. Ebbesen, T. W., Lezec, H. J., Ghaemi, H. F., Thio, T., & Wolff, P. A. (1998). Extraordinary optical transmission through sub-wavelength hole arrays. *Nature, 391*(6668), 667–669. https://doi.org/10.1038/35570

3. Cottat, M., Goyard, D., Manesse, M., Varenne, C., & Chassagneux, Y. (2013). Localized Surface Plasmon Resonance (LSPR) Biosensor for the Protein Detection. *Plasmonics, 8*(2), 699–704.
    https://doi.org/10.1007/s11468-012-9460-3

4. Samsuri, N. D., Mukhtar, W. M., Rashid, A. R. A., Dasuki, K. A., & Yussuf, A. A. R. H. A. (2017). Synthesis methods of gold nanoparticles for Localized Surface Plasmon Resonance (LSPR) sensor applications. *EPJ Web of Conferences, 162,* 01002. https://doi.org/10.1051/epjconf/201716201002

5. Dos Santos, P. S. S., Gomes, A. L., Peres, D. R. M., Fonseca, D. R., Rodrigues, D. A., De Freitas, D. S., ... & Zucolotto, V. (2023). Spectral Analysis Methods for Improved Resolution and Sensitivity: Enhancing SPR and LSPR Optical Fiber Sensing. *Sensors, 23*(3), 1666.
    https://doi.org/10.3390/s23031666

6. Kastner, S., Mayr, K., Ziegler, S., & Sinner, E.-K. (2023). LSPR-Based Biosensing Enables the Detection of Antimicrobial Resistance Genes. *Small, 19*(33), 2207953. https://doi.org/10.1002/smll.202207953

7. Mayer, K. M., & Hafner, J. H. (2011). Localized surface plasmon resonance sensors. *Chemical Reviews, 111*(6), 3826–3857.
    https://doi.org/10.1021/cr100313v

8. Solis-Tinoco, V., Marquez, S., Quesada-Lopez, T., Villarroya, F., Homs-Corbera, A., & Lechuga, L. M. (2019). Building of a flexible microfluidic plasmo-nanomechanical biosensor for live cell analysis. *Sensors and Actuators B: Chemical, 291,* 48–57. https://doi.org/10.1016/j.snb.2019.04.038

9. Jazayeri, M. H., Aghaie, T., Nedaeinia, R., Manian, M., & Nickho, H. (2020). Rapid noninvasive detection of bladder cancer using survivin antibody-conjugated gold nanoparticles (GNPs) based on localized surface plasmon resonance (LSPR). *Cancer Immunology, Immunotherapy, 69*(9), 1833–1840. https://doi.org/10.1007/s00262-020-02559-y

10. Lertvachirapaiboon, C., Baba, A., Shinbo, K., & Kato, K. (2021). Colorimetric detection based on localized surface plasmon resonance for determination of chemicals in urine. *Analytical Sciences, 37*(7).
https://doi.org/10.2116/analsci.20R005

11. António, M., Vitorino, R., & Daniel-da-Silva, A. L. (2023). LSPR-based aptasensor for rapid urinary detection of NT-proBNP. *Biosensors, 13*(7).
https://doi.org/10.3390/bios13070736

12. Biosensors. (2024). Recent advancements of LSPR fiber-optic biosensing: Combination methods, structure, and prospects. *MDPI*. Retrieved April 10, 2024, from:
https://www.mdpi.com/2079-6374/13/3/405

13. Paul, D., & Biswas, R. (2022). Clad modified varying geometries of fiber optic LSPR sensors towards detection of hazardous volatile liquids and their comparative analysis. *Environmental Technology & Innovation, 25,* 102112.
https://doi.org/10.1016/j.eti.2021.102112

14. Wei, X. Z., & Mulvaney, P. (2014). Optical properties of strongly coupled plasmonic nanoparticle clusters. In N. V. Richardson & S. Holloway (Eds.), *Handbook of Surface Science, Modern Plasmonics* (Vol. 4, pp. 75–108). North-Holland.
https://doi.org/10.1016/B978-0-444-59526-3.00003-3

15. IntechOpen. (2024). The influence of geometry on plasmonic resonances in surface- and tip-enhanced Raman spectroscopy. Retrieved April 10, 2024, from:
https://www.intechopen.com/chapters/84716
https://doi.org/10.5772/intechopen.108182

16. Wang, H., et al. (2023). Plasmonic nanostructure biosensors: A review. *Sensors, 23*(19).
https://doi.org/10.3390/s23198156

17. Kim, D. M., Park, J. S., Jung, S.-W., Yeom, J., & Yoo, S. M. (2021). Biosensing applications using nanostructure-based localized surface plasmon resonance sensors. *Sensors, 21*(9).
https://doi.org/10.3390/s21093191

18. De Leebeeck, A., Kumar, L. K. S., de Lange, V., Sinton, D., Gordon, R., & Brolo, A. G. (2007). On-chip surface-based detection with nanohole arrays. *Analytical Chemistry, 79*(11), 4094–4100.
https://doi.org/10.1021/ac070001a

19. Gomez-Cruz, J., Nair, S., Ascanio, G., & Escobedo, C. (2017). Flow-through nanohole array-based sensor implemented on analogue smartphone components. In *Proceedings of SPIE* (Vol. 10395, p. 80).
https://doi.org/10.1117/12.2272433

20. Hosseinpour, M., Zendehnam, A., Hamidi Sangdehi, S. M., & Ghomi Marzdashti, H. (2021). Simulation of the improvement in the performance of a silver-based surface plasmon resonance biosensor using experimental results of cold plasma treatment of glass substrate. *Journal of Computational Science, 54,* 101410.
https://doi.org/10.1016/j.jocs.2021.101410

21. Zhao, E., et al. (2017). Localized surface plasmon resonance sensing structure based on gold nanohole array on beveled fiber edge. *Nanotechnology, 28*(43), 435504.
https://doi.org/10.1088/1361-6528/aa847a

22. Li, X., Soler, M., Özdemir, C. I., Belushkin, A., Yesilköy, F., & Altug, H. (2017). Plasmonic nanohole array biosensor for label-free and real-time analysis of live cell secretion. *Lab on a Chip, 17*(13), 2208–2217.
https://doi.org/10.1039/C7LC00277G

23. Escobedo, C. (2013). On-chip nanohole array-based sensing: A review. *Lab on a Chip, 13*(13), 2445–2463.
https://doi.org/10.1039/C3LC50107H

24. Ferreira, J., et al. (2009). Attomolar protein detection using in-hole surface plasmon resonance. *Journal of the American Chemical Society, 131*(2), 436–437.
https://doi.org/10.1021/ja807704v

25. Gomez-Cruz, J., Nair, S., Manjarrez-Hernandez, A., Gavilanes-Parra, S., Ascanio, G., & Escobedo, C. (2018). Cost-effective flow-through nanohole array-based biosensing platform for the label-free detection of uropathogenic *E. coli* in real time. *Biosensors and Bioelectronics, 106,* 105–110.
https://doi.org/10.1016/j.bios.2018.01.055

26. Wang, Y., Chong, H. B., Zhang, Z., & Zhao, Y. (2020). Large-area fabrication of complex nanohole arrays with highly tunable plasmonic properties. *ACS Applied Materials & Interfaces, 12*(33), 37435–37443.
https://doi.org/10.1021/acsami.0c06936

27. Jia, H., Fredriksson, H., Hole-Mask, C. L., et al. (2022). Plasmonic nanohole arrays with enhanced visible light photoelectrocatalytic activity. *ACS Photonics, 9*(2), 652–663.
https://doi.org/10.1021/acsphotonics.1c01684

28. Fredriksson, H., Alaverdyan, Y., Dmitriev, A., Höök, F., Langhammer, C., Sutherland, D. S., Zäch, M., & Käll, M. (2007). Hole–mask colloidal lithography. *Advanced Materials, 19*(23), 4297–4302.
https://doi.org/10.1002/adma.200700680

29. Wang, Q., & Wang, L. (2020). Lab-on-fiber: Plasmonic nano-arrays for sensing. *Nanoscale, 12*(14), 7485–7499.
https://doi.org/10.1039/D0NR00040J

30. Colombelli, A., Manera, M. G., Rella, R., & Vasanelli, L. (2014). FEM modeling of nanostructures for sensor application. In C. Di Natale, V. Ferrari, A. Ponzoni, G. Sberveglieri, & M. Ferrari (Eds.), *Sensors and Microsystems* (pp. 287–291). Springer International Publishing.
https://doi.org/10.1007/978-3-319-00684-0_55

31. Hsiao, A., Gartia, M. R., Chang, T.-W., Wang, X., Khumwan, P., & Liu, G. L. (2015). Colorimetric plasmon resonance microfluidics on nanohole array sensors. *Sensors and Bio-Sensors Research, 5*, 24–32.
https://doi.org/10.1016/j.sbsr.2015.06.001

32. Agharazy Dormeny, A., Abedini Sohi, P., & Kahrizi, M. (2020). Design and simulation of a refractive index sensor based on SPR and LSPR using gold nanostructures. *Results in Physics, 16*, 102869.
https://doi.org/10.1016/j.rinp.2019.102869

NUMERICAL MODELING OF SURFACE ACOUSTIC WAVES FOR ELECTRONIC FILTER DESIGN

Alonso Fernández García[1], Ericka Yatzil García Figueroa[2], Luis Alfonso Villa Vargas[3], Juan Carlos Sánchez García[1], Marco Antonio Ramírez-Salinas[3], Verónica Iraís Solís-Tinoco[3,4*], Miguel Ángel Alemán-Arce[3]

[1]Escuela Superior de Ingeniería Mecánica y Eléctrica, Instituto Politécnico Nacional, 04440, Ciudad de México, México.

[2]Unidad Profesional Interdisciplinaria en Ingeniería y Tecnologías Avanzadas UPIITA -IPN. Ingeniería Mecatrónica. Ciudad de México, 07340, México.

[3]Centro de Investigación en Computación del Instituto Politécnico Nacional, Laboratorio de Microtecnología y Sistemas Embebidos. Ciudad de México, 07738. México.

[4]Instituto de Ciencias Aplicadas y Tecnología, Universidad Nacional Autónoma de México, Ciudad de México, 04510, México.

*irais.solis@cic.ipn.mx

Abstract

Surface acoustic wave (SAW) filters are widely used in most of the electronic industry. In this work, a detailed methodology for the design and numerical simulation of a SAW bandpass filter in a 128° YX LiNbO$_3$ piezoelectric material is presented. The SAW filter operates using a delay line configuration. It consists of N$_p$ = 20 double finger pairs, with a port separation of l = 1293.6 μm, an acoustic aperture of W = 2597.32 μm, a finger width of r = 16.17 μm, and a finger thickness of h = 300 nm with an acoustic wavelength of λ = 129.36 μm. The results showed an insertion loss level of IL = -10.39 dB, side lobe levels of SLL = -33.01 dB, and a null bandwidth value of NBW = 3 MHz. The conductance calculations exhibited a maximum value of 83 mS, while the susceptance showed maximum and minimum values of 120 mS and 8 mS, respectively. This methodology is beneficial for enhancing the understanding of SAW filter design. Besides, this approach helps optimize the design process, providing alternatives to traditional filters that rely on multiple reactive components for high-order filtering.

Keywords: surface acoustic waves, electronic filters, piezoelectric, numerical simulation.

1. Introduction

Nowadays, sensors are one of the most essential components of any sophisticated electronic system. Their role is indispensable for the functioning of modern electronics. They serve as the interface between the physical world, governed by the laws of physics, and the digital area, which interprets the acquired data for many applications. Thus, sensor technology is emerging in novel application fields and widespread markets such as smart cities, industrial automation and control, communications, and health, among others [1-3].

Once electronic sensors detect and interact with the physical phenomena around them, processing the response data via signals is necessary to comprehend the outcomes once they are analyzed. Then, the measurements can be affected by any background noise source; due to this, the purpose of electronic filters [4] is to eliminate or dim the background noise that could affect the measurements or discriminate a specific frequency that goes through it, allowing the modification of the amplitude and phase [5].

The rate at which something occurs is known as frequency; signals obtained from measurement can be transformed from the time domain to the frequency domain. It has been shown that any waveform that exists in the world can be represented by the addition of multiple sine waves. Amplitudes, frequencies, and phases of these, spliced correctly, can generate a waveform identical to the one desired. Understanding how signals are a combination of multiple waveforms with different amplitudes and frequencies leads to the fact that sometimes, it is necessary to get rid of some of them. A filter is a device that allows just a specified frequency of signals to pass through it, rejecting the ones that do not meet the desired specifications [6].

The frequency response of a circuit is the response when it experiences changes in the input signal frequency. Electronic devices usually have a frequency range where their response is close to the ideal; the output signal can be distorted out of this range. Owing to the device's dependence on the frequency, filters are used to isolate the functional frequencies for the device's optimal operation.

The operating range of each device or circuit depends on the type of components used and their configuration. This determines the cut-off frequency, which is defined as the boundary where the signal passing through the system

begins to be attenuated. There are four basic types of circuit filters based on their behavior near the cutoff frequency.

The low-pass filter allows signals from 0 Hz up to a specified cut-off frequency to pass through, while a high-pass filter only allows high frequencies, typically above 1 kHz. A band-pass filter allows signals within a bandwidth defined by two cut-off frequencies while attenuating those outside it. Conversely, a notch or band-stop filter attenuates waves within a defined range, allowing those outside the limits to pass. Additionally, filters can be classified into two categories passive filters, designed with passive components such as resistors, capacitors, and inductors, or active filters, designed with active components like operational amplifiers [7].

The main complication during the implementation of filters is the real response they have, while operating within the cut-off frequency bandwidth, which is the difference between the higher and lower cut-off frequency, the signal ideally should not exhibit significant distortion in amplitude or phase. An ideal filter should maintain a constant response during the specified period of frequencies and completely remove frequencies higher or lower than the cut-off frequency, depending on the type of filter [8]. However, the real filter output signal gradually decreases or becomes distorted as the frequency approaches the cut-off frequency, making it useless.

Hence, designing filters with a response as close as possible to the ideal response by increasing the filter's order without adding more reactive components (e.g., inductors or capacitors) poses a significant challenge for researchers. Additionally, there is a prevailing trend in the progression of sensor technology towards miniaturization, coupled with a growing utilization of multi-sensor configurations and wireless systems.

Therefore, thanks to advancements in computing and microfabrication techniques, it's now feasible to conceive and fabricate innovative structures tailored for application in sensor technology.

For example, surface acoustic wave (SAW) filters are electromechanical components at the microscale whose operation principle is turning the electrical signals into mechanical waves through the properties of piezoelectric substrates. The operation of this kind of filter begins with the input transducer, which converts the electrical signal to a mechanical wave. This wave propagates across

the surface of the substrate from one end to another. As the wave travels, it interacts with an array of electrodes designed to attenuate or let through the desired frequency. Once the mechanical wave reaches the output transducer, it is converted back to an electrical signal without the undesired frequencies [9].

SAW filters are at the forefront of advancing technologies and high-precision electronic systems. SAW filters are not just limited to one field of high-frequency electronics. Their unique characteristics, such as high selectivity and low insertion loss, make them versatile and ideal for integration into various applications [10]. From wireless communication systems [11] and radars to temperature and pressure sensors and medical devices like heart rate resonators and glucose monitors [12 - 16].

Designing SAW filters involves a process that starts with defining the filter specifications, such as center frequency, bandwidth, and insertion loss requirements. The design typically progresses by selecting appropriate substrate materials with suitable acoustic properties, determining the interdigital transducer (IDT) geometry, and optimizing the electrode configuration for desired performance characteristics. Advanced simulation tools like COMSOL Multiphysics are then utilized to model the SAW filter, analyze its frequency response, and refine the design until meeting the specified criteria.

The application of numerical simulations in COMSOL to design surface acoustic wave (SAW) filters, offers considerable advantages, such as enabling efficient and cost-effective exploration and access to a wide range of design parameters and configurations, which leads to optimized filter performance. Advanced SAW filter simulation of complex physical phenomena by COMSOL significantly aids the comprehension of SAW filter behavior as well as its performance characteristics. This brings the possibility to visualize and analyze simulation results and identify the potential design improvements for fine turning the filter design to meet specific requirements accurately. Implementing COMSOL for SAW filter design ensures a streamlined and efficient design process, resulting in high-performance filters designed especially for each application's needs.

In this work, we present a detailed methodology for the numerical simulation of a surface acoustic wave (SAW) filter using the delay line configuration with lithium niobate in 128° YX LiNbO$_3$ rotation as a piezoelectric substrate. The methodology covers the conceptualization of filter design as a bandpass filter with

a center frequency at 30 MHz with a Null bandwidth of 3 MHz, the description of the use of COMSOL Multiphysics for numerical simulation divided into the definition of SAW filter's geometry, material properties and boundary conditions, mesh settings, and study configuration. Finally, the results are exported, analyzed, and discussed.

We focused on SAW filter design and simulation due to multiple advantages, such as the miniaturization of electronic filters when compared with LC filters such as Chebyshev, Butterworth, or Bessel filters. For a 3rd order filter, each variation has approximately 3 capacitors and 3 inductors, and the number of components grows proportionally to filter order. Thus, dealing with high numbers of components includes managing with component variation and tolerance properties. By contrast, SAW filters employ the use of a unique electronic passive component made in a single substrate and offer high-temperature stability and precise frequency response.

2. Methodology

2.1. *Filter design conceptualization*

Different techniques can be used to design surface acoustic wave filters. As a first approach for a bandpass filter design, a delay line configuration was selected, as shown in Figure 1, consisting of two ports of metallic structures deposited on the surface of a piezoelectric substrate with an input port and an output port, each formed by identical interdigital transducers (IDTs) of determined numbers of finger pairs (N_p) with finger width (r), acoustic aperture (W), and separation between ports (l). The IDT geometry and the physical properties of the piezoelectric substrate almost wholly determine the filter's electromechanical behavior.

a)   b)
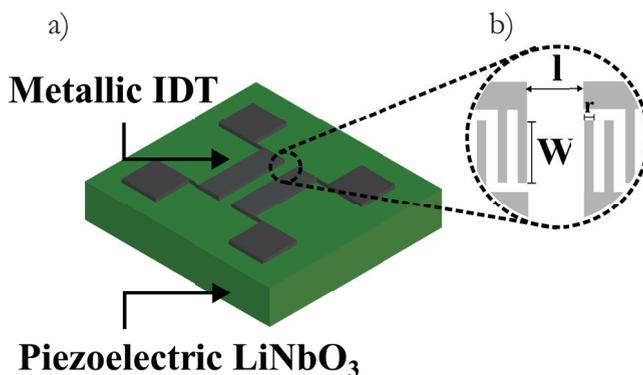
Figure 1. (a) The scheme shows a SAW filter with a delay line configuration. (b) Zooms in on the details of IDT geometry, including the separations between ports (l), acoustic aperture (W), and finger width (r).

COMSOL Multiphysics, like various numerical modeling tools, allows the consistent and straightforward modeling of the filter's electrical behavior and response to many environmental and microfabrication parameters. However, these numerical simulations in COMSOL were complemented with analytical results to explain the geometrical design of IDTs.

Filter simulation involves precisely defining the geometric parameters and objectives. The operating resonant frequency (f_0), desired performance metrics like Null bandwidth (NBW), the filter's piezoelectric material selection (the most used materials are Quartz, ZnO, $LiTaO_3$ or $LiNbO_3$), and desired ripples level, which in turn defines the insertion loss levels (IL) must be specified.

The most common IDT configurations are single-finger, double-finger, and single-phase unidirectional transducers (SPUDT). Design details of the desired configuration are shown in Table 1 and form the basis for creating an accurate simulation model using COMSOL, ensuring a detailed analysis of the SAW filter's electrical behavior.

Substrate material	128° YX $LiNbO_3$
Electrode configuration	Double finger
Resonant frequency	30 MHz
Null Bandwidth	3 MHz
Phase ripple	<1°
Insertion loss	~-10 dB

Table 1. Principal desired characteristics for the SAW bandpass filter design.

The selection of 128° YX $LiNbO_3$ as a piezoelectric material is due to its high piezoelectric coupling factor (k^2= 0.055), a direct measure of its transduction efficiency. The center frequency is selected for 30 MHz. Still, a similar process is valid for arbitrary frequency, considering that the lower the frequency, the larger the size of the SAW filter, making low-frequency filter fabrication almost impractical. Frequency value is related to IDT geometry through the dispersion relation of Equation 1: $f = v/\lambda$ 1

Where λ is the equivalent acoustic wavelength, the relation between finger width (r) and acoustic wavelength $\lambda = 8r$ is fulfilled for the double-finger IDT configuration. Also, the double-finger geometry is chosen as a non-reflectivity IDT to avoid internal reflection and distortion of frequency response. On the other hand, is the surface acoustic wave velocity propagation, considering the IDT as a dispersive medium given by Equation 2 described by Bløtekjær et al. [17].

$$v = \frac{v_f}{(1 + 0.85(v_f - v_m)/v_m)} \qquad 2$$

Where $v_f = 3975$ m/s and $v_m = 3865$ m/s are the free and metalized propagation velocities of SAW in the piezoelectric substrate, respectively.

The frequency response could be represented as a combination of the frequency response of each SAW filter port. We can search desired IL levels and amplitude of phase ripples ($\Delta\alpha$), which are deeply correlated. Usually, we can set the desired levels of amplitude-phase ripples and then relate this with the number of finger pairs through the attenuation of triple transit signals (TTS) and insertion loss, as described by Soluch et al. [18] with

$$2N_p = N^2 \approx \frac{\sqrt{A_{tt} y_1 y_2}}{G_p W/\lambda} \qquad 3$$

Where N is defined as the number of spaces between opposite polarity with non-zero overlap, W and   previously defined, y_1 and y_2 are the source and load admittances and are usually selected as 50 Ω, G_p is a constant of conductance dependent on IDT geometry and $A_{tt} \approx tan (\Delta\alpha)$ is the attenuation of TTS.

For the NBW value,

$$NBW = \frac{2f_0}{N_p} \qquad 4$$

Where f_0 is the resonant frequency and N_p is the number of finger pairs.

2.2. *Geometry of the SAW filter*

All configurations were made to save computational time, taking advantage of available hardware: an Intel core i7 11th Gen. with 32 GB of RAM. We used the piezoelectric branch of the AC/DC module in COMSOL V6.0, which couples electrical and mechanical physics and allows for modeling piezoelectric problems.

The SAW filter was simplified in 2D geometry. The geometry of $N_p = 20$ finger pairs, acoustic aperture W = 2587.32 μm, and separation between ports of l=1293.6 μm were considered for filter design. Figure 2a shows the geometry of an azimuthal cut of the piezoelectric substrate and of the IDT on its surface as shown in Figure 2b, where w = 16.17 μm represents the finger width, h = 300 nm the finger thickness, and λ = 129.36 μm the equivalent acoustic wavelength.
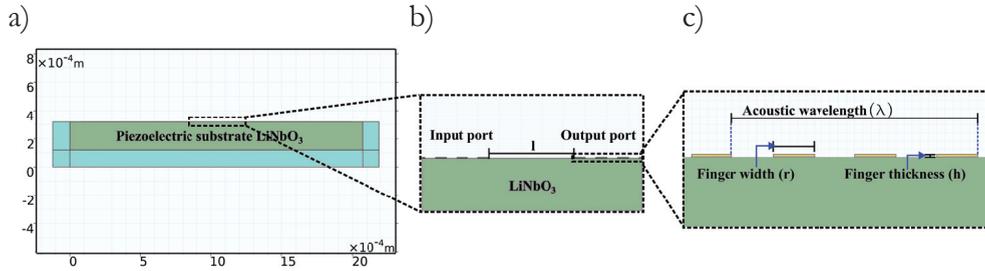
Figure 2. (a) 2D simplification of SAW filter geometry in an azimuthal cut. (b) zoom in on the details of port separation distance (l). (c) Zoom in on the details of the double-finger IDT configuration, including the definition of finger width (r) and finger thickness (h).

2.3. *Material properties and boundary conditions*

Lithium niobate (LiNbO$_3$) with a YZ-cut orientation is available in the COMSOL materials library. Obtaining particular cut orientation properties could be done using Euler angles rotation ((0,38,0) for 128° YX rotation) or calculating the properties of rotated material as in Auld et al. [19], with the use of rotation matrix operation for piezoelectric constant tensors.

We set the mechanical and electrical boundary conditions once the 128° YX LiNbO$_3$ properties are defined. Mechanical fixed and free boundary conditions are selected at the bottom and top of the piezoelectric substrate, respectively, as shown in Figure 3a. Equivalent electrical boundary conditions are chosen for the input and output ports, as depicted in Figure 3b, with a selection of ground and terminal boundaries as input excitation sources, such as voltage signals for simulation. Additionally, we use a perfect-matched layer (PML) as a perfectly absorbing domain or nonreflecting boundary condition to avoid reflection of the geometric boundary of the piezoelectric substrate.
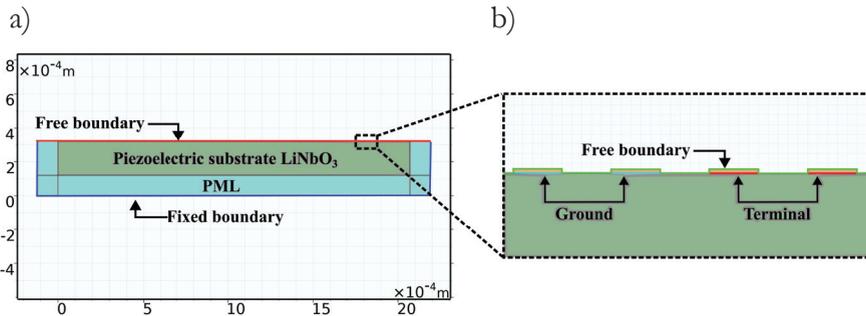
Figure 3. (a) Mechanical boundaries condition with the addition of Perfect Matched Layer (PML). (b) zoom in on the detail of the electrical boundary condition with the definition of excitation condition with ground and terminal configuration

2.4. *Study settings*

With the aim of optimizing the simulation, we made the necessary configurations from mesh settings. Correctly setting the mesh configuration could reduce the computational time of a frequency-domain study. COMSOL permits the configuration of the mesh geometry as defined by physics or as defined by the user. The second option to enhance the simulation resolution near and directly below the finger geometry was used.

Different configurations permit the use of personalized mesh geometry. The one selected here is the mapped mesh, a particular type of mesh that allows the creation of a quadrilateral mesh for each domain in 2D geometry and maps the mesh to the desired geometry under selected domains to cover any area of interest uniformly.

To create a mapped mesh, we first use a custom element size to control the maximum size. The finger domain and upper boundary to create separate meshes, one controlled by the mesh of the finger's elements and one controlled by the upper edge boundary were selected, as shown in Figure 4a. A distributed mesh along the geometry depth until it reaches the substrate's bottom surface, copying the source mesh to define regular mesh elements at the lower substrate boundary was used (see Figure 4b).
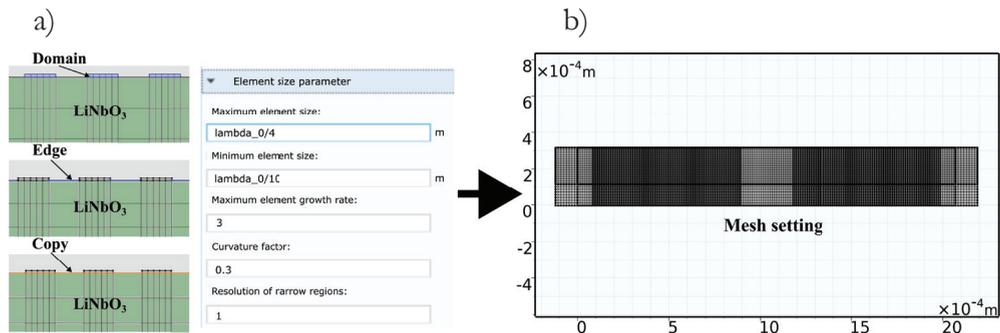
Figure 4. (a) shows the steps to configure a mapped mesh, selecting domains and edges and then copying the mesh properties from one boundary to another, with a desired element size of the quadrilateral mesh. (b) shows the size parameters of the mesh configuration for the mapped mesh geometry.

The filter frequency response is obtained using a frequency domain study configured directly from the main menu and general study selection. For this, it is necessary to set a frequency range with a start, stop, and step value. We use a symmetric frequency interval ranging from f_0-5 MHz to f_0+5 MHz with a 0.1 MHz step resolution, see Figure 5a.
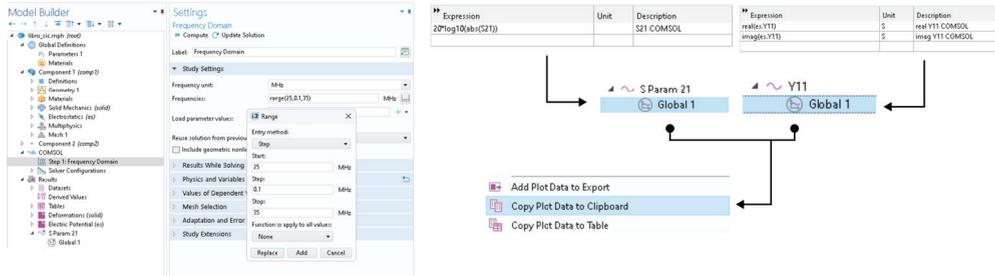
Figure 5. (a) shows the frequency study selection and the definitions of the frequency range. (b) shows the use of S21 for S-parameter definition and es.Y11 special function of COMSOL for Y-parameters in a 1D plot group and its data exportation.

To characterize the filter frequency response through the S_{21} parameter, conductance (G), and susceptance (B), we use a 1D plot group. We obtain the S_{21} parameter using the appropriate COMSOL variable definitions for S-parameters. Using one global subnode of the 1D plot group created, we called the *S21* variable and operated over this to obtain the IL levels using Equation 5, as shown in Figure 5b:

$$IL = 20 \ |S_{21}| \qquad 5$$

Equivalently, values of conductance (G) and susceptance (B) of each IDT port were extracted, which are related through the relation $Y = G + iB$ for each port. Thus, in another global subnode, we use the COMSOL definition of Y-parameters; we call the *es.Y11* variable as *real(es.Y11)* to obtain the real part of admittance (conductance) and *imag(es.Y11)* to get the imaginary part of admittance (susceptance).

Once obtained, the results could be exported to plot externally in any graphical analysis software by copying the data, clicking right on the global subnode, and selecting the option of copying plot data to the clipboard (see also Figure 5b).

3. Results and discussion

Once exported, the simulation data was plotted using OriginPro software. As shown in Figure 6a, the frequency response of a SAW filter with IL levels at the resonant frequency of -10.39 dB, Null Bandwidth of 3 MHz, and average side lobe levels of SLL = -33.01 dB, all near the desired characteristics of the SAW filter is shown. On the other side, Figure 6b shows the conductance and
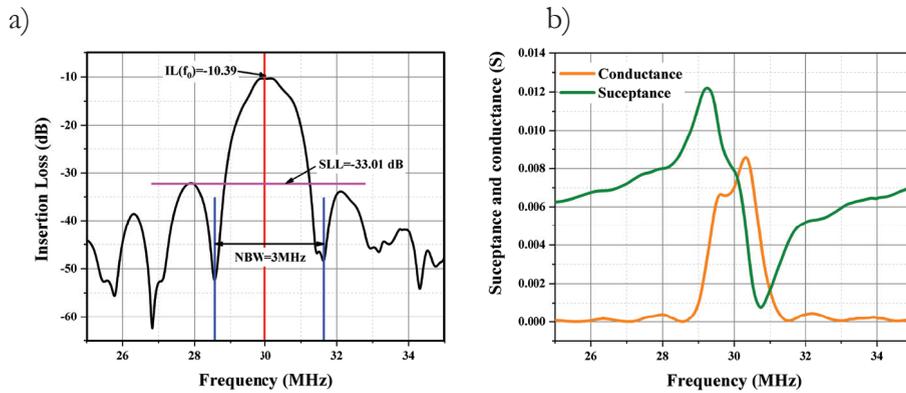
Figure 6. (a) shows the frequency response of the SAW filter, showing the insertion loss at the resonant frequency, side lobe levels, and Null bandwidth value, and (b) Graph shows the conductance and susceptance response.

susceptance results, easily extracted from simulation, showing a maximum conductance value of 83 mS and maximum and minimum values of susceptance of 120 mS and 8 mS, respectively.

While the frequency response obtained corresponds with the classical band-pass filter response, and its characteristics represent part of the electrical behavior of the filter SAW, the conductance and susceptance response complement crucial information about filter behavior. As a designer, is important to consider the frequency response distortion caused by undesired effects of mass loading due to the deposition of the metallic structure that conforms to the IDT geometry, generation of triple transit signals (TTS), bulk wave generation, etc., some of this distortion effects could be avoided analyzing the conductance and susceptance behavior. Susceptance and conductance response symmetry is expected when distortion is nullified. For example, much of the distortion or frequency shift of maximum conductance value to higher or lower values could be attributed to second-order effects.

More than frequency response or susceptance and conductance values, COMSOL enables other special functions that could be called with simple line commands. For example, we can extract the deformation measurement from Rayleigh surface displacement, as shown in Figure 7a, using u, v, or w field displacement in a 2D plot group. Similarly, we can use the voltage variable V in a 2D plot group to plot the electric potential distribution, as shown in Figure 7b. Both functions could perform different analyses of wave travel and potential distribution as a function of waveguides deposited on filter surfaces or temperature compensation of SAW filters.

a)   b)
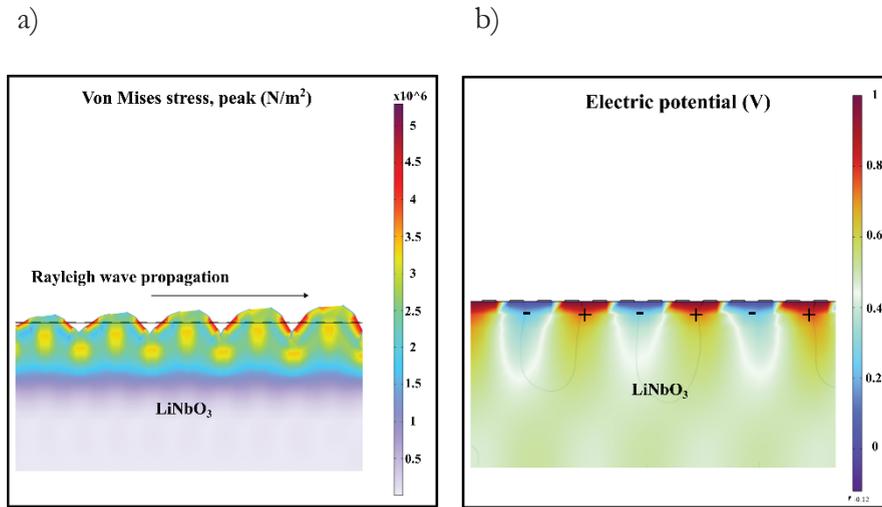
Figure 7. (a) Surface deformation of piezoelectric substrate. (b) Electric potential travels in the volume of $LiNbO_3$, where the distribution of electric potential is depicted graphically.

The presented work includes the analysis of key factors suitable for an SAW filter design such as its frequency response, conductance, susceptance, substrate deformation, and the electric potential distribution. Using computational tools like COMSOL allows engineers and researchers to obtain a deep understanding of the physical mechanisms influencing the behavior of these filters. These tools have wide advantages compared to analytical methods, such as more precise tuning and enhanced filter response. Furthermore, the use of numerical simulations reduces the time used in the design process and opens the door to advanced design techniques when combined with machine learning and artificial intelligence tools.

4. Conclusions

We presented a 2D numerical simulation methodology of a SAW bandpass filter design using the COMSOL Multiphysics software. The methodology permits to analyze and simulate the scattering parameters, conductance, and susceptance values as well as the 2D visualization of the voltage propagation and the material surface deformation, usable to measure the acoustic surface energy. The methodology includes the definition of piezoelectric properties, geometric configurations, and the necessary boundary conditions to replicate the electromechanical behavior of the device.

The numerical results showed insertion loss levels of IL = -10.39 dB, SLL = -33.01 dB, and NBW = 3 MHz. These values permit effectively obtaining a bandpass filter with the levels of phase ripples imposed sacrificing the increase in the IL to the levels shown. On the other side, the simulations reveal conductance maximum values of 83 mS, and susceptance measurements presented maximum and minimal values of 120 mS and 8 mS, respectively. Furthermore, the use of numerical simulation tools permits to enhancement of the study of physical mechanisms including the voltage SAW propagation and surface deformation of piezoelectric material, something that opens the door to advanced design techniques including waveguiding.

All the calculations were made using 2D COMSOL simplification, to save time and computational costs, simulations were made with 0.1 MHz steps, and computed within 20 minutes. The satisfactory results validate, prove, and promote COMSOL Multiphysics for SAW filter design. Thus, this methodology achieves specific goals: firstly, it acts as a comprehensive guide for new students and researchers in the development of numerical simulations, and secondly, it generates a broad and deep understanding of the complex electromechanical behavior of SAW filters. These filters are widely acknowledged as an alternative to conventional filter design techniques.

Acknowledgments

References

1. Park, J., Kim, K. T., & Lee, W. H. (2020). Recent advances in information and communications technology (ICT) and sensor technology for monitoring water quality. *Water (Switzerland)*, *12*(2).
    https://doi.org/10.3390/w12020510

2. Guerrero-Ibáñez, J., Zeadally, S., & Contreras-Castillo, J. (2018). Sensor technologies for intelligent transportation systems. *Sensors (Switzerland)*, *18*(4).
    https://doi.org/10.3390/s18041212

3. Morello, R., Mukhopadhyay, S. C., Liu, Z., Slomovitz, D., & Samantaray, S. R. (2017). Advances on sensing technologies for smart cities and power grids: A review. *IEEE Sensors Journal*, *17*(23).
    https://doi.org/10.1109/JSEN.2017.2735539

4. Singh, B., AlHaddad, K., & Chandra, A. (1999). A review of active filters for power quality improvement. *IEEE Transactions on Industrial Electronics*, *46*(5).
    https://doi.org/10.1109/41.793345

5. Sáenz, E. M., de la Cruz, J. P., & Garzón, H. S. (2020). *Fundamentos de circuitos eléctricos II*.

6. Williams, A. B., & Taylor, F. J. (2006). *Electronic filter design handbook, Fourth Edition. Proceedings of the IEEE*, *70*(3).

7. Dimopoulos, H. G. (2012). *Analog electronic filters: Theory, design and synthesis*.
    https://doi.org/10.1007/978-94-007-2190-6

8. Chen, P., Li, G., & Zhu, Z. (2022). Development and application of SAW filter. *Micromachines*, *13*(5).
    https://doi.org/10.3390/mi13050656

9. Morgan, D., & Paige, E. G. S. (2007). *Surface acoustic wave filters: With applications to electronic communications and signal processing*.

10. Mandal, D., & Banerjee, S. (2022). Surface acoustic wave (SAW) sensors: Physics, materials, and applications. *Sensors*, *22*(3).
    https://doi.org/10.3390/s22030820

11. Pan, Y., Mu, N., Liu, B., Cao, B., Wang, W., & Yang, L. (2018). A novel surface acoustic wave sensor array based on wireless communication network. *Sensors (Switzerland)*, *18*(9).
    https://doi.org/10.3390/s18092977

12. Luo, J., et al. (2013). A new type of glucose biosensor based on surface acoustic wave resonator using Mn-doped ZnO multilayer structure. *Biosensors and Bioelectronics*, *49*.
    https://doi.org/10.1016/j.bios.2013.05.021

13. Agostini, M., Greco, G., & Cecchini, M. (2019). Full-SAW microfluidics-based lab-on-a-chip for biosensing. *IEEE Access*, *7*.
https://doi.org/10.1109/ACCESS.2019.2919000

14. Liu, B., et al. (2016). Surface acoustic wave devices for sensor applications. *Journal of Semiconductors*, *37*(2).
https://doi.org/10.1088/1674-4926/37/2/021001

15. Liu, X., Chen, X., Yang, Z., Xia, H., Zhang, C., & Wei, X. (2023). Surface acoustic wave-based microfluidic devices for biological applications. *Sensors and Diagnostics*, *2*(3).
https://doi.org/10.1039/D2SD00203E

16. Länge, K., Rapp, B. E., & Rapp, M. (2008). Surface acoustic wave biosensors: A review. *Analytical and Bioanalytical Chemistry*.
https://doi.org/10.1007/s00216-008-1911-5

17. Bløtekjær, K., Ingebrigtsen, K. A., & Skeie, H. (1973). Acoustic surface waves in piezoelectric materials with periodic metal strips on the surface. *IEEE Transactions on Electron Devices*, *20*(12).
https://doi.org/10.1109/T-ED.1973.17807

18. Soluch, W. (1998). Design of SAW delay lines for sensors. *Sensors and Actuators A: Physical*, *67*(1–3).
https://doi.org/10.1016/S0924-4247(97)01737-8

19. Auld, B. A., & Green, R. E. (1974). Acoustic fields and waves in solids: Two volumes. *Physics Today*, *27*(10).
https://doi.org/10.1063/1.3128926

SILVER AND COPPER NANOFLUIDS, SYNTHESIS, CHARACTERIZATION AND THEIR ANTIMICROBIAL PROPERTIES AGAINST PATHOGENIC MICROORGANISMS

Andrea Marisol Medina Solano[1*],
José Abraham Balderas López[1],
María de Lourdes Moreno Rivera[1],
Blanca Estela Chávez Sandoval[2]

[1]Instituto Politécnico Nacional - IPN, Unidad Profesional Interdisciplinaria de Biotecnología-UPIBI, Mexico.

[2]Instituto Politécnico Nacional, Escuela Nacional de Ciencias Biológicas-ENCB, Mexico.

*abrahambalderas@hotmail.com

Abstract

Nanofluids, which are not strong oxidants and are not expected to produce harmful disinfection by-products, have demonstrated excellent antimicrobial properties against a range of microorganisms, including Gram-negative and Gram-positive bacteria, viruses, yeasts, and fungi.

Given the rise in antimicrobial resistance and the limitations of traditional antibiotics, there is an urgent need for new disinfection alternatives. Several patents reveal the commonly used types of nanofluids and their potential disinfection and decontamination mechanisms. This study focuses on the synthesis and characterization of silver and copper nanofluids, evaluating their effectiveness against pathogenic strains such as *Pseudomonas sp., Escherichia coli, Staphylococcus aureus,* and *Salmonella sp.*

These bacterial strains were chosen due to their medical importance and role in common nosocomial infections. The World Health Organization (WHO) identifies *Escherichia coli*, *Staphylococcus aureus*, *Pseudomonas aeruginosa*, and *Salmonella sp.* as critical pathogens because of their high resistance to multiple antibiotics and their involvement in severe infections.

The synthesized nanofluids demonstrated significant antimicrobial activity. These findings suggest that nanostructured sanitizers could be a viable alternative to traditional disinfectants, potentially reducing infection rates and combating antimicrobial resistance.

Keywords: Pathogenic microorganisms, Antimicrobial resistance, Nosocomial infections, metallic nanoparticles, nanofluids

1. Introduction

The significant health implications of pathogenic microorganisms have driven extensive research into new antimicrobial strategies. Metallic nanoparticles, specifically silver (AgNPs) and copper ($CuSO_4$NPs), are gaining considerable attention due to their unique physicochemical properties and potent biological activities. These nanomaterials offer a high surface area to volume ratio, biocompatibility, and the ability to support surface modifications, making them ideal candidates for medical applications. Crucially, they do not promote antimicrobial resistance, a major drawback associated with conventional antibiotics [1].

Metallic nanoparticles have attracted considerable attention in the realms of physics and chemistry because of their unique characteristics compared to bulk materials. They are utilized in drug delivery systems, biomolecules, antimicrobials, nucleic acids, and play crucial roles in diagnostics and treatment.

To further expand on the significance of innovative antimicrobial strategies, it's crucial to acknowledge the limitations and risks associated with conventional sanitizers and antibiotic therapies. The chemical composition of many sanitizers makes them harmful or toxic not only to humans but also to other organisms. In addition, its spectrum of action, activation start time, activity time, residual effect, toxicity, penetration capacity, and possible materials or circumstances that inactivate them may vary from one product to another [2]. Moreover, nosocomial infections, such as catheter-related bloodstream infections, ventilator-associated pneumonia, surgical site infections, and catheter-associated urinary tract infections, predominantly caused by *Staphylococcus*, *Pseudomonas*, and *Escherichia coli*, pose significant health risks [3].

Addressing these challenges requires new methods of prevention and treatment. Postoperative antibiotic therapy, while initially effective, has led to increased antimicrobial resistance, especially among methicillin- and vancomycin-resistant *Staphylococcus aureus*, vancomycin-resistant *Enterococcus*, and extended-spectrum beta-lactamase-producing Gram-negative bacilli. This scenario necessitates the exploration of alternative antimicrobial approaches [3].

In response to these challenges, this study focuses on synthesizing and characterizing silver and copper nanofluids (AgNPs and $CuSO_4$NPs) and evaluating their antimicrobial properties against medically significant pathogenic

microorganisms: *Pseudomonas sp.*, *Escherichia coli*, *Staphylococcus aureus*, and *Salmonella sp.* Through this inquiry, leveraging the unique properties of these nanofluids aims to develop effective and safe disinfectants applicable in various healthcare settings.

2. Metodology

2.1. *Materials and methods*

The materials and equipment utilized for this study were sourced from the Pharmaceutical Microbiology Laboratory at UPIBI. All reagents employed in the nanoparticle synthesis and evaluation of antimicrobial activity were of analytical grade.

The bacterial strains evaluated were *Escherichia coli* (ATCC 25922), *Staphylococcus aureus* (ATCC 25923), *Pseudomonas aeruginosa* (ATCC 27853), and *Salmonella* (ATCC 14028).

The analyses for TEM (Transmission Electron Microscopy) characterization were conducted at the Center for Nanosciences and Micro/Nanotechnologies (CNMN) of IPN.

2.2. *Nanoparticles Synthesis*

Nanoparticles were synthesized using the Turkevich method, which involves the use of microwaves instead of traditional synthesis, as described in Turkevich et al., 1951. This approach represents an innovative deviation from conventional methods.

The reagents used were: Silver Nitrate ($AgNO_3$) (PM $\approx$ 169.87 g/mol) $\geq$ 99.0%, Sodium Citrate ($Na_3C_6H_5O_7$) (PM $\approx$ 294.10 g/mol) $\geq$ 99.0%, Ascorbic Acid ($C_6H_8O_6$) (PM $\approx$ 176.13 g/mol) $\geq$ 99.0%, Copper(II) Sulfate Pentahydrate ($CuSO_4 \cdot 5H_2O$) (PM $\approx$ 2 49.685 g/mol) $\geq$ 99.0%, distilled water, and double-deionized water (Milli-Q). All these reagents were purchased from Sigma-Aldrich.

The samples were labeled and stored at 4ºC to be later characterized.

3. Nanoparticles UV-Vis Characterization

For this characterization, a GBC UV-Vis spectrophotometer, model Cintra 1010, with a wavelength range of 190 to 1100 nm, was employed. UV-Vis spectroscopy is a common technique used to characterize nanoparticles based on their absorption of ultraviolet and visible light.

UV-Vis characterization provides valuable information about the optical properties of the synthesized nanoparticles, confirming their successful synthesis and providing initial insights into their size and morphology. Furthermore, the presence of absorption peaks is related to the phenomenon of surface plasmon resonance, a unique physical property exhibited by metallic materials when they have nanoscale dimensions.

3.1. *Nanoparticles TEM Characterization*

Transmission Electron Microscopy (TEM) was employed for characterization. The equipment used was a scanning electron microscope in transmission mode of the JEOL brand model JEM-ARM200F (Japan) of the Electron Microscopy Laboratory of the Center for Nanosciences and Micro and Nanotechnologies (CNMN) of the IPN.

The objective of employing this technique was to obtain high-resolution images of the synthesized nanoparticles, allowing for precise characterization of their morphology, size distribution, and structural properties.

3.2. *Evaluation of the effectiveness and antimicrobial activity of synthesized nanoparticles (AgNPs and CuSO$_4$NPs)*

The antimicrobial susceptibility test was performed using the Kirby-Bauer Disk Diffusion Susceptibility Test [4]. This antimicrobial susceptibility test was used to observe the inhibition halo presented by copper nanoparticles (CuSO$_4$NPs) and silver nanoparticles (AgNPs) synthesized with respect to each selected strain and with two trademark sanitizers. The objective of using this technique is to determine the antibacterial efficacy of the synthesized nanoparticles by measuring the zones of inhibition they produce against various bacterial strains.

The interpretation of the results of the Kirby-Bauer Disk Diffusion Susceptibility Test is based on the measurement of the diameter of the inhibition zone. The larger the diameter of the area, the greater the susceptibility of the bacterial strain to the antimicrobial agent. Resistant bacterial strains will have smaller or no zones of inhibition.

3.3. *Use of Nanostructured Sanitizer*

The sanitizer developed in this work offers versatile application methods. It can be used by spraying, misting, or fine spraying using a spraying device, with the ability

to adjust the droplet size from 50 to 200 µm. This allows for effective coverage of surfaces, as the sanitizer primarily acts in the liquid phase by moistening the surfaces. Additionally, a small proportion of the sanitizer also acts in the gas phase, enhancing its efficacy.

Alternatively, the sanitizer can be used by immersion, where objects are simply submerged in the solution for a minimum contact time of 5 to 10 minutes. This method ensures thorough disinfection of items.

The nanostructured sanitizer is suitable for use on various surfaces, including floors, utensils, locker rooms, human skin, leather, and medical supplies, among others. Its broad applicability makes it a valuable tool for maintaining hygiene and preventing the spread of pathogens.

4. Results and discussion

4.1. *Synthesis*

The application of the chemical reduction method with microwaves resulted in the production of silver nanoparticles (AgNPs) with an estimated size of around 20 nm and copper nanoparticles ($CuSO_4$NPs) ranging between 5 to 100 nm. The use of microwave synthesis techniques facilitated the generation of both silver and copper nanoparticles, as depicted in Figure 1.
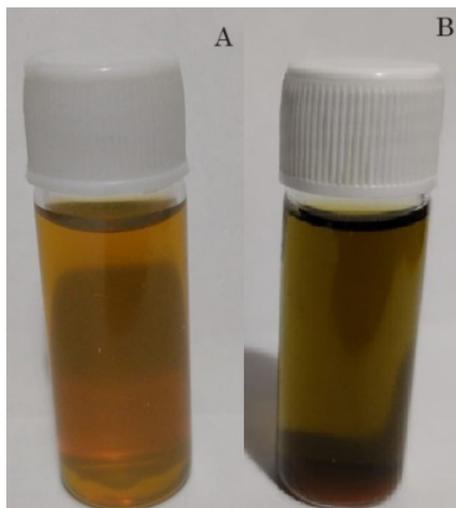
Figure 1. A) Suspensions of silver nanoparticles (AgNPs) and B) copper nanoparticles ($CuSO_4$NPs).

4.2. *UV-Vis Characterization*

UV-Vis spectroscopy was conducted to obtain absorption spectra of the nanoparticle suspensions and observe the phenomenon known as the "surface plasmon resonance (SPR)," which corresponds to a physical property exhibited only by metallic materials when they have nanoscale dimensions. This appears as a characteristic strong absorption band. Therefore, these spectra confirm the presence of nanoparticles and provide an estimate of their approximate size.

Characterization through UV-Vis spectroscopy revealed distinct peaks, indicating the presence of silver and copper nanoparticles. The absorption peak observed for AgNPs at 425 nm suggested a predominant size of approximately 20 nm, consistent with previous literature [5]. On the other hand, copper nanoparticles displayed a peak at 575 nm, suggesting a size range spanning from 5 to 100 nm (Figure 2).
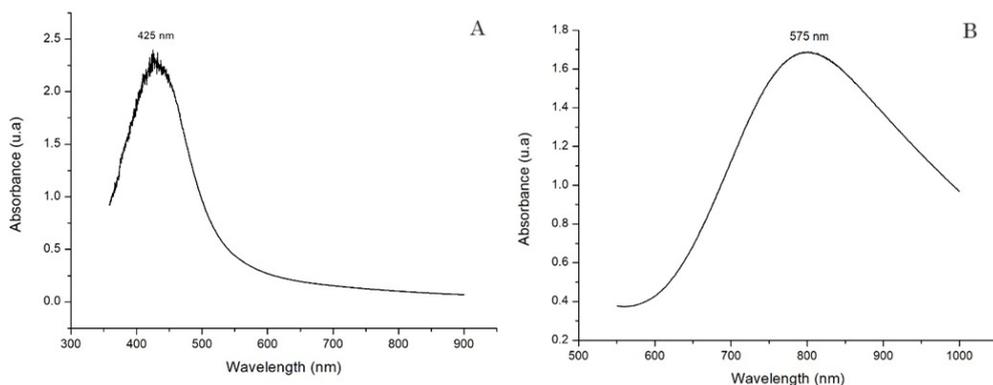
Figure 2. UV-Vis spectrum of silver nanoparticles (AgNPs) and copper nanoparticles ($CuSO_4$NPs).

4.3. *TEM*

The TEM analysis presented in Figures 3 provides insights into the structural characteristics of   silver nanoparticles. Specifically, the images confirm the presence of AgNPs with an average size of around 20 nm, alongside smaller 5 nm particles, indicating variability in size and shape, predominantly spherical. Conversely, $CuSO_4$NPs appear aggregated, potentially influenced by the timing of the characterization process, conducted approximately three months post-synthesis, or inherent properties of the reactants. This aggregation precluded a clear observation of the size and shape of $CuSO_4$NPs during characterization.
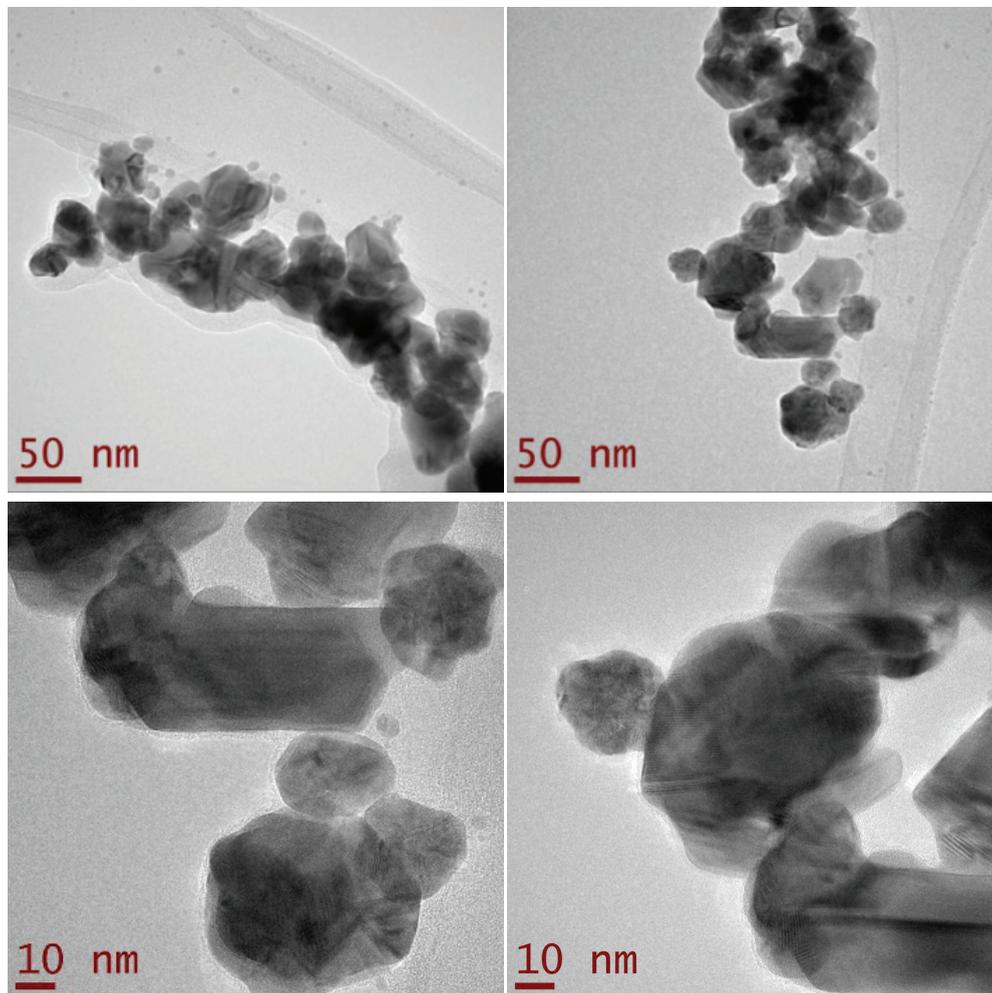
Figure 3. Silver nanoparticles (AgNPs).

4.4. *Antimicrobial effect by Kirby-Bauer Disk Diffusion Susceptibility Test*

The antimicrobial efficacy of the synthesized nanoparticles was assessed using the Kirby-Bauer Disk Diffusion Susceptibility Test. Following incubation for 24 hours, bacterial growth was observed, and the resulting inhibition zones were measured, including the 7 mm diameter of the disc. Detailed results for each trial were documented in Figures 4-5 and Tables 1, providing a comprehensive overview of the antimicrobial activity exhibited by the nanoparticles against the evaluated bacterial strains.
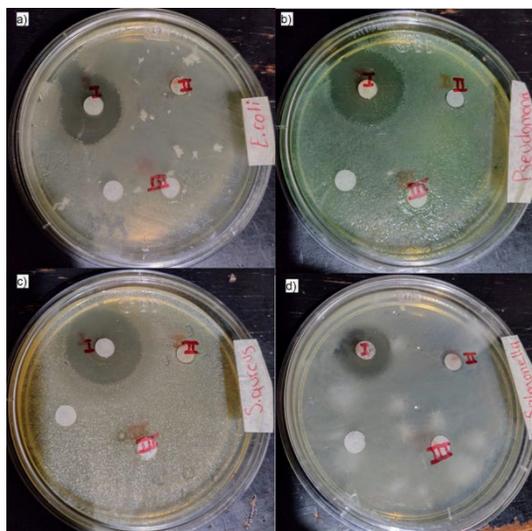
Figure 4. Inhibition zones generated by the copper nanoparticles CuSO4NPs (I), AgNPs (II) and the Trademark 1 (III), against the bacterial strains a) *Escherichia coli*, b) *Pseudomonas sp.* c) *Staphylococcus aureus*, and d) *Salmonella sp.* Images obtained 24 hours after incubation.
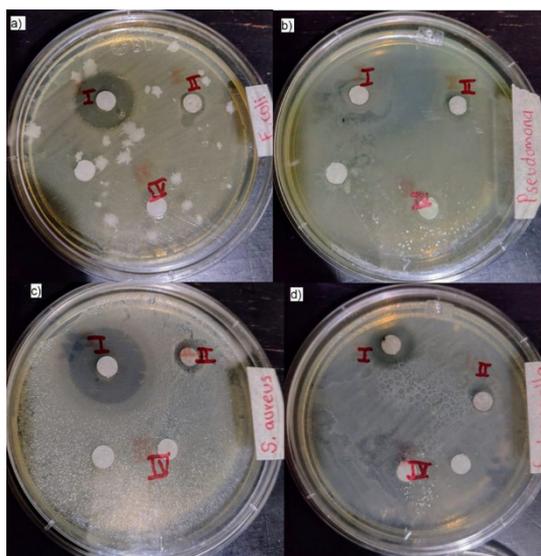
Figure 5. Inhibition zones generated by the copper nanoparticles $CuSO_4NPs$ (I), AgNPs (II) and the Trademark 2 (IV), against the bacterial strains a) *Escherichia coli*, b) *Pseudomonas sp.* c) *Staphylococcus aureus*, and d) *Salmonella sp.* Images obtained 24 hours after incubation.

Microorganisms	Kirby-Bauer Disk Diffusion Susceptibility Test (mm) 24 hours after incubation			
	I. CuNP's	II. AgNP's	III. Trade-Mark 1	IV. Trade-Mark 2
Escherichia coli	22	10	10	10
Pseudomonas	20	9	9	9
Staphylococcus aureus	26	10	8	9
Salmonella	17	9	8	8

Table 1. Results of Kirby-Bauer Disk Diffusion Susceptibility Test.
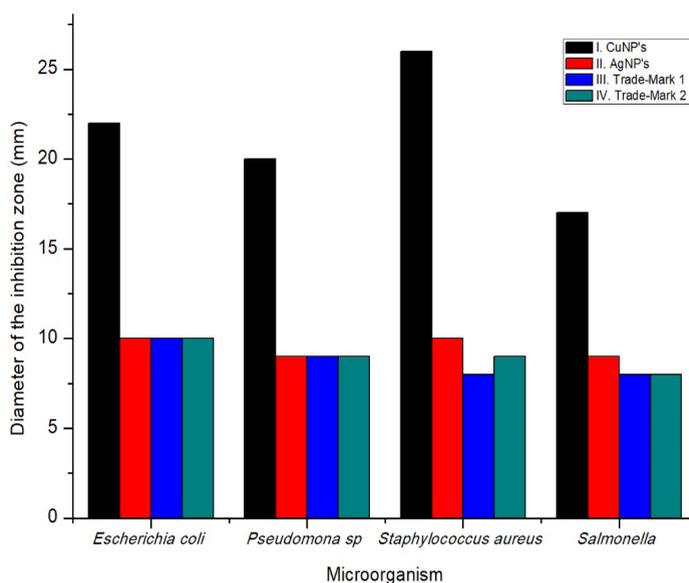
Figure 6 . Diameter of the inhibition zone in mm. After 24 h incubation.

The observed results suggest a more potent antimicrobial effect of copper nanoparticles compared to silver nanoparticles, as evidenced by the larger inhibition zones observed in all experiments. However, it is imperative to consider the potential toxicity associated with copper nanoparticles.

The precise mechanisms underlying the antibacterial action of nanoparticles remain incompletely understood. Although the exact mode of action against bacteria has yet to be fully elucidated, some researchers have proposed potential effects of nanoparticles on bacterial cells. Specifically, it is suggested that ions released by nanoparticles may bind to the bacterial cell wall, causing disruption [6]. These ions can penetrate bacterial cells, disrupting biochemical processes by

generating reactive oxygen species (ROS) that interact with membrane proteins, affecting their permeability [7]. Furthermore, it is suggested that nanoparticle exposure may also impact bacterial DNA [8].

Further research is warranted to comprehensively understand the mechanisms underlying the antibacterial activity of nanoparticles and to evaluate their safety and efficacy for various applications.

5. Conclusions

The synthesis and characterization of silver and copper nanofluids have demonstrated promising antimicrobial properties against pathogenic microorganisms, including *Escherichia coli*, *Staphylococcus aureus*, *Pseudomonas* sp., and *Salmonella.* The nanofluids, particularly those containing copper nanoparticles, exhibited significant inhibition zones in antimicrobial susceptibility tests, suggesting their potential as effective disinfectants.

These findings highlight the importance of exploring alternative antimicrobial strategies amidst rising concerns over antimicrobial resistance and the limitations of traditional antibiotics. By leveraging the unique physicochemical properties of metallic nanoparticles, such as high surface area to volume ratio and biocompatibility.

However, further research is necessary to elucidate the precise mechanisms underlying the antimicrobial activity of these nanoparticles and to assess their safety and efficacy for widespread use.

Acknowledgments

References

1. Grumezescu, A. M., & Chifiriuc, C. M. (2014). Prevention of microbial biofilms - The contribution of micro and nanostructured materials. *Current Medicinal Chemistry, 21*(29), 3311. https://doi.org/10.2174/0929867321666140304101314

2. Ramaiah, G. B., Tegegne, A., & Melese, B. (2021). Developments in nano-materials and analyzing its role in fighting COVID-19. *Materials Today Proceedings, 47*, 4357–4363. https://doi.org/10.1016/j.matpr.2021.05.020

3. Polívková, M., Hubáček, T., Staszek, M., Švorčík, V., & Siegel, J. (2017). Antimicrobial treatment of polymeric medical devices by silver nanomaterials and related technology. *International Journal of Molecular Sciences, 18*(2), 419. https://doi.org/10.3390/ijms18020419

4. Yang, X., Wang, D., Zhou, Q., Nie, F., Du, H., Pang, X., Fan, Y., Bai, T., & Xu, Y. (2019). Antimicrobial susceptibility testing of Enterobacteriaceae: Determination of disk content and Kirby-Bauer breakpoint for ceftazidime/avibactam. *BMC Microbiology, 19*(1), 240. https://doi.org/10.1186/s12866-019-1613-5

5. Haiss, W., Thanh, N. T., Aveyard, J., & Fernig, D. G. (2007). Determination of size and concentration of gold nanoparticles from UV-vis spectra. *Analytical Chemistry, 79*(11), 4215–4221.
    https://doi.org/10.1021/ac0702084

6. Antonoglou, O., Giannousi, K., Arvanitidis, J., Mourdikoudis, S., Pantazaki, A., & Dendrinou-Samara, C. (2017). Elucidation of one-step synthesis of PEGylated CuFe bimetallic nanoparticles. Antimicrobial activity of CuFe@PEG vs Cu@PEG. *Journal of Inorganic Biochemistry, 177*, 159–170.
    https://doi.org/10.1016/j.jinorgbio.2017.09.014

7. Loredo-Becerra, G. M., Durán-Almendárez, A., Calvillo-Anguiano, A. K., DeAlba-Montero, I., Hernández-Arteaga, L. O., & Ruiz, F. (2022). Waterborne antifouling paints containing nanometric copper and silver against marine Bacillus species. *Bioinorganic Chemistry and Applications, 2022*, 2435756.
    https://doi.org/10.1155/2022/2435756

8. Paesa, M., Remirez de Ganuza, C., Alejo, T., Yus, C., Irusta, S., Arruebo, M., Sebastián, V., & Mendoza, G. (2023). Elucidating the mechanisms of action of antibiotic-like ionic gold and biogenic gold nanoparticles against bacteria. *Journal of Colloid and Interface Science, 633*, 786–799.
    https://doi.org/10.1016/j.jcis.2022.11.138

SYNTHESIS OF CHITOSAN SCAFFOLDS FOR TISSUE ENGINEERING USING SCHIFF REACTIONS

Gabriela Martínez-Mejía[1], Andrés Castell-Rodríguez[2], Rogelio Jiménez-Juárez[3], Mónica Corea[1*]

[1]Escuela Superior de Ingeniería Química e Industrias Extractivas, Instituto Politécnico Nacional, San Pedro Zacatenco, Gustavo A. Madero 07738, Ciudad de México, México.

[2]Departamento de biología celular y tisular, Universidad Nacional Autónoma de México, Facultad de Medicina, Circuito interior, Ciudad universitaria, Av. Universidad 3000, C.P. 04510, Ciudad de México, México

[3]Departamento de Química Orgánica, Escuela Nacional de Ciencias Biológicas, Instituto Politécnico Nacional, Prolongación de Carpio y Plan de Ayala s/n, Miguel Hidalgo, 11340, Ciudad de México, México.

   * mcoreat@yahoo.com.mx, mcorea@ipn.mx

Abstract

Chitosan (CS) and glutaraldehyde (GA) hydrogels were synthesized for tissue engineering applications using a Schiff reaction. CS was reacted with GA (a cross-linker) at different concentrations, which were expressed as percentage of weigh. The effect of GA concentration on the swelling and rheological properties was evaluated. The Schiff crosslinking reaction was monitored by UV–vis spectroscopy (550 nm) to determine the reaction kinetic at 60 °C. The hydrogel structures were characterized by NMR, FT-IR, HR-MS and SEM, while the degree of cross-linking was examined with TGA-DA. The smaller pores and greatest swelling were found in hydrogels containing 10 wt% of GA. However, only the hydrogels with 2, 4 and 6 wt.% of GA displayed viable cells, indicating their *in vitro* cytocompatibility. The rheological studies showed that the values of the loss and storage modules in the hydrogels increased with temperature. Further research is needed to verify the adequacy of these hydrogels as a scaffold for tissue engineering *in vivo*.

Keywords: Scaffolds; Tissue engineering; Schiff reactions; chitosan; hydrogels

1. Introduction

The development of suitable scaffolds for tissue engineering is still one of the most important fields in regenerative medicine [1]. Creating scaffolds with the satisfactory physicochemical factors to sustain cell growth and tissue formation allow to regenerative medicine to improve, restore or replace the biological functions of damaged tissues and organs [2]. The scaffolds should serve as templates to guide adhesion, proliferation, differentiation and cell maturation. Furthermore, they must provide the cells a free space for vascularization, penetration and transfer of nutrients, oxygen and waste products [1, 3]. In other words, the scaffolds need to have appropriate mechanical properties and porous structures that allow the free diffusion of nutrients and waste. Also, the degradation process rate should be equal to the cellular growth rate [4, 5]. Essentially, scaffolds serve as an artificial extracellular matrix to offer structural support for the cells and free space for the flow of growth factors. The extracellular matrix consists of a crosslinked mesh between fibrous proteins and glycosaminoglycans (GAGs, such as heparan sulfate, chondroitin sulfate and keratan sulfate) to form proteoglycans [6]. These compounds have been reported for the regeneration of cartilage [7], bone [8], hair [9], nerves [10], tendons [10], ligaments [11], skin [12], fibrous tissue, blood vessels [13] and even heart and valves [14, 15].

The used synthetic polymers to prepare scaffolds are inexpensive but, they allow better functionality than natural polymers [16]. Furthermore, used polymeric materials to create structures in the form of scaffolds include the hydrogels [17], porous nanostructures and nanofibers [16]. Hydrogels are three-dimensional polymer networks able to swell and absorb a large amount of aqueous solution without losing their structure [17 - 19]. In addition, they can retain solvent at least 20 % of their own weight and swell significantly by absorbing water, followed by shrinking again after de-swelling. However, the process of cross-linking creates an insoluble network [20, 21].

Several monomers and crosslinking agents have been employed to synthesize hydrogels with a wide range of chemical compositions, many of which could be employed as scaffolds [22, 23]. There are several routes of synthesis of these platforms including Michael, Click and Schiff reactions. A Michael reaction involves the nucleophilic addition of a carbanion or a nucleophile (e.g., thiols and amines) to create a reaction with an α, β unsaturated carbonyl compound [24].

Hence, it is important to choose the type of reaction and depends on each special polymer. For example, chitosan (CS) has been used for the preparation of hydrogels via the Schiff base reaction.[16] CS is a linear heteropolymer of glucosamine and N-acetyl glucosamine residues (Figure 1) are obtained by the deacetylation of chitin. This weak base is soluble in acidic solution (pH 6.5) and insoluble in water and organic solvents [25 - 31]. It is biodegradable, biocompatible and non-toxic and exhibits mucoadhesive properties [20].
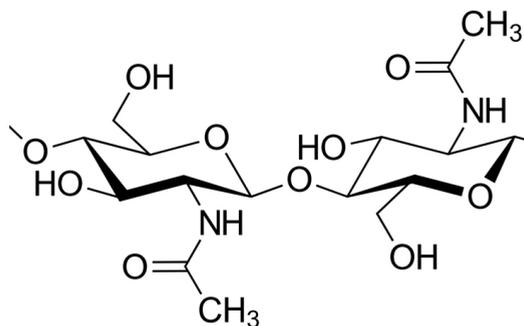
Figure 1. Chemical structure of chitosan.

2. Materials

CS (75% deacetylated) and 2,4-dinitrophenylhydrazine (DNP) (99%) were obtained from Sigma-Aldrich (Iceland), 99% acetic acid from J.T. Baker (Mexico), ethanol and dichloromethane from Alveg (Mexico), and 25 wt% GA from Merck (Germany). Distilled water grade II was used as solvent. The high glucose Dulbecco's modified Eagle's medium (DMEM), antibiotic-antimitotic 100X and fetal bovine serum (FBS) were purchased from Biowest (Mexico). Trypsin/ EDTA solution and phosphate buffed saline (PBS, pH 7.4) were acquired from Gibco (Mexico). Calcein AM and ethidium homodimer (EthD-1) were provided by Life Technologies (USA).

3. Methods

3.1. *Synthesis of chitosan platforms*

The synthesis of CS scaffolds **3** (Scheme 1) started by dissolving 0.03 g CS **1** in 1% acetic acid aqueous solution. Different aliquots (0.05, 0.1, 0.15, 0.20 and 0.25 mL) of GA **2** (1.25% aqueous solution) were added drop wise and the reaction mixture was stirred for 2 h at 60 °C. Assays were performed by triplicate.
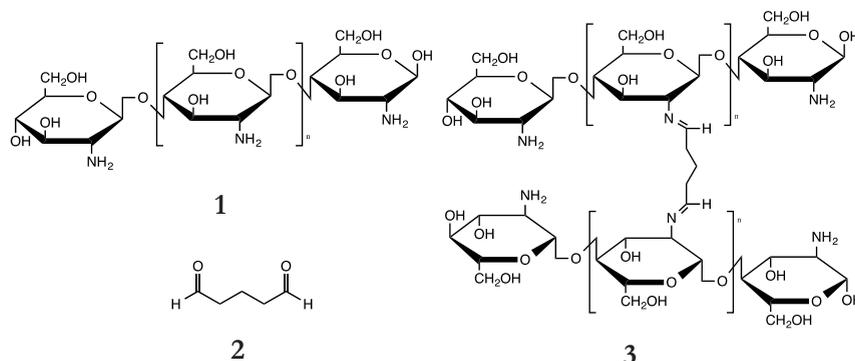
Scheme 1. Crosslinked hydrogels of chitosan-glutaraldehyde.

3.2. Reaction kinetics

The reaction between CS and GA was monitored by UV-vis spectroscopy at 550 nm in a PerkinElmer Lamda 25 UV-vis double beam spectrophotometer (Model 643, USA), taking samples every 5 min. Samples were extracted with methylene chloride under vigorous agitation and then, 2 mL of ethanol and 2 mL 2,4-dinitrophenylhydrazine of acid alcoholic solution (DNP) were added to the organic phase and the mixture was stirred[21]. The samples were analyzed by UV-vis spectroscopy.

3.3. Nuclear Magnetic Resonance

One-dimensional (1D) ^{1}H-NMR spectrum was recorded at 499.85 MHz on a Varian (now Agilent) NMR System 500 spectrometer (Agilent Technologies, Inc., Santa Clara, CA, USA). A sample of 30 mg hydrogel with GA at 10 wt% as well as its uncrossed fraction were dissolved in deuterated acetic acid/deuterated water (D_2O) (1:1). The non-crosslinked part of polymer was extracted washing the hydrogels by Soxhlet techniques using ethyl acetate as solvent. The ^{1}H NMR spectrum was recorded by employing a PRESAT pulse sequence to suppress the residual H_2O signal.

3.4. Fourier Transform Infrared Spectroscopy (FT-IR)

The fresh hydrogels were analyzed by Fourier transform infrared spectroscopy (FT-IR) in an infrared spectrophotometer, equipped with ATR in the mid-infrared region, from 400 to 4000 cm^{-1}.

3.5. *High-resolution mass spectrometry*

Fresh hydrogel was also examined by high-resolution mass spectrometry (HR-MS) on a mass spectrophotometer with micrOTOF II-Q and electrospray ionization (BrukerDaltonisc, Billerica, MA, USA).

3.6. *Scanning electron microscopy (SEM)*

The surface morphologies and cross sections of the chitosan scaffolds were coated with gold and observed with a field emission scanning electron microscope (JEOL JSM 6400) at an accelerating voltage of 5 kV.

3.7. *Thermogravimetric*

Derivate thermogravimetric analysis (DA-TGA) of the hydrogel was carried out on a 6000 PerkinElmer simultaneous thermal analyzer (Germany). The samples were heated from 25 to 500 °C at a rate of 10 °C/min under nitrogen atmosphere.

3.8. *Rheological analysis*

Rheological properties were evaluated with a Modular Compact Rheometer (model MCR 502, Anton Paar, Austria) using PP25 parallel plate geometry (25 mm diameter, 0°). The sample was placed in the center of the bottom plate. The upper plate was immediately lowered to a gap of 1 mm and the measurement was performed. The analysis was made at 30, 35 and 40 °C.

3.9. *Degree of cross-linking*

Fresh gel sample was washed in a Soxhlet system using ethyl acetate as solvent until constant weight. The degree of cross-linking was calculated gravimetrically using equation (1).

$$\%D = \frac{W_g}{W_0} \text{ x } 100 \qquad\qquad (1)$$

Where W_g is the weight of the sample after washing and W_0 is the initial weight.

3.10. *Cytotoxicity assay*

For testing the capacity of the scaffolds to support cell growth, primary cultures of human fibroblasts were used. These cells were obtained from the skin of healthy donors with prior informed consent. Thin layers samples of hydrogels were put on 0.5 x 0.5 mm coverslip frames, these were put in 48-well plates and sterilized by UV irradiation. Subsequently, 18 μL of cell suspension in DMEM were seeded onto hydrogel samples (5000 cells per sample) and incubated for 1 h at 37 °C, adding DMEM to the hydrogels. The cell-seeded hydrogels were cultivated for 1 week at 37 °C, changing the medium every 2 days. After 3 days, the cultivation medium was removed from the wells. The hydrogels were rinsed with PBS solution, stained with 1 mL of calcein/ethidium homodimer solution, and incubated for 1 h at 37 °C. With this dye, living cells fluoresce green and the nuclei of dead cells is red, thus providing the basis of the fluorescence live/dead assay.

4. Results

A series of hydrogels of CS and GA were synthesized (at 60 °C) by means of the Schiff base method, obtaining five concentrations of GA (2, 4, 6, 8 and 10 wt%) and therefore a range in the degree of cross-linking in the polymer. The synthesis was carried out by triplicate.

To know the progress of the reaction, the conversion of glutaraldehyde from the formation of hydrazones was determined. The reaction scheme 2 shows the carbonyl of glutaraldehyde **1** reacting with 2,4-dinitrophenylhydrazine **2** to form phenylhydrazones **3** obtaining a yellow complex. This is an indicator of the presence of aldehyde in the medium [32].
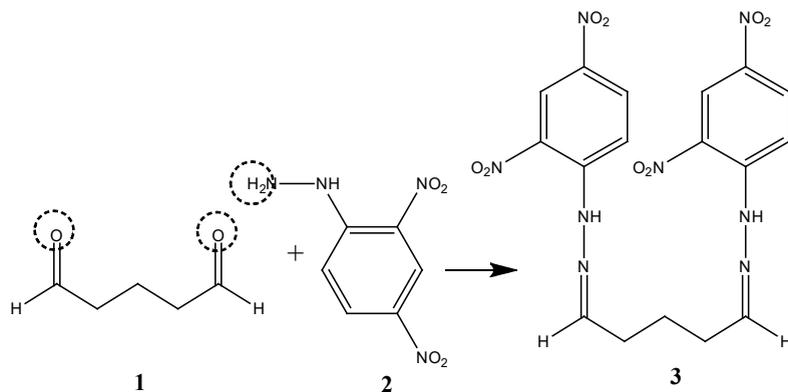
Scheme 2. Aldehyde identification reaction scheme.

The reaction progress was monitored for each hydrogel at 60 °C. The conversion data of GA as a function of time for hydrogels with a concentration of 2 wt% and 10 wt% are illustrative of the results as an example (Figure 2). The hydrogel containing GA at 2 wt% was completely consumed at 50 min of reaction. For the hydrogel with GA at 10 wt%, this occurred at 120 min of reaction.
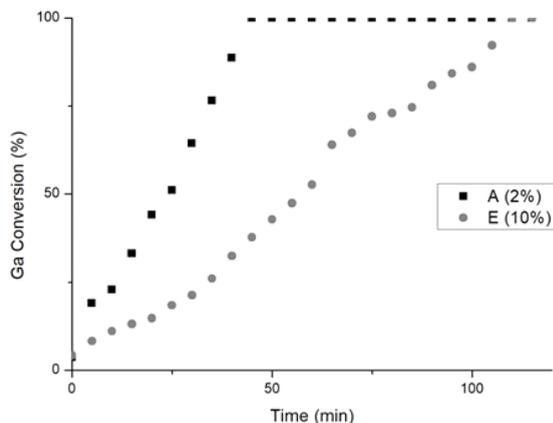

Figure 2. GA conversion of 2 wt% (■) and 10 wt% (●) hydrogel.

The reaction order was calculated from the GA conversion data for each hydrogel. Figure 3 shows the reaction order results for hydrogels with 2 wt% (■) and 10 wt% (●). It is possible to observe that the reaction between chitosan and glutaraldehyde has zero-order kinetic. That is, the reaction rate is independent of the concentration of reactants. Some authors have reported this reaction as spontaneous and immediate [19].
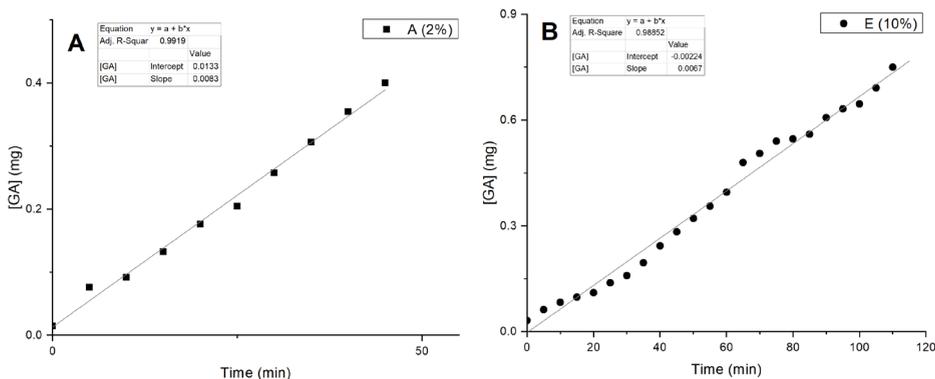
Figure 3. Reaction order of hydrogel at 2% by weight (■) and 10% by weight (●).

Spectra of ^{1}H NMR, result is shown for the crosslinking in the hydrogel containing GA at 10 wt% (Figure 4). A signal at δ=7.75 ppm was attributed to the imine protons for cross-linking between GA and CS (-N=CH-), in agreement with the report by Ali Reza Karimi [23]. A wide signal at δ=4.66 ppm corresponds to hydroxyl (-OH) groups in the CS chain, δ=3.16 ppm to oxygen base protons near hydroxyls (OH-CH-), and δ=1.83 ppm to methylene groups of the cross-linked glutaraldehyde chain.
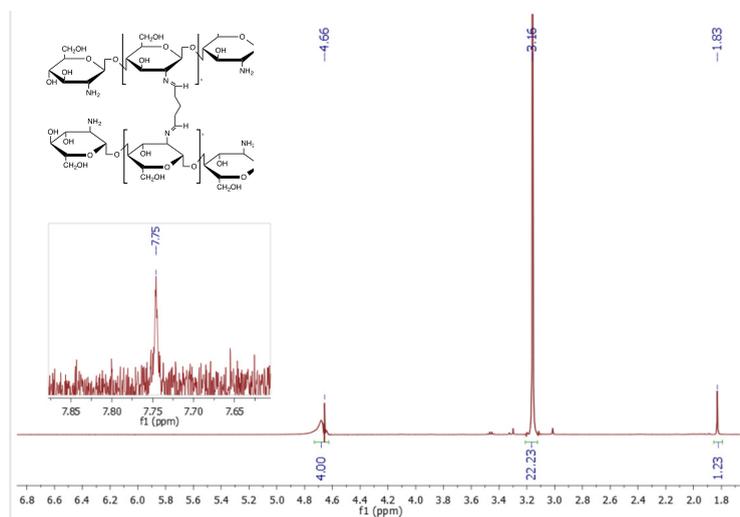
Figure 4. ^{1}H NMR of hydrogel at 10 wt%.

FT-IR analysis was carried out on fresh hydrogels with the crosslinking agent at 2 wt%, 6 wt% and 10 wt% (Figure 5). The absorption band at 1632 cm^{-1} corresponds to the stretching frequencies of the imine bond (HC=N-). This is
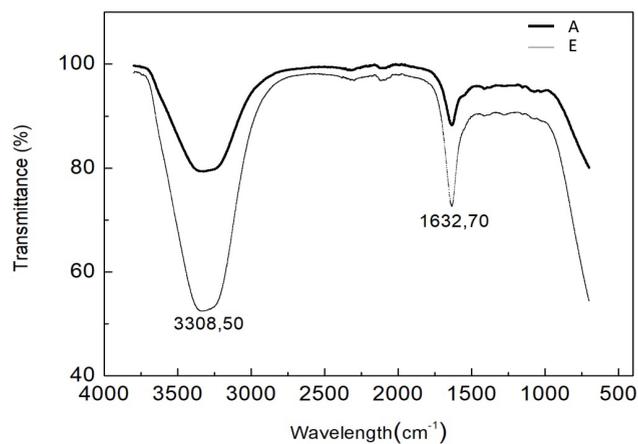

Figure 5. FT-IR spectra of chitosan-glutaraldehyde hydrogels containing the crosslinking agent at 2 wt% and 10 wt%.

according with a previous study, which employ the same reaction that assigned the imine group to 1568 cm^{-1} [26] and the overlapped stretching vibration of -N-H and –OH to 3308 cm^{-1} [26]. Both these signals presently increased when there was a greater cross-linking degree in the hydrogels.

HR-MS reveals a wide distribution of the molecular mass for each hydrogel (Figure 6). Some chains were found with high molecular weight and others with low molecular weight. The latter are attributed to a slow reaction that does not permit the fast growth of polymeric chains. This evidence corroborates the findings of the NMR spectrum in which residual CS and GA were detected.
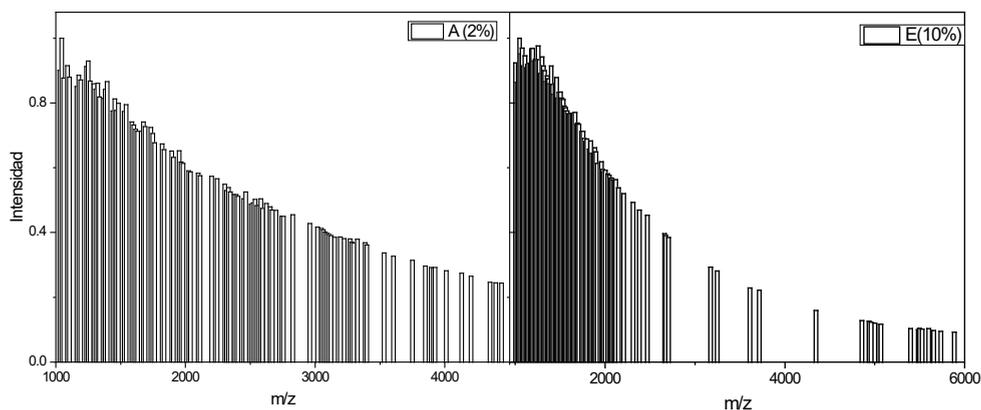

Figure 6. HR-MS spectra of chitosan-glutaraldehyde hydrogels containing the crosslinking agent at 2 wt% and 10 wt%.

The morphology of fresh and freeze-dried hydrogels was examined by SEM. Micrographs of the hydrogels containing 2 and 10 wt% of the crosslinking agent (Figure 7) show highly porous surfaces and the formation of flakes in fresh (Panel A) and lyophilized (Panel B) gels. There are studies that document the importance of a porous surface for cells to be implanted inside of the hydrogel and for nutrients to be able to flow to such cells, thus enabling tissue growth on the scaffold [3].

The DA-TGA test indicated that the hydrogel with the greatest concentration of GA decomposed at the highest temperature (Figure 8), caused by the greater crosslinking density and therefore a higher average molecular weight of the polymer chains. At first, the hydrogels with GA at 2, 4 and 6 wt.% presented the same weight loss at $25 < T/°C < 52$, attributed to dehydration of the material
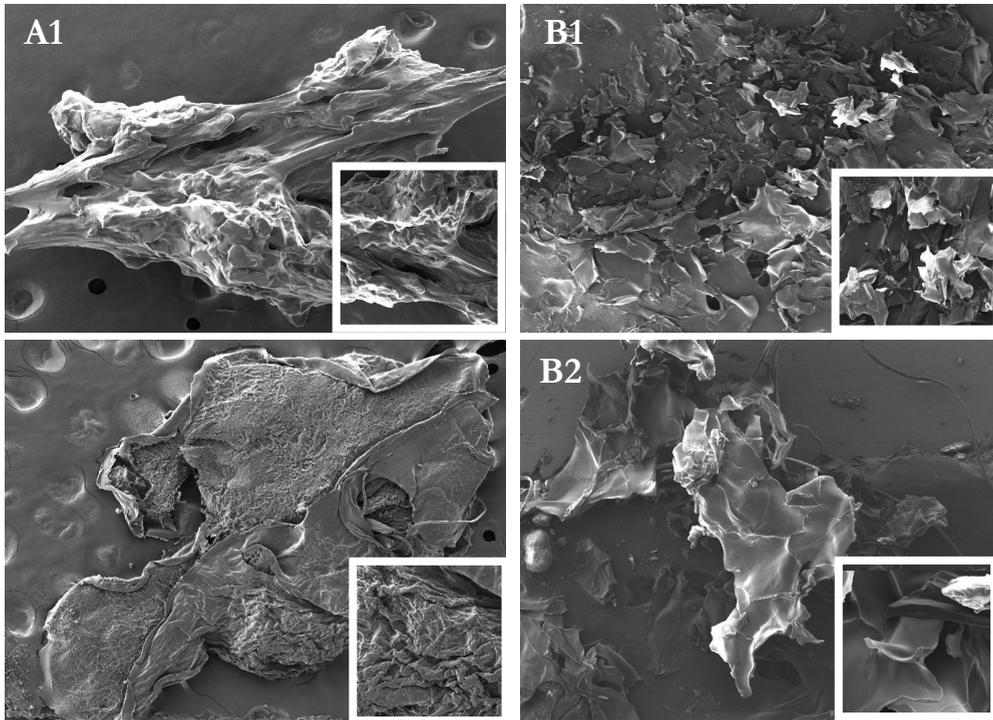
Figure 7. Microscopy images of the surfaces of hydrogels, both fresh (A) and lyophilized (B), containing 2 wt% and 10 wt% of the crosslinking agent.
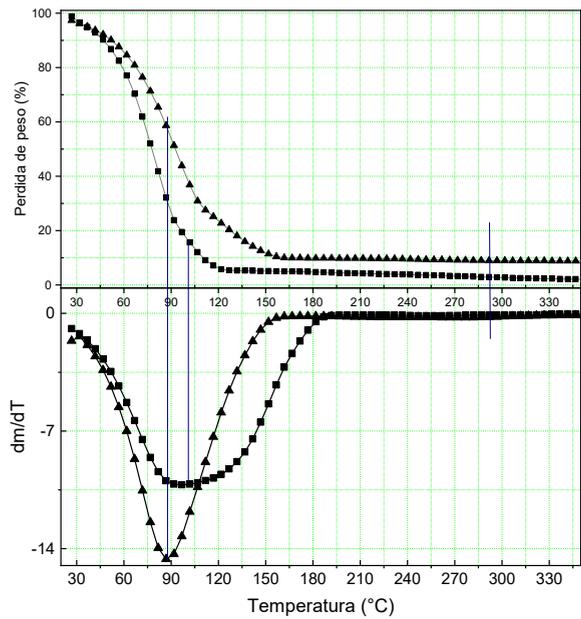

Figure 8. TGA and derivate analyses of crosslinked hydrogels with glutaraldehyde at 2 wt% (■) and 10 wt% (▲).

and the beginning of the decomposition of shorter chains. As the temperature approached 100 °C, there was a faster decomposition of the hydrogels containing GA at 2 and 6 wt.%. On the other hand, the hydrogel with GA at 10 wt.% di0d not accelerate its decomposition (due to its greater water retention).

The rheological properties of the hydrogels were studied by oscillatory rheology at 30, 35 and 40 °C. The storage modulus (G') and loss modulus (G'') were determined as a function of strain, (Figure 9), finding that G' was higher than G''. Thus, the G' represents the elastic response of the sample, which is reportedly typical for gels or samples with a certain rigidity in their structure [33]. The shape of the storage modulus curve at low frequencies is typical of the shape of a polymer with mechanically weak cross-links [34].
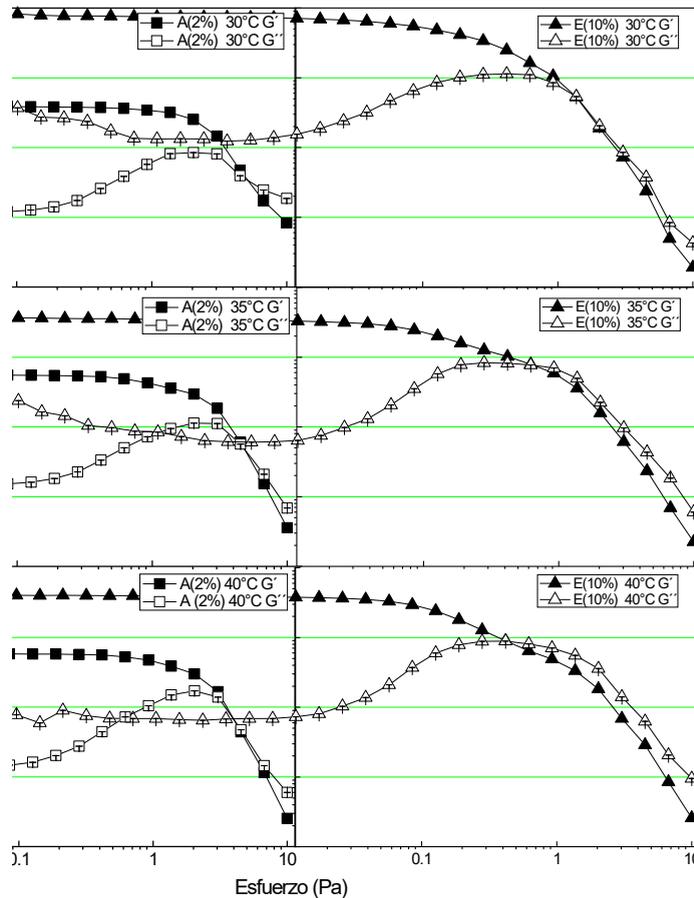

Figure 9. Storage modulus and loss modulus behavior of hydrogels with glutaraldehyde at 2 wt% (■) and 10 wt% (▲).

The degree of swelling of the material was determined by the quantity of water absorbed by the hydrogel. The percent of swelling was calculated as a function of the time. The material was immersed in water, using hydrogels with 2, 6 and 10 wt% of GA (Figure 10). The results reveal that the degree of crosslinking strongly influenced the swelling volume. That means, the material with the greatest degree of swelling was the material with the greatest percentage of the crosslinking agent (10 versus 2 wt%, respectively). Accordingly, the hydrogels containing 10 wt% GA absorbed 60% of water in the first 1.5 min, while the materials with 2 wt% only absorbed 20 %.
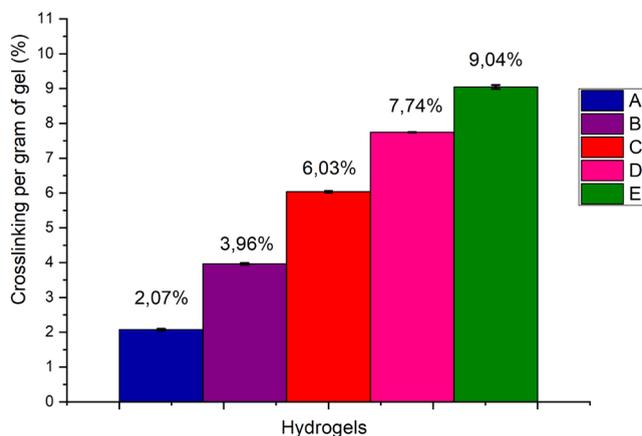

Figure 10. Crosslinking agent percentage of hydrogels at
2 wt% (■), 6 wt% (●) and 10 wt% (▲).

The cytocompatibility of CS-GA hydrogels with human fibroblasts was evaluated by using a live/dead cytotoxicity assay. The cells were seeded on the hydrogels and left for three days at 37 °C. Subsequently, the hydrogel platforms were stained with calcein/ethidium homodimer for the visualization of viable cells under an epifluorescence microscope (Figure 11). Viable fibroblasts were clearly seen in the platforms containing 2, 4 and 6 wt.% GA, indicating cytocompatibility at those concentrations. Viable cells can be appreciated alone or clusters, both on the surface of hydrogels. The hydrogels with GA at 8 and 10 wt% did not display cell viability, cells could not adhere perhaps due to the higher concentration of GA.
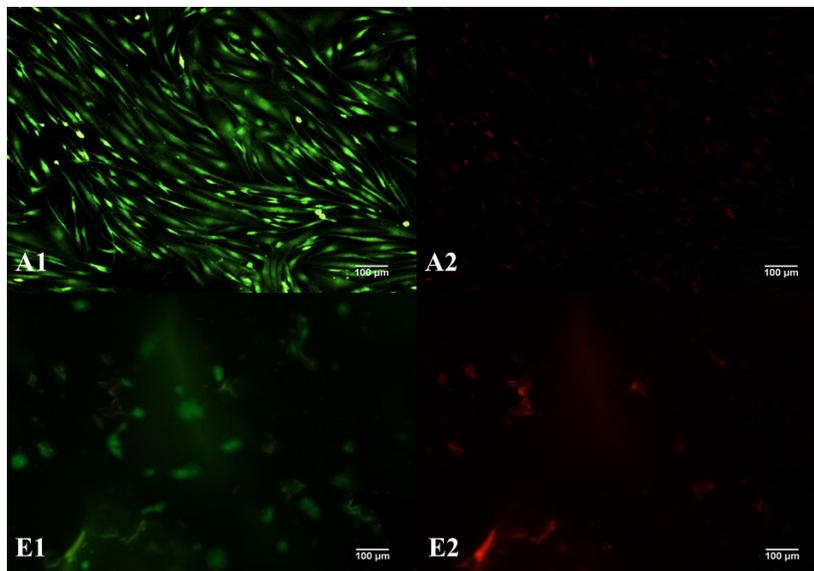
Figure 11. Fluorescence micrographs of the fibroblast cells onto hydrogels with the crosslinking agent at 2 wt% (A) and 10 wt% (E). Live cells are visible as green (1), dead cells are observed as red (2).

5. Conclusions

Novel hydrogels were synthesized by using Schiff reactions to cross-link CS with GA. Hydrogels having different concentrations of GA were tested to determine the effect on swelling and rheological properties. Examination was made of the degree of crosslinking bond formation (with TGA-DA) and of the presence of residual GA in the uncrossed part (with NMR). The reaction kinetic and reaction order assessed with UV-vis spectroscopy, showed a pseudo-zero order for the reaction. Moreover, the constant rate values were dependent on the concentration of GA. The rheological properties evidenced a decrease in the strain strength when a more rigid network is formed. There was a significant increase in the swelling capacity of the material with greater GA content, finding the best water absorption capacity at 10 wt%. However, only the hydrogels at 2, 4 and 6 wt% were cytocompatible. The results suggest that hydrogels consisting of CS cross-linked with GA could possibly provide an adequate scaffold for tissue engineering. Further research is needed to explore the in vivo plausibility of such a scaffold.

Acknowledgement

References

1. Demina, T. S., Zaytseva-Zotova, D. S., Akopova, T. A., Zelenetskii, A. N., & Markvicheva, E. A. (2017). Macroporous hydrogels based on chitosan derivatives: Preparation, characterization, and in vitro evaluation. *Journal of Applied Polymer Science, 134*(17-19). https://doi.org/10.1002/app.44651

2. Scaplehorn, N. (2012). Regenerative medicine. *Cell, 149*(727–729). https://doi.org/10.1016/j.cell.2012.04.022

3. Kim, S., Kawai, T., Wang, D., & Yang, Y. (2016). Engineering a dual-layer chitosan–lactide hydrogel to create endothelial cell aggregate-induced microvascular networks in vitro and increase blood perfusion in vivo. *ACS Applied Materials & Interfaces, 8*(19245–19255). https://doi.org/10.1021/acsami.6b04431

4. Jin, R., Moreira Teixeira, L. S., Krouwels, A., Dijkstra, P. J., van Blitterswijk, C. A., Karperien, M., et al. (2010). Synthesis and characterization of hyaluronic acid-poly(ethylene glycol) hydrogels via Michael addition: An injectable biomaterial for cartilage repair. *Acta Biomaterialia, 6*(1968–1977). https://doi.org/10.1016/j.actbio.2009.12.024

5. Lee, K. Y., & Mooney, D. J. (2001). Hydrogels for tissue engineering. *Chemical Reviews, 101*(1869–1879). https://doi.org/10.1021/cr000108x

6. Ahadian, S., Sadeghian, R. B., Salehi, S., Ostrovidov, S., Bae, H., Ramalingam, M. et al. (2015). Bioconjugated hydrogels for tissue engineering and regenerative medicine. *Bioconjugate Chemistry, 26*(1984–2001). https://doi.org/10.1021/acs.bioconjchem.5b00360

7. King-Martínez, A. C., Doger-Echegaray, P., & Hoyo-Pérez, L. I. (2020). Identificación por imágenes del paciente con pie diabético del tipo de lesiones que requirieron o requirirán amputación. *Acta Ortopédica Mexicana, 34*(2), 77–80. https://doi.org/10.35366/95318

8. Montoya, A., Gallardo-Rincón, H., Silva-Tinoco, R., García-Cerde, R., Razo, C., Ong, L. et al. (2023). Type 2 diabetes epidemic in Mexico. Burden of disease 1990-2021 analysis and implications for public policies. *Gaceta Médica de México, 159*(474–486). https://doi.org/10.24875/GMM.23000378

9. Holl, J., Kowalewski, C., Zimek, Z., Fiedor, P., Kaminski, A., Oldak, T. et al. (2021). Chronic diabetic wounds and their treatment with skin substitutes. *Cells, 10*(3), 655. https://doi.org/10.3390/cells10030655

10. Funakoshi, T., Majima, T., Iwasaki, N., Suenaga, N., Sawaguchi, N., Shimode, K. et al. (2005). Application of tissue engineering techniques for rotator cuff regeneration using a chitosan-based hyaluronan hybrid fiber scaffold. *The American Journal of Sports Medicine, 33*, 1193–1201.
    https://doi.org/10.1177/0363546504272689

11. Funakoshi, T., Majima, T., Iwasaki, N., Yamane, S., Masuko, T., Minami, A. et al. (2005). Novel chitosan-based hyaluronan hybrid polymer fibers as a scaffold in ligament tissue engineering. *Journal of Biomedical Materials Research Part A, 74*, 338–346.
    https://doi.org/10.1002/jbm.a.30237

12. Wu, R. D. (2009). Application of synthetic and natural scaffold materials in skin tissue engineering. *Journal of Clinical Rehabilitation Tissue Engineering Research, 12*, 2317–2320.

13. Scherner, M., Reutter, S., Klemm, D., Sterner-Kock, A., Guschlbauer, M., Richter, T. et al. (2014). In vivo application of tissue-engineered blood vessels of bacterial cellulose as small arterial substitutes: Proof of concept? *Journal of Surgical Research, 189*, 340–347.
    https://doi.org/10.1016/j.jss.2014.02.011

14. Blan, N. R., & Birla, R. K. (2008). Design and fabrication of heart muscle using scaffold-based tissue engineering. *Journal of Biomedical Materials Research Part A, 86*, 195–208.
    https://doi.org/10.1002/jbm.a.31642

15. Fallahiarezoudar, E., Ahmadipourroudposht, M., Idris, A., & Yusof, N. M. (2015). A review of: Application of synthetic scaffold in tissue engineering heart valves. *Materials Science and Engineering C, 48*, 556–565.
    https://doi.org/10.1016/j.msec.2014.12.016

16. Yang, J. A., Yeom, J., Hwang, B. W., Hoffman, A. S., & Hahn, S. K. (2014). *In situ*-forming injectable hydrogels for regenerative medicine. *Progress in Polymer Science, 39*, 1973–1986.
    https://doi.org/10.1016/j.progpolymsci.2014.07.006

17. Miranda, D. G., Malmonge, S. M., Campos, D. M., Attik, N. G., Grosgogeat, B., & Gritsch, K. J. (2016). A chitosan-hyaluronic acid hydrogel scaffold for periodontal tissue engineering. *Journal of Biomedical Materials Research Part B: Applied Biomaterials, 104*, 1691–1702.
    https://doi.org/10.1002/jbm.b.33516

18. Ray, M., Pal, K., Anis, A., & Banthia, A. K. (2010). Development and characterization of chitosan-based polymeric hydrogel membranes. *Designed Monomers and Polymers, 13*, 193–206.
    https://doi.org/10.1163/138577210X12634696333479

19. Buwalda, S. J., Boere, K. W. M., Dijkstra, P. J., Feijen, J., Vermonden, T., & Hennink, W. E. (2014). Hydrogels in a historical perspective: From simple networks to smart materials. *Journal of Controlled Release, 190*, 254–273.

20. https://doi.org/10.1016/j.jconrel.2014.03.052

21. Santillán, R., Nieves, E., Alejandre, P., Pérez, E., Del Río, J. M., & Corea, M. (2014). Comparative thermodynamic study of functional polymeric latex particles with different morphologies. *Colloids and Surfaces A: Physicochemical and Engineering Aspects, 444*, 189–208.
https://doi.org/10.1016/j.colsurfa.2013.12.004

22. Shu, X. Z., Liu, Y., Palumbo, F. S., Luo, Y., & Prestwich, G. D. (2004). In situ crosslinkable hyaluronan hydrogels for tissue engineering. *Biomaterials, 25*, 1339–1348.
https://doi.org/10.1016/j.biomaterials.2003.08.014

23. Thürmer, M. B., Diehl, C. E., Brum, F. J. B., & dos Santos, L. A. (2014). Preparation and characterization of hydrogels with potential for use as biomaterials. *Materials Research, 17*, 109–113.
https://doi.org/10.1590/1516-1439.223613

24. Kopeček, J. (2007). Hydrogel biomaterials: A smart future? *Biomaterials, 28*, 5185–5192.
https://doi.org/10.1016/j.biomaterials.2007.07.044

25. Jansen, L. E., Negrón-Piñeiro, L. J., Galarza, S., & Peyton, S. R. (2018). Control of thiol-maleimide reaction kinetics in PEG hydrogel networks. *Acta Biomaterialia, 70*, 120–128.
https://doi.org/10.1016/j.actbio.2018.01.043

26. Desai, R. M., Koshy, S. T., Hilderbrand, S. A., Mooney, D. J., & Joshi, N. S. (2015). Versatile click alginate hydrogels crosslinked via tetrazine–norbornene chemistry. *Biomaterials, 50*, 30–37.
https://doi.org/10.1016/j.biomaterials.2015.01.048

27. Karimi, A. R., Rostaminejad, B., Rahimi, L., Khodadadi, A., Khanmohammadi, H., & Shahriari, A. (2018). Chitosan hydrogels cross-linked with tris (2-(2-formylphenoxy) ethyl) amine: Swelling and drug delivery. *International Journal of Biological Macromolecules, 118*, 1863–1870.
https://doi.org/10.1016/j.ijbiomac.2018.07.037

28. Giri, T. K., Thakur, A., Alexander, A., Ajazuddin, Badwaik, H., & Tripathi, D. K. (2012). Modified chitosan hydrogels as drug delivery and tissue engineering systems: Present status and applications. *Acta Pharmaceutica Sinica B, 2*, 439–449.
https://doi.org/10.1016/j.apsb.2012.07.004

29. Arakawa, C., Ng, R., Tan, S., Kim, S., Wu, B., & Lee, M. (2017). Photopolymerizable chitosan–collagen hydrogels for bone tissue engineering. *Journal of Tissue Engineering and Regenerative Medicine, 11*, 164–174.
https://doi.org/10.1002/term.1896

30. Croisier, F., & Jérôme, C. (2013). Chitosan-based biomaterials for tissue engineering. *European Polymer Journal, 49*, 780–792.
https://doi.org/10.1016/j.eurpolymj.2012.12.009

31. Duan, J., Liang, X., Cao, Y., Wang, S., & Zhang, L. (2015). High strength chitosan hydrogels with biocompatibility via new avenue based on constructing nanofibrous architecture. *Macromolecules, 48*, 2706–2714.
https://doi.org/10.1021/acs.macromol.5b00117

32. Franzén, H. M., Draget, K. I., Langebäck, J., & Nilsen-Nygaard, J. (2015). Characterization and properties of hydrogels made from neutral soluble chitosan. *Polymers, 7*, 373–389.
https://doi.org/10.3390/polym7030373

33. Jones, L., Kinney, C., & Seligman, R. (1961). The reaction of 2,4-dinitrophenylhydrazine with some dicarbonyl compounds and α-substituted carbonyl compounds. *Journal of the American Chemical Society, 26*, 228–232.
https://doi.org/10.1021/jo01060a056

34. Mourycová, J., Datta, K. K. R., Procházková, A., Plotěná, M., Enev, V., Smilek, J. et al. (2018). Facile synthesis and rheological characterization of nanocomposite hyaluronan-organoclay hydrogels. *International Journal of Biological Macromolecules, 111*, 680–684.
https://doi.org/10.1016/j.ijbiomac.2018.01.068

35. Klompen, E. T. J. (2005). *Mechanical properties of solid polymers: Constitutive modelling of long and short term behaviour*. Eindhoven: Technische Universiteit Eindhoven.

Many of the great advances in materials, medical and measurement devices have been the result of research in the area of nanotechnology, a multidisciplinary field to which many research groups in the world are dedicating their human and economic efforts. A spectacular development of nanotechnology in the medical field was, for instance, the obtaining, in record time, of vaccines to face the recent COVID-19 pandemic; others important advances are in the field of semiconductor devices, with the development of integrated circuits with greater density of active elements, as well as new light-emitting devices or semiconductor materials for applications in optoelectronics. It is not surprising then that many research groups in Mexico are devoted to do research in this field of science and technology, especially due the fact of the transfer of industries which are expecting to be moved to the country as result of the nearshoring, that is, the transfer of factories from the country of origin to places close to the market. Because of these facts, the National Polytechnic Institute, one of the best research institutions in México, is carrying out active research in the field of nanotechnology in its multiple disciplines. Some of these results are summarized in this new volume, which constitutes the fifth in a series of books generated as result of investigations of members of the nanoscience and micro-nanotechnologies network of the National Polytechnic Institute.